Correlated Exotic States: Fractionalization, Fermi Arcs, Competing Phases

I n a u g u r a l - D i s s e r t a t i o n

zur

Erlangung des Doktorgrades

der Mathematisch-Naturwissenschaftlichen Fakultät

der Universität zu Köln

vorgelegt von

Heidrun Weber

aus Aalen/Württemberg

Köln, 2009

Berichterstatter: Prof. Dr. Matthias Vojta
Prof. Dr. Johann Kroha

Tag der mündlichen Prüfung: 29. Juni 2009

Abstract

This thesis in the field of condensed matter theory is concerned with various correlated exotic states in different materials. The topic selection is three-fold, covering aspects of graphene, heavy fermion compounds and high-temperature superconductors.

In Part I, a symmetrically biased graphene bilayer is considered, which is discussed to host an exciton condensate. It is shown that in the continuum limit an oddly-quantized vortex in this condensate binds exactly one zero mode per valley index of the bilayer. Intervalley mixing occurring in the full lattice model slightly splits the zero modes in energy. This result is supported by an exact numerical diagonalization of the lattice Hamiltonian for a finite-size system. Such a vortex binds an irrational fraction of "axial" charge and obeys fractional exchange statistics.

Part II is concerned with heavy fermion materials and discusses the consequences of a momentum-dependent hybridization between the conduction band and the localized f electrons, especially in the case where the hybridization function has nodes in momentum space. Such a situation is motivated by experiments, and is in contrast to the commonly studied local hybridization. In the low-temperature regime a highly anisotropic Fermi liquid evolves, for which thermodynamical and optical properties are studied. We find that thermodynamics is dominated by the heavy quasiparticles present in the antinodal direction in momentum space, where the hybridization is strong, while transport is dominated by the behavior of light, nodal quasiparticles. Based on a mean-field approximation, we furthermore study the phase competition between Kondo screening and ordering phenomena induced by intermoment exchange. According to our findings, it is greatly influenced by the interplay of symmetries of the order parameters in momentum space. The results are applicable to $CeCoIn_5$ and other related heavy fermion compounds.

Part III discusses the recently observed quantum oscillations in the underdoped regime of cuprates and advertises a new mechanism that requires only finite segments of a Fermi surface to exist. Such a situation is indicated by angle resolved photoemission spectroscopy (ARPES) studies, which exhibit so-called Fermi arcs in the normal state of cuprates. We consider a BCS-like model in the vortex state with a pairing gap producing such Fermi arcs. By exact diagonalization of the gauge transformed real-space Hamiltonian it is shown that the density of states at the Fermi level exhibits an oscillatory behavior.

Zusammenfassung

Die vorliegende Arbeit auf dem Gebiet der Theorie der kondensierten Materie beschäftigt sich mit diversen korrelierten exotischen Zuständen in verschiedenen Festkörpern. Die Themenauswahl deckt Aspekte dreier Materialientypen ab: Graphene, Schwerfermionenverbindungen und Hochtemperatursupraleiter.

In Teil I wird Zweischicht-Graphene mit symmetrisch angelegter Gatespannung untersucht, das als Host für ein Exzitonenkondensat diskutiert wird. Es wird gezeigt, dass ein ungerade quantisierter Vortex in diesem Kondensat im Kontinuumlimes genau eine Zero Mode pro Valley-Index bindet. Die Wechselwirkung zwischen den Valleys, die im vollen Gittermodell existiert, führt zu einer leichten Energieaufspaltung der Zero Modes. Dieses Ergebnis wird gestützt durch eine exakte numerische Diagonalisierung des Gitter-Hamilton-Operators für ein endlich großes System. Ein solcher Vortex bindet einen irrationalen Anteil an "axialer" Ladung und unterliegt fraktionaler Statistik.

Teil II beschäftigt sich mit Schwerfermionenverbindungen und diskutiert die Konsequenzen einer impulsabhängigen Hybridisierung zwischen Leitungsband und lokalisierten f-Elektronen, insbesondere wenn die Hybridisierungsfunktion Knotenlinien im Impulsraum aufweist. Dieser Ansatz ist motiviert durch Experimente, und hebt sich ab gegenüber der gemeinhin untersuchten lokalen Hybridisierung. Im Tieftemperaturbereich bildet sich eine stark anisotrope Fermiflüssigkeit aus, für die thermodynamische und optische Eigenschaften untersucht werden. Unsere Ergebnisse zeigen, dass die Thermodynamik von schweren Quasiteilchen dominiert wird, die sich in den Regionen im Impulsraum ausbilden, wo die Hybridisierung stark ist. Transporteigenschaften hingegen werden hauptsächlich durch das Verhalten der leichten Quasiteilchen bestimmt, die in der Nähe der Knotenlinien der Hybridisierung leben. Basierend auf einer Mean-Field-Näherung wird die Phasenkonkurrenz zwischen Kondoabschirmung und Ordnungsphänomenen, die sich aus der Wechselwirkung zwischen den lokalen Momenten entwickeln, untersucht. Gemäß der Ergebnisse ist diese stark beeinflusst durch das Zusammenspiel der Symmetrien der Ordnungsparameter im Impulsraum. Die gewonnenen Erkenntnisse sind anwendbar auf $CeCoIn_5$ und artverwandte Schwerfermionenverbindungen.

In Teil III werden die erst vor kurzem beobachteten Quantenoszillationen im unterdotierten Bereich von Kupraten diskutiert. Es wird ein neuer Mechanismus zur Erzeugung dieser Oszillationen beworben, der nur endliche Abschnitte einer Fermifläche benötigt. Solch eine Situation wird von den Ergebnissen winkelaufgelöster Photoemissionsexperimente (ARPES) gestützt, die sogenannte Fermi Arcs im normalleitenden Zustand der Kuprate zeigen. Es wird ein BCS-artiges Modell im Vortexzustand untersucht mit einer Paarungsfunktion, die Fermi Arcs produziert. Mit exakter Diagonalisierung des eichtransformierten Hamilton-Operators im Ortsraum wird gezeigt, dass ein solcher Ansatz zu einem oszillatorischem Verhalten der Zustandsdichte am Ferminiveau führt.

Contents

1 General introduction

"Traditional" condensed matter theory is basically built on two cornerstones, which were already developed in the 1930s and 1950s: Landau's Fermi liquid theory and Landau's theory of symmetry breaking. Fermi liquid (FL) theory introduces a one-to-one correspondence between the underlying particles, consisting of interacting fermions, and the emerging single-particle fermionic excitations.

FL theory may survive even in the presence of strong correlations - a surprising result regarding the fact that this concept can be understood as a perturbation theory around the non-interacting ground state. In certain regimes heavy fermion compounds are described by this theory exceedingly well exhibiting heavy quasiparticle excitations. However, the occurrence of unconventional superconductivity, magnetism and non-Fermi liquid behavior in these materials go way beyond the FL approach (reviews are e.g. given by Stewart, 2001; Coleman, 2007). Cuprates refuse the description in terms of a FL picture for large parts of the accessible phase diagram, but rather show highly unusual physics like a Mott insulating state, high-temperature superconductivity or a pseudogap state, for which a consistent picture could not be established yet (reviews: Damascelli et al., 2003; Lee et al., 2006). The fractional quantum Hall effect, on the other hand, reveals new types of quantum liquids with quasiparticles that have fractional quantum numbers and possibly obey different statistics than the underlying fermions (review: Stormer et al., 1999).

The mentioned discoveries posed new challenges in the field of condensed matter. While all these phenomena arise from the existence of strong correlations between the constituent particles (review: Fulde et al., 2006), the recently isolated material graphene shows that exotic physics can also occur in weakly correlated systems (for a short overview see Geim and Novoselov, 2007).

This thesis is concerned with various correlated exotic states in different materials. By exotic, we denote two different types of properties: (i) a FL with unconventional properties, like a symmetry breaking in the style of unconventional superconductivity, or (ii) systems that cannot be described from a FL point of view at all, e.g., because of topological excitations leading to fractionalized quantum numbers or strong correlations like in the underdoped phase of cuprates. To be more specific, we are dealing with the following topics:

Part I: We present a bilayer graphene system with a symmetrically applied gate voltage and study the effect of a vortex in the exciton condensate, which is produced by an interlayer Coulomb interaction.

Part II: We consider a heavy fermion system with a non-local hybridization, study the properties of the highly anisotropic, unconventional Fermi liquid that evolves at low temperatures, as well as the phase competition between Kondo screening and ordering phenomena like superconductivity or magnetic ordering.

Part III: We make an attempt to reconcile the recently observed quantum oscillations in the

underdoped regime in cuprates with the Fermi arcs observed by angle-resolved photoemission spectroscopy (ARPES) in the normal-conducting pseudogap phase by investigating the properties of a BCS-like Hamiltonian with a pairing gap producing Fermi arcs.

Bibliography

Coleman, P. *Handbook of magnetism and advanced magnetic materials*, volume 1, page 95. Wiley, New York (2007).

Damascelli, A., Z. Hussain, and Z.-X. Shen. *Angle-resolved photoemission studies of the cuprate superconductors.* Rev. Mod. Phys. **75**, 473 (2003).

Fulde, P., P. Thalmeier, and G. Zwicknagl. *Strongly correlated electrons.* In H. Ehrenreich and F. Spaepen, editors, *Advances in research and applications*, volume 60 of *Solid state physics*, pages 1 – 180. Academic Press (2006).

Geim, A. K. and K. S. Novoselov. *The rise of graphene.* Nature Materials **6**, 183 (2007).

Lee, P. A., N. Nagaosa, and X.-G. Wen. *Doping a Mott insulator: Physics of high-temperature superconductivity.* Rev. Mod. Phys. **78**, 17 (2006).

Stewart, G. *Non-Fermi-liquid behavior in d- and f-electron metals.* Rev. Mod. Phys. **73**, 797 (2001).

Stormer, H. L., D. C. Tsui, and A. C. Gossard. *The fractional quantum Hall effect.* Rev. Mod. Phys. **71**, S298 (1999).

Part I

Bilayer graphene exciton condensate: Vortices, zero modes, and fractionalization

2 Introduction

Topological states of matter with emergent anyons as quasiparticle excitations are not only characterized by exotic physics, but also have potential applications in the field of topological quantum computation. This explains the quest for easily controllable structures exhibiting such kind of properties.

This part of the thesis is devoted to the topological properties of a physical system that is likely to be realized in a laboratory in the near future: It consists of two layers of graphene separated by a dielectric barrier and subjected to an external electric field. As recently argued, such bilayer systems possibly develop an exciton condensate up to room temperature. We study the possibility of zero modes and fractional excitations arising from vortices in the excitonic order parameter.

In this introductory chapter, we discuss the three underlying aspects of this work. Section 2.1 introduces the material graphene, which due to its lattice structure shows a specific band structure leading to highly unusual physical properties. Section 2.2 reviews the efforts in stabilizing an excitonic condensate, which was mostly pursued in the framework of semiconductor physics. Section 2.3 is concerned with general aspects of fractionalization, anyonic statistics and the importance of zero modes. An outline in Sec. 2.4 concludes this chapter.

2.1 Graphene

The first fabrication of graphene (Novoselov et al., 2004), an atomic monolayer of carbon atoms arranged in a honeycomb lattice structure, set off an avalanche of experimental and theoretical investigations. It is a strictly two-dimensional material and was therefore expected to be thermodynamically unstable (Fradkin, 1986). However, five years ago Novoselov et al. (2004) were able to isolate graphene on an insulating SiO_2 substrate.

Graphene can be regarded as the building material of all graphitic forms in various dimensions, see Fig. 2.1(a). Three-dimensional (3D) graphite, which can be found in every pencil, is nothing but stacked graphene with interlayer van-der-Waals interactions. Nanotubes (1D) can be thought of as rolled up graphene, while fullerenes (0D) consists of wrapped up graphene with introduced pentagons leading to the required curvature.

Graphene is a zero-gap semiconductor and shows very high crystal quality (Novoselov et al., 2004, 2005; Zhang et al., 2005) with a high mobility of the charge carriers in a large temperature range (Berger et al., 2006). Its band structure is rather special: the low-energy excitations are massless chiral Dirac fermions equivalent to quantum electrodynamics (QED) in 2+1 dimensions (Castro Neto et al., 2006; Katsnelson et al., 2006; Katsnelson and Novoselov, 2007). It is therefore a unique example of 'relativistic' condensed matter physics.

Reviews on graphene are e.g. given by Geim and Novoselov (2007) focusing on experimental aspects or Castro Neto et al. (2009) illuminating the theoretical background. In the framework

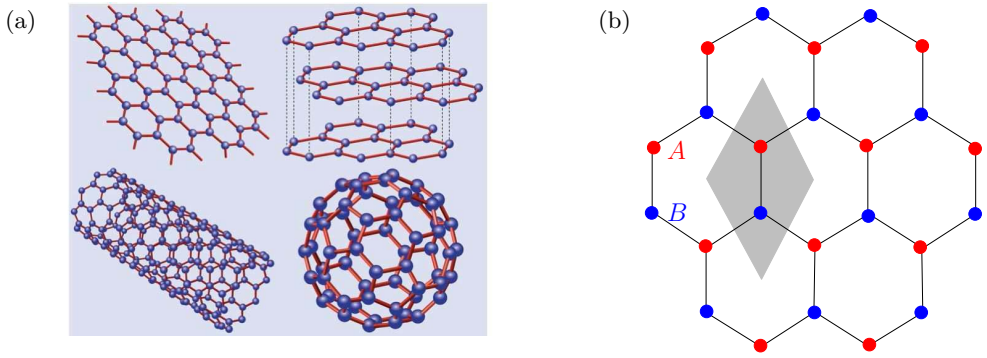

Figure 2.1: (a) Different structures consisting of carbon atoms: graphene (top left), graphite (top right), carbon nanotubes (bottom left) and fullerens (bottom right). (Figure from Castro Neto et al., 2009) (b) A honeycomb lattice consists of two triangular sublattices A and B. The gray shaded zone is the unit cell containing an A and B lattice site.

of this introduction, we will familiarize the reader with the calculation of the band structure based on a tight-binding approximation, show the existence of Dirac fermions, and touch upon transport properties.

Band structure

The honeycomb lattice present in graphene is depicted in Fig. 2.1(b). It is a hexagonal structure consisting of two interpenetrating triangular sublattices A and B. Considering a position in the A-sublattice, the vectors to the nearest neighbors are

$$\mathbf{r}_A = \begin{pmatrix} 0 \\ -a \end{pmatrix}, \frac{a}{2}\begin{pmatrix} -\sqrt{3} \\ 1 \end{pmatrix}, \frac{a}{2}\begin{pmatrix} \sqrt{3} \\ 1 \end{pmatrix}, \tag{2.1}$$

where a is the distance between two neighboring A and B sites.

The robustness and flexibility of this material is due to the strong covalent σ bonds connecting the carbon atoms, originating from the sp^2 hybridization of the atomic orbitals. The remaining p_z orbitals are perpendicular to the plane and have weak overlap leading to the formation of a half-filled π band. The physics of the π electrons can be modeled by a tight-binding Hamiltonian with nearest-neighbor hopping

$$H = -t\sum_{\langle ij\rangle}\left(c^\dagger_{Ai}c_{Bj} + \text{h.c.}\right), \tag{2.2}$$

where $\langle ij\rangle$ restricts the summation to nearest neighbored sites and $c_{\alpha i}$ is the annihilation operator for an electron at site $\mathbf{R}_i$ on sublattice α. Already 60 years prior to isolation of a graphene sheet, its band structure was calculated by Wallace (1947) based on a tight-binding approximation.

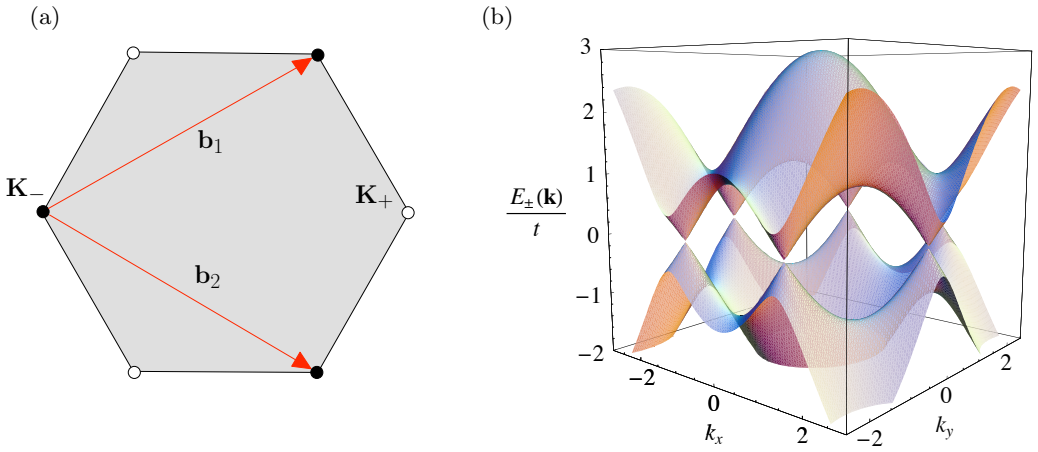

Figure 2.2: (a) The gray region is the first Brillouin zone. The corners of the hexagon are nodal points of the dispersion $t_\mathbf{k}$. $\mathbf{K}_-$ ($\mathbf{K}_+$) is equivalent to the other two corners marked by filled (unfilled) circles. (b) The two bands $E_\pm(\mathbf{k}) = \pm|t_\mathbf{k}|$ show linear dispersion at the nodal points.

With the Fourier transform $c_{\alpha i} = \sqrt{\frac{2}{\mathcal{N}}} \sum_\mathbf{k} e^{i\mathbf{k}\mathbf{R}_i} c_{\alpha\mathbf{k}}$, where $\mathcal{N}$ is the total number of sites in the system and $\mathcal{N}/2$ is the number of unit cells, this Hamiltonian can be rewritten as

$$H = \sum_\mathbf{k} (c^\dagger_{A\mathbf{k}}, c^\dagger_{B\mathbf{k}}) \begin{pmatrix} 0 & t_\mathbf{k} \\ t^*_\mathbf{k} & 0 \end{pmatrix} \begin{pmatrix} c_{A\mathbf{k}} \\ c_{B\mathbf{k}} \end{pmatrix}, \tag{2.3}$$

with the dispersion $t_\mathbf{k} = -t \sum_{\mathbf{r}_A} e^{i\mathbf{k}\mathbf{r}_A}$. Since the model is spin-degenerate, spin indices were omitted here and their effect will be included in the discussion later on.

The Brillouin zone (BZ) is spanned by the two vectors

$$\mathbf{b}_1 = \frac{2\pi}{3a} \begin{pmatrix} \sqrt{3} \\ 1 \end{pmatrix}, \qquad \mathbf{b}_2 = \frac{2\pi}{3a} \begin{pmatrix} \sqrt{3} \\ -1 \end{pmatrix}, \tag{2.4}$$

and can be shifted into a hexagonal shape, see Fig. 2.2(a). The two evolving bands, the eigenvalues of H, $E_\pm(\mathbf{k}) = \pm|t_\mathbf{k}|$, vanish at the corners of the hexagonal BZ and vary linearly with momentum in the vicinity of these gapless points, see Fig. 2.2(b). Two inequivalent nodal points can be distinguished: $\mathbf{K}_\pm = \left(\pm\frac{4\pi}{3\sqrt{3}a}, 0\right)$.

A linear expansion of the bands around $\mathbf{K}_\pm$ with $\mathbf{k} = \mathbf{K}_\pm + \mathbf{p}$ leads to

$$E_\pm(\mathbf{p}) \simeq \pm v_F |\mathbf{p}| + \mathcal{O}((p/K)^2) \tag{2.5}$$

with $K = |\mathbf{K}_\pm|$ and the Fermi velocity $v_F = 3ta/2$, which takes up the role of the speed of light c in this QED 2+1 theory. The experimental data indicate that $v_F \simeq 10^6$m/s, which is orders of magnitude smaller than c. In contrast to a quadratic dispersion, the Fermi velocity does not depend on energy, but is constant. The system is degenerate with respect to the valley ($\pm$) and spin indices, and therefore SU(4) symmetric.

The massless low-energy excitations are Dirac particles with distinct chirality, which will be shown explicitly in the following.

Dirac fermions

In the low-energy limit the Schrödinger equation with Hamiltonian (2.3) becomes a Dirac equation (Slonczewski and Weiss, 1958; Semenoff, 1984; Haldane, 1988) turning the low-energy excitations into Dirac fermions. In order to prove this claim the $\mathbf{k}$ summation in (2.3) is substituted by $\sum_{\mathbf{p},n=\pm}$, where n denotes the valley index:

$$H = \sum_{\mathbf{p},n=\pm} \hat{\Psi}^\dagger_{\mathbf{K}_n}(\mathbf{p}) \begin{pmatrix} 0 & t_{\mathbf{K}_n+\mathbf{p}} \\ t^*_{\mathbf{K}_n+\mathbf{p}} & 0 \end{pmatrix} \hat{\Psi}_{\mathbf{K}_n}(\mathbf{p}) \,, \tag{2.6}$$

with the operators $\hat{\Psi}^\dagger_{\mathbf{K}_+}(\mathbf{p}) = (c^\dagger_{B\mathbf{K}_++\mathbf{p}}, c^\dagger_{A\mathbf{K}_++\mathbf{p}})$ and $\hat{\Psi}^\dagger_{\mathbf{K}_-}(\mathbf{p}) = (c^\dagger_{A\mathbf{K}_-+\mathbf{p}}, c^\dagger_{B\mathbf{K}_-+\mathbf{p}})$. Linearizing around the nodal points $t_{\mathbf{K}_\pm+\mathbf{p}} \simeq v_F(\pm p_x + \mathrm{i}p_y)$ leads to

$$H \simeq v_F \sum_{\mathbf{p}} \left[\hat{\Psi}^\dagger_{\mathbf{K}_-}(\mathbf{p})(-p_x\sigma_x - p_y\sigma_y)\hat{\Psi}_{\mathbf{K}_-}(\mathbf{p}) + \hat{\Psi}^\dagger_{\mathbf{K}_+}(\mathbf{p})(p_x\sigma_x + p_y\sigma_y)\hat{\Psi}_{\mathbf{K}_+}(\mathbf{p}) \right] , \tag{2.7}$$

where σ_x and σ_y denote the Pauli matrices. With $\mathbf{p} \to -\mathrm{i}\nabla$ this can be written as a real-space integral,

$$H \simeq \mathrm{i}v_F \int dxdy \left[\hat{\Psi}^\dagger_{\mathbf{K}_-}(\mathbf{r})(\boldsymbol{\sigma}\cdot\nabla)\hat{\Psi}_{\mathbf{K}_-}(\mathbf{r}) + \hat{\Psi}^\dagger_{\mathbf{K}_+}(\mathbf{r})(-\boldsymbol{\sigma}\cdot\nabla)\hat{\Psi}_{\mathbf{K}_+}(\mathbf{r}) \right] , \tag{2.8}$$

where $\boldsymbol{\sigma} = (\sigma_x, \sigma_y)$. Expressed in first quantization, the Hamiltonian reveals that the two-component wave function $\psi_+(\mathbf{r})$ of a particle near one of the Dirac point $\mathbf{K}_+$ obeys the two-dimensional Dirac equation

$$-\mathrm{i}v_F \left(\boldsymbol{\sigma}\cdot\nabla\right)\psi_+(\mathbf{r}) = E\psi_+(\mathbf{r}) \,. \tag{2.9}$$

For $\psi_-(\mathbf{r})$ a similar relation holds. The wave functions $\psi_\pm(\mathbf{r})$ are connected by time reversal, which in this context corresponds to the operation $(k_x, k_y) \to (-k_x, k_y)$: While the origin is placed in the center of the hexagonal BZ, Fig. 2.2(a), reciprocal space inversion is accomplished by flipping the sign of the x-component due the symmetry of the problem.

By writing the Hamiltonian (2.7) in terms of the four-component operator

$$\hat{\Psi}^\dagger(\mathbf{p}) = \left(\hat{\Psi}^\dagger_{\mathbf{K}_+}(\mathbf{p}), \hat{\Psi}^\dagger_{\mathbf{K}_-}(\mathbf{p}) \right) , \tag{2.10}$$

it can be shown that it commutes with the γ_5 matrix, which is given by a product of all other gamma matrices (e.g. in Weyl representation $\gamma_5 = -\mathrm{i}\gamma_0\gamma_1\gamma_2\gamma_3 = \sigma_3 \otimes \mathbb{1}$). This translates into conservation of chirality (Gusynin et al., 2007). The 4-spinors

$$\phi_+ = (\psi_+, 0), \quad \phi_- = (0, \psi-), \tag{2.11}$$

which describe the quasiparticle excitations at $\mathbf{K}_\pm$, are eigenvectors of γ_5 with opposite chirality:

$$\gamma_5\phi_+ = +\phi_+, \quad \gamma_5\phi_- = -\phi_- \,. \tag{2.12}$$

For massless particles chirality coincides with helicity, the projection of the momentum operator on the direction of the spin. However, in 2D, the concept of helicity, well defined in 3D, looses its physical meaning. Furthermore, the operator $\boldsymbol{\sigma}$ does not describe the real spin of the electrons, which is omitted in the Hamiltonian, but rather represents a pseudo-spin produced by the lattice structure. Nevertheless, a pseudo-helicity $h = \frac{1}{2}\boldsymbol{\sigma}\frac{\mathbf{p}}{|\mathbf{p}|}$ can be considered, for which the wave functions $\psi_\pm$ are eigenfunctions (Gusynin et al., 2007).

For a broken particle-hole symmetry, e.g. produced by a next-nearest neighbor hopping t' in the tight-binding approach, the (pseudo-)helicity is not conserved any more, and therefore the particles are not chiral.

The existence of Dirac cones in the spectrum substantially influences the transport properties of graphene. In the following, we provide a short overview about this topic.

Transport properties

Transport in graphene shows highly unusual properties due to the relativistic spectrum in the vicinity of the Dirac points and the spin and valley degeneracy in the system. We summarize what happens under the influence of external electric and/or magnetic fields.

Keeping a single layer of graphene at a gate voltage, the Fermi energy is shifted up or down, which induces electron and hole charge carriers, respectively. The conductivity depends linearly on the applied voltage, as indicated by measurements of the electric field effect (Novoselov et al., 2005). This allows the conclusion that all induced charge carriers are mobile and not trapped at holes. The mobility stays constant in a temperature range from 10 to 100 K. At the charge neutrality point, i.e., in the absence of a gate voltage, graphene exhibits a finite conductivity, whose origin is still under discussion.

The presence of a magnetic field B perpendicular to the graphene layer introduces a new length scale in the system, the magnetic length $l_B = \sqrt{\hbar c/(eB)}$. Together with the already existing scale, the Fermi velocity v_F, there is only one way to construct an energy scale, given by v_F/l_B (Castro Neto et al., 2009). The cyclotron frequency $\omega_c = \sqrt{2}v_F/l_B$ turns out to be proportional to $\sqrt{B}$, whereas it is linear in B in the non-relativistic case. Therefore, the same magnetic field leads to a higher cyclotron energy, which has e.g. the striking effect that the quantum Hall effect (Novoselov et al., 2005; Zhang et al., 2005) survives up to room temperatures (Novoselov et al., 2007)!

The relativistic spectrum, as well as valley and spin degeneracies have strong influence on the quantization itself. For example, in the case of monolayer graphene, the sequence of Hall plateaus, $\sigma_{xy} = -4e^2/h(N+1/2)$, acquires an overall factor of 4 and is shifted by an additional $1/2$ in comparison to the integer quantum Hall effect observed in GaAs. The Landau levels in monolayer graphene are given by $E_{\pm,N} = \pm\omega_c\sqrt{N}$ (Gusynin and Sharapov, 2005; Peres et al., 2006; Herbut, 2007).

Up to now, the discussion was restricted to monolayer graphene. Upon stacking layers of graphene, interesting new effects develop. In the framework of this thesis we are especially interested in the possible evolution of an exciton condensate in bilayer graphene. In the next section we discuss various approaches for stabilizing an exciton condensate.

2.2 Exciton condensates

Generally speaking, an exciton is a bound state of an electron and a hole, well known from semiconductor physics. In this type of material the electron usually sits in the conduction band and the hole corresponds to an unfilled state. The exciton is a charge neutral bosonic particle, which can be created in a semiconductor by shining light at the sample, and decays when the electron and the hole recombine and a photon is emitted. A weakly coupled gas of excitons is expected to form a Bose-Einstein condensate (BEC), similar to Helium-4 or ultracold alkali atoms in vapors (Leggett, 2001; Ketterle, 2002; Cornell and Wieman, 2002), where the condensation leads to superfluidity and coherent matter waves, respectively.

The physical systems that are considered as candidates for hosting an exciton condensate are of layered structure. The motion of the excitons is therefore restricted to two dimensions, and off-diagonal-long-range order is destroyed by phase fluctuations. Two temperatures can be distinguished in such a system: the Bose-Einstein condensation temperature T_{BEC} and the Kosterlitz-Thouless temperature T_{KT} with $T_{\mathrm{BEC}} < T_{\mathrm{KT}}$. For increasing temperature the Bose-Einstein condensate with a macroscopically occupied ground state turns into a quasicondensate at T_{BEC}, where only the low energy states are macroscopically occupied. This quasicondensate is superfluid and dissipationless, vortices with opposite circulation are bound in pairs. At T_{KT} vortices become unbound leading to a dissipation in the flow. For 2D and infinite system size T_{BEC} is zero and becomes finite for finite system size. Since experimentally a distinction between a BEC and a quasicondensate is not possible, the relevant scale for experiments is the Kosterlitz-Thouless temperature, below which superfluidity is present.

Exciton condensate in layered semiconductors

A bulk semiconductor is not very useful when it comes to the observation of an exciton condensate (EC): electrons and holes recombine too fast for achieving the required exciton densities (O'Hara et al., 1999). For stabilization, so-called coupled quantum wells are used - systems consisting of layered semiconductor structures: Two semiconductor layers are separated by a thin insulating barrier layer. In experiments three different approaches are basically pursued:

(i) A bilayer system, where an electron-hole plasma is generated by optical pumping. By applying an electric field the electron and hole within one exciton are spatially separated creating a condensate of indirect excitons. Each exciton pair is associated with a dipole moment. The dipolar repulsion between the pairs as well as the spatial separation decreases the recombination rate. Signatures of the condensate are detected by photoluminescence (Butov et al., 2002; Snoke et al., 2002; Lai et al., 2004), however a direct probe of the superfluidity is missing.

(ii) Undoped electron-hole bilayers with an external gate voltage, which induces electrons in one layer and holes in the other (Sivan et al., 1992; Kane et al., 1994; Joglekar et al., 2005). As in system (i) the excitons feel dipolar repulsion, and a dipolar superfluid develops (Balatsky et al., 2004). At high densities, theoretical investigations (Joglekar et al., 2006) hint at the evolution of a Wigner supersolid, a Bose-Einstein condensate with broken translational symmetry.

(iii) A biased electron-electron bilayer quantum Hall systems at $\nu_T = 1$ (Spielman et al.,

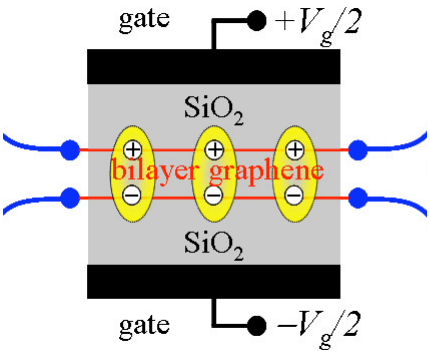

Figure 2.3: Suggested experimental setup for producing an exciton condensate in bilayer graphene. The layers are embedded in a dielectric, e.g. SiO_2, and subjected to the electric field produced by a parallel-plate capacitor. (Figure from Min et al., 2008).

2000; Eisenstein and MacDonald, 2004; Eisenstein, 2004; Tutuc et al., 2004; Kellogg et al., 2004). In this case both of the semiconducting layers serve as a well for electrons. However, in the quantum Hall regime the system can be mapped onto an electron-hole system with attractive interaction: An external magnetic field leads to Landau levels with a filling factor ν denoting the fraction between the number of electrons in the system and the number of states in each Landau level. The system is invariant under particle-hole transformation, which can be performed in only one of the two layers leading to a hole filling factor of $1-\nu$. The former empty sites are now seen as occupied by holes with positive charge and the interaction between holes and electrons in different layers is attractive. The number of electrons and holes in the system becomes equal for $\nu = 1/2$ for each layer, i.e., a total filling factor $\nu_T = 1/2 + 1/2 = 1$. As above the excitons carry a dipole moment, but unlike in system (ii) this is not expected to lead to a supersolid state. Such a system seems to be the most promising candidate among semiconductor heterostructures for exciton condensation.

A first experimental hint for excitonic BEC in an electron-electron quantum Hall bilayer system was given by measurements of the interlayer tunneling rate (Spielman et al., 2000), which reveal strong interlayer electron-hole correlations. Striking evidence was given by measurements of the counterflow of electrons and holes by independently electrically connecting to the layers (Tutuc et al., 2004; Kellogg et al., 2004). The small, but measurable dissipation in the counterflow channel was argued to arise from unbound vortices produced by disorder in the sample (Eisenstein and MacDonald, 2004). All experimental evidence was achieved in a temperature regime well below 1 K.

Exciton condensate in bilayer graphene

Recently, interest arose in exciton condensation in graphene bilayers (Min et al., 2008; Zhang and Joglekar, 2008). A possible experimental setup is depicted in Fig. 2.3: Two layers of graphene separated by a dielectric are subjected to a perpendicular electric field that induces electron charge carriers in one layer and holes in the other. The intervening dielectric suppresses inter-layer hopping, which would counteract the evolution of an EC (Dillenschneider and Han, 2008). The value of the Kosterlitz-Thouless transition temperature is sensitive on the strength of the Coulomb interaction and its possible screening by the carriers in the layer. Depending on the importance of screening, T_{KT} was estimated to be in the range of room tem-

perature (Min et al., 2008; Bistritzer et al., 2008) or a few mK (Kharitonov and Efetov, 2008, 2009). T_{KT} is expected to be reduced by disorder (Kharitonov and Efetov, 2009): Electrons and holes do not scatter identically at impurities in the two layers, which leads to a breaking of the electron-hole pair. As argued by Zhang and Joglekar (2008), no Wigner crystallization occurs in graphene bilayers despite the dipole moments carried by the excitons.

Differences between such a bilayer graphene and a layered semiconductor structure are various. Since graphene is a gapless semiconductor, higher carrier densities can be achieved. The fairly good particle-hole symmetry of the band structure favors the evolution of an EC.

In contrast to the phonon-mediated superconductors, with transition temperatures orders of magnitudes smaller than room temperature, the Coulomb interaction producing the EC ranges over the full band width instead of a narrow shell around the Fermi surface of the order of the Debye energy.

Like a superconductor, an exciton condensate can develop vortices, which are possibly related to zero energy eigenfunctions, so-called zero modes. Their relation to fractionalization is pointed out in the next section.

2.3 Fractionalization

Fractionalized quantum numbers and fractional statistics arising from nontrivial topological configurations are not just interesting by themselves as exotic phenomena. Systems with theses properties might offer a route to fault-tolerant quantum computation (Kitaev, 2003; Nayak et al., 2008), because the states are topologically protected from local perturbations.

Up to now only two systems are known that host the required non-Abelian anyonic excitations: the fractional quantum Hall state with filling factor $\nu = 5/2$ (Moore and Read, 1991) and the planar spin-polarized p+ip superconductor (Read and Green, 2000). Since both systems are not easy to produce and control, it is highly desirable to investigate the occurrence of quasiparticles with fractional statistics in other systems.

In this section, we first discuss the relation between fractional quantum numbers and fractional statistics, and then present examples of systems with fractional excitations, while pointing out the importance of zero modes.

Fractional statistics

Exchanging two equivalent particles in a system leads to an additional phase factor $\exp(\mathrm{i}\theta)$ in the global wave function. Twice an exchange of the same two particles corresponds to tracking one particle around the other, called braiding. In a three-dimensional system such a two-fold exchange leaves the wave function unchanged due to topology, and all particles fall in one of the two categories: either they are bosons with an exchange phase $\theta = 2\pi$ or fermions with $\theta = \pi$. In two dimensions the situation is different: θ is not restricted to 2π and π, but can in principle take *any* value, which however mostly is a faction of π, leading to a new particle species dubbed anyon (Wilczek, 1990).

In order to illustrate the relation between the fractional charge of a quasiparticle and the associated fractional statistics, we consider the example of the fractional quantum Hall effect

(FQHE) with filling factor $\nu = 1/3$, where the low-energy excitations are Abelian anyons. At $\nu = 1/3$ the lowest Landau level is filled to one third and the ration between electrons and penetrating flux quantums in the system is 1:3. Upon a Chern-Simons transformation, where two flux quanta are attached to each electron, the ground state can be regarded as being equivalent to a fully filled lowest Landau level ($\nu = 1$) of composite fermions. Quasi-hole excitations above this ground state are composite objects carrying one flux quantum and a charge $e/3$ (Laughlin, 1983). The exchange statistics $\theta = 2\pi\nu\phi/\phi_0$, where $\phi_0 = h/e$ is the flux quantum and ϕ denotes the flux carried by the quasiparticle, is obtained by calculating the Berry phase on the basis of the underlying Laughlin wave function (Arovas et al., 1984). This is in agreement with the interpretation that the exchange of two flux-charge composite objects with flux ϕ and charge q leads to a topological phase (Wilczek, 1990)

$$\theta = 2\pi \frac{\phi}{\phi_0} \frac{q}{e} \,. \tag{2.13}$$

Such a phase can be regarded as a generalization of the Aharonov-Bohm phase (Aharonov and Bohm, 1959), where the wave function of an electron acquires a phase $2\pi\phi/\phi_0$ when encircling a magnetic flux ϕ. From relation (2.13) it becomes clear how fractional charge in combination with flux can be connected to fractional statistics. Please note that the existence of fractional charge itself is not a sufficient condition for the occurrence of fractional statistics.

Anyons, whose braiding simply manifests itself in a phase change, Eq. (2.13), are Abelian. In this case the ground of a system consisting of several anyonic quasiparticles is unique. Therefore, the order of braiding operations does not matter for the overall phase change: the braid group is commutative. For non-Abelian anyons this is not the case. The ground state is degenerate, and braiding two particles does not necessarily correspond to only a phase change in the initial wave function. This property is needed for the concept of topological quantum computation (Nayak et al., 2008).

In the following we point out the role of zero modes for the occurrence of fractional quantum numbers.

Zero modes and fractionalization

Given that charge is a good quantum number, a single localized zero energy eigenfunction in a gapped system with a symmetric spectrum binds a charge of 1/2 (Jackiw and Rebbi, 1976; Su et al., 1979; Hou et al., 2007; Seradjeh et al., 2008b). In some cases this can be illustrated by simple counting arguments regarding the real-space structure of the system, e.g. (Seradjeh et al., 2008b). The existence of a zero mode itself is not a necessary condition for the existence of fractionalization. Mid-gap bound states away from zero energy for instance can bind fractional charge as well (Chamon et al., 2008).

Systems with fractionalization can be divided into those, where time reversal is broken or conserved. On the basis of two examples we illuminate the relation between zero modes and fractionalization. We discuss the planar chiral p-wave superconductor, whose half-quantum vortices bind fermionic zero modes leading to non-Abelian anyonic excitations, and, as a representative of systems with conserved time reversal symmetry, present a graphene-like structure with a Kekulé dimerization pattern.

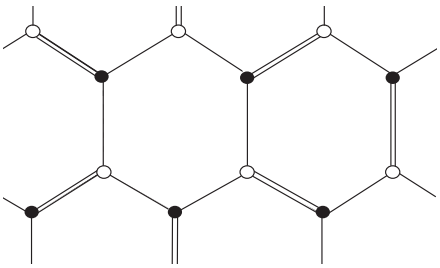

Figure 2.4: Illustration of a Kekulé distortion on a honeycomb lattics. Atoms linked by double bonds are closer than those linked by single bonds. (Figure from Jackiw, 2007).

A spin-polarized p+ip superconductor exhibits vortices with a flux of $h/2e$. The physics in the presence of a vortex can be analyzed in terms of a BCS mean-field theory. The solution of the Bogoliubov-de Gennes (BdG) equations reveals a bound fermionic mid-gap zero-energy mode (Read and Green, 2000; Gurarie and Radzihovsky, 2007) localized in the vicinity of the vortex core. Since the considered system is a superconductor and therefore the degrees of freedom are in the particle-particle channel, this mode corresponds to a self-conjugated fermion, termed Majorana fermion, for which the creation operator $\gamma^\dagger$ fulfills the relation $\gamma^\dagger = \gamma$. In a system with several vortices this leads to a ground state degeneracy (Read and Green, 2000; Ivanov, 2001) and the vortices behave as anyons with non-Abelian statistics. The fractional statistics, however, in this example is not accompanied by charge fractionalization, since charge is not conserved in a superconductor.

Examples of systems exhibiting zero modes and fractionalization, while conserving time reversal symmetry, are for instance lattice models with a specific dimerization pattern (Hou et al., 2007; Seradjeh et al., 2008b). They can be regarded as a two-dimensional generalization of the concept of fractionalization in polyacetylene, a dimerized chain, where a domain wall in the dimerization pattern binds a mid-gap zero-energy excitation and is associated with fractionalized charge 1/2 (Jackiw and Rebbi, 1976; Su et al., 1979; Goldstone and Wilczek, 1981). The system considered by Hou et al. (2007) is a graphene-like structure: a honeycomb lattice with spinless, charged fermions with Kekulé distortion (Fig. 2.4), a dimerization pattern that generates a mass term for the Dirac electrons. A U(1) vortex in this mass, analogously to an Abrikosov vortex in a superconducting condensate, is associated with a 2π phase twist around the vortex core. In the presence of such a vortex the low-energy Dirac equations are equivalent to the BdG equations for a chiral p-wave superconductor with a half-quantum vortex (Read and Green, 2000). A vortex binds an unpaired zero mode and a charge of $\pm e/2$. In contrast to the p-wave superconductor, the zero mode cannot be expressed as a Majorana fermion. Therefore, the exchange statistics of these vortices is Abelian (Seradjeh et al., 2008b).

So far, in all considered systems, only vortices with odd vorticity bind zero modes.

2.4 Outline

The possibility of creating zero modes and fractional excitations in the exciton condensate evolving in a bilayer graphene system with an applied gate voltage is explored. In the low-energy limit we show that an oddly-quantized vortex in the excitonic order parameter binds two zero modes - one per valley index. The inter-valley mixing, which is not captured by the low-energy theory, leads to a slight splitting of these zero modes. Based on an exact numerical

diagonalization of the full lattice Hamiltonian in real space, we study the charge content and the exchange statistics of these vortices. Although not associated with a total charge, each vortex binds an irrational fraction of "axial" charge defined as the charge difference between the layers and obeys fractional exchange statistics. The results presented in the framework of this thesis have been published in (Seradjeh et al., 2008a).

Section 3 introduces the Hamiltonian modeling the symmetrically biased bilayer system and studies its instability towards an excitonic condensate at the mean-field level. Section 4 discusses the approximations arising in the low-energy limit and studies the effect of a vortex in the excitonic order parameter. Section 5 provides numerical and analytical results showing the splitting of zero modes due to inter-valley mixing beyond the low-energy regime. It furthermore shows the association of a vortex with axial charge. Section 6 discusses the theoretical background and numerical results studying the exchange statistics of the vortices. A summary of the results and an outlook to possible experimental observations in Sec. 7 concludes this part.

3 Exciton condensate in bilayer graphene

In this chapter we consider a symmetrically biased bilayer graphene system and investigate its instability towards an excitonic condensate using a mean-field approximation. We derive the critical value for the Coulomb repulsion and the dependence of the excitonic order parameter on the values of the Coulomb repulsion and the gate voltage.

The schematic structure of the regarded system is depicted in Fig. 3.1(a) - each of the graphene layers is kept on an electric potential $\pm V$. The layers are separated by a dielectric material at a distance much larger than the lattice spacing within the layers. A finite gate voltage $V > 0$ shifts the spectrum up and down, respectively, in the upper and lower layer. At half filling this leads to a Fermi surface of particles in one layer, and of holes in the other one. Therefore, a Coulomb interaction between the layers condenses a finite density of particle-hole bound states. The exciton condensate (EC) possibly exists even up to room temperature (Min et al., 2008). Only weak dependence on the actual type of stacking is expected (Zhang and Joglekar, 2008). Therefore, direct stacking will be assumed.

The considered model containing the essential physics is described by the Hamiltonian $H = H_1 + H_2 + H_U$ with the in-layer Hamiltonian

$$H_\alpha = -t \sum_{\langle ij \rangle} (c^\dagger_{Ai,\alpha} c_{Bj,\alpha} + \text{h.c.}) - (-)^\alpha V \sum_{\nu i} n_{\nu i,\alpha} \,, \tag{3.1}$$

where $\langle ij \rangle$ denotes the summation over nearest-neighbored sites, $\alpha = 1, 2$ represents the layer and $\nu = A, B$ the sublattice index. $c_{\nu i,\alpha}$ is the fermionic annihilation operator for an electron sitting at position $\mathbf{R}_i$ on sublattice ν and layer α, and $n_{\nu i,\alpha} = c^\dagger_{\nu i,\alpha} c_{\nu i,\alpha}$ is the corresponding

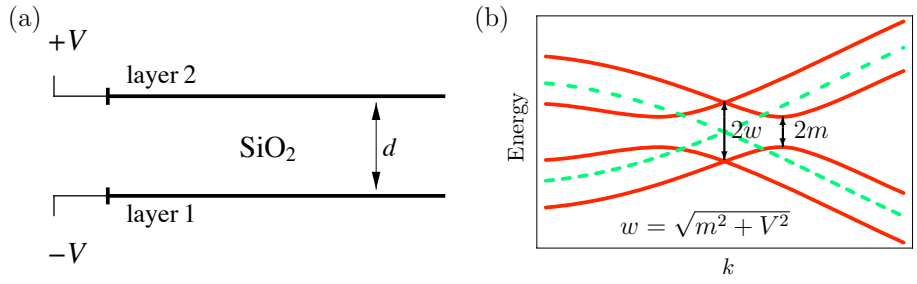

Figure 3.1: (a) Structure of bilayer graphene subjected to a gate voltage V and separated by a dielectric, e.g. SiO_2, at a distance $d \gg a$, where a is the intra-layer lattice spacing. (b) Spectrum for bilayer graphene close to a nodal point in the non-interacting case with zero gate voltage (green dashed line, doubly degenerate) and in the presence of an exciton condensate (red solid line) with finite gate voltage V, an exciton gap $m = \Delta_-$ and a nodal shift of $w = \sqrt{m^2 + V^2}$.

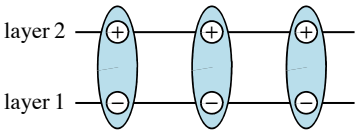

Figure 3.2: Schematic illustration of excitons that consist of a hole and an electron from different layers.

number operator. The interaction term is given by

$$H_U = U \sum_{\nu i} n_{\nu i,1} n_{\nu i,2} \,. \tag{3.2}$$

Since spin indices do not influence the behavior of the EC, just a single spin projection is considered. Inter-layer hopping is exponentially suppressed by the comparably large inter-layer distance and the intervening dielectric, and is therefore omitted in the Hamiltonian. Electrons can hop within each layer to nearest neighbored sites. The assumed interaction is short-ranged and acting between two particles in different layers and on the same planar site, neglecting a possible long-ranged tail of the Coulomb interaction, which however is only expected to enhance the formation of the EC.

A mean-field decoupling in the excitonic order parameter $\Delta_{\nu i} = U \left\langle c^\dagger_{\nu i,2} c_{\nu i,1} \right\rangle$, where ν represents the sublattice index, leads to the mean-field Hamiltonian

$$H_{\mathrm{MF}} = H_1 + H_2 - \sum_{\nu i} \left(\Delta_{\nu i} c^\dagger_{\nu i,1} c_{\nu i,2} + \mathrm{h.c.} \right) + \frac{1}{U} \sum_{\nu i} |\Delta_{\nu i}|^2 . \tag{3.3}$$

A phase with a finite value of $\Delta_{\nu i}$ describes an exciton condensate illustrated in Fig. 3.2. Under the assumption that $\Delta_{\nu i}$ only depends on the sublattice index, there are two mean-field parameters Δ_A and Δ_B in the system, which can be combined to $\Delta_\pm = \frac{1}{2}(\Delta_A \pm \Delta_B)$. We can define the spinor field operator $\psi_i = (c_{Bi,1}, -c_{Ai,1}, c_{Bi,2}, c_{Ai,2})^T$. The Hamiltonian (3.3) is compactly written as

$$H_{\mathrm{MF}} = \frac{1}{N} \sum_{\mathbf{k}} \psi^\dagger_{\mathbf{k}} h_{\mathbf{k}} \psi_{\mathbf{k}} + E_0 \tag{3.4}$$

using N as the number of sites per layer, $E_0 = (N/U)(|\Delta_+|^2 + |\Delta_-|^2)$ and

$$h_{\mathbf{k}} = \gamma_0 \Big[\gamma_1 \mathrm{Re}\, t_{\mathbf{k}} + \gamma_2 \mathrm{Im}\, t_{\mathbf{k}} + V \gamma_0 \gamma_5 + |\Delta_-| e^{-\mathrm{i}\chi_- \gamma_5} - \mathrm{i}\gamma_1 \gamma_2 |\Delta_+| e^{\mathrm{i}\chi_+ \gamma_5} \Big] . \tag{3.5}$$

$t_{\mathbf{k}} = -t \sum_{\mathbf{r}_A \in \mathrm{n.n.}} e^{\mathrm{i}\mathbf{k}\mathbf{r}_A}$ is the non-interacting dispersion relation, where $\mathbf{r}_A$ denotes the vectors pointing from an A site to the nearest neighbored B sites, see Eq. (2.1), and $\gamma_\mu = \mathrm{i}\sigma_2 \otimes \sigma_\mu$, $\gamma_0 = \sigma_1 \otimes \mathbb{1}$ and $\gamma_5 = -\mathrm{i}\gamma_0\gamma_1\gamma_2\gamma_3 = \sigma_3 \otimes \mathbb{1}$ are the Dirac matrices in Weyl representation. The field $\Delta_\pm = |\Delta_\pm| e^{\mathrm{i}\chi_\pm}$ was decomposed in a polar representation.

The eigenvalues of $h_{\mathbf{k}}$, Eq. (3.5), are given by $\pm E_{\mathbf{k}\tau}$ with

$$\begin{aligned} E_{\mathbf{k}\tau} = \Big(& |t_{\mathbf{k}}|^2 + V^2 + |\Delta_+|^2 + |\Delta_-|^2 + \\ & -(-1)^\tau 2 \left[|t_{\mathbf{k}}|^2 \left(V^2 + |\Delta_+|^2 \right) + \mathrm{Re}^2 (\Delta_- \Delta_+^*) \right]^{1/2} \Big)^{1/2} , \end{aligned} \tag{3.6}$$

where $\tau = 1, 2$ is the band index. For half filling the ground state energy of the system reads

$$E_{GS} = -\sum_{\mathbf{k}\tau} |E_{\mathbf{k}\tau}| + E_0 \quad \text{with} \quad E_0 = \frac{2N}{U}(|\Delta_+|^2 + |\Delta_-|^2). \tag{3.7}$$

The energy gap E_g in the system is given by the minimal energetical distance between the ground state and an excited state. Since $|E_{\mathbf{k}2}| \leq |E_{\mathbf{k}1}|$, we minimize the energy $\partial|E_{\mathbf{k}2}|/\partial t_{\mathbf{k}} \equiv 0$, which leads to the condition

$$|t_{\mathbf{k}}|^2 \equiv \frac{v^4 - \mathrm{Re}^2(\Delta_-\Delta_+^*)}{v^2}, \tag{3.8}$$

where the shortcut $v^2 = V^2 + |\Delta_+|^2$ was introduced. $E_{\mathbf{k}2}$ evaluated with this condition leads to an expression for the energy gap

$$E_g = \left(\frac{|\Delta_-|^2V^2 + \mathrm{Im}(\Delta_-\Delta_+^*)^2}{V^2 + |\Delta_+|^2}\right)^{1/2}. \tag{3.9}$$

The maximum value of the gap is realized when $\mathrm{Re}(\Delta_- - \Delta_+^*) = 0$, or equivalently $|\Delta_A| = |\Delta_B|$.

For the two parameters Δ_+ and Δ_- two separate gap equations hold with different critical values $U_{c\pm}$. The gap equations are obtained by minimizing the ground state energy $\frac{\partial E_{GS}}{\partial \Delta_\pm} = 0$. In the limit $\Delta_\pm \to 0$ the value of the critical interaction $U_{c\pm}$ can be extracted. The explicit calculation of $U_{c\pm}$ presented in the following shows an instability at infinitesimal U towards an EC with non-zero Δ_- and zero Δ_+.

While setting $\Delta_- = 0$, the gap equation for Δ_+

$$4N = U\sum_{\mathbf{k}\tau} \frac{v - (-1)^\tau|t_{\mathbf{k}}|}{v|E_{\mathbf{k}\tau}|} \tag{3.10}$$

leads to the critical value

$$\frac{1}{U_{c+}} = \sum_{\mathbf{k},|t_{\mathbf{k}}|<V} \frac{1}{NV}. \tag{3.11}$$

In the vicinity of the nodes, we approximate the non-interacting dispersion as $|t_{\mathbf{k}}| = (3ta/2)|\mathbf{k}|$, which implies a density of states linear in energy for $V \ll t$. Within this limit, we can estimate $U_{c+} \sim t^2/V \gg t$.

In an analogous calculation for Δ_- the gap equation becomes

$$2N = U\sum_{\mathbf{k}\tau} \frac{1}{|E_{\mathbf{k}\tau}|}. \tag{3.12}$$

In the limit $\Delta_- \to 0$ with $\Delta_+ = 0$, this reduces to

$$\frac{1}{U_{c-}} = \frac{1}{2N}\sum_{\mathbf{k}\tau} \frac{1}{||t_{\mathbf{k}}| - (-1)^\tau V|} \tag{3.13}$$

The right-hand side diverges logarithmically in the vicinity of the nodes for $\tau = 2$. Hence, the critical value U_{c-} is equal to zero. At infinitesimal U the system is unstable towards an EC with non-zero Δ_-, but zero Δ_+. The resulting spectrum of the system $\pm E_{\mathbf{k}\tau}$ with

$$E_{\mathbf{k}\tau} = \sqrt{\left(|t_{\mathbf{k}}| - (-1)^{\tau} V\right)^2 + |\Delta_-|^2}. \tag{3.14}$$

is depicted in Fig. 3.1(b).

In a nodal approximation with $|t_{\mathbf{k}}| \approx (3ta/2)|\mathbf{k}| = v_F|\mathbf{k}|$ the dependence of $|\Delta_-|$ on U and V can be derived. Taking the gap equation (3.12) for Δ_- as a starting point, the summation over $\mathbf{k}$ can be transformed into an integral over the first Brillouin zone with volume $V_{BZ} = 8\pi^2/(3\sqrt{3}a^2)$, which will be cut at an ultraviolet momentum cutoff Λ:

$$\frac{2}{N}\sum_{\mathbf{k}} = \int\limits_{BZ} \frac{d^2k}{V_{BZ}} \approx \frac{2\pi}{V_{BZ}} \int\limits_0^{\Lambda} \mathrm{d}k k \tag{3.15}$$

The gap equation transforms into

$$\frac{1}{U} = \pi \int\limits_0^{\Lambda} \frac{dk}{V_{BZ}} \frac{1}{\sqrt{\left(v_F k - V\right)^2 + |\Delta_-|^2}} \tag{3.16}$$

$$= \frac{\pi}{V_{BZ} v_F^2} \left[\sqrt{|\Delta_-|^2 + \left(\Lambda v_F - V\right)^2} - \sqrt{|\Delta_-|^2 + V^2} + \right. \tag{3.17}$$

$$\left. + V \ln \left(\frac{\Lambda v_F - V + \sqrt{|\Delta_-|^2 + \left(\Lambda v_F - V\right)^2}}{\sqrt{|\Delta_-|^2 + V^2} - V} \right) \right].$$

An expansion of the right-hand side for large $\Lambda v_F \gg V, |\Delta_-|$ leads to

$$\frac{1}{U} \approx \frac{\pi}{V_{BZ} v_F^2} \left(\Lambda v_F - V - \sqrt{|\Delta_-|^2 + V^2} + V \ln \left(\frac{2 v_F \Lambda}{\sqrt{|\Delta_-|^2 + V^2} - V} \right) \right). \tag{3.18}$$

By further assuming that $|\Delta_-| \ll V$ this simplifies to

$$\frac{1}{U} \approx \frac{\pi}{V_{BZ} v_F^2} \left(\Lambda v_F - 2V + V \ln \left(\frac{4 v_F \Lambda V}{|\Delta_-|^2} \right) \right), \tag{3.19}$$

which can be rearranged as

$$\frac{4 \Lambda v_F V}{|\Delta_-|^2} = \exp\left(\frac{V_{BZ} v_F^2}{\pi U V} \right) \exp\left(-\frac{\Lambda v_F - 2V}{V} \right) \approx \exp\left(\frac{V_B Z v_F^2}{\pi U V} \right). \tag{3.20}$$

Therefore, the dependence of $|\Delta_-|$ on the applied gate voltage V and the inter-layer Coulomb repulsion U is

$$|\Delta_-| \approx 2\sqrt{v_F \Lambda V} \exp\left(-\frac{\sqrt{3}\pi t^2}{UV} \right), \tag{3.21}$$

where $v_F\Lambda$ has the unit of energy and is of the order t.

In this chapter a Hamiltonian was introduced describing the physics of a bilayer graphene system with intra-layer hopping and inter-layer Coulomb repulsion subjected to an applied gate voltage. This system is unstable towards an exciton condensate with non-zero Δ_-, i.e., an infinitesimal U leads to the formation of an EC. An additional next-nearest neighbor hopping destroying the perfect nesting between the electron and hole Fermi surfaces is likely to render the critical U finite. In this phase an energy gap develops, whose value is given by Δ_-. This mean-field parameter depends exponentially on the strength of the Coulomb repulsion. A phase with $\Delta_- \neq 0$ and $\Delta_+ = 0$ was also studied by Min et al. (2008) and Zhang and Joglekar (2008). The next chapter is concerned with an approximation of the EC phase in the low-energy limit.

4 Low-energy theory

In the low-energy limit the physics of the system is dominated by excitations around the two Dirac points. We formulate a theory in the continuum limit only taking into account these contributions and discuss the symmetries of the low-energy Hamiltonian (Sec. 4.1). In the framework of this approximation, we study the effect of a vortex in the excitonic order parameter (Sec. 4.2): It binds exactly one zero mode per valley index.

4.1 Nodal approximation

In the vicinity of the nodal points $\mathbf{K}_\pm = \left(\pm 4\pi/(3\sqrt{3}a), 0\right)$, the approximation $t_{\mathbf{K}_\pm+\mathbf{p}} \approx \pm p_x + \mathrm{i}p_y$ for the non-interacting dispersion holds, where the Fermi velocity v_F was set to 1. In the limit of long wavelengths the mean-field Hamiltonian (3.4) can be linearized around these nodal points and reduces to two contributions,

$$H_{\text{nodal}} = \int d\mathbf{r} \left(\Psi_+^\dagger(\mathbf{r}) h_+(\mathbf{r}) \Psi_+(\mathbf{r}) + \Psi_-^\dagger(\mathbf{r}) h_-(\mathbf{r}) \Psi_-(\mathbf{r}) \right), \tag{4.1}$$

with the spinors $\Psi_\pm = (c_{B1\pm}, -c_{A1\pm}, c_{B2\pm}, c_{A2\pm})^T$. The matrices $h_\pm$ are related to each other via

$$h_+ = \gamma_1\gamma_3 h_- \gamma_3\gamma_1 \equiv \mathcal{H}, \tag{4.2}$$

with

$$\mathcal{H} = \gamma_0 \left(\gamma_1 \hat{p}_x + \gamma_2 \hat{p}_y + V\gamma_0\gamma_5 + |m| e^{-\mathrm{i}\chi\gamma_5} \right). \tag{4.3}$$

We used the momentum operator $\hat{\mathbf{p}} = -\mathrm{i}\nabla$ and the replacement $\Delta_- \equiv m = |m| e^{\mathrm{i}\chi}$. The mass m is not necessarily uniform in space. Since $h_\pm$ are connected by a unitary transformation, Eq. (4.2), the eigenstates of h_- can easily be found by transforming the eigenstates of h_+. In the remainder of this chapter we will focus on the solution of h_+ and comment at the end how the doubling of the number of nodes changes the results.

Based on a anticommutation property of the Hamiltonian $\mathcal{H}$, it can be shown that its spectrum is symmetric around 0. At first, we consider the relation

$$\gamma_2 \mathcal{H}^* \gamma_2 = \mathcal{H}\,, \tag{4.4}$$

which can be shown by explicitly plugging in $\mathcal{H}$, Eq. (4.3), and using the properties of the Dirac matrices $\{\gamma_\mu, \gamma_\nu\} = 2\eta_{\mu\nu}\mathbb{1}_4$, where $\eta_{\mu\nu}$ is the Minkowski metric ($\{\eta_{\mu\nu}\} = \mathrm{diag}(1, -1, -1, -1)$ with $\mu, \nu = 0, 1, 2, 3$).

The antiunitary operator $\Omega = K\gamma_2$, where K is the operator for complex conjugation ($K\mathcal{H} = \mathcal{H}^*K$), is its own inverse $\Omega^{-1} = \Omega$. By considering Eq. (4.4), we see that Ω anticommutes with $\mathcal{H}$:

$$\Omega\mathcal{H}\Omega = -\mathcal{H}, . \tag{4.5}$$

Thus, for every eigenstate Ψ_E of $\mathcal{H}$ ($\mathcal{H}\Psi_E = E\Psi_E$) an eigenstate $\Omega\Psi_E$ with the energy $-E$ exists,

$$\mathcal{H}(\Omega\Psi_E) = -E(\Omega\Psi_E)\,, \tag{4.6}$$

leading to a symmetric spectrum.

In this section, it has been shown how the mean-field Hamiltonian is linearized in the limit of low energy. General considerations prove the symmetry of the resulting spectrum. The next section discusses the effect of a vortex in the order parameter m binding a zero mode.

4.2 Zero modes bound by a vortex

In this section we study the effect of a vortex in the EC order parameter

$$m(r,\theta) = m_0(r)e^{\mathrm{i}n\theta}\,, \tag{4.7}$$

with vorticity $n \in \mathbb{Z}$ and $m_0(r) > 0$ in the low-energy limit. The radius r and the angle θ parametrize polar coordinates. It will be shown that such a vortex with odd vorticity n binds exactly one zero mode per node.

In the formal limit of $V = 0$ (with non-zero order parameter m) the Hamiltonian $\mathcal{H}$, Eq. (4.3), is equivalent to the system discussed in (Hou et al., 2007; Seradjeh et al., 2008b; Jackiw and Pi, 2007). In this case, it is shown that an n-fold vortex binds exactly $|n|$ zero modes (Jackiw and Rossi, 1981). In the regime far from the vortex, the spectrum remains gapped. In the presence of a non-zero V at least one zero modes survives for an oddly-quantized vortex due to the symmetric spectrum, compare Eq. (4.6). Since the spectral symmetry for finite V is generated by the antiunitary operator as in the case of a chiral p-wave superconductor with half-quantum vortices, not more than one zero mode is expected to survive (Gurarie and Radzihovsky, 2007).

In order to seek for these solutions with zero energy $\mathcal{H}\psi_0 = 0$, it is important to notice that the antiunitary operator Ω and $\mathcal{H}$ share the same eigenfunctions in the zero energy subspace. If ψ_1 is a zero mode ($\mathcal{H}\psi_1 = 0$), then $\psi_2 = \Omega\psi_1$ is a zero mode as well. In the case of $\psi_2 = \lambda\psi_1$, ψ_1 is an eigenstate of Ω with $\lambda = \pm 1$ because of $\Omega^2 = \mathbb{1}$. If ψ_1 and ψ_2 are linearly independent, one can always choose a combination of these states $\psi_\pm = (\psi_1 \pm \psi_2)/\sqrt{2}$, which is an eigenstate of Ω:

$$\Omega\psi_\pm = \Omega\frac{1}{\sqrt{2}}(1 \pm \Omega)\psi_1 = \frac{1}{\sqrt{2}}(\Omega \pm \Omega^2)\psi_1 = \mp\frac{1}{\sqrt{2}}(1 \pm \Omega)\psi_1 = \mp\psi_\pm\,. \tag{4.8}$$

In general, the eigenstates ϕ_λ of Ω ($\Omega\phi_\lambda = \lambda\phi_\lambda$) fulfill the relation

$$\Omega(e^{-\frac{\mathrm{i}\beta}{2}}\phi_\lambda) = (e^{\mathrm{i}\beta}\lambda)(e^{-\frac{\mathrm{i}\beta}{2}}\phi_\lambda). \tag{4.9}$$

This shows that the eigenstates for $\lambda = 1$ and -1 are connected by a phase factor. Therefore, it is sufficient to restrict ourselves to the eigenstate for $\lambda = -1$, which has the structure $\psi_0 = (\psi, -\sigma_2\psi^*)^T$. ψ is a two component spinor, which we can write as $(f, g)^T$ with arbitrary complex functions f and g. Then ψ_0 reads

$$\psi_0 = (f, g, \mathrm{i}g^*, -\mathrm{i}f^*)^T. \tag{4.10}$$

The following calculation assumes a vortex in the quantum limit,

$$m(r \neq 0, \theta) = m_0 e^{\mathrm{i}n\theta}\,, \tag{4.11}$$

with constant m_0, i.e., the vortex is only phase twist without a radial dependence. The more general case of a radially symmetric vortex could be treated in a similar way. We write the linearized Hamiltonian $\mathcal{H}$, Eq. (4.3), in matrix form

$$\mathcal{H} = \begin{pmatrix} \hat{h} & \hat{\Delta} \\ \hat{\Delta}^\dagger & -\hat{h} \end{pmatrix} \tag{4.12}$$

with

$$\hat{h} = \begin{pmatrix} V & -\Pi_- \\ -\Pi_+ & V \end{pmatrix} \quad \text{and} \quad \hat{\Delta} = \begin{pmatrix} m_0 e^{\mathrm{i}n\theta} & 0 \\ 0 & m_0 e^{\mathrm{i}n\theta} \end{pmatrix} \tag{4.13}$$

using

$$\Pi_\pm = p_x \pm \mathrm{i}p_y = -\mathrm{i}e^{\pm\mathrm{i}\theta}\left(\partial_r \pm \frac{\mathrm{i}}{r}\partial_\theta\right). \tag{4.14}$$

Because of $\sigma_2\hat{h}\sigma_2 = \hat{h}^*$ and $\hat{\Delta} = \hat{\Delta}^*$, the four equations contained in $\mathcal{H}\psi_0 = 0$ collapse to two inequivalent ones:

$$\hat{h}\psi - \hat{\Delta}\sigma_2\psi^* = 0\,, \tag{4.15}$$

which can be explicitly written as

$$e^{\mathrm{i}\theta}(\partial_r + \mathrm{i}r^{-1}\partial_\theta)f - m_0 e^{\mathrm{i}n\theta} f^* - \mathrm{i}Vg = 0, \tag{4.16a}$$
$$e^{-\mathrm{i}\theta}(\partial_r - \mathrm{i}r^{-1}\partial_\theta)g + m_0 e^{\mathrm{i}n\theta} g^* - \mathrm{i}Vf = 0. \tag{4.16b}$$

An additional phase factor $e^{\mathrm{i}\beta}$ in the parameter m_0 can be absorbed in the function f and g by multiplying them with a factor of $e^{\mathrm{i}\beta/2}$. Hence, we can choose $0 < m_0 \in \mathbb{R}$.

With the *one-phase* ansatz

$$f(r, \theta) = F(r)e^{\mathrm{i}a\theta}, \quad g(r, \theta) = G(r)e^{\mathrm{i}b\theta}, \tag{4.17}$$

the angular dependence in Eq. (4.16) can be eliminated by $a = b - 1 = \frac{n-1}{2}$. Please note that a *two-phase* ansatz

$$f(r, \theta) = F_1(r)e^{\mathrm{i}a_1\theta} + F_2(r)e^{\mathrm{i}a_2\theta}, \quad g(r, \theta) = G_1(r)e^{\mathrm{i}b_1\theta} + G_2(r)e^{\mathrm{i}b_2\theta} \tag{4.18}$$

made by Jackiw and Rossi (1981) does not give more solutions for $V \neq 0$,

Even (odd) values of n are connected to (half-)integer values of a and b. Since wave functions that contain a factor of $e^{\mathrm{i}\theta/2}$ have a branch cut for $\theta = 0$ and would therefore not fulfill the differential equations (4.16), zero modes only occur for odd vorticity n. The resulting set of equations are

$$\left(\partial_r + \frac{b}{r}\right) G(r) + m_0 G^*(r) - \mathrm{i}VF(r) = 0, \tag{4.19a}$$

$$\left(\partial_r - \frac{a}{r}\right) F(r) - m_0 F^*(r) - \mathrm{i}VG(r) = 0. \tag{4.19b}$$

By plugging in $G(r) = e^{-m_0 r}\widetilde{G}(r)$ and $F(r) = -\mathrm{i}e^{-m_0 r}\widetilde{F}(r)$ we get

$$\left(\partial_r + \frac{b}{r}\right) \widetilde{G}(r) - V\widetilde{F}(r) = 0, \tag{4.20a}$$

$$\left(\partial_r - \frac{a}{r}\right) \widetilde{F}(r) + V\widetilde{G}(r) = 0. \tag{4.20b}$$

This set of differential equations reduces to one equation with $\widetilde{G}(r) = \left(\partial_r - \frac{n-1}{2r}\right)\widetilde{F}(r)$:

$$\left(\partial_r + \frac{b}{r}\right)\left(\partial_r - \frac{n-1}{2r}\right)\widetilde{F}(r) - V\widetilde{F}(r) = 0 \tag{4.21}$$

By identifying this as a Bessel differential equation, we can write the overall result as

$$G(r) = e^{-m_0 r} J_b(Vr), \quad F(r) = -\mathrm{i}e^{-m_0 r} J_a(Vr). \tag{4.22}$$

where $J_a(x)$ and $J_b(x)$ are bound-state Bessel functions of the first kind. For integer values of a and b, i.e. odd vorticity n, there is only a single solution, which is in agreement with the general arguments above.

The singularity at $r = 0$ in the initial definition of $m(r, \theta)$, Eq. (4.11), is re-regularized in the solution for the zero mode, Eq. (4.22), due to the behavior of the Bessel functions in the limit $r \to 0$.

In the limit $V \to 0$ and a vorticity $n = \pm 1$, this solution is equivalent to what is reported by Hou et al. (2007). As already discussed in this reference, the corresponding zero modes only have support on one sublattice: sublattice A for $n = 1$ and sublattice B for $n = -1$. For $|n| > 1$ the limit $V \to 0$ is singular, and therefore not continously connected to the results for $V = 0$ by Hou et al. (2007): While for $V \neq 0$ the number of zero modes is fixed to 1 due to antiunitarity operator producing the symmetry of the spectrum, an n-fold vortex at $V = 0$ is associated with $|n|$ zero modes leading to different numbers of zero modes for $V = 0$ and $V \to 0$ with $|n| > 1$.

We discovered that an oddly quantized vortex in the order parameter of the EC develops one zero mode, while taking into account only one valley index and one spin species. While the spin indices are independent of each other and a vortex theoretically can occur for just one spin species, the doubling of valley indices in the total system doubles the number of zero modes. Therefore, an oddly quantized vortex is associated with two zero modes. It is known that a localized zero mode in a gapped system obeying particle-hole symmetry binds a charge

of $\pm e/2$ (Jackiw and Rebbi, 1976; Su et al., 1979; Hou et al., 2007; Seradjeh et al., 2008b). Hence, the existence of an even number of zero modes should not lead to fractionalization.

However, the mixing between the valleys, which was not considered within the low-energy theory, leads to a slight splitting of the zero modes, which we will discuss in detail in the next chapter. Due to the splitting the vortex binds a fractional "axial charge", which is a measurable quantity in the experimental setup.

5 Zero mode splitting

The nodal approximation introduced in the previous chapter is valid in the low-energy limit and shows that an oddly-quantized vortex binds two zero modes. In this chapter, we present numerical and analytical evidence for the splitting of zero modes due to inter-valley mixing in the full system and the association of a vortex with "axial" charge, the charge difference between the two layers.

Section 5.1 presents numerical results from an exact diagonalization of the real-space Hamiltonian of a finite-size system. Section 5.2 discusses general arguments why a vortex binds axial charge. In Sec. 5.3, an analytic expression for the energy splitting of the zero modes is derived.

5.1 Exact diagonalization

For the mean-field Hamiltonian in real space, Eq. (3.3), exact diagonalization was performed with the standard LAPACK diagonalization routine up to a lattice size of 51×30 sites per layer. Due to the shape of the honeycomb lattice a system with $N_x \times N_y$ sites has an extension of $\frac{\sqrt{3}}{2} a N_x \times \frac{3}{2} a N_y$ in real space.

We consider an n-fold vortex sitting at the position $\mathbf{r}_V$ (which in the numerics is chosen to be the center of the finite-size system) modeled by an order parameter

$$\Delta_{\nu i} = (-1)^\nu m_0 e^{\mathrm{i}n\theta_i} \quad \text{with} \quad \nu = 1, 2 \quad \text{for} \quad \mathbf{r}_i \in A, B \tag{5.1}$$

in the mean-field Hamiltonian (3.3), where $\theta_i = \arg(x_i - x_V + \mathrm{i}(y_i - y_V))$. The alternating sublattice-dependent sign ensures that $\Delta_+ = 0$ and $|\Delta_-| = m_0$. The system without vortex ($n = 0$) has a spectral gap $E_g = m_0$, compare Eq. (3.9).

The spectrum as a function of the vorticity n is depicted in Fig. 5.1. For $n = 1$ two near-zero modes evolve, while for $n = 2$ the spectrum is gapped. By increasing vorticity, the value of the gap and the splitting between the zero modes shrink. The splitting is independent of the

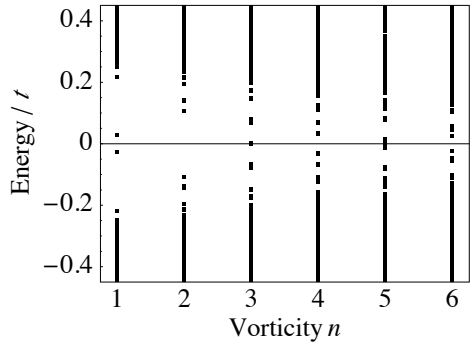

Figure 5.1: Spectrum in terms of the vorticity n for a system with $51 \times 30 \times 2$ lattice sites, $m_0/t = 0.3$, $V/t = 0.4$ and a vortex placed in the center of the lattice.

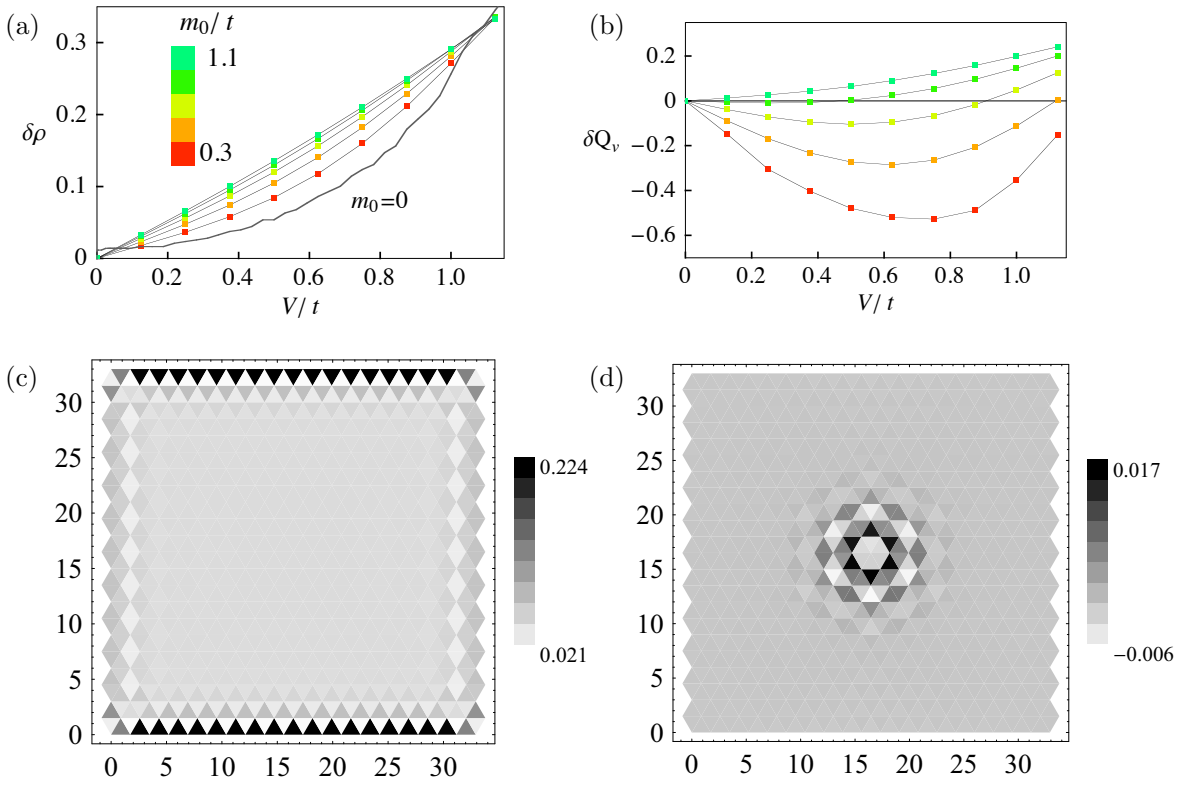

Figure 5.2: Numerical results from exact diagonalization for a system size of $39 \times 22 \times 2$. Axial density $\delta\rho$ over the gate voltage in units of t, V/t, for various values of m_0 for a system without a vortex (a), the additional axial charge δQ_v in the presence of a vortex (b), and the corresponding density profiles for $V/t = 0.4$ and $m_0/t = 0.3$ without (c) and with (d) a vortex. The honeycomb lattice sites are located in the center of the triangles. The electron charge is set to 1.

system size, and therefore not a finite size effect. Apart from the splitting, the results from the previous section predicting two zero modes for an oddly quantized vortex are confirmed.

For half filling, which will be assumed throughout this chapter, the site-dependent charge $Q(r) = Q_1(r) + Q_2(r)$, where 1 and 2 refer to the layer index, is spatially uniform for the configuration with and without vortex. The charge difference $\delta Q(r) = Q_2(r) - Q_1(r)$, to which we will refer as "axial charge" as argued in Sec. 5.2, has interesting properties. It corresponds to the dipole moment between the layers.

First we will focus on the situation without a vortex. The axial density $\delta\rho = \sum_r \delta\rho(r)$ with $\delta\rho(r) = \delta Q(r)/N$, Fig. 5.2(a), depends linearly on the gate voltage V for $V < m_0$ and turns into a quadratic dependence for $V > m_0$. In the gapless case ($m_0 = 0$) the system consists of two decoupled layers with different chemical potentials controlled by the voltage. A straightforward calculation subtracting the number of particles in each layer leads to

$$\delta\rho|_{m_0=0} = \frac{1}{N} \sum_{|t_{\mathbf{k}}|<V} 1 \approx \frac{1}{\sqrt{3}\pi} \left(\frac{V}{t}\right)^2 . \tag{5.2}$$

The corresponding plot of $\delta\rho$ for $m_0 = 0$ in Fig. 5.2(a) has an offset and ripples - both features are due to finite size effects. The density profile $\delta\rho(r)$ for finite m_0, Fig. 5.2(c), is uniform in the center and has axial charge bound to the edges showing different characteristics for zig-zag (horizontal) and arm-chair (vertical) edges.

The total charge associated with a vortex is given by the electron charge and therefore not fractionalized. However, a vortex binds additional fractionalized axial charge δQ_v on top of the background, which is uniform for an infinite system. The bound axial charge as a function of V for various values of m_0 is shown in Fig. 5.2(b). Varying these two parameters can tune the sign as well as the value continuously, which is now an *irrational* fraction of the electron charge. The density profile Fig. 5.2(d) shows an $e^{-m_0 r}$ dependence and oscillating behavior like the zero mode wave function, Eq. (4.22).

As already mentioned, the actual type of stacking is expected to have only minor influence on the development of the exciton condensate (Zhang and Joglekar, 2008). With a spatial extension much larger than the lattice spacing, we also expect the vortex and its properties to only depend weakly on the type of stacking.

An antivortex, created by a phase twist $e^{-\mathrm{i}\theta}$, annihilates a vortex if both are put at the same spatial position. They carry opposite flux, but, as numerics shows, the same axial charge.

The next section will shed light on the issue predict consequences for the exchange statistics of vortices.

5.2 Axial flux and axial charge

Based on a gauge transformation, we illustrate that a vortex in the excitonic order parameter is an object carrying "axial" flux and "axial" charge. This might be counterintuitive at first sight, since the EC order parameter gets dressed with a phase twist of 2π and therefore a full flux quantum. However, this phase twist only affects the inter-layer bonds and can be shifted to the intra-layer hopping upon applying a gauge transformation.

For the particular choice

$$c_{i1} \;\rightarrow\; c_{i1} e^{-\mathrm{i}\theta_i}\,, \tag{5.3a}$$

$$c_{i2} \;\rightarrow\; c_{i2}\,, \tag{5.3b}$$

$$t_{ij}^{(1)} \;\rightarrow\; t_{ij} e^{\mathrm{i}(\theta_i - \theta_j)}\,, \tag{5.3c}$$

$$t_{ij}^{(2)} \;\rightarrow\; t_{ij}\,, \tag{5.3d}$$

the hopping parameters on layer (1) and (2) are transformed separately, and the phase factor $e^{\mathrm{i}\theta_i}$ is shifted to the intra-layer bonds in (1), while layer (2) stays unaffected. In this gauge a full flux quantum is inserted in layer (1), but does not leave through layer (2).

By adding a half flux $\bar{\mathbf{A}}$ coupling to the total charge $Q_1(r) + Q_2(r)$, which is distributed homogeneously over all lattice sites, we end up with an axial half flux quantum coupling to the charge difference $\delta Q = Q_2(r) - Q_1(r)$, see Fig. 5.3.

Hence, a vortex effectively is an (axial charge, axial flux) composite object, which in addition carries a regular half-flux quantum. In analogy to the case of a (charge, flux) object (Wilczek,

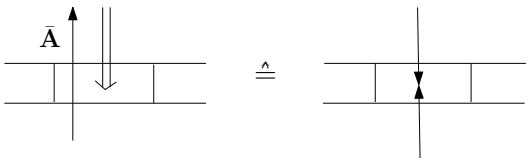

Figure 5.3: Schematic illustration showing the additional insertion of a half flux quantum $\bar{\mathbf{A}}$ and how it reduces to an axial half flux quantum coupling to the charge difference δQ_v

1990), we expect an exchange phase of $\Gamma = 2\pi \frac{\phi_v}{\phi_0} \frac{\delta Q_v}{e}$, where $\phi_v = \phi_0/2$ is the axial flux and δQ_v is the axial charge bound to a vortex. $\phi_0 = h/e$ is the flux quantum. The exchange statistics will be discussed in more detail in Chapter 6, where numerical calculations are presented that support this conjecture.

In the next section we include inter-valley mixing in the nodal approximation developed in Sec. 4.1 and derive an analytic expression for the energy splitting between the zero modes.

5.3 Analytic estimate of the zero mode splitting

In order to take into account inter-valley mixing in the framework of a nodal approximation, the equations have to be generalized to a non-uniform value of the parameter m, which was originally assumed to be uniform in Sec. 4.1. In this case the inter-layer hopping term in Hamiltonian (3.3) becomes

$$\delta H = \frac{1}{N^2} \sum_{\mathbf{kq}} m_{\mathbf{k}-\mathbf{q}} (c^\dagger_{A1\mathbf{k}} c_{A2\mathbf{q}} - c^\dagger_{B1\mathbf{k}} c_{B2\mathbf{q}}). \tag{5.4}$$

Mixing between the two valleys happens for $\mathbf{k} - \mathbf{q} \approx \pm(\mathbf{K}_+ - \mathbf{K}_-) \equiv \pm\mathbf{Q}$. We approximate $m(r) = \frac{1}{N} \sum_{\mathbf{k}} e^{\mathrm{i}\mathbf{k}\mathbf{r}} m_{\mathbf{k}}$ around these two wave vectors by

$$m_\pm(r) = \frac{1}{N} \sum_{\mathbf{p}} e^{\mathrm{i}\mathbf{p}\mathbf{r}} m_{\mathbf{p}\pm\mathbf{Q}} \approx e^{\mp \mathrm{i}\mathbf{Q}\mathbf{r}} m_0 \,. \tag{5.5}$$

In the nodal approximation the inter-layer mixing δH becomes

$$\delta H = -\int \mathrm{d}\mathbf{r} \Psi^\dagger(\mathbf{r}) \begin{pmatrix} 0 & \delta h(\mathbf{r}) \\ \delta h^\dagger(\mathbf{r}) & 0 \end{pmatrix} \Psi(\mathbf{r}) \,, \tag{5.6}$$

with

$$\delta h(\mathbf{r}) = \begin{pmatrix} m_+(\mathbf{r}) & 0 \\ 0 & m_-^*(\mathbf{r}) \end{pmatrix}. \tag{5.7}$$

The spinor can be written as $\Psi(\mathbf{r}) = (\Psi_+, \Psi_-)^T$, where $\pm$ refers to the valley index. The total Hamiltonian in the low-energy limit is given by $H_{\mathrm{nodal}} + \delta H$, where H_{nodal} is defined by Eq. (4.1).

The two zero modes $\psi_{0\pm}$ of H_{nodal} are associated with the two valleys $\pm$. According to Eq. (4.2) they are related by

$$\psi_{0+} = \gamma_1 \gamma_3 \psi_{0-} \equiv \psi_0 \,, \tag{5.8}$$

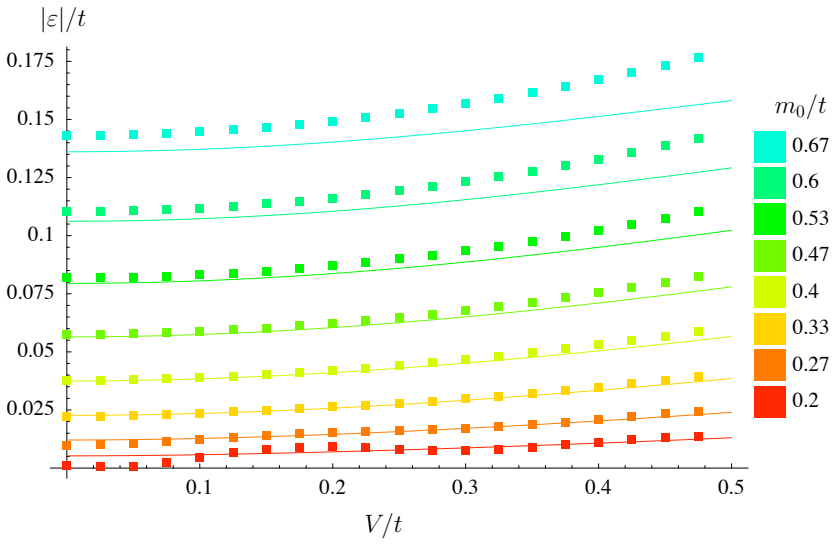

Figure 5.4: Zero mode energy splitting $|\varepsilon|$ in units of t over gate voltage V/t. Colors indicate different values of the EC order parameter m_0. The solid lines are a fit obtained by Eq. (5.11) with $\mathbf{Q} \to \eta^{-1}\mathbf{Q}$ and $\eta = 3.0$ (for explanation see text), the squares are values found by exact diagonalization of a lattice with 39×22 sites per layer and a vortex sitting in the center.

where $\psi_0 = (f, g, ig^*, -if^*)^T$, compare Eq. (4.10). Within this two dimensional subspace we can make the ansatz

$$(\delta H)_{E=0} = \begin{pmatrix} 0 & \varepsilon \\ \varepsilon^* & 0 \end{pmatrix}. \tag{5.9}$$

The value of ε can be found by projecting it out:

$$\varepsilon = -\langle \psi_{+0} | \delta h | \psi_{-0} \rangle \ . \tag{5.10}$$

Plugging in the wave functions for the zero modes and taking into account their proper normalization yields

$$\varepsilon = \mathrm{i}m_0 \frac{\int \mathrm{d}^2 r e^{-\mathrm{i}\mathbf{Q}\cdot\mathbf{r}} \mathrm{Re}\left[e^{-\mathrm{i}\theta}\left(f^2 + g^2\right)\right]}{\int \mathrm{d}^2 r \left(|f|^2 + |g|^2\right)} \ . \tag{5.11}$$

The two zero modes are split by an energy 2ε. For a quantitative comparison to the numerical values, the internodal wave vector $\mathbf{Q}$ is substituted by an effective wave vector $\eta^{-1}\mathbf{Q}$ correcting the effects of the nodal approximation. In the case with no mixing such a renormalization of the internodal wave vector is not neccesary, as the calculation is independent of $\mathbf{Q}$. Numerical and analytical results are shown in Fig. 5.4, using $\eta \approx 3.0$ yielding best fits for low to intermediate values of V and m_0.

The two zero modes appearing in the presence of an oddly-quantized vortex slightly split in energy due to an inter-valley mixing, which was not captured by the nodal approximation in

the previous chapter. This was furnished by a numerical simulation of a finite-size system and an analytical estimate in the low-energy limit. A vortex in the excitonic order parameter is neutral in the total charge channel, but binds an irrational fraction of "axial" charge and can be viewed as an (axial flux, axial charge) composite object. The associated fractional exchange statistics between two vortices is studied in the next chapter.

6 Fractional statistics

As discussed in Sec. 5.2, a vortex in the exciton condensate is an object composed of an axial half flux quantum ϕ_v and an irrationally fractionalized charge δQ_v, which furthermore carries an additional half flux quantum, but no net charge. We expect these objects to have a statistical angle of $\Gamma = 2\pi\phi_v\delta Q_v$.

In the case of bosons and fermions, the statistical angle Γ determining the statistics of the considered particle is 2π and π, respectively. It is half the geometric phase γ that is acquired by the wave function of a system, when two particles of the same type are tracked around each other (in real space) and end up in their initial position.

In general the acquired geometric phase γ in a wave function is independent of the dynamics of the system and does therefore not depend on time. It is only determined by topological properties, i.e, it only depends on the path taken in parameter space. Given an adiabatic evolution of quantum states (which for practical purposes means that the changing rate of particles is smaller than the excitation gap of the system) the geometric phase is called Berry phase.

This chapter is concerned with determining the statistical angle of vortices in the exciton condensate of a graphene bilayer system. We calculate the Berry phase acquired by the global wave function after one vortex is tracked around another one. Since the bilayer system is under the influence of a static electric field and each vortex is associated with a vector potential, a gauge-invariant formulation of the Berry phase becomes necessary, developed in Sec. 6.1. Section 6.2 describes a discretized version of the phase expression using a Bargmann invariant. Numerical results are presented in Sec. 6.3.

6.1 Gauge-invariant Berry phase

While we first focus on the derivation of a general expression for the gauge-invariant geometric phase after a cyclic evolution of quantum states, which does not require adiabaticity, we specialize this to an expression for the Berry phase, where the cyclic motion is accompanied by adiabatic changes in the Hamiltonian.

For the derivation of a gauge-invariant Berry phase, we consider the Hamiltonian $H(t)$ in the presence of an t-dependent electromagnetic potential $(A_0(t), \mathbf{A}(t))$.

$$H(t) = h(\mathbf{A}(t); t) + A_0(t) \tag{6.1}$$

defining the Schrödinger equation ($\hbar = 1$)

$$\mathrm{i}\partial_t|\Psi(t)\rangle = H(t)|\Psi(t)\rangle \tag{6.2}$$

We can define a gauge-invariant wave function

$$|\widetilde{\Psi}(t)\rangle = \exp\left(\mathrm{i}\int_{-\infty}^{t} A_0(s)ds\right)|\Psi(t)\rangle\,, \tag{6.3}$$

which fulfills

$$\mathrm{i}\partial_t|\widetilde{\Psi}(t)\rangle = \widetilde{h}(t)|\widetilde{\Psi}(t)\rangle\,, \tag{6.4}$$

with

$$\widetilde{h}(t) = \exp\left(\mathrm{i}\int_{-\infty}^{t} A_0(s)ds\right) h(\mathbf{A}(t);t)\exp\left(-\mathrm{i}\int_{-\infty}^{t} A_0(s)ds\right)\,. \tag{6.5}$$

In this section a tilde denotes gauge-invariance. For simplicity, it was assumed that the scalar potentials at different times commute: $[A_0(s_1), A_0(s_2)] = 0$. In the case of non-commuting potentials, the relations have to be defined with time-ordered exponential integrals, which does not affect the overall result.

In order to show the gauge-invariance explicitly a gauge transformation by a function $\Lambda(t)$ is considered leading to

$$A_0 \;\rightarrow\; A_0 + \partial_t\Lambda(t)\,, \tag{6.6a}$$

$$|\Psi(t)\rangle \;\rightarrow\; e^{-\mathrm{i}\Lambda(t)}|\Psi(t)\rangle\,, \tag{6.6b}$$

$$h(\mathbf{A}(t);t) \;\rightarrow\; e^{-\mathrm{i}\Lambda(t)}h(\mathbf{A}(t);t)e^{\mathrm{i}\Lambda(t)}\,, \tag{6.6c}$$

Upon applying this transformation $|\widetilde{\Psi}(t)\rangle$ and $\widetilde{h}$ become

$$|\widetilde{\Psi}(t)\rangle \;\rightarrow\; e^{-\mathrm{i}\Lambda(-\infty)}|\widetilde{\Psi}(t)\rangle\,, \tag{6.7a}$$

$$\widetilde{h}(t) \;\rightarrow\; e^{-\mathrm{i}\Lambda(-\infty)}\widetilde{h}(t)e^{\mathrm{i}\Lambda(-\infty)}\,, \tag{6.7b}$$

proofing their gauge-invariance apart from a constant phase $\Lambda(-\infty)$, which is chosen to be zero.

After a cyclic motion the gauge-invariant wave function $|\widetilde{\Psi}(t)\rangle$ acquires a phase α: $|\widetilde{\Psi}(T)\rangle = e^{\mathrm{i}\alpha}|\widetilde{\Psi}(0)\rangle$, where T is the encircling time. An expression for the phase α can be derived by defining

$$|\widetilde{\phi}(t)\rangle = e^{-\mathrm{i}f(t)}|\widetilde{\Psi}(t)\rangle\,, \tag{6.8}$$

where the function $f(t)$ is chosen in a way that the condition $|\widetilde{\phi}(T)\rangle = |\widetilde{\phi}(0)\rangle$ is fulfilled. Therefore, $\alpha = f(T) - f(0)$. Plugging in the ansatz (6.8) into the Schrödinger equation (6.4) and mulitplying the equation by $\langle\widetilde{\Psi}|$ leads to an equation for $f(t)$:

$$\frac{df}{dt} = \langle\widetilde{\phi}|\mathrm{i}\partial_t|\widetilde{\phi}\rangle - \langle\widetilde{\phi}|\widetilde{h}|\widetilde{\phi}\rangle\,. \tag{6.9}$$

Hence, the total phase change α consists of two parts

$$\alpha = \gamma - \int_0^T dt \langle \widetilde{\phi}(t) | \widetilde{h}(t) | \widetilde{\phi}(t) \rangle \,, \tag{6.10}$$

where

$$\gamma = \int_0^T dt \langle \widetilde{\phi}(t) | \mathrm{i}\partial_t | \widetilde{\phi}(t) \rangle \tag{6.11}$$

is the geometric part, which is independent of the Hamiltonian and the parametrization of the closed curve in the projective Hilbert space.

For the derivation of γ no adiabatic motion had to be assumed, what leads to the fact that to this stage the geometric phase γ is more general than the Berry phase. In the regarded case the phase is associated with the motion of the states in the Hilbert space, whereas the Berry phase requires an adiabatic change of the Hamiltonian. In the following the connection between these two phases is made by assuming that the motion of the states is generated by an adiabatic change in the Hamiltonian.

We introduce $\mathbf{R} = \mathbf{R}(t)$, a set of parameters encoding a cyclic motion, and assume that the Hamiltonian $H(t) \equiv H[\mathbf{R}(t)]$ changes adiabatically along this closed curve in the parameter space. Since we aim to describe a system with a moving vortex that carries flux, but no charge, the electric field is considered to be static, while the vector potential keeps its time-dependence leading to

$$H(t) = h(-\mathrm{i}\nabla - \mathbf{A}(t)) + A_0 \,. \tag{6.12}$$

The gauge-invariant wave functions are modeled by the ansatz

$$|\widetilde{\Psi}(t)\rangle = e^{-\mathrm{i}Et} e^{\mathrm{i}A_0 t} e^{\mathrm{i}\int \mathbf{A}(t) d\mathbf{r}} |\Psi_E\rangle \,. \tag{6.13}$$

Under the assumption of adiabaticity of the Hamiltonian, the Schrödinger equation (6.4) reduces to the stationary eigenequation

$$\left[h(-\mathrm{i}\nabla) + A_0 + \int^x \frac{d\mathbf{A}(t)}{dt} d\mathbf{r} \right] |\Psi_E\rangle = E |\Psi_E\rangle \,, \tag{6.14}$$

where we can identify the third term on the left-hand side with the fields induced by the moving vector potential:

$$\delta A_0(x) = \int^x \frac{d\mathbf{A}(t)}{dt} d\mathbf{r} = \int^x \frac{d\mathbf{R}}{dt} \frac{d\mathbf{A}}{d\mathbf{R}} d\mathbf{r} \,. \tag{6.15}$$

An adiabatic change in the Hamiltonian will change the (gauge-invariant) states $|\Psi_E\rangle$. As soon as the Hamiltonian H returns to its initial form, the wave function $|\Psi_E\rangle$ will also do. So, we can identify $|\Psi_E\rangle \equiv |\widetilde{\phi}\rangle$ and write the Berry phase as

$$\gamma = \oint \langle \Psi_E | \mathrm{i} \frac{d}{d\mathbf{R}} | \Psi_E \rangle \cdot d\mathbf{R} \,. \tag{6.16}$$

In the next section a discretized version of this formula based on a Bargmann invariant is presented.

6.2 Discrete version

For the calculation of the exchange statistics of a vortex in the EC, a system with two vortices is considered, where one remains static and the other moves on a path enclosing the first one. The global wave function acquires a geometric phase $\gamma = 2\Gamma$, where Γ is the statistical angle.

In the discrete version, where the encircling path is approximated by a n-sided polygon, the expression for the Berry phase, Eq. (6.16), transforms into (Simon and Mukunda, 1993; Rabei et al., 1999)

$$\gamma = -\arg\left(\langle\Psi_0|\Psi_1\rangle\langle\Psi_1|\Psi_2\rangle \ldots |\Psi_{n-1}\rangle\langle\Psi_{n-1}|\Psi_0\rangle\right) , \tag{6.17}$$

corresponding to a generalized n-vertex Bargmann invariant. $|\Psi_i\rangle$ is given by the ground state of the stationary Schrödinger equation (6.14), where h describes a system with the dynamical vortex sitting at the i-th position of the polygon. A 2π ambiguity in the phase γ can be excluded by following the evolution of the intermediate phase

$$\gamma_{\text{intermediate}}(i) = -\arg\left(\langle\Psi_0|\Psi_1\rangle\langle\Psi_1|\Psi_2\rangle \ldots |\Psi_i\rangle\langle\Psi_i|\Psi_0\rangle\right) , \tag{6.18}$$

with $\gamma_{\text{intermediate}}(n-1) = \gamma$, while $|\gamma_{\text{intermediate}}(i+1)| > |\gamma_{\text{intermediate}}(i)|$.

Since the vortex is associated with a half flux quantum in the $\hat{z}$-direction and its motion is in-plane ($\mathbf{v} = d\mathbf{R}/dt \perp \hat{z}$), the induced field δA_0, Eq. (6.15), vanishes: $\delta A_0 = \mathbf{v} \cdot \mathbf{A} = 0$.

The overlaps between many-body wavefunctions contained in Eq. (6.17) are evaluated via

$$\langle\Psi_0|\Psi_1\rangle = \det\left(\left\{\sum_{r=1}^{2N} \Phi_{i,r}^{(0)*} \Phi_{j,r}^{(1)}\right\}\right) , \tag{6.19}$$

where $\Phi_{i,r}^{(a)}$ is the r-th entry of the eigenvector corresponding to the i-th eigenenergy of the Hamiltonian, describing the system with the dynamic vortex sitting at position (a). Appendix A gives a detailed explanation of how such a many-body state $|\Psi_a\rangle$ is described by the corresponding eigenvectors and how the formula for the overlap is derived.

The next section presents numerical results for the geometric phase γ as a function of the axial charge bound to a vortex calculated by exact diagonalization of a finite-size system.

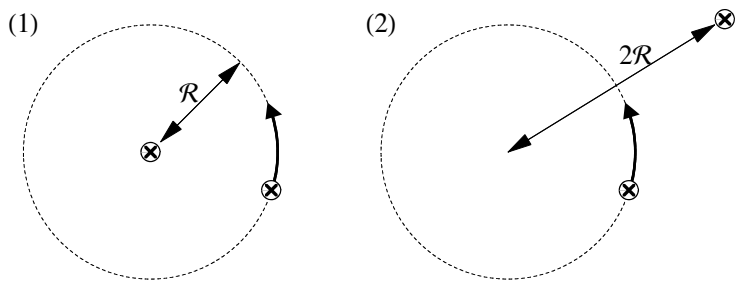

Figure 6.1: Illustration of the configurations (1) and (2).

6.3 Numerical results

In the numerics the real-space Hamiltonian (3.3) for a finite-size system with $2N$ lattice sites, which is given by a $2N \times 2N$ matrix, is treated by exact diagonalization implemented by the LAPACK routine, compare Sec. 5.1. The system contains two vortices, a static and a dynamical one. In order to subtract possible background phases, the resulting geometrical phase for the encircling procedure is the difference between the phases calculated for two configurations, $\gamma = \gamma^{(1)} - \gamma^{(2)}$ with (1) a static vortex sitting at the center of the finite-size lattice and a dynamical vortex moving around it on a circle with radius $\mathcal{R}$, whereas for (2) the dynamical vortex follows the same motion as before, while the static vortex is now at a position outside the loop at a distance $2\mathcal{R}$ from its initial position. These two configurations are illustrated in Fig. 6.1. The vortices are put to the desired positions by hand. On a formal level, the Hamiltonian does not create the vortex movement, which does not influence the validity of the results.

As discussed in Sec. 5.1, a vortex binds irrationally fractionalized axial charge, whose value depends on the gate voltage V and the excitonic order parameter m_0, compare Fig. 5.2(b). In order to investigate the dependence of the exchange phase on the axial charge, γ is calculated for various values of the gate voltage tuning δQ_v. While for the one-vortex system in Sec. 5.1 the definition of δQ_v is straightforward, it is less clear for a finite-size system with two vortices, where the distance $\mathcal{R}$ is roughly of the order of the size of the vortex ξ. In the following, we consider four different approaches defining the axial charge bound to one vortex in such a situation; the mentioned colors refer to the plot of the numerical results depicted in Fig. 6.2.

The definitions

$$\text{blue:} \quad \delta Q_v = \frac{1}{2} \sum_{r=1}^{N} \delta Q_v^{(1)}(r)\,, \tag{6.20}$$

and

$$\text{green:} \quad \delta Q_v = \frac{1}{2} \sum_{r=1}^{N} \delta Q_v^{(2)}(r)\,, \tag{6.21}$$

sum up the axial charge in the two-vortex system in configuration (1) and (2) (see Fig. 6.1), respectively, and address half of it to being bound by one vortex. This approach ignores the

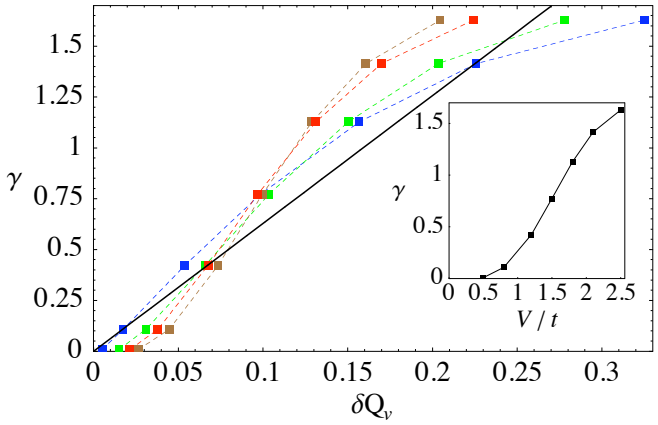

Figure 6.2: Geometric phase γ acquired by the global wave function after a vortex is encircled by a second one as a function of axial charge δQ_v bound to one vortex. The color-coded plots refer to different definitions of δQ_v, see Eqs. (6.20) to (6.23). The black line is a guide to the eyes and has a slope of 2π. The system size ($N_x = 39, N_y = 22$) corresponds to a size of approximately $(35a)^2$ in real space. The encircling radius is $\mathcal{R} = 5\sqrt{3}a$, the circle is approximated by a $n = 30$ polygon. The EC order parameter is $m_0 = 1$. The inset shows the considered values of the gate voltage V tuning the axial charge.

fact that charge might be bound to either the edge of the finite-size system or in between the two vortices.

In an attempt to only take into account axial charge that actually contributes to the geometric phase, we define

$$\text{brown:} \quad \delta Q_v = \frac{1}{2}\left(\sum_{r\in A_{\text{center},1}} \left(\delta Q_v^{(1)}(r) - \delta Q_V^{(2)}(r) \right) + \sum_{r\in A_{\text{dyn}}} \delta Q_v^{(2)}(r) \right) . \tag{6.22}$$

The areas $A_{\text{center},1}$ and A_{dyn} are depicted in Fig. 6.3(a). The former one is centered around the position of the static vortex inside the loop with a radius of $\mathcal{R}/2$. The latter one moves accordingly to the position of the dynamical vortex, also covering a disk with radius $\mathcal{R}/2$. The first term in this definition describes the encircled axial charge with a subtraction of a possible background axial charge. The second term represents the axial charge bound to the moving vortex.

A slight variation of the last definition is given by

$$\text{red:} \quad \delta Q_v = \frac{1}{2}\left(\sum_{r\in (A_{\text{center},2}\setminus A_{\text{dyn}})} \left(\delta Q_v^{(1)}(r) - \delta Q_v^{(2)}(r) \right) + \sum_{r\in A_{\text{dyn}}} \delta Q_V^{(2)}(r) \right) , \tag{6.23}$$

where $A_{\text{center},2}$ has a radius $\mathcal{R}$, see the illustration in Fig. 6.3(b).

Please note that the values of δQ_v plotted in Fig. 6.2 represent the average with respect to all positions of the dynamical vortex in the n-sided polygon.

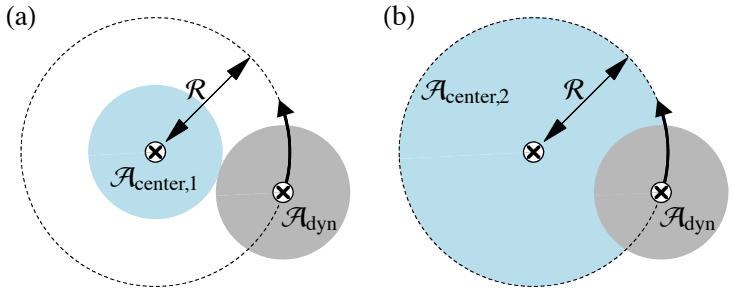

Figure 6.3: Illustration of the areas occurring in the definitions (6.22) and (6.23).

The data points depicted in Fig. 6.2 deviate from the expected behavior $\gamma = 2\pi\delta Q_v$ in a systematic way producing s-shaped curves. However, we expect these deviations as well as the deviations between the plots to be due to finite size effects, which are minimized in the following limits. If the localization ξ of a vortex tuned by m_0, compare Eq. (4.22), is much smaller than the encircling radius $\mathcal{R}$, no axial charge is bound in between the two vortices. At the same time we need $\xi \gg a$, where a is the lattice spacing. For $\mathcal{R}$ much smaller than the real-space size of the system, axial charge associated with the edges can easily be excluded in the calculation. Furthermore, the distance between two neighboring vertices in the n-sided polygon should be comparable to ξ, so that the overlap between the wave functions in Eq. (6.17) is sufficiently large. However, these requirements cannot fully be implemented by the system sizes we were able to compute (up to $(N_x = 50, N_y = 31)$ corresponding to $(45a)^2$ in real space).

Figure 6.4 shows the averaged result for the exchange phase Γ as a function of the axial δQ_v associated with one vortex. The error bar width is estimated by the difference between minimal and maximal calculated axial charges for each considered gate voltage phase averaged over all V. These results show good agreement with the expected behavior $\Gamma = \pi\delta Q_v$ illustrated by a red line in Fig. 6.4.

The theoretical derivation of a gauge-invariant Berry phase for a cyclic adiabatic evolution of quantum states accompanied by a numerical evaluation furnished the claim that vortices in the exciton condensate obey an irrationally fractionalized exchange statistics with an exchange phase $\Gamma = \pi\delta Q_v$. A summary of all essential results and a discussion of possible experimental

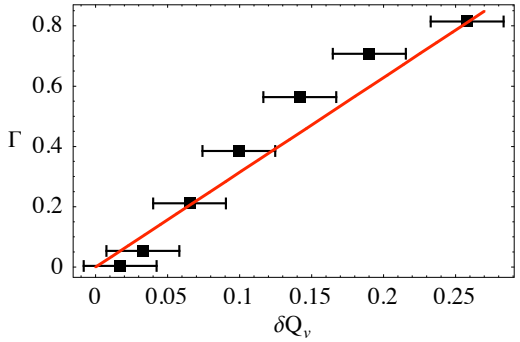

Figure 6.4: Exchange phase Γ as a function of the averaged axial charge δQ_v bound to one vortex using the data shown in Fig. 6.2. The error bars indicate the averaged ambiguity. The red line represents the expected behavior $\Gamma = \pi\delta Q_v$.

realizations and measurements is presented in the next chapter.

7 Conclusion

Bilayer graphene separated by an insulating barrier develops an instability towards an exciton condensate at infinitesimal layer coupling upon applying a symmetrically biased gate voltage. In the low-energy limit, oddly-quantized vortices in this condensate bind two zero modes, one per valley index of the bilayer. Their real-space structure shows oscillatory Bessel-function behavior located in the vicinity of the vortex core. Inter-valley mixing present in the full lattice model leads to a slight energy splitting of the two zero modes and the vortex is associated with irrationally fractionalized "axial" charge corresponding to the layer charge difference, which is an irrational fraction of e, while it is neutral in the total charge channel. Vortices correspond to (axial charge, axial flux) composite objects with an irrationally fractionalized exchange statistics depending on the induced axial charge. The bound axial charge and the associated exchange phase are not protected by symmetry or topology like in the situation of anyons in the fractional quantum Hall effect, but rather depend continuously on external parameters like the applied gate voltage or the inter-layer Coulomb interaction.

In contrast to previously studied systems exhibiting zero modes, the system at hand does not have Dirac points, but rather hole and electron Fermi surfaces in the two layers. These underlying Fermi surfaces and the inter-layer Coulomb interaction are the two essential ingredients for the development of an excitonic instability. In comparison to semiconducting bilayers hosting an exciton condensate, the linear dispersion substantially influences the low-energy behavior in such a bilayer graphene system. We therefore do not expect similar physics for semiconducting coupled quantum wells.

Possible experimental setups and measurements

The bilayer graphene structure with applied voltage is an insulator in the total charge channel and a superconductor in the axial charge channel. If the layers can be contacted separately, as it is already possible for semiconductor bilayer structures (Vignale and MacDonald, 1996; Eisenstein and MacDonald, 2004; Keogh et al., 2005), this property should be observable experimentally by measuring the counterflowing currents.

The exciton order parameter Δ couples to the vector potential difference $\mathbf{A}_1 - \mathbf{A}_2$ (Balatsky

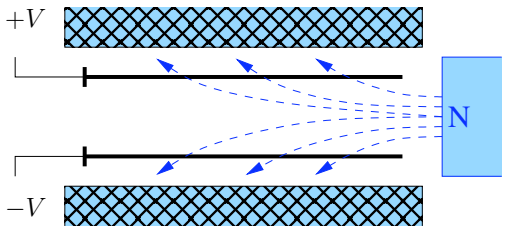

Figure 7.1: Bilayer graphene with applied gate voltage V in an inhomogeneous magnetic field, which is proposed to create vortices in the excitonic condensate

et al., 2004), where the indices refer to the two layers. The associated field $\mathbf{B}_1 - \mathbf{B}_2$ is believed to produce vortices, analogously to Abrikosov vortices in a type-II superconductor, which are produced by a uniform magnetic field. A possible experimental setup with a strong perpendicular axial component in the field $\delta B = (\mathbf{B}_1 - \mathbf{B}_2)_\perp \gg (\mathbf{B}_1 + \mathbf{B}_2)_\perp$ is schematically shown in Fig. 7.1.

The energy splitting ϵ sets the relevant energy scale in the system: The temperature T as well as the axial magnetic field δB should be much smaller than ϵ. This should not lead to any relevant restriction, since ϵ is at least one order of magnitude higher than room temperature. A more severe restriction of T arises from the Kosterlitz-Thouless transition temperature denoting the onset of the excitonic condensation. Depending on how the Coulomb interaction is actually screened in such a system, it was estimated to be $10^{-7}\epsilon_F$ (of the order of a few mK) with $\epsilon_F = 0.3$ eV in combination with an inter-layer distance $d \lesssim 0.5$ nm (Kharitonov and Efetov, 2008, 2009), or $0.1\epsilon_F$ (of the order of room temperature) with $d < 2$ nm (Min et al., 2008; Bistritzer et al., 2008). The applied gate voltage should fulfill $V \lesssim t/e$, where the hopping parameter in graphene is given by $t = 2.8$ eV, ensuring that the spectrum can still be approximately linearized at low temperatures.

The axial charge carried by a vortex might possibly be measured using the Hall effect. In analogy to type-II superconductors, where the Magnus force leads to a drift of magnetic flux lines orthogonal to the superconducting current, an axial Hall voltage can be induced in the considered system, telling how much axial charge is attached to one vortex. The axial current needed for this setup might be produced by a temperature gradient across the sample or an in-plane magnetic field.

A How to calculate an overlap between two many-body states

For the calculation of the Bargmann invariant, Eq. (6.17), overlaps between several many-body wave functions have to be taken. In this secion we will first focus on the description of such a many-body state and then derive a formula for the overlap.

The bilayer system contains $2N$ lattice sites, has $2N$ states in the spinless case and is therefore described by a Hamiltonian $\mathcal{H}$ that is represented by a $2N \times 2N$ matrix with the eigenequation $\mathcal{H}\mathbf{\Phi}_n = \epsilon_n \mathbf{\Phi}_n$. It is diagonalized by the transformation $T = [\mathbf{\Phi}_1, \mathbf{\Phi}_2, \ldots, \mathbf{\Phi}_{2N}]$.

The ground state containing ν fermions is described by

$$|\Psi\rangle = \tilde{c}_1^\dagger \tilde{c}_2^\dagger \ldots \tilde{c}_\nu^\dagger |\mathrm{vac}\rangle\,, \tag{A.1}$$

and the corresponding antisymmetrized real space wave function reads

$$\Psi(r_1, r_2, \ldots, r_\nu) = \frac{1}{\sqrt{\nu!}} \det \begin{pmatrix} \Phi_{1,r_1} & \Phi_{2,r_1} & \cdots \\ \Phi_{1,r_2} & \Phi_{2,r_2} & \cdots \\ \vdots & \vdots & \ddots \end{pmatrix} = \frac{1}{\sqrt{\nu!}} \det(\{\Phi_{i,r_j}\})\,. \tag{A.2}$$

The particle positions $r_1, \ldots, r_\nu$ are used as an index here.

The overlap of two many-body states containing ν particles can be calculated as

$$\langle \Psi_0 | \Psi_1 \rangle = \frac{1}{\nu!} \sum_{r_1,\ldots,r_\nu=1}^{2N} \Psi_0^*(r_1, \ldots, r_\nu) \Psi_1(r_1, \ldots, r_\nu) \tag{A.3}$$

$$= \frac{1}{\nu!} \sum_{r_1,\ldots,r_\nu=1}^{2N} \det(\{\Phi^{(0)}_{i,r_j}\}) \det(\{\Phi^{(1)}_{i',r_j'}\}) \tag{A.4}$$

$$= \frac{1}{\nu!} \sum_{r_1,\ldots,r_\nu=1}^{2N} \det\left(\left\{ \underbrace{\sum_{m=1}^{\nu} \Phi^{(0)*}_{i,r_m} \Phi^{(1)}_{j,r_m}}_{=A_{ij}} \right\} \right)\,. \tag{A.5}$$

For further simplification of the expression the determinant can be explicitly written by summing over all possible permutations $\mathcal{P}$:

$$\langle \Psi_0 | \Psi_1 \rangle = \frac{1}{\nu!} \sum_{r_1,\ldots,r_\nu=1}^{2N} \sum_{\mathcal{P}} \epsilon_{\mathcal{P}} A_{1\mathcal{P}_1} A_{2\mathcal{P}_2} \ldots A_{\nu\mathcal{P}_\nu} \tag{A.6}$$

$$= \frac{1}{\nu!} \sum_{r_1,\ldots,r_\nu=1}^{2N} \sum_{\mathcal{P}} \epsilon_{\mathcal{P}} \left(\sum_{m_1=1}^{\nu} \Phi^{(0)*}_{1,r_{m_1}} \Phi^{(1)}_{\mathcal{P}_1,r_{m_1}} \right) \ldots \left(\sum_{m_\nu=1}^{\nu} \Phi^{(0)*}_{\nu,r_{m_\nu}} \Phi^{(1)}_{\mathcal{P}_\nu,r_{m_\nu}} \right)\,. \tag{A.7}$$

The factor $\epsilon_{\mathcal{P}}$ contains the sign arising from the permutation. The second line is just the explicit writing of the first one. Only for $m_i \neq m_j$ the antisymmetrized combination will not vanish. Since there are $\nu!$ possibilities of choosing values for $(m_1, m_1, \ldots, m_\nu)$ out of $(1, 2, \ldots, \nu)$, Eq. (A.7) simplifies to

$$\langle \Psi_0 | \Psi_1 \rangle = \sum_{\Pi} \epsilon_{\Pi} \left(\sum_{r_1=1}^{2N} \Phi^{(0)*}_{1,r_1} \Phi^{(1)}_{\Pi_1,r_1} \right) \ldots \left(\sum_{r_\nu=1}^{2N} \Phi^{(0)*}_{\nu,r_\nu} \Phi^{(1)}_{\Pi_\nu,r_\nu} \right) \tag{A.8}$$

$$= \det \left(\left\{ \sum_{r=1}^{2N} \Phi^{(0)*}_{i,r} \Phi^{(1)}_{j,r} \right\} \right) . \tag{A.9}$$

Bibliography: Graphene

Aharonov, Y. and D. Bohm. *Significance of electromagnetic potentials in the quantum theory.* Phys. Rev. **115**, 485 (1959).

Arovas, D., J. R. Schrieffer, and F. Wilczek. *Fractional statistics and the quantum Hall effect.* Phys. Rev. Lett. **53**, 722 (1984).

Balatsky, A. V., Y. N. Joglekar, and P. B. Littlewood. *Dipolar superfluidity in electron-hole bilayer systems.* Phys. Rev. Lett. **93**, 266 801 (2004).

Berger, C., Z. Song, X. Li, X. Wu, N. Brown, C. Naud, D. Mayou, T. Li, J. Hass, A. N. Marchenkov, E. H. Conrad, P. N. First, and W. A. de Heer. *Electron confinement and coherence in patterned epitaxial graphene.* Science **312**, 1191 (2006).

Bistritzer, R., H. Min, J. J. Su, and A. H. MacDonald. *Comment on "Electron screening and excitonic condensation in double-layer graphene systems".* arxiv:0810.0331 (2008).

Butov, L. V., A. C. Gossard, and D. S. Chemla. *Macroscopically ordered state in an exciton system.* Nature **417**, 47 (2002).

Castro Neto, A. H., F. Guinea, and N. M. R. Peres. *Drawing conclusions from graphene.* Physics World **19**, 33 (2006).

Castro Neto, A. H., F. Guinea, N. M. R. Peres, K. S. Novoselov, and A. K. Geim. *The electronic properties of graphene.* Rev. Mod. Phys. **81**, 109 (2009).

Chamon, C., C.-Y. Hou, R. Jackiw, C. Mudry, S.-Y. Pi, and G. Semenoff. *Electron fractionalization for two-dimensional Dirac fermions.* Phys. Rev. B **77**, 235 431 (2008).

Cornell, E. A. and C. E. Wieman. *Nobel lecture: Bose-Einstein condensation in a dilute gas, the first 70 years and some recent experiments.* Rev. Mod. Phys. **74**, 875 (2002).

Dillenschneider, R. and J. H. Han. *Exciton formation in graphene bilayer.* Phys. Rev. B **78**, 045 401 (2008).

Eisenstein, J. P. *Half full or half empty?* Science **305**, 950 (2004).

Eisenstein, J. P. and A. H. MacDonald. *Bose-Einstein condensation of excitons in bilayer electron systems.* Nature **432**, 691 (2004).

Fradkin, E. *Critical behavior in disordered degenerate semiconductors. II. Spectrum and transport properties in mean-field theory.* Phys. Rev. B **33**, 3263 (1986).

Geim, A. K. and K. S. Novoselov. *The rise of graphene.* Nature Materials **6**, 183 (2007).

Goldstone, J. and F. Wilczek. *Fractional quantum numbers on solitons.* Phys. Rev. Lett. **47**, 986 (1981).

Gurarie, V. and L. Radzihovsky. *Zero modes of two-dimensional chiral p-wave superconductors.* Phys. Rev. B **75**, 212 509 (2007).

Gusynin, V., S. Sharapov, and J. Carbotte. *AC conductivity of graphene: From tight-binding model to 2+1-dimensional quantum electrodynamics.* Int. J. Mod. Phys. B **21**, 4611 (2007).

Gusynin, V. P. and S. G. Sharapov. *Unconventional integer quantum Hall effect in graphene.* Phys. Rev. Lett. **95**, 146 801 (2005).

Haldane, F. D. *Model for a quantum Hall effect without Landau levels: Condensed-matter realization of the "parity anomaly".* Phys. Rev. Lett. **61**, 2015 (1988).

Herbut, I. *Theory of integer Quantum Hall effect in graphene.* Phys. Rev. B **75**, 165 411 (2007).

Hou, C.-Y., C. Chamon, and C. Mudry. *Electron fractionalization in two-dimensional graphenelike structures.* Phys. Rev. Lett. **98**, 186 809 (2007).

Ivanov, D. A. *Non-Abelian statistics of half-quantum vortices in p-wave superconductors.* Phys. Rev. Lett. **86**, 268 (2001).

Jackiw, R. *Fractional charge from topology in polyacetylene and graphene.* In *International Workshop on Theoretical High Energy Physics*, volume 939, page 341 (2007).

Jackiw, R. and S.-Y. Pi. *Chiral gauge theory for graphene.* Phys. Rev. Lett. **98**, 266 402 (2007).

Jackiw, R. and C. Rebbi. *Solitons with fermion number 1/2.* Phys. Rev. D **13**, 3398 (1976).

Jackiw, R. and P. Rossi. *Zero modes of the vortex-fermion system.* Nuclear Physics B **190**, 681 (1981).

Joglekar, Y. N., A. V. Balatsky, and M. P. Lilly. *Excitonic condensate and quasiparticle transport in electron-hole bilayer systems.* Phys. Rev. B **72**, 205 313 (2005).

Joglekar, Y. N., A. V. Balatsky, and S. D. Sarma. *Wigner supersolid of excitons in electron-hole bilayers.* Phys. Rev. B **74**, 233 302 (2006).

Kane, B. E., J. P. Eisenstein, W. Wegscheider, L. N. Pfeiffer, and K. W. West. *Separately contacted electron-hole double layer in a $GaAs/Al_xGa_{1-x}As$ heterostructure.* Appl. Phy. Lett. **65**, 3266 (1994).

Katsnelson, M. I. and K. S. Novoselov. *Graphene: New bridge between condensed matter physics and quantum electrodynamics.* Sol. Stat. Comm. **143**, 3 (2007).

Katsnelson, M. I., K. S. Novoselov, and A. K. Geim. *Chiral tunneling and the Klein paradox in graphene.* Nature Physics **2**, 620 (2006).

Kellogg, M., J. P. Eisenstein, L. N. Pfeiffer, and K. W. West. *Vanishing Hall resistance at high magnetic field in a double-layer two-dimensional electron system.* Phys. Rev. Lett. **93**, 036 801 (2004).

Keogh, J. A., K. D. Gupta, H. E. Beere, D. A. Ritchie, and M. Pepper. *Fabrication of closely spaced, independently contacted electron-hole bilayers in GaAs-AlGaAs heterostructures.* Appl. Phys. Lett. **87**, 202 104 (2005).

Ketterle, W. *Nobel lecture: When atoms behave as waves: Bose-Einstein condensation and the atom laser.* Rev. Mod. Phys. **74**, 1131 (2002).

Kharitonov, M. Y. and K. B. Efetov. *Electron screening and excitonic condensation in double-layer graphene systems.* Phys. Rev. B **78**, 241 401(R) (2008).

Kharitonov, M. Y. and K. B. Efetov. *Exciton condensation in a double-layer graphene system.* arxiv:0903.4445 (2009).

Kitaev, A. Y. *Fault-tolerant quantum computation by anyons.* Ann. Phys. **303**, 2 (2003).

Lai, C. W., J. Zoch, A. C. Gossard, and D. S. Chemla. *Phase diagram of degenerate exciton systems.* Science **303**, 503 (2004).

Laughlin, R. B. *Anomalous quantum Hall effect: An incompressible quantum fluid with fractionally charged excitations.* Phys. Rev. Lett. **50**, 1395 (1983).

Leggett, A. J. *Bose-Einstein condensation in the alkali gases: Some fundamental concepts.* Rev. Mod. Phys. **73**, 307 (2001).

Min, H., R. Bistritzer, J.-J. Su, and A. H. MacDonald. *Room-temperature superfluidity in graphene bilayers.* Phys. Rev. B **78**, 121 401 (2008).

Moore, G. and N. Read. *Nonabelions in the fractional quantum Hall effect.* Nucl. Phys. B **360**, 362 (1991).

Nayak, C., S. H. Simon, A. Stern, M. Freedman, and S. D. Sarma. *Non-Abelian anyons and topological quantum computation.* Rev. Mod. Phys. **80**, 1083 (2008).

Novoselov, K. S., A. K. Geim, S. V. Morozov, D. Jiang, M. I. Katsnelson, I. V. Grigorieva, S. V. Dubonos, and A. A. Firsov. *Two-dimensional gas of massless Dirac fermions in graphene.* Nature **438**, 197 (2005).

Novoselov, K. S., A. K. Geim, S. V. Morozov, D. Jiang, Y. Zhang, S. V. Dubonos, I. V. Grigorieva, and A. A. Firsov. *Electric field effect in atomically thin carbon films.* Science **306**, 666 (2004).

Novoselov, K. S., Z. Jiang, Y. Zhang, S. V. Morozov, H. L. Stormer, U. Zeitler, J. C. Maan, G. S. Boebinger, P. Kim, and A. K. Geim. *Room-temperature quantum Hall effect in graphene.* Science **315**, 1379 (2007).

O'Hara, K. E., L. O. Suilleabhain, and J. P. Wolfe. *Strong nonradiative recombination of excitons in Cu_2O and its impact on Bose-Einstein statistics.* Phys. Rev B **60**, 10 565 (1999).

Peres, N. M., F. Guinea, and A. H. Castro Neto. *Electronic properties of disordered two-dimensional carbon.* Phys. Rev. B **73**, 125 411 (2006).

Rabei, E. M., Arvind, N. Mukunda, and R. Simon. *Bargmann invariants and geometric phases: A generalized connection.* Phys. Rev. A **60**, 3397 (1999).

Read, N. and D. Green. *Paired states of fermions in two dimensions with breaking of parity and time-reversal symmetries and the fractional quantum Hall effect.* Phys. Rev. B **61**, 10 267 (2000).

Semenoff, G. W. *Condensed-matter simulation of a three-dimensional anomaly.* Phys. Rev. Lett. **53**, 2449 (1984).

Seradjeh, B., H. Weber, and M. Franz. *Vortices, zero modes and fractionalization in bilayer-graphene exciton condensate.* Phys. Rev. Lett. **101**, 246 404 (2008a).

Seradjeh, B., C. Weeks, and M. Franz. *Fractionalization in a square-lattice model with time-reversal symmetry.* Phys. Rev. B **77**, 033 104 (2008b).

Simon, R. and N. Mukunda. *Bargmann invariant and the geometry of the Güoy effect.* Phys. Rev. Lett. **70**, 880 (1993).

Sivan, U., P. M. Solomon, and H. Shtrikman. *Coupled electron-hole transport.* Phys. Rev. Lett. **68**, 1196 (1992).

Slonczewski, J. C. and P. R. Weiss. *Band structure of graphite.* Phys. Rev. **109**, 272 (1958).

Snoke, D., S. Denev, Y. Liu, and K. West. *Long-range transport in excitonic dark states in coupled quantum wells.* Nature **418**, 754 (2002).

Spielman, I. B., J. P. Eisenstein, L. N. Pfeiffer, and K. W. West. *Resonantly enhanced tunneling in a double layer quantum Hall ferromagnet.* Phys. Rev. Lett. **84**, 5808 (2000).

Su, W. P., J. R. Schrieffer, and A. J. Heeger. *Solitons in polyacetylene.* Phys. Rev. Lett. **42**, 1698 (1979).

Tutuc, E., M. Shayegan, and D. A. Huse. *Counterflow measurements in strongly correlated GaAs hole bilayers: Evidence for electron-hole pairing.* Phys. Rev. Lett. **93**, 036 802 (2004).

Vignale, G. and A. H. MacDonald. *Drag in paired electron-hole layers.* Phys. Rev. Lett. **76**, 2786 (1996).

Wallace, P. R. *The band theory of graphite.* Phys. Rev. **71**, 622 (1947).

Wilczek, F. *Fractional statistics and anyon superconductivity.* World Scientific, Singapore (1990).

Zhang, C.-H. and Y. N. Joglekar. *Excitonic condensation of massless fermions in graphene bilayers.* Phys. Rev. B **77**, 233 405 (2008).

Zhang, Y., Y.-W. Tan, H. L. Stormer, and P. Kim. *Experimental observation of the quantum Hall effect and Berry's phase in graphene.* Nature **438**, 201 (2005).

Part II

Heavy fermion compounds: Unconventional hybridization

8 Introduction

Properties in heavy fermion compounds deviate from those of a normal metal and are dominated by the existence of strong correlations. In comparison to a normal metal the values of the specific heat coefficient and the prefactor of the T^2 contribution in the low-temperature resistivity and susceptibility are significantly enhanced. In the framework of Landau's Fermi liquid theory this can be interpreted as originating from strongly renormalized electronic quasiparticles with a 100 to 1000 times heavier mass than an electron. This property was first observed in 1975 in the material $CeAl_3$ (Andres et al., 1975). Strong interactions, which are responsible for this effect, lead to a large variety of unusual properties and different phases in these materials, like superconductivity, which was discovered by Steglich et al. (1979) in $CeCu_2Si_2$. With this discovery heavy fermion compounds attracted attention and a series of investigations followed.

On a microscopic level heavy fermion compounds are intermetallic compounds based on rare earth elements like Ce, or actinides like U. Conduction electrons coexist with localized electrons from partially filled f-bands.

In the framework of this thesis we are concerned with the influence of a non-local hybridization between conduction and localized electrons and study its consequences for the band structure and physical observables.

This introductory chapter gives an overview of the physics involved in heavy fermion compounds, which arises from the Kondo effect and magnetic ordering phenomena, and reviews the experimental situation. The first two sections focus on the theoretical aspects: Section 8.1 explains the single-impurity Kondo effect, Sec. 8.2 introduces its lattice generalization, which turns out to be the appropriate model for heavy fermion systems. As in most of the literature we are for now dealing with a local hybridization. More exhaustive overviews of the theory of heavy fermion compounds are e.g. given by Hewson (1997) or Coleman (2007). Section 8.3 presents the experimental phase diagram. Section 8.4 introduces the heavy-fermion compound series $CeMIn_5$ (M=Rh,Ir,Co) comprised under the name 115-family. These materials show evidence for a non-local hybridization between localized and conduction electrons, which is discussed further in Sec. 8.5. An outline in Sec. 8.6 concludes this chapter.

8.1 The Kondo effect: Single-impurity physics

A basic ingredient to the physics of heavy fermion compounds is the Kondo effect, which is produced by a magnetic impurity in a sea of conduction electrons. An ordinary and well behaved metal in the low-temperature regime follows the laws of Fermi liquid theory. This for example means that the specific heat is linear in T, the magnetic susceptibility χ is approximately temperature-independent, and the resistivity has the shape $\rho(T) = \rho_0 + AT^2$, where ρ_0 arises from (non-magnetic) impurity scattering and the quadratic contribution is due to electron-electron scattering processes. In the presence of a magnetic impurity the most

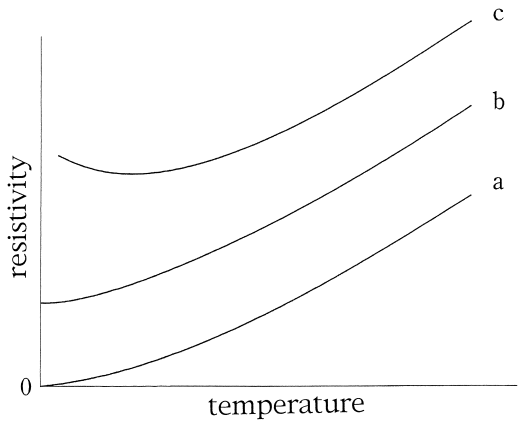

Figure 8.1: Schematic plot for the resistivity as a function of temperature in the low-temperature regime for a clean metal (a), a metal with non-magnetic impurities (b) and a metal in the presence of magnetic impurities (c). (Figure from Kondo, 2006).

significant change arises in the resistivity, compare Fig. 8.1. A resistivity minimum develops, which experimentally was already observed in the 1930s in Au (de Haas et al., 1934). The first theoretical explanation however followed thirty years later by Kondo (1964), who introduced the (single-impurity) Kondo model

$$H_{\mathrm{SIKM}} = \sum_{\mathbf{k}\sigma} \epsilon_{\mathbf{k}} c^{\dagger}_{\mathbf{k}\sigma} c_{\mathbf{k}\sigma} + J_{\mathrm{K}} \mathbf{S} \cdot \mathbf{s}(\mathbf{r}=0)\,. \tag{8.1}$$

$c^{\dagger}_{\mathbf{k}\sigma}$ denotes the creation operator for a conduction electron with momentum $\mathbf{k}$, spin σ and energy $\epsilon_{\mathbf{k}}$. The conduction electron spin density $\mathbf{s}(\mathbf{r}=0) = \frac{1}{2}\sum_{\mathbf{k}\mathbf{k}'\sigma\sigma'} c^{\dagger}_{\mathbf{k}\sigma} \boldsymbol{\sigma}_{\sigma\sigma'} c_{\mathbf{k}'\sigma'}$ at the impurity site is coupled to the impurity spin $\mathbf{S}$ via the Kondo coupling J_{K}. The antiferromagnetic coupling (i.e. $J_{\mathrm{K}} > 0$) leads to interesting physics, which is discussed in the following.

Although this model looks simple and innocent, its solution was a long-standing issue. Kondo himself calculated up to third order perturbation theory in the Kondo coupling J_{K}. Within this approach the resistivity has a $\ln T$ contribution, which means that it increases while approaching the zero-temperature limit. Accompanied by a decreasing phonon contribution this procedure is able to explain a resistivity minimum. However, the logarithmic divergence at $T \to 0$ is rather unpleasant. An expansion of the perturbational approach by considering parquet summations of an infinite number of diagrams (Abrikosov, 1965) shifts the divergence to a finite temperature

$$T_{\mathrm{K}} = D e^{-\frac{1}{N_0 J_{\mathrm{K}}}}\,, \tag{8.2}$$

where D is the bandwidth and N_0 the density of states of the conduction band at the Fermi level. The non-perturbative approach studied by Nagaoka (1965) in terms of a Green's functions and an equivalent approach by Suhl (1965) using scattering theory are able to produce a non-singular resistivity at $T = T_{\mathrm{K}}$, but still the physics below the Kondo scale T_{K} cannot be accessed with these techniques.

Anderson's ansatz of poor man's scaling (Anderson, 1970) was successful in capturing the correct physics in the weak-coupling regime above T_{K}. By reducing the bandwidth D and formulating an effective problem, where renormalized parameters carry the effect of the eliminated higher-order excitations, he was able to show that the effective Kondo coupling $\widetilde{J}$ becomes large at T_{K}. This suggests a ground state with a local singlet, but however is not able to describe the dynamics below T_{K}. For the strong-coupling regime, Nozières (1974) introduced a spin-dependent scattering picture based on the existence of such a Kondo singlet leading to a Landau Fermi liquid. The behavior for temperatures $T \ll T_{\mathrm{K}}$ is similar to the physics of a system with a non-magnetic impurity. Finally, Wilson (1975) gave a full explanation of the physics of the (one-channel) single impurity Kondo model. He introduced a non-perturbative scaling approach, the numerical renormalization group.

In 1961, Anderson (1961) suggested a different model, which later on turned out to be connected to the Kondo model in specific parameter limits, the Kondo limit. In the following we discuss this Anderson model, apply the Schrieffer-Wolff transformation (Schrieffer and Wolff, 1966), which connects the two models and fix the parameters to the Kondo limit.

The single-impurity Anderson model contains conduction electrons and localized electrons at a single site that are subjected to an on-site Coulomb repulsion U:

$$H_{\mathrm{SIAM}} = \sum_{\mathbf{k}\sigma} \epsilon_{\mathbf{k}} c^{\dagger}_{\mathbf{k}\sigma} c_{\mathbf{k}\sigma} + V \sum_{\mathbf{k}\sigma} \left(c^{\dagger}_{\mathbf{k}\sigma} f_{\sigma} + f^{\dagger}_{\sigma} c_{\mathbf{k}\sigma} \right) + \epsilon_f \sum_{\sigma} f^{\dagger}_{\sigma} f_{\sigma} + U n_{f\uparrow} n_{f\downarrow} \,. \tag{8.3}$$

The conduction electrons $c_{\mathbf{k}\sigma}$ and the localized f_{σ}-electrons are hybridized with V due to their wavefunction overlap.

The Coulomb repulsion as well as the hybridization lead to strong interactions among the electrons. For a vanishing hybridization, c- and f-electrons are decoupled and the configuration of f-electrons is simply determined by U and ϵ_f. The Hilbert space of the f-level is spanned by three charge sectors with empty, single and double occupancy. Upon turning on the hybridization V the f-electrons immerse in the sea of conduction electrons.

In the Kondo limit

$$\epsilon_f < 0, \qquad \epsilon_f + U > 0, \qquad \Gamma \ll |\epsilon_f|, |\epsilon_f + U| \,, \tag{8.4}$$

where $\Gamma = \pi |V|^2 N_0$ is the effective hybridization and N_0 is the conduction electrons density of states at the Fermi level, the f-level is occupied by one electron. The small, but non-zero V produces virtual excitations to the empty and the doubly occupied subspaces. The f-level can be regarded as a local moment with spin 1/2. The Schrieffer-Wolff transformation, developed with a perturbative treatment of the hybridization, projects out empty and doubly occupied subspaces.

In the lowest order in V the resulting effective Hamiltonian contains a spin exchange interaction between the spins of the conduction and local electron with the antiferromagnetic exchange coupling

$$J_{\mathrm{K}} = |V|^2 \left(\frac{1}{U + \epsilon_f} + \frac{1}{|\epsilon_f|} \right) > 0 \,. \tag{8.5}$$

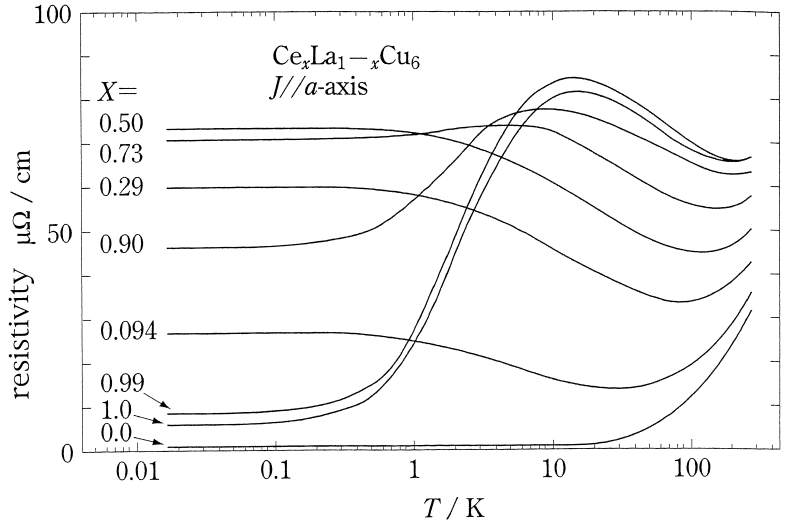

Figure 8.2: Electrical resistivity as a function of temperature in $Ce_xLa_{1-x}Cu_6$ for different doping levels x. All finite doping concentrations lead to a minimum in the resistivity. For $x \geq 0.73$ an additional maximum evolves. (Figure from Kondo, 2006).

As we have seen, the Anderson model in the Kondo limit has a local moment and an antiferromagnetic exchange coupling with the conduction sea, just like the Kondo model.

For a sufficiently dilute concentration of magnetic impurities the ground state of the Kondo model is determined by Kondo singlets. Higher concentrations are accompanied by magnetic interactions among the impurities, which drastically change the physical properties. The theoretical approaches are discussed in the next section.

8.2 The Kondo lattice and the existence of multiple energy scales

In analogy to the single-impurity case, lattice generalizations of both the Anderson and the Kondo model can be formulated, which are connected via a lattice version of the Schrieffer-Wolff transformation. Within this section we will introduce these two lattice models. We present the emerging energy scales in this problem and discuss the ground state physics, which is controlled by the competition between Kondo screening and magnetic ordering.

The generalization of the single-impurity Anderson model to the lattice case is given by the Anderson lattice model (ALM):

$$H_{\mathrm{ALM}} = \sum_{\mathbf{k}\sigma} \epsilon_{\mathbf{k}} c^{\dagger}_{\mathbf{k}\sigma} c_{\mathbf{k}\sigma} + V \sum_{i\sigma} \left(f^{\dagger}_{i\sigma} c_{i\sigma} + h.c. \right) + \epsilon_f \sum_{i\sigma} f^{\dagger}_{i\sigma} f_{i\sigma} + U \sum_{i} n_{f,i\uparrow} n_{f,i\downarrow} \,. \tag{8.6}$$

The f-electrons as well as the c-electrons sit on lattice sites. For simplicity we here assume that these two lattices are identical and the hybridization V is local. No direct magnetic exchange between the f-electrons exists and the f-band is assumed to be non-dispersive.

A large value of U and a negative ϵ_f leads to a situation of mainly single f-occupancy per site, and a description of the f-electrons in terms of localized spin-1/2 moments becomes valid. After a lattice Schrieffer-Wolff transformation the Anderson lattice model transforms into the Kondo lattice model, which describes a dense configuration of magnetic "impurities" in a sea of conduction electrons:

$$H_{\mathrm{KLM}} = \sum_{\mathbf{k}\sigma} \epsilon_{\mathbf{k}} c^{\dagger}_{\mathbf{k}\sigma} c_{\mathbf{k}\sigma} + J_{\mathrm{K}} \sum_i \mathbf{S}_i \cdot \mathbf{s}(\mathbf{r}_i)\,. \tag{8.7}$$

The local spins $\mathbf{S}_i$ are coupled antiferromagnetically to the spin densities $\mathbf{s}$ of the conduction electron at the "impurity" sites $\mathbf{r}_i$. The Kondo coupling J_{K} is defined by Eq. (8.5).

As apparent from Fig. 8.2, the physics of the single-impurity result cannot easily be generalized to the lattice case: The resistivity results for $Ce_xLa_{1-x}Cu_6$ qualitatively change for different doping levels x. For increasing doping x, non-magnetic La ions are gradually substituted by magnetic Ce ions. Low x represents the single-impurity case, whereas high x corresponds to the case of a Kondo lattice. In dense Kondo systems an additional maximum appears due to the existence of a coherent state at low temperatures. Two energy scales can be identified: the Kondo temperature T_{K}, a generalization of the single-impurity to the lattice case, and T_{coh} associated with the onset of coherence.

The identification of T_{K} and T_{coh} with the minimum and maximum positions in the resistivity is not exact, but simply describes the qualitative behavior at these temperatures. Both energy scales can be defined using thermodynamic properties (Burdin, 2008). At T_{K} the crossover happens between an asymptotically free spin for high temperatures and a spin bound in a singlet pair. This behavior can be quantified by the entropy per site, which becomes $\ln 2$ in the presence of a free spin and decreases throughout the crossover regime. Therefore, T_{K} can be defined as the temperature where the entropy has a value of e.g. $0.8 * \ln 2$. Experimentally, T_{K} is accessible via specific heat measurements, which are closely related to the entropy. The coherence scale T_{coh} determines all low-temperature properties of the Kondo lattice system, which obey Fermi liquid behavior. We therefore can define T_{coh} via the specific heat coefficient γ as $T_{\mathrm{coh}} = 1/\gamma$ (with $k_B = 1$) or e.g fix it to $T_{\mathrm{coh}} = 1/\chi(0)$, where $\chi(0)$ is the zero-temperature magnetic susceptibility (Burdin, 2008).

The relation between these two energy scales was widely discussed, starting with Nozières (1985). On the level of mean-field arguments Burdin et al. (2000) showed that in the weak-coupling regime the ratio between T_{K} and T_{coh} only depends on the filling and the shape of the conduction band. Pruschke et al. (2000) employed the numerical method of dynamical mean-field theory (DMFT) (Metzner and Vollhardt, 1989; Georges et al., 1996), which is able to go beyond the mean-field approximation and takes into account local quantum fluctuations: For less than half filling ($n_c = 1$) the ratio $T_{\mathrm{K}}/T_{\mathrm{coh}}$ is either constant or depends on n_c. These results clearly contradict Nozières (1985), who suggested the scenario of exhaustion, i.e., an insufficient screening of localized electrons in the presence of low conduction electron density, and predicted the relation $T_{\mathrm{coh}} \sim T_{\mathrm{K}}^2/D$. However, it turned out that the arguments underlying this exhaustion principle are too simplistic (Nozières, 2005) and do not capture the right physics.

In contrast to the single-impurity scenario the ground state of a dense Kondo system is strongly influenced by the magnetic interaction between two impurity spins. Although not

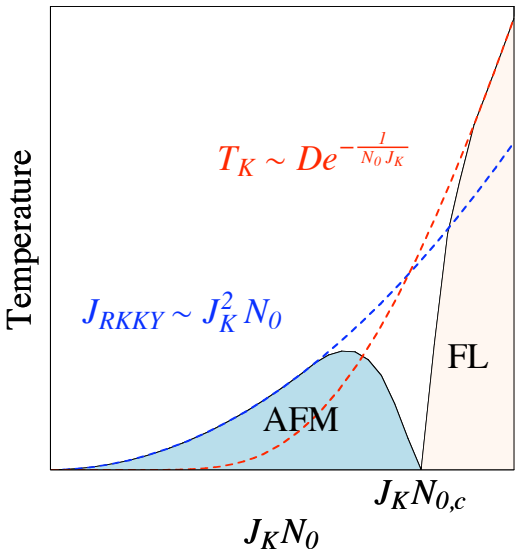

Figure 8.3: Schematic illustration of the Doniach phase diagram for dense Kondo systems in dependence of temperature T and $J_\mathrm{K}N_0$, where J_K denotes the Kondo coupling and N_0 the conduction electron density. Two regimes can be distinguished - an antiferromagnetic regime for $T_\mathrm{K} \ll J_\mathrm{RKKY}$ and a heavy fermion regime for $T_\mathrm{K} \gg J_\mathrm{RKKY}$, seperated by a quantum critical point at $J_\mathrm{K}N_{0,c}$. (Figure after Coleman, 2007).

present as a direct magnetic interaction term, the Kondo lattice Hamiltonian (8.7) contains a magnetic interaction between the impurity spins mediated by the conduction electrons, termed RKKY interaction (Ruderman and Kittel, 1950; Kasuya, 1956; Yosida, 1957). In the presence of an impurity spin the conduction electrons become spin-polarized and Friedel oscillations are induced in the conduction spin density. The RKKY exchange coupling mainly depends on the Kondo coupling and the distance dependent spin-spin correlation function χ_S as

$$J_\mathrm{RKKY} \sim J_\mathrm{K}^2 \chi_S(r) \approx J_\mathrm{K}^2 N_0 \frac{\cos(2k_F r)}{k_F r}\,, \tag{8.8}$$

where k_F is the Fermi wave vector and N_0 is the conduction electron density of states at the Fermi level. In order to estimate its order of magnitude the r-dependence in this expression is neglected: $J_\mathrm{RKKY} \approx J_\mathrm{K}^2 N_0$.

By comparing the two energy scales T_K and J_RKKY, Doniach (1977) suggested a phase diagram that illustrates the interplay of antiferromagnetic ordering and Kondo screening, see Fig. 8.3. Depending on the Kondo coupling and the conduction electron density the Kondo and the magnetic energy scale change and an antiferromagnetic and a Fermi liquid phase evolve in different parameter regimes. In the original work, the considered system was assumed to be one-dimensional and insulating. The predicted ground state second-order phase transition would actually be smeared out by the strong quantum fluctuations, which are present in one dimension. However, higher dimensional systems in fact show signatures of a quantum phase transition, see the review by von Löhneysen et al. (2007).

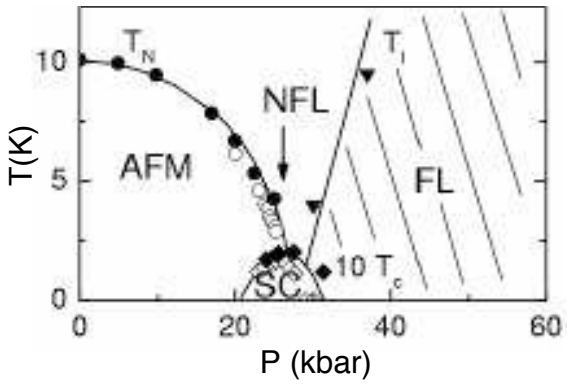

Figure 8.4: Experimental pressure-temperature phase diagram for $CeIn_3$ containing a non-Fermi liquid regime (NFL), an antiferromagnetic (AFM), a superconducting (SC) and a Fermi liquid (FL) phase. (Figure from Flouquet, 2005)

The theoretical concept of a Kondo lattice is realized in heavy fermion materials. In the next section we present an experimental phase diagram and discuss the emerging phases.

8.3 Heavy fermion compounds: experiments

The physics of heavy fermion compounds is very rich and cannot be pressed into a single phase diagram. An overview from an experimentalist's point of view is, e.g., given by Grewe and Steglich (1991), more recent ones by Stewart (2001) and Flouquet (2005). In the following we simply consider the example material $CeIn_3$, which happens to be the "parent compound" of the 115-family we will discuss in more detail later on. Its pressure-temperature phase diagram, see Fig. 8.4, illustrates the competition between antiferromagnetic order, Kondo screening and superconductivity. Apart from the superconducting instability it strongly resembles the Doniach phase diagram, Fig. 8.3, following from the fact that the application of pressure directly influences the product of Kondo coupling and density of states, $J_K N_0$.

The physical observables in the Fermi liquid (FL) phase follow the laws of Landau's Fermi liquid theory and correspond to those of a Fermi liquid with strongly renormalized parameters. The properties in this phase imply huge effective quasiparticle masses giving the heavy fermion compounds their name.

In the presented example the magnetically ordered phase is antiferromagnetic (AFM) with a $(\pi/2, \pi/2, \pi/2)$ ordering wave vector. However, the exact type of magnetic ordering differs for different compounds; also ferromagnetic instabilities are observed.

The superconductivity emerging in heavy fermion systems can only to certain extent be described by BCS theory. The original BCS-theory for conventional superconductors describes phonon-mediated pairing, whereas the pairing in heavy fermion compounds is expected to be mediated by magnetic fluctuations. The BCS-like pairs are built from heavy quasiparticles, which feel a strong on-site Coulomb repulsion. The pairing becomes anisotropic, leading to an additional symmetry breaking on top of the broken U(1) gauge symmetry, which defines the

class of unconventional superconductors (Sigrist and Ueda, 1991). In heavy fermion materials there are indications for a superconducting order parameter that exhibits a d-wave symmetry. For a broad discussion of the interplay between magnetism and superconductivity in heavy fermion compounds see Thalmeier and Zwicknagl (2005). Under the influence of a magnetic field the system exhibits vortices, a property that may arise for unconventional as well as for conventional superconductors.

In $CeIn_3$ as well as in some other Ce- and U-based heavy fermion compounds the superconducting instability emerges in the vicinity of a quantum critical point terminating an antiferromagnetic second order phase transition line. While in $CeIn_3$ AFM and SC do not coexist, a coexistence of these two phases seems possible for other compounds like e.g. $CePd_2Si_2$.

The transition temperatures T_c for this material class are of the order of a few Kelvin and roughly one order of magnitude lower than in high-temperature superconductors, for which transition temperatures above 100 K are possible. However, both exhibit anisotropic order parameters, while their underlying pairing mechanisms are to date not fully understood. Their similarities make superconductivity in heavy fermion compounds an attractive field of research.

Non-Fermi liquid (NFL) behavior, often found near a magnetically ordered phase is expected to be closely linked to the underlying magnetic quantum critical point (QCP) (Stewart, 2001, 2006).

The next section is concerned with the $CeMIn_5$ series of compounds, which besides interesting features in the superconducting phase are excellent candidates to study quantum criticality. We will discuss their crystal structure and present their phase diagram.

8.4 The 115-family

The term 115-family denotes the series of compounds $CeMIn_5$ with M=Co,Rh,Ir discovered only a few years ago (Hegger et al., 2000; Petrovic et al., 2001a,b). These materials attracted a lot of interest due to the evolution of a superconducting phase with a relatively high transition temperature compared to other heavy fermion compounds: $CeCoIn_5$ has a T_c of 2.4 K. Their crystal structure is of $HoCoGa_5$ type, depicted in Fig. 8.5(a). It consists of alternating layers with $CeIn_3$ and MIn_2 giving rise to a two-dimensional behavior confirmed by explorations of the Fermi surfaces (Hall et al., 2001; Settai et al., 2001; Shishido et al., 2002) and local density approximation band structure calculations (Maehira et al., 2003). This isostructural alloy series exhibit different ground states at ambient pressure. The doping phase diagram, see Fig. 8.5(b), shows the competition between superconductivity and magnetism as well as the coexistence of these two phases. In this context the doping level x tunes the chemical pressure by incorporating larger or smaller ions, while the charge carrier concentration does not change.

The application of pressure changes the ground state of these materials, e.g. driving the ambient-pressure antiferromagnet $CeRhIn_5$ to superconductivity . This makes them excellent candidates for studying quantum phase transitions (von Löhneysen et al., 2007). Similarly to the parent compound $CeIn_3$ the superconductivity occurs in the vicinity of a quantum critical point. The ambient pressure superconductor $CeCoIn_5$ is therefore a material close to quantum criticality.

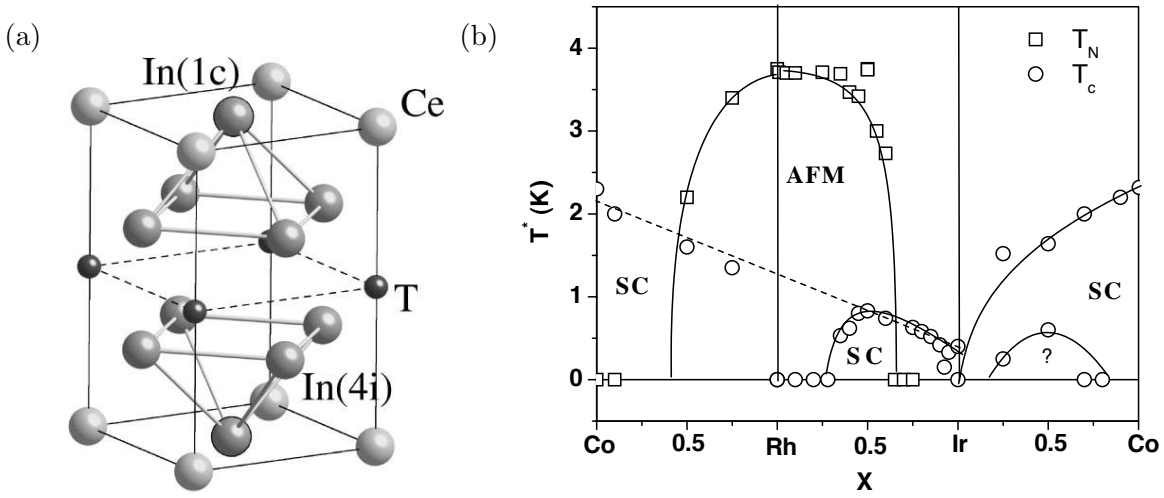

Figure 8.5: (a) $HoCoGa_5$ type tetragonal structure realized in $CeTIn_5$ (T=Rh,Ir,Co). (Figure from Maehira et al., 2003). (b) Doping-temperature phase diagram for the 115-series at ambient pressure. (Figure from Pagliuso et al., 2002).

$CeCoIn_5$ is the most prominent representative of the 115-family. It is a clean type-II superconductor with singlet pairing and a d-wave order parameter; its anisotropy is e.g. observed in thermal conductivity measurements in a rotating magnetic field (Izawa et al., 2001b). The superconductivity in the presence of an external magnetic field is Pauli-limited, i.e., it is destroyed by parallel spin alignment due to the Zeeman term rather than orbital pair breaking. For low temperatures and a magnetic field close to H_{c2} speculations arose (Bianchi et al., 2003) about the existence of a FFLO superconducting state (Fulde and Ferrell, 1964; Larkin and Ovchinnikov, 1965), where Cooper pairs have a finite momentum and the order parameter oscillates in space, leading to a spatially inhomogeneous phase. However, more recent experiments (Kenzelmann et al., 2008) simply suggest coexistence of magnetism and superconductivity in this regime.

Optical conductivity measurements in 115-materials show indications for a non-local hybridization between f- and c-electrons. So far for simplicity reasons such a property was not accounted for in most theoretical calculations. In the next section we will discuss its experimental evidence and compare it to other HF compounds, where the assumption of a local hybridization is justified.

8.5 Motivation: Unconventional hybridization

In the Anderson lattice model defined by the Hamiltonian (8.6) f- and c-electrons are coupled via a hybridization V produced by their wavefunction overlap. In the low-temperature Fermi liquid regime a constant hybridization leads to an indirect gap, whose size is related to the renormalized hybridization taking into account the effect from the on-site f-electron repulsion. Optical conductivity measurements in certain HF compounds reveal the existence of such a gap, e.g. for $YbFe_4Sb_{12}$, compare Fig. 8.6(a) (Degiorgi, 1999; Dordevic et al., 2001; Degiorgi

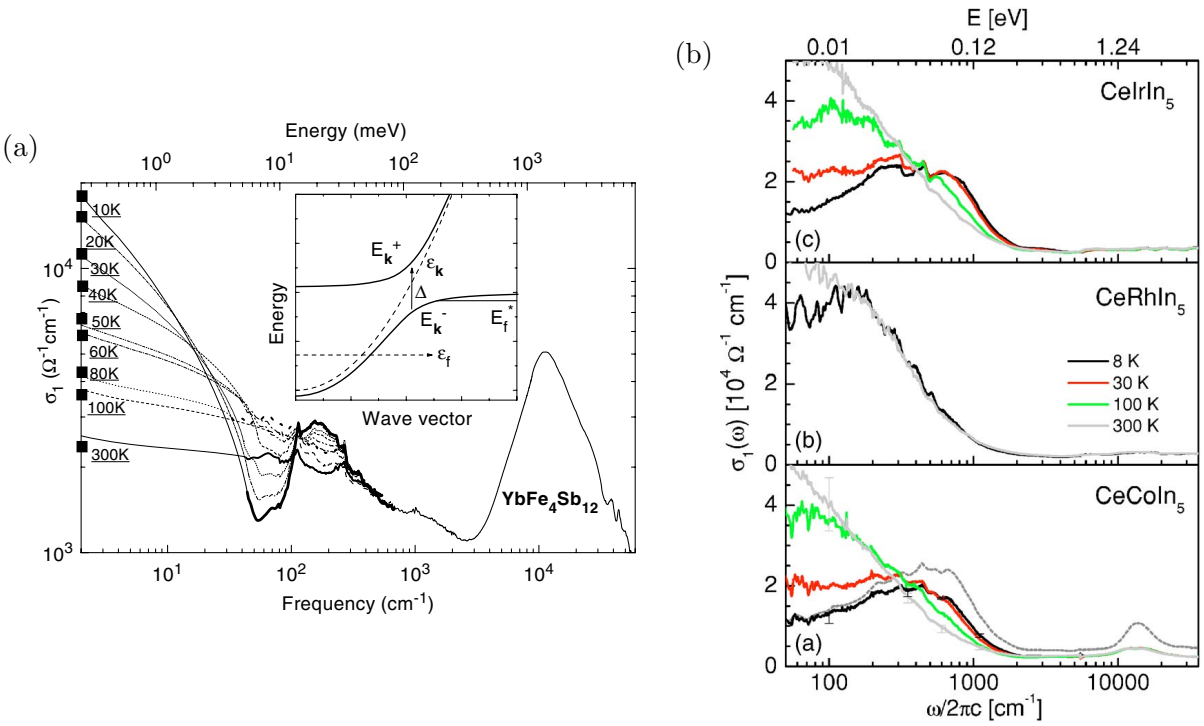

Figure 8.6: (a) Real part of the optical conductivity for the heavy fermion compound $YbFe_4Sb_{12}$ over frequency for various temperatures. Below $T_{\mathrm{coh}} \approx 50$K a gap-like feature at approximately 18meV appears. (Figure from Dordevic et al., 2001). (b) Real part of the optical conductivity for the compounds of the 115-series as a function of frequency. (Figure from Mena et al., 2005).

et al., 2001). Its size scales with the effective quasiparticle mass, which is closely related to the coherence temperature (Hancock et al., 2004; Okamura et al., 2007). In contrast, optical spectroscopy in 115-materials shows a gapless feature (Singley et al., 2002; Mena et al., 2005), compare Fig. 8.6(b), previously interpreted by a distribution of gap values (Burch et al., 2007).

By regarding the crystal structure of CeMIn$_5$, Fig. 8.5(a), the assumption of a non-local and therefore $\mathbf{k}$-dependent hybridization seems reasonable: f-electrons possibly hybridize with the c-electrons on adjacent sites. The presence of line nodes in $V_{\mathbf{k}}$ can significantly change the physics, for example produce the observed gapless feature in the optical conductivity, as we will show in this work. Such a $\mathbf{k}$-dependence can be seen in the spirit of unconventional superconductivity, where a Cooper pair carries an internal angular momentum and the pairing function acquires a $\mathbf{k}$-dependence.

An unconventional, i.e., $\mathbf{k}$-dependent hybridization is accompanied by a strong anisotropy in momentum space, which will leave some physical properties unchanged while strongly influencing others. Significant changes are expected in the phase competition with superconductivity and the character of the favored superconducting phase, since both the Kondo lattice effect and superconducting pairing compete for the same electrons.

Up to now a momentum-dependent hybridization for heavy fermion system was only considered a few times starting with Doniach (1987). Ikeda and Miyake (1996) and Moreno and

Coleman (2000) modeled the physics of a Kondo insulator, describing the properties of CeNiSn and its isostructural compounds. Ghaemi and Senthil (2007) used a similar ansatz as the one that will be considered in the following. However, Ghaemi et al. discuss different physical properties. The results presented in the framework of this thesis are published in (Weber and Vojta, 2008).

8.6 Outline

In this work we are dealing with a momentum dependent hybridization between localized f and conduction electrons in the framework of the Anderson and Kondo lattice models. We consider this ansatz in order to model the behavior of heavy fermion compounds with a non-local hybridization exhibiting momentum-space nodes. Our special focus lies on the isostructural alloy series CeMIn$_5$ with M=Ir, Rh, Co.

We analyze the low-temperature properties in the Fermi liquid regime in the framework of a mean-field approximation. Results are shown for the Fermi surface, the band structure, thermodynamical properties like the specific heat as well as transport properties like optical conductivity, electrical and thermal transport. We discuss the behavior of the resistivity in the high-temperature regime, i.e., above T_K. Furthermore, we are interested in the influence of the momentum-dependent hybridization on the phase competition between Kondo screening and magnetically mediated superconductivity, supplemented by a study of the role of magnetic ordering in the phase diagram.

This work is organized as follows: Chapter 9 introduces the considered model, subjected to a mean-field approximation in Chapter 10. Thermodynamics as well as transport properties in the low-temperature Fermi liquid regime are presented in Chapter 11. Chapter 12 discusses resistivity calculations for the high-temperature regime using perturbation theory in the Kondo coupling. In Chapter 13 we comment on methods for going beyond the considered mean-field approximation. Chapter 14 studies the phase competition of the Kondo screening with superconductivity and magnetic ordering and presents phase diagrams from a mean-field treatment. A summary of the results in Chapter 15 concludes this part.

9 Model

The introductory chapter 8 gave a first glance on the Anderson and the Kondo lattice models, which are used to describe heavy fermion systems. Both are generalizations of the corresponding single-impurity model dealing with a local magnetic ion in a metallic host and are connected via the Schrieffer-Wolff transformation. In this chapter we generalize these models to the case of a non-local hybridization. We compare the presented ansatz with the ones suggested by Ghaemi and Senthil (2007) and Ghaemi et al. (2008).

In order to preserve the full translational invariance of the underlying lattice, on which c- and f-electrons live, the hybridization function in real space only depends on the relative position:

$$\sum_{i,j} V(\mathbf{r}_j - \mathbf{r}_i)(f^\dagger_{i\sigma} c_{j\sigma} + h.c.)\,. \tag{9.1}$$

Therefore, in $\mathbf{k}$-space the Anderson lattice model with non-local hybridization is given by

$$\mathcal{H}_{\mathrm{ALM}} = \sum_{\mathbf{k}\sigma} (\epsilon_{\mathbf{k}} - \mu) c^\dagger_{\mathbf{k}\sigma} c_{\mathbf{k}\sigma} + \sum_{\mathbf{k}\sigma} V_{\mathbf{k}} (f^\dagger_{\mathbf{k}\sigma} c_{\mathbf{k}\sigma} + h.c.) + \sum_{\mathbf{k}\sigma} (\epsilon_f - \mu) f^\dagger_{\mathbf{k}\sigma} f_{\mathbf{k}\sigma} + U \sum_i n_{f,i\uparrow} n_{f,i\downarrow}\,. \tag{9.2}$$

As before, $c^\dagger_{\mathbf{k}\sigma}$ ($f^\dagger_{\mathbf{k}\sigma}$) creates a conduction (local) electron with momentum $\mathbf{k}$, spin σ and energy $\epsilon_{\mathbf{k}}$ (ϵ_f), and $n_{f,i\sigma} = f^\dagger_{i\sigma} f_{i\sigma}$ denotes the number operator for f electrons at site i. The localized f-electrons are objected to an on-site Coulomb repulsion. The chemical potential μ has been introduced to fix the total number of electrons in the system, $n_f + n_c$.

The position-dependent $V(\mathbf{r}_j - \mathbf{r}_i)$, or rather its Fourier transform, the momentum-dependent hybrization function $V_{\mathbf{k}}$, serves as a phenomenological input to the theory, not reflecting microscopic details in the overlap between conduction and localized electrons. The dependence on the direction $\mathbf{k}/k$ can be expanded in spherical harmonics. In contrast to unconventional superconductivity there are no symmetry restrictions for the parity of the internal angular momentum. We can split the hybridization function as $V_{\mathbf{k}} = V\beta_{\mathbf{k}}$, where $\beta_{\mathbf{k}}$ is chosen to be normalized as $\sum_{\mathbf{k}} |\beta_{\mathbf{k}}|^2 = \mathcal{N}$ with $\mathcal{N}$ being the total number of sites in the system. As we will see by proceeding in this chapter, thermodynamics as well as most observable quantities only depend on $\left|V^2_{\mathbf{k}}\right|$.

In the Kondo limit fluctuations in the charge degrees of freedom of the localized electrons are frozen out, and the infinite value of the Coulomb repulsion ensures that each site is occupied by exactly one f electron ($n_f = 1$). As in the impurity case, this limit is determined by Eq. (8.4), now with an effective hybridization $\Gamma = \pi \sum_{\mathbf{k}} |V_{\mathbf{k}}|^2 \delta(\epsilon_{\mathbf{k}} - \mu)$. Alternatively, this limit is imposed by $V \to \infty$, $U \to \infty$, and $\epsilon_f \to -\infty$, while V^2/ϵ_f is kept finite.

The Schrieffer-Wolff transformation (SWT), originally performed in the single impurity case (Schrieffer and Wolff, 1966), projects out empty and doubly occupied f levels. It leads to the

KLM (Hewson, 1997)

$$\mathcal{H}_{\mathrm{KLM}} = \sum_{\mathbf{k}\sigma} \bar{\epsilon}_{\mathbf{k}} c^{\dagger}_{\mathbf{k}\sigma} c_{\mathbf{k}\sigma} + \underbrace{\sum_{\mathbf{k}\mathbf{k}'i} 2J_{\mathbf{k}\mathbf{k}'} e^{-i(\mathbf{k}'-\mathbf{k})\mathbf{R}_i} \mathbf{S}_i \cdot \mathbf{s}_{\mathbf{k},\mathbf{k}'}}_{\mathcal{H}_J} , \tag{9.3}$$

which is equivalent to the ALM in the Kondo limit. The conduction electron spin is expressed via $\mathbf{s}_{\mathbf{k}\mathbf{k}'} = \sum_{\sigma\sigma'} c^{\dagger}_{\mathbf{k}\sigma} \sigma_{\sigma\sigma'} c_{\mathbf{k}'\sigma'}/2$, which couples to $\mathbf{S}_i$ corresponding to the spin of the f-electron sitting at site i. We introduced the shortcut $\bar{\epsilon}_{\mathbf{k}} = \epsilon_{\mathbf{k}} - \mu$.

In the presence of a momentum-dependent hybridization the Kondo coupling becomes

$$J_{\mathbf{k}\mathbf{k}'} = V_{\mathbf{k}} V^*_{\mathbf{k}'} \left(\frac{1}{U + \epsilon_f - \mu} + \frac{1}{-(\epsilon_f - \mu)} \right) = J_0 \beta_{\mathbf{k}} \beta^*_{\mathbf{k}'} , \tag{9.4}$$

with $J_0 = V^2(\frac{1}{U+\epsilon_f-\mu} + \frac{1}{-(\epsilon_f-\mu)})$. Other interaction terms produced by the SWT like an electron-electron scattering term, which can be absorbed in the chemical potential, or a polarization of the conduction electrons by the impurity spins leading to an RKKY interaction are omitted in this discussion. Please note that the RKKY interaction will explicitly be re-introduced and discussed in Chapter 14. The SWT eliminates the hybridization term in favor of a spin-spin interaction between the local and the conduction electrons, which finally produces the Kondo effect.

A momentum-dependent hybridization in the context of heavy fermion metals has also been considered by Ghaemi and Senthil (2007). They discuss the exchange term

$$\mathcal{H}'_J = \sum_{\langle im \rangle} J_{im} \mathbf{S}_i \cdot \mathbf{s}_{mm} , \tag{9.5}$$

with $\mathbf{s}_{mm} = \sum_{\sigma\sigma'} c^{\dagger}_{m\sigma} \sigma_{\sigma\sigma'} c_{m\sigma'}/2$. In order to compare their ansatz with ours we rewrite the Kondo term $\mathcal{H}_J$ in real space:

$$\mathcal{H}_J = 2J_0 \sum_{imn} \beta_{m-i} \beta^*_{n-i} \mathbf{S}_i \cdot \mathbf{s}_{mn} . \tag{9.6}$$

The function β_{m-i} is equal to $V(\mathbf{r}_m - \mathbf{r}_i)/V$ and denotes the Fourier transform of $\beta_{\mathbf{k}}$ depending on the distance $\mathbf{r}_m - \mathbf{r}_i$. $\mathbf{s}_{mn} = \sum_{\sigma\sigma'} c^{\dagger}_{m\sigma} \sigma_{\sigma\sigma'} c_{n\sigma'}/2$ is a *non-local* conduction-electron spin density.

$\mathcal{H}_J$ is based on the underlying Anderson model, which fixes the exchange symmetry contained in the Kondo coupling. As argued by Coleman and Tsvelik (1998), only in the presence of correlations in the conduction band an Anderson model can lead to a multi-channel Kondo model because of conduction electron interactions suppressing charge fluctuations. This means, we are dealing with a *single-channel* Kondo model. In contrast, $\mathcal{H}'_J$ describes a *multi-channel* Kondo model: The localized spin at site i separately couples to linear combinations of conduction electron spin densities at the neighboring sites $\sum_{m=\text{n.n. of } i} J_{im} \mathbf{s}_{mm}$. Each linear combination represents a screening channel. The number of screening channels is given by the coordinate number of the lattice. These channels compete with each other. The one leading to the lowest ground state energy will dominate the low-energy properties of the system (Nozières

and Blandin, 1980). Depending on the microscopic properties of the system it is possible that a higher-angular momentum channel like d-wave is favored. Within a slave-boson mean-field treatment, discussed for our model in the subsequent chapter, each screening channel corresponds to a different saddle point. Therefore the single- and multi-channel models $\mathcal{H}_J$ and $\mathcal{H}_{J'}$ become equivalent, if $\mathcal{H}_{J'}$ is dominated by only one channel.

Instead of dealing with a phenomenological ansatz, Ghaemi et al. (2008) considered a full microscopic treatment of a f^1 band in a Ce-based heavy fermion metal. Due to the influence of spin-orbit coupling and crystal field interaction the f^1-level splits up (Cox and Zawadowski, 1999). The microscopic model takes into account the low-energy Kramers doublet.

The presence of a non-local wave function overlap between c- and f-electrons is able to produce a momentum-dependent hybridization, which is taken into account in the considered ALM and KLM. In the next chapter these models are simplified by a mean-field approximation, which is able to capture the basic properties in the Fermi liquid phase.

10 Mean-Field Approximation

The Anderson and the Kondo lattice models, both describing heavy fermion compounds, were introduced in the previous chapter. For treating the contained interaction terms we apply a mean-field approximation reducing the problem to a non-interacting two-band Hamiltonian with renormalized parameters. This description is able to capture the properties in the Fermi liquid phase.

The mean-field approximation for both models will be discussed separately: For the ALM slave bosons are introduced, whereas in the KLM the local spins are expressed via a pseudo-fermion representation and the spin interaction term is decoupled using auxiliary fields. It will further be shown that the results become equivalent in the Kondo limit.

The development of a mean-field treatment for the Kondo and related models started in 1979 with Lacroix and Cyrot (1979) introducing a Hartree-Fock treatment for the Kondo lattice model. Read and Newns (1983b) studied the Coqblin-Schrieffer model, a generalization of the Kondo model with an N-fold spin degeneracy (Coqblin and Schrieffer, 1969). The impurity spin is represented by fermionic auxiliary particles obeying a number constraint. In a functional integral formalism the constraint is enforced by a dynamic Bose-like field, which plays the role of a Lagrange multiplier. By applying a Hubbard-Stratonovich transformation the Kondo interaction is decoupled in favor of extra Bose fields. In a static approximation those fields and the Lagrange multiplier are substituted by constants, whose values are determined by claiming stationarity of the action with respect to these mean-field parameters. In the limit of large spin degeneracy N the fluctuations around the mean-field solution freeze out and this approach becomes exact.

With the slave boson method (Coleman, 1984), this approximation scheme was applied to the degenerate single-impurity Anderson model at infinite U by Read and Newns (1983a). The infinite Coulomb repulsion prohibits double occupancy of the f-level. This constraint is implemented by introducing an additional slave boson operator creating an empty f-level. The total number of f-electrons and slave bosons in the system is therefore always 1. This scheme can easily be generalized to the $U = \infty$ Anderson lattice model, e.g. discussed by Millis and Lee (1987).

The lattice version of the Coqblin-Schrieffer model, the SU(N) KLM, was studied by Read et al. (1984) showing the stability of the nonmagnetic state in the large-N limit.

An overview about these mean-field methods and other techniques tackling this problem is given by Hewson (1997).

Please note that the models we are dealing with do not have a large spin degeneracy but have spin-1/2. However, the mean-field solutions derived in this chapter correspond to $N = \infty$ saddle points of certain SU(N) Anderson and Kondo lattice models.

Now, we will explain how the slave boson method can be adapted to our ALM with non-local hybridization.

10.1 Anderson lattice model

In the limit of infinite Coulomb repulsion U, doubly occupied states are projected out and the f-level at each site i is either empty or occupied by an up or a down spin electron. Therefore, the physical f-electrons can be subsituted by an auxiliary fermion $\bar{f}_{i\sigma}$ and a slave boson r_i (Coleman, 1984), via

$$f_{i\sigma} \to r_i^\dagger \bar{f}_{i\sigma}. \tag{10.1}$$

In order to project out the unphysical states in the enlarged Hilbert space, the additional constraint

$$\sum_\sigma \bar{f}_{i\sigma}^\dagger \bar{f}_{i\sigma} + r_i^\dagger r_i = 1 \tag{10.2}$$

has to be imposed.

Using the substitution (10.1) the bare f-level term in Eq. (9.2) becomes

$$\sum_{i\sigma} \epsilon_f f_{i\sigma}^\dagger f_{i\sigma} \to \sum_{i\sigma} \epsilon_f \bar{f}_{i\sigma}^\dagger r_i r_i^\dagger \bar{f}_{i\sigma} = \sum_{i\sigma} \epsilon_f \bar{f}_{i\sigma}^\dagger \bar{f}_{i\sigma} + \sum_{i\sigma} \epsilon_f \bar{f}_{i\sigma}^\dagger \bar{f}_{i\sigma} r_i^\dagger r_i \,. \tag{10.3}$$

The second term on the right-hand side of the equality sign contains the number operator of the auxiliary fermion and the slave boson at site i, which cannot be finite simultaneously due to the constraint (10.2). Therefore, this term vanishes.

By taking the static approximation in the corresponding functional integral formalism, the slave boson condenses ($\langle r_i \rangle = r$) to a translationally invariant constant in order to preserve the translational symmetry of the lattice. The hybridization between c- and $\bar{f}$-band is therefore rigid and the mean-field Hamiltonian reads

$$\begin{aligned} \mathcal{H}_{\mathrm{ALM,MF}} = &\sum_{\mathbf{k}\sigma} \epsilon_{\mathbf{k}} c_{k\sigma}^\dagger c_{\mathbf{k}\sigma} + \sum_{\mathbf{k}\sigma} \epsilon_f \bar{f}_{\mathbf{k}\sigma}^\dagger \bar{f}_{\mathbf{k}\sigma} + \sum_{\mathbf{k}\sigma} V_{\mathbf{k}} r (\bar{f}_{\mathbf{k}\sigma}^\dagger c_{\mathbf{k}\sigma} + c_{\mathbf{k}\sigma}^\dagger \bar{f}_{\mathbf{k}\sigma}) \\ &- \lambda \left(\sum_{\mathbf{k}\sigma} \bar{f}_{\mathbf{k}\sigma}^\dagger \bar{f}_{\mathbf{k}\sigma} + \mathcal{N}(r^2 - 1) \right) - \mu \left(\sum_{\mathbf{k}\sigma} c_{\mathbf{k}\sigma}^\dagger c_{\mathbf{k}\sigma} - \mathcal{N} n_c \right). \end{aligned} \tag{10.4}$$

The occupation number constraint (10.2) was implemented using a Lagrange multiplier λ, in which the effect of the chemical potential μ on the auxiliary fermions $\bar{f}$ was absorbed.

The values of the parameters r, λ and μ are determined by the minimum of the free energy of the system leading to the mean-field equations

$$\sum_{\mathbf{k}\sigma} V_{\mathbf{k}} \langle \bar{f}_{\mathbf{k}\sigma}^\dagger c_{\mathbf{k}\sigma} + h.c. \rangle = 2\mathcal{N}\lambda r \,, \tag{10.5a}$$

$$\sum_{\mathbf{k}\sigma} \langle \bar{f}_{\mathbf{k}\sigma}^\dagger \bar{f}_{\mathbf{k}\sigma} \rangle = \mathcal{N}(1 - r^2) \,, \tag{10.5b}$$

$$\sum_{\mathbf{k}\sigma} \langle c_{\mathbf{k}\sigma}^\dagger c_{\mathbf{k}\sigma} \rangle = \mathcal{N} n_c \,, \tag{10.5c}$$

which are solvable in a self-consistent manner. The occurring expectation values can be expressed by Green functions of the two-band mean-field Hamitonian (10.4), listed in Appendix B.1.

10.2 Kondo lattice model

For a mean-field treatment of the KLM we first introduce Abrikosov pseudo-fermions $\widetilde{f}_{i\sigma}$ (Abrikosov, 1965), with whom the spin $\mathbf{S}_i$ can be expressed as

$$\mathbf{S}_i = \frac{1}{2}\sum_{\sigma\sigma'} \widetilde{f}^{\dagger}_{i\sigma}\sigma_{\sigma\sigma'}\widetilde{f}_{i\sigma'}\,. \tag{10.6}$$

If we consider the KLM as being produced from the ALM via the Schrieffer-Wolff transformation, the Abrikosov fermions can be viewed as the equivalents to the local f-electrons in the original ALM.

The number of pseudo-fermions per site has to be fixed with an additional constraint:

$$\sum_{\sigma} \widetilde{f}^{\dagger}_{i\sigma}\widetilde{f}_{i\sigma} = 1\,. \tag{10.7}$$

The Kondo term becomes

$$\mathcal{H}_J = -J_0 \sum_{imn\sigma\sigma'} \beta_{m-i}\beta^{*}_{n-i}\widetilde{f}^{\dagger}_{i\sigma}c_{n\sigma}c^{\dagger}_{m\sigma'}\widetilde{f}_{i\sigma'}. \tag{10.8}$$

Bilinear terms arising from this substitution are neglected, since they can be absorbed in a redefinition of the chemical potential μ and the Lagrange multiplier λ_0, which is introduced to fix the particle number constraint for the $\widetilde{f}$-electrons, Eq. (10.7).

With a Hubbard-Stratonovich transformation in the corresponding path integral this four-operator term $\mathcal{H}_J$ is decoupled by introducing an auxiliary field b_i conjugate to

$$-J_0\sum_{n\sigma}\beta^{*}_{n-i}\widetilde{f}^{\dagger}_{i\sigma}c_{n\sigma}\,, \tag{10.9}$$

reflecting the hybridization between the $\widetilde{f}$-electron at site i and the c-band. At the saddle point the field b_i condenses to the homogeneous value b, leading to a Kondo lattice mean-field Hamiltonian of the form

$$\begin{aligned}\mathcal{H}_{\mathrm{KLM,MF}} &= \sum_{\mathbf{k}\sigma}\epsilon_{\mathbf{k}}c^{\dagger}_{\mathbf{k}\sigma}c_{\mathbf{k}\sigma} + b\sum_{\mathbf{k}\sigma}\beta_{\mathbf{k}}\left(c^{\dagger}_{\mathbf{k}\sigma}\widetilde{f}_{\mathbf{k}\sigma} + h.c.\right) + \mathcal{N}\frac{b^2}{J_0}\\ &- \lambda_0\left(\sum_{\mathbf{k}\sigma}\widetilde{f}^{\dagger}_{\mathbf{k}\sigma}\widetilde{f}_{\mathbf{k}\sigma} - \mathcal{N}\right) - \mu\left(\sum_{\mathbf{k}\sigma}c^{\dagger}_{\mathbf{k}\sigma}c_{\mathbf{k}\sigma} - \mathcal{N}n_c\right)\end{aligned} \tag{10.10}$$

The Lagrange parameter λ_0, as well replaced by a constant in the static and homogeneous approximation, fixes the constraint (10.7) on average. The self-consistency equations for the mean-field parameters b, λ_0 and μ, obtained by minimizing the free energy, are

$$\sum_{\mathbf{k}\sigma}\beta_{\mathbf{k}}\langle\widetilde{f}^{\dagger}_{\mathbf{k}\sigma}c_{\mathbf{k}\sigma} + h.c.\rangle = -\mathcal{N}\frac{2b}{J_0}, \tag{10.11a}$$

$$\sum_{\mathbf{k}\sigma}\langle\widetilde{f}^{\dagger}_{\mathbf{k}\sigma}\widetilde{f}_{\mathbf{k}\sigma}\rangle = \mathcal{N}, \tag{10.11b}$$

$$\sum_{\mathbf{k}\sigma}\langle c^{\dagger}_{\mathbf{k}\sigma}c_{\mathbf{k}\sigma}\rangle = \mathcal{N}n_c. \tag{10.11c}$$

Both presented mean-field approaches for the ALM and the KLM map the original model onto an effective non-interacting two-band model with self-consistently determined hybridization. As temperature grows, the value of the hybridization field b decreases and vanishes at the Kondo temperature T_K, implicitly defined by

$$\frac{2}{J_0} = \frac{1}{\mathcal{N}} \sum_{\mathbf{k}} \frac{\beta_{\mathbf{k}}^2}{\bar{\epsilon}_{\mathbf{k}}} \tanh \frac{\bar{\epsilon}_{\mathbf{k}}}{2T_\mathrm{K}}. \tag{10.12}$$

Above T_K the two bands correspond to the original, decoupled c- and f-bands.

The mean-field solution breaks a local gauge invariance of the Bose fields (corresponding to the slave bosons in the ALM and the auxiliary bose field b_i in the KLM), which is restored upon inclusion of fluctuations (Read, 1985). These fluctuations are included by minimally coupling the $\widetilde{f}$ and c particles to a U(1) gauge field, see Chapter 13.

In the Fermi liquid regime the Kondo lattice system exhibits two temperature scales: the Kondo scale T_K, which marks the onset of local Kondo screening, and the coherence temperature T_coh, below which the electrons scatter coherently and the heavy Fermi liquid evolves.

Because non-local effects are weak, the self-energy of the f-electrons has a negligible k-dependence ($\partial \Sigma_f / \partial k \approx 0$) and the Fermi liquid is local. As pointed out in Sec. 8.2, T_coh is the energy scale determining all Fermi liquid properties and can therefore be defined via the specific heat coefficient γ as

$$T_\mathrm{coh} = \frac{1}{\gamma}, \tag{10.13}$$

setting $k_B = 1$. Derived in the framework of a local hybridization, T_coh can approximately be estimated with this definition from the $T = 0$ mean-field solution as (Burdin et al., 2000; Burdin, 2008)

$$T_\mathrm{coh} = \frac{b_0^2}{D}, \tag{10.14}$$

where $b_0 = b(T = 0)$ and D is the bandwidth of the conduction electron band. The minimal direct gap between the two effective non-interacting bands is given by $2b_0$, while the indirect gap is b_0^2/D. The Lagrange multiplier behaves as $\lambda_0 \sim T_\mathrm{coh}$. The low-temperature correction to all parameters is quadratic in T similar to

$$\frac{b(T) - b_0}{b_0} \sim -\frac{T^2}{T_\mathrm{coh}^2}. \tag{10.15}$$

Within a mean-field treatment of the KLM, Burdin et al. (Burdin et al., 2000; Burdin, 2001) show that the ratio between the two temperature scales T_K and T_coh only depends on the density of conduction electrons n_c and the band structure. We assume this remains valid in the presence of a non-local hybridization. In the following the filling n_c and the shape of the conduction band are kept fixed and it will not be differentiated between the two scales T_K and T_coh.

According to the Luttinger theorem the particle density is related to the volume enclosed by the Fermi surface, which is fulfilled in the considered model, at least in the Fermi liquid regime.

The large Fermi surface contains conduction electrons as well as localized spins ($n_c + n_f$ with $n_f = 1$ in the Kondo limit).

The next section shows the equivalence of the discussed mean-field theories for the ALM and the KLM in the Kondo limit.

10.3 Equivalence of Anderson and Kondo mean-field theories

The equivalence of both introduced mean-field theories does not come as a surprise. As already pointed out, the Abrikosov pseudo-fermions are reminiscent of the f-electrons in the framework of the ALM considering the connection via the Schrieffer-Wolff transformation. The auxiliary fermions $\bar{f}$ in the mean-field treatment of the ALM are introduced in order to describe the local spin degrees of freedom. Furthermore, both models are mapped onto an effective model, where all the interactions are contained in a renormalized hybridization between c- and f-band. In this section we prove this conjecture on a formal level by showing that the mean-field equations become equivalent in the Kondo limit.

The Kondo limit is imposed in the parameter limit $U \to \infty$, $V \to \infty$ and $\epsilon_f \to -\infty$, while rV and $\epsilon_f - \lambda$ are kept finite. In the limit of infinite U the Kondo coupling becomes $J_0 = V^2/|\epsilon_f|$.

In this parameter limit the slave boson condensation parameter r vanishes, since the renormalized hybridization rV has to stay finite. Therefore, the average occupation of $\bar{f}$ electrons per site becomes unity, and $\bar{f}$ and $\widetilde{f}$ electrons are formally equivalent.

The unrenormalized f-level ϵ_f goes to $-\infty$, while the normalized level $\epsilon_f - \lambda$ stays a finite fraction of the bandwidth in order to fix the occupation constraint $\sum_\sigma \bar{f}_i^\dagger \bar{f}_i = 1$. Therefore, the ratio $V^2/|\lambda|$ becomes equivalent to $J_0 = V^2/|\epsilon_f|$ in the Kondo limit.

By using this knowledge about the behavior of the parameters, we see that the mean-field equation (10.5a) transforms as

$$rV = \frac{1}{2\mathcal{N}} \langle \sum_{\mathbf{k}\sigma} \frac{V^2 \beta_{\mathbf{k}}}{\lambda} \left(\bar{f}^\dagger_{\mathbf{k}\sigma} c_{\mathbf{k}\sigma} + c^\dagger_{\mathbf{k}\sigma} \bar{f}_{\mathbf{k}\sigma} \right) \rangle \to -\frac{J_0}{2\mathcal{N}} \langle \sum_{\mathbf{k}\sigma} \beta_{\mathbf{k}} \left(\widetilde{f}^\dagger_{\mathbf{k}\sigma} c_{\mathbf{k}\sigma} + c^\dagger_{\mathbf{k}\sigma} \widetilde{f}_{\mathbf{k}\sigma} \right) \rangle = b \qquad (10.16)$$

into the Kondo mean-field equation (10.11a). Both, rV and b describe the effective hybridization in these two models.

The equivalence of the other two mean-field equations, (10.5b,c) and (10.11b,c), can be seen directly. We have therefore shown the formal correspondence of the two mean-field theories in the Kondo limit.

In conclusion, the developed approximation scheme on the level of mean-field theory leads to an effective non-interacting two-band model reflecting the low-temperature properties of the system in the Fermi liquid regime. The next chapter will study these properties while focusing on the effects arising from the non-local hybridization.

11 Low-temperature properties of the Fermi liquid state

In the previous chapter we described a mean-field approximation for the Anderson and Kondo lattice model. A self-consistent solution of the mean-field equations gives an appropriate description of the low-temperature Fermi liquid state in the absence of inter-moment exchange and ordering. In this chapter we study thermodynamical as well as transport properties in this regime.

Since the focus lies on the 115-family, whose layered structure leads to a quasi two-dimensional behavior, the calculations are carried out for two-dimensional systems. On a square lattice a nearest-neighbor hopping of conduction electrons leads to the tight-binding dispersion

$$\epsilon_{\mathbf{k}} = -2t\,(\cos k_x + \cos k_y)\,. \tag{11.1}$$

If we assume that f- and c-electrons live on the same lattice sites $\{\mathbf{r}_i\}$, the hybridization, $V_{\mathbf{k}} = V\beta_{\mathbf{k}}$, can be on-site leading to a s-wave configuration or can be composed as a linear combination of the overlaps between a f-electron and the c-electrons on neighboring sites. In the following we will consider

$$\beta_{\mathbf{k}} = \begin{cases} 1 & \text{s-wave} \\ \cos k_x + \cos k_y & \text{extended s-wave} \\ \cos k_x - \cos k_y & \mathrm{d}_{x^2-y^2}\text{-wave} \end{cases} . \tag{11.2}$$

Similar hybridization functions have been used by Ghaemi and Senthil (2007).

Band-structure calculations (Maehira et al., 2003) suggest an effective two-dimensional model for the 115-materials, compare Fig. 11.1, where conduction (In $5p$) and localized electrons (Ce $4f$) live on two different interpenetrating square lattice. We will also touch upon

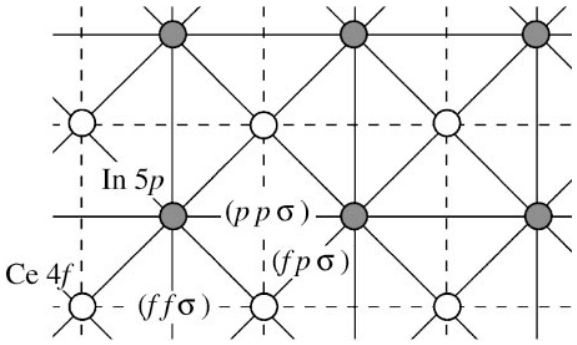

Figure 11.1: Lattice configuration for an effective model for 115-materials: In $5p$ (conduction electrons) and Ce $4f$ (localized electrons) live on two interpenetrating square lattices. (Figure from Maehira et al., 2003).

this more realistic spatial setup and study the hybridization functions that can be constructed from such a configuration:

$$\beta_{\mathbf{k}} = \begin{cases} 2\cos\frac{k_x}{2}\cos\frac{k_y}{2} & \text{extended S-wave} \\ 2\sin\frac{k_x}{2}\sin\frac{k_y}{2} & \mathrm{D}_{xy}\text{-wave} \end{cases} . \tag{11.3}$$

In contrast to superconductivity there are no symmetry restrictions forbidding odd parity hybridization functions. Most results obtained for even parity hybridizations (corresponding to an even angular momentum ℓ) like the $\beta_{\mathbf{k}}$-functions defined in Eqs. (11.2) and (11.3), can be generalized to systems with odd parity, since most physical observables only depend on $|V_{\mathbf{k}}|^2$ and are only sensitive to the position of nodal lines in the hybridization function. An exception from this is the case of p_x or p_y breaking down the discrete rotational lattice symmetry C_4 to C_2 with strong influence on the transport properties. This specific case will be briefly discussed in the transport section 11.5.

In the remainder of this chapter we discuss the influence of $\beta_{\mathbf{k}}$ on the band structure and the Fermi surface, Sec. 11.1, calculate thermodynamical properties, Sec. 11.2, with a focus on the specific heat and the definition of the effective mass. Then, we study the effect of an external magnetic field that couples to the spin degrees of freedom, Sec. 11.3. We show how the influence of the non-local hybridization becomes significant for the optical conductivity, Sec. 11.4. Finally we calculate electrical and thermal transport properties in Sec. 11.5 and check the validity of the Wiedemann-Franz law. Unless otherwise noted the subsequent calculations are carried out in the framework of the Kondo model.

11.1 Band structure and Fermi surface

The eigenvalues of Eq. (10.4) determine the band structure

$$z_{1,2\mathbf{k}} = \frac{1}{2}\left(-\lambda_0 + \bar{\epsilon}_{\mathbf{k}} \pm \sqrt{(\lambda_0 + \bar{\epsilon}_{\mathbf{k}})^2 + 4b^2\beta_{\mathbf{k}}^2}\right) . \tag{11.4}$$

The hybridization $\beta_{\mathbf{k}}$ vanishes along so-called "nodal" directions implying a band structure along this direction that consists of the original c-and $\widetilde{f}$-bands crossing each other, compare Fig. 11.2(a). In a direction where the hybridization is finite the two bands are hybridized leading to two repelling quasiparticle bands $z_{1,2\mathbf{k}}$. Therefore a heavy band at the Fermi surface evolves (Fig. 11.2(b)). The repulsion is at its maximum along the antinodal direction. Please note that a vanishing hybridization along certain lines does *not* mean that some local moments remain unscreened; in fact the Kondo effect is fully developed in this Fermi liquid regime.

For a $\mathrm{d}_{x^2-y^2}$ hybridization nodal lines lie along the diagonals $k_x = \pm k_y$, antinodal directions are given by lines with $k_x = 0$ and $k_y = 0$, respectively. The $\widetilde{f}$-level is assumed to be non-dispersive, the two bands $z_{1,2\mathbf{k}}$ thus do not overlap and below half filling, $n_c < 1$, the upper band $z_{1\mathbf{k}}$ is empty and the Fermi surface is determined by $z_{2\mathbf{k}} = 0$.

The momentum distribution function $n_{\mathbf{k}} = \langle c_{\mathbf{k}}^\dagger c_{\mathbf{k}} \rangle$, also shown in Fig. 11.2 for the corresponding directions, consists of a sharp step along the diagonal, and becomes rounded for finite hybridization at the "small" Fermi surface, the Fermi surface of the original c-electrons

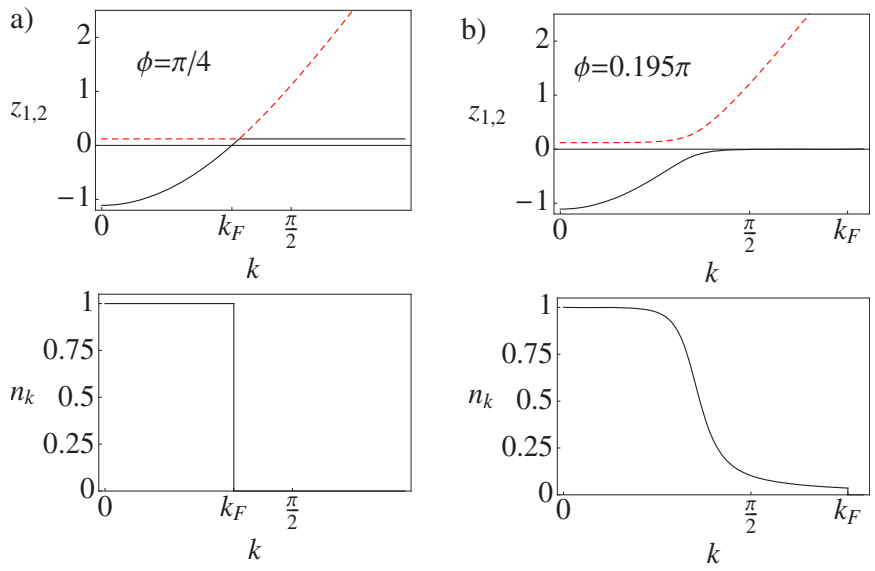

Figure 11.2: Band dispersion of the hybridized bands $z_{1,2\mathbf{k}}$, Eq. (11.4) and the corresponding momentum distribution function $n_{\mathbf{k}}$ for a $d_{x^2-y^2}$ hybridization along (a) the momentum space diagonal and (b) along a direction enclosing an angle $\phi = 0.195\pi$ with the k_x axis. Parameters are chosen as $J_0/t = 2.0$ and $n_c = 0.4$.

with vanishing hybridization. The jump height at k_F corresponds to the quasiparticle weight Z, discussed in the next section.

For all plots shown in Figs. 11.3, 11.4, 11.5 and 11.6, a set of mean-field parameters obeying the mean-field equations (10.11) was determined numerically. Each set of parameters used to generate these plots leads to an identical value of the specific heat coefficient γ implying identical coherence scales T_{coh}, compare Eq. (10.13). The Fermi surfaces in Fig. 11.3 refer to the hybridization functions defined in Eq. (11.2). In the case of $d_{x^2-y^2}$ hybridization (Fig. 11.3(c) and (d)) the Fermi momentum k_F is small in nodal and large in antinodal direction. Due to the momentum dependence in $\beta_{\mathbf{k}}$ the function $k_F(\phi)$ can be multivalued, as depicted in Fig. 11.3(d). This preferably happens at low band fillings n_c. For the extended s-wave hybridization the lower band crosses the Fermi surface twice leading to two Fermi sheets.

Fermi surfaces of D_{xy} and extended S-wave hybridization defined in Eq. (11.3) are displayed in Fig. 11.4. Apart from a rotation by 45 degrees the structure of the D_{xy} and the $d_{x^2-y^2}$ Fermi surface are similar.

The next section is concerned with changes in the thermodynamical properties arising from the strong angular dependence in the band structure.

11.2 Thermodynamical properties

The introduced non-interacting two-band picture with effective parameters containing the interaction of the original model reflects the low-energy thermodynamic properties of the

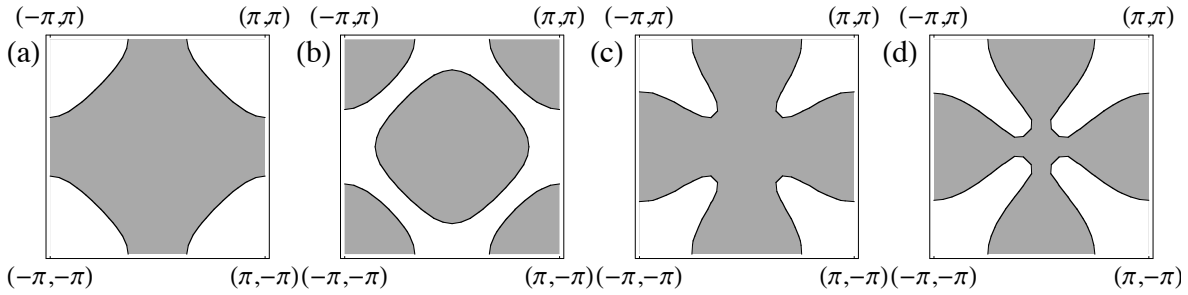

Figure 11.3: Fermi surfaces for (a) s-wave, (b) extended s-wave, and (c,d) $d_{x^2-y^2}$-wave hybridization. The band filling is $n_c = 0.3$ in panels (a)–(c), whereas $n_c = 0.1$ in panel (d). The Kondo coupling is chosen such that the specific heat coefficient and therefore the coherence scale $T_{\rm coh}$ are identical in all four cases: (a) $J_0/t = 1.0$ ($\lambda_0/t = -0.025$, $\mu/t = -2.47$, $b/t = 0.281$), (b) $J_0/t = 0.89$ ($\lambda_0/t = -0.0067$, $\mu/t = -2.3$, $b/t = 0.281$), (c) $J_0/t = 0.97$ ($\lambda_0/t = -0.0061$, $\mu/t = -2.46$, $b/t = 0.173$), (d) $J_0/t = 1.957$ ($\lambda_0/t = -0.0385$, $\mu/t = -3.698$, $b/t = 0.466$).

Figure 11.4: Fermi surfaces using the hybridization functions (11.3) for interpenetrating c and f square lattices. (a) Extended S-wave with $J_0/t = 0.46$ ($\lambda_0/t = -0.001$, $\mu/t = -2.34$, $b/t = 0.138$), (b) D_{xy}-wave with $J_0/t = 1.975$ ($\lambda_0/t = -0.011$, $\mu/t = -2.38$, $b/t = 0.187$). In both cases, $n_c = 0.3$, and the parameters are chosen such that $T_{\rm coh}$ is the same as for the data in Fig. 11.3.

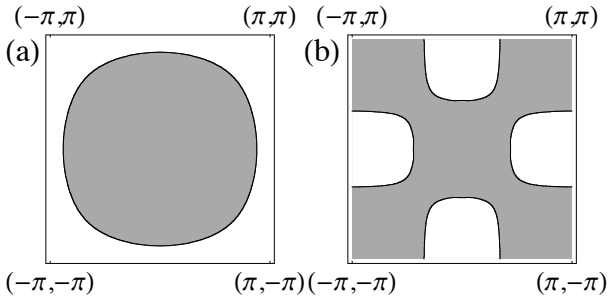

system. From the free energy of the system

$$\mathcal{F} = -\frac{1}{\beta}\sum_{\mathbf{k}}\left[\ln\left(1+e^{-\beta z_{1\mathbf{k}}}\right)+\ln\left(1+e^{-\beta z_{2\mathbf{k}}}\right)\right]+\mathcal{N}\mu n_c+\mathcal{N}\frac{b^2}{J_0}+\mathcal{N}\lambda_0 \tag{11.5}$$

and invoking expressions (11.4) of $z_{1\mathbf{k}}$ and $z_{2\mathbf{k}}$, the specific heat can be calculated as

$$C_V = -T\frac{d^2\mathcal{F}[T,b,\mu,\lambda_0]}{dT^2} \approx -T\frac{\partial^2\mathcal{F}[T,b,\mu,\lambda_0]}{\partial T^2}\,. \tag{11.6}$$

In this approximation the temperature-dependence of the mean-field parameters, given by Eq. (10.15), is neglected, since it only produces corrections in C_V of the order T^2, which become subleading in the low-temperature limit in comparison to the linear T-contribution. The calculation of these corrections is presented in Appendix C. We find an explicit expression for the specific heat

$$C_V = \beta^2\sum_{\mathbf{k}}\left[\frac{z_{2\mathbf{k}}^2 e^{\beta z_{2\mathbf{k}}}}{\left(1+e^{\beta z_{2\mathbf{k}}}\right)^2}+\frac{z_{1\mathbf{k}}^2 e^{\beta z_{1\mathbf{k}}}}{\left(1+e^{\beta z_{1\mathbf{k}}}\right)^2}\right]. \tag{11.7}$$

This can further be simplified by a Sommerfeld expansion in the low-temperature regime. We neglect the influence of upper band $z_{1\mathbf{k}}$, which does not cross the Fermi surface, and rewrite

$$C_V = \beta \int_{-\infty}^{\infty} d\epsilon g(\epsilon) \left[-n_F'(\epsilon)\right], \tag{11.8}$$

where $n_F(\epsilon) = 1/(1+e^{\epsilon})$ denotes the dimensionless Fermi distribution. The function g is defined by $g(\epsilon) = \epsilon^2 N(\epsilon)$ with the density of states

$$N(\epsilon) = \frac{1}{\mathcal{N}} \sum_{\mathbf{k}} \delta(\epsilon - z_{2\mathbf{k}}). \tag{11.9}$$

Since at low temperatures the derivative of the Fermi distribution is peaked around the Fermi level at $\epsilon = 0$, we Taylor-expand the function $g(\epsilon)$ around this point. The first non-vanishing contribution arises from the second order term $g''(0) = 2N_0$ (with $N_0 = N(0)$) leading to

$$C_V = \gamma T, \qquad \text{with} \qquad \gamma = \frac{2\pi^2}{3} N_0. \tag{11.10}$$

The value of the Sommerfeld coefficient γ as well as the linear T behavior of C_V result from the fact that at low temperatures only fermions in the vicinity of the Fermi surface contribute to thermodynamics.

In the following an appropriate definition of the effective mass in the presence of a strongly angular-dependent band structure is developed. We first have a look at the case with isotropic band structure and generalize the result to the anisotropic case. For an isotropic system the quasiparticle energy is approximated by $\epsilon_{\mathbf{k}}^{QP} = v_F(|\mathbf{k}| - k_F)$, where the Fermi velocity v_F, the slope of the dispersion at the Fermi level, is related to the effective mass m^* and the Fermi momentum k_F via $v_F = k_F/m^*$. In d dimensions the density of states is given by $N_0 = m^* k_F^{d-2}/\mathcal{C}_d$, where $\mathcal{C}_2 = 2\pi$ and $\mathcal{C}_3 = 2\pi^2$.

In an anisotropic system the gradient of the dispersion generally depends on the direction; the density of states at the Fermi level becomes

$$N_0 = \int_{\mathrm{FS}} \frac{d^{d-1}k}{(2\pi)^d} \frac{1}{\left|\nabla_{\mathbf{k}} \epsilon_{\mathbf{k}}^{QP}\right|}, \tag{11.11}$$

suggesting a suitable re-definition of a direction-dependent(!) effective mass

$$\frac{1}{m^*(\mathbf{k})} = \frac{1}{k} \left|\nabla_{\mathbf{k}} \epsilon_{\mathbf{k}}^{QP}\right|_{\mathrm{FS}}. \tag{11.12}$$

The density of states at the Fermi level can be written as

$$N_0 = \int_{\mathrm{FS}} \frac{d^{d-1}k}{(2\pi)^d} \frac{m^*(\mathbf{k})}{k}. \tag{11.13}$$

In the presence of a non-vanishing first derivative of the quasiparticle dispersion around the Fermi level, all higher derivatives only contribute to subleading corrections in thermodynamics.

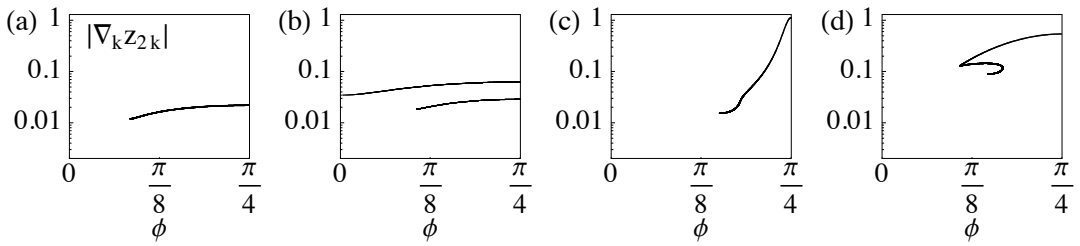

Figure 11.5: The quasiparticle velocity at the Fermi level, $|\nabla_{\mathbf{k}} z_{2\mathbf{k}}|$, in a logarithmic plot vs. momentum-space angle ϕ for (a) s-wave, (b) extended s-wave, and (c,d) $d_{x^2-y^2}$-wave hybridization. Parameters are as in Fig. 11.3(a)-(d). In all four cases, the averaged effective mass $\overline{m^*}$ (as derived from the specific heat) is approximately 125 times the bare electron mass.

It therefore makes sense to define the effective mass via the first, and not the second derivative as done by Ghaemi and Senthil (2007).

In the considered two-band system the quasiparticle dispersion in the presence of less than half filling is given by $\epsilon_{\mathbf{k}}^{QP} = z_{2\mathbf{k}}$. In two dimensions N_0 simplifies to

$$N_0 = \frac{\overline{m^*}}{2\pi} = \frac{1}{4\pi^2} \int\limits_{\mathrm{FS}} \frac{dA_k}{|\nabla_{\mathbf{k}} z_{2\mathbf{k}}|}, \tag{11.14}$$

where dA_k denotes the Fermi surface element and $\overline{m^*}$ is the effective mass which can actually be extracted from specific heat measurements and correponds to the effective mass in the isotropic case with the same Sommerfeld coefficient γ. If the Fermi surface can be parameterized with $k = k_F(\phi)$, the occurring integral can be rewritten as an integral over the angle ϕ:

$$N_0 = \frac{\overline{m^*}}{2\pi} = \frac{1}{4\pi^2} \int \mathrm{d}\phi \frac{\sqrt{(k_F(\phi))^2 + (k_F'(\phi))^2}}{|\nabla_{\mathbf{k}} z_{2\mathbf{k}}|_{k=k_F(\phi)}}. \tag{11.15}$$

Figure 11.5(a)-(d) depicts the quasiparticle velocity $|\nabla_{\mathbf{k}} z_{2\mathbf{k}}|$ for the different hybridizations introduced in Eq. (11.2). The parameters and underlying hybridization functions are the same as for the Fermi surfaces in Fig. 11.3(a) -(d). Every set of parameters leads to the same specific heat coefficient. Its corresponding effective mass $\overline{m*}$ is approximately 125 times the bare electron mass. For the $d_{x^2-y^2}$ hybridization the quasiparticle velocity $|\nabla_{\mathbf{k}} z_{2\mathbf{k}}|$ is maximal at the diagonal $\phi = \pi/4$, the nodal line of the hybridization, while the effective mass $m^*(\mathbf{k})$ is minimal at these points and approximately equal to the bare electron mass. Away from the diagonal the velocity rapidly changes. Both s-wave hybridizations lead to a constant or nearly constant velocity at all positions on the Fermi surface.

The quasiparticle weight Z is defined as the overlap between the c-electron and the low-energy quasiparticle whose dispersion crosses the Fermi level. In the framework of our two-band model it is given by (Ghaemi and Senthil, 2007)

$$Z(\mathbf{k}) = \frac{(z_{1\mathbf{k}} - \bar{\epsilon}_{\mathbf{k}})^2}{(z_{1\mathbf{k}} - \bar{\epsilon}_{\mathbf{k}})^2 + b^2 \beta_{\mathbf{k}}^2}\,. \tag{11.16}$$

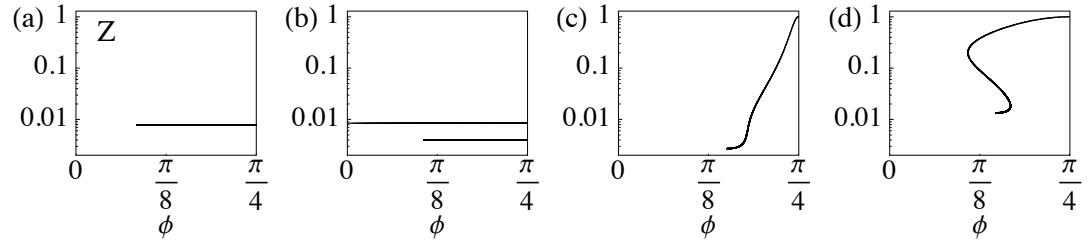

Figure 11.6: As in Fig. 11.5, but now showing the quasiparticle weight Z in a logarithmic plot vs. angle ϕ.

Figure 11.6 shows plots of Z versus the angle ϕ. The set of parameters and the hybridization functions correspond to the ones in Figs. 11.3 and 11.5. The $\mathrm{d}_{x^2-y^2}$ hybridization leads to a strong angle dependence with a maximum of Z at the nodal line $\phi = \pi/4$. The quasiparticle weight for both s-wave hybridizations is constant. For standard s-wave this is due to $V_{\mathbf{k}} =$ const., for extended s-wave because $V_{\mathbf{k}}$ and $\epsilon_{\mathbf{k}}$ coincidentally have the same $\mathbf{k}$ dependence.

In the next section we discuss the effect of an additional Zeeman term in the Hamiltonian. We comment on the changes arising for the Fermi surface and the density of states and compare the thermodynamic effective mass with the cyclotron mass.

11.3 Influence of a magnetic field

A weak external magnetic field coupling to the spin degrees of freedom is expressed by an additional Zeeman term in the Hamiltonian

$$\mathcal{H}_Z = -\mathbf{B} \sum_i (g_c \mathbf{s}_i + g_f \mathbf{S}_i) \tag{11.17}$$

where $\mathbf{s}_i$ and $\mathbf{S}_i$ denote the spins at site i carried by c- and f-electron, respectively.

For simplicity the Landé factors g_c and g_f are set to 1. For a constant hybridization and at zero temperature effects on the band structure and the effective mass have been discussed by Beach (2005). The presence of a momentum-dependent hybridization does not change their qualitative behavior.

The Zeeman term leads to a spin-splitting of the Fermi surface. The distance between spin-up and spin-down Fermi sheets in momentum space is angle-dependent due to the strongly anisotropic shape of $V_{\mathbf{k}}$. The effective masses - and likewise the density of states - become spin-split and field-dependent. The density of states at the Fermi level can be expressed as (Beach, 2005)

$$N_\sigma(B) = (1 + \sigma B/B_0) N_0 \qquad \text{with} \qquad \sigma = \pm 1\,. \tag{11.18}$$

The characteristic field strength B_0 is proportional to the Kondo temperature T_K.

Within the discussed mean-field approach the Zeeman term splits the two bands $z_{1,2\mathbf{k}}$ into $z_{1,2\mathbf{k}} + \sigma B/2$. The mean-field parameters acquire a quadratic B dependence via the changes

in the mean-field equations. This behavior leads to subleading B^2 corrections in the density of states $N_\sigma(B)$ and the effective masses.

The cyclotron mass, which can be extracted from magneto-oscillation measurements like the de Haas-van Alphen effect, is defined as

$$m_c = \frac{1}{2\pi}\frac{\partial A(E)}{\partial E} \tag{11.19}$$

where $A(E)$ describes the area in momentum space enclosed by the quasiparticle iso-energy curve at zero magnetic field perpendicular to the field direction. In general a three-dimensional system has a cyclotron mass that depends on the direction of the applied field. Due to the two-dimensionality and despite the momentum-space anisotropies the cyclotron mass for our discussed system becomes equivalent to the (spin-averaged) effective mass related to the Sommerfeld coefficient apart from second order corrections in B.

An example for a significant change in physical observables arising from the **k**-dependence of the hybridization is discussed in the next section: Nodal lines strongly influence the results for the optical conductivity.

11.4 Optical conductivity

We calculate the optical conductivity on the mean-field level in the framework of linear response theory. It will be shown that nodal lines in the hybridization crossing the Fermi surface significantly reduce the size of the optical gap. While the gap for a s-wave hybridization scales with $\sqrt{T_{\mathrm{coh}}D}$, a $\mathrm{d}_{x^2-y^2}$-hybridization function implies a scaling with T_{coh}.

In most heavy fermion compounds the optical conductivity consists of a zero-frequency Drude peak and a well-separated infrared peak produced by intraband and interband excitations, respectively (Degiorgi, 1999; Dordevic et al., 2001; Degiorgi et al., 2001), compare e.g. Fig. 8.6(a), which shows optical conductivity measurements in $YbFe_4Sb_{12}$. The optical gap exhibits a scaling with the coherence temperature: $\Delta_{\mathrm{opt}} \sim \sqrt{T_{\mathrm{coh}}}$ (Hancock et al., 2004; Okamura et al., 2007).

The non-interacting two-band mean-field model with a local hybridization serves as a good theoretical explanation for this behavior. Within this model the minimal direct gap between the bands is twice the renormalized hybridization b and therefore $\Delta_{\mathrm{opt}} \sim \sqrt{T_{\mathrm{coh}}D}$ (D is the conduction electron bandwidth), compare Sec. 10.2. Inelastic scattering is not captured within the mean-field approach, but as the method of dynamical mean-field theory (DMFT) (explained and discussed in more detail in Chapter 13.1) for the Anderson lattice model with large U (Grenzebach et al., 2006) shows, the inelastic processes lead to a smeared out gap even at zero temperature, which is still distinguishable. The DMFT takes full account of dynamic local correlations and is able to treat elastic as well as inelastic scattering on the same footing.

Although nicely applicable to a group of heavy fermion systems, the two-band model with a local hybridization cannot describe the optical conductivity observed in $CeMIn_5$ (M=Ir,Rh,Co), compare Fig. 8.6(b). Here, no well-defined gaps develop.

The finite frequency part of the optical conductivity σ can be expressed in linear response

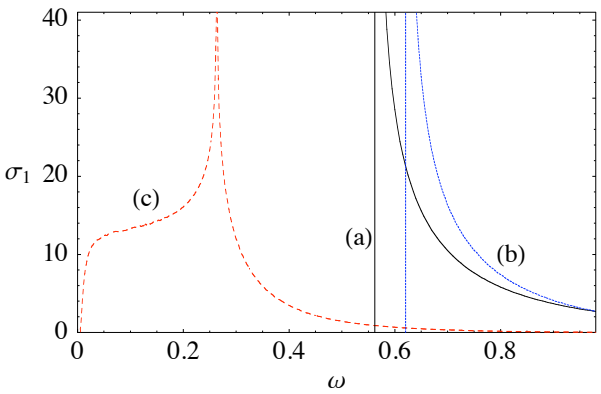

Figure 11.7: Theoretical result for the real part of the optical conductivity $\sigma_1(\omega > 0)$ under the assumption of (a) s-wave (black line), (b) extended s-wave (blue line) and (c) $d_{x^2-y^2}$-wave (red line) hybridization. Mean-field parameters correspond to the ones in Fig. 11.3 (a)-(c).

via the retarded current-current-correlation function $\Pi(\mathrm{i}\omega)$ as

$$\sigma^{(ij)}(\omega) = \frac{\mathrm{i}}{\omega}\Pi^{(ij)}(\omega + \mathrm{i}\delta) + \mathrm{i}\frac{n_0}{m\omega}\delta_{ij}\,, \tag{11.20}$$

where the second term denotes the diamagnetic contribution with the average density n_0 and mass m of the charge carriers, and

$$\Pi^{(ij)}(\mathrm{i}\omega) = -\int_0^\beta \mathrm{d}\tau e^{\mathrm{i}\omega\tau}\langle T_\tau j^{(i)\dagger}(\tau) j^{(j)}(0)\rangle. \tag{11.21}$$

The electron charge is set to 1 throughout this chapter. Upon neglecting inter-band excitations the current operator can be expressed as the time derivative of the polarization operator $\mathbf{P}$

$$\mathbf{j} = \mathrm{i}\,[\mathcal{H}, \mathbf{P}]\,, \tag{11.22}$$

where $\mathbf{P}$ contains all charge-carrying particles a_i with charge q_i in the following way

$$\mathbf{P} = \sum_{i\sigma} q_i \mathbf{R}_i a_i^\dagger a_i\,. \tag{11.23}$$

On the mean-field level the system consists of non-interacting quasiparticles and in leading order the current-current correlation function $\Pi(\mathrm{i}\omega)$ reduces to the bare bubble diagram containing mean-field propagators and a mean-field current vertex. The approximation has to account for charge conservation, which is expressed by the corresponding Ward identity.

The physical system with charge-carrying localized f electrons contributing to the Fermi surface is easier to describe in the framework of the ALM: The auxiliary fermion $\bar{f}$ carries the full charge of the physical f electrons while the condensation parameter $r \sim \langle \bar{f}^\dagger c\rangle$ is charge-conserving. Since ALM and KLM become equivalent in the Kondo limit we choose to work in the Anderson picture within this section.

According to the formula for the current operator, Eq. (11.22), the mean-field current operator reads

$$\mathbf{j}_{\mathrm{MF}} = \mathrm{i}\,[\mathcal{H}_{\mathrm{ALM,MF}}, \mathbf{P}_{\mathrm{MF}}]\,, \tag{11.24}$$

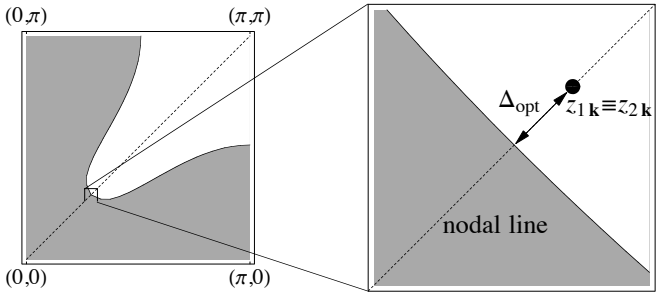

Figure 11.8: Schematic illustration of the origin of the optical gap Δ_{opt} for a $\mathrm{d}_{x^2-y^2}$-wave hybridization. The left panel shows the Fermi surface in one quarter of the Brillouin zone in the presence of $\mathrm{d}_{x^2-y^2}$-wave hybridization. The right panel depicts a zoom into the region, where the nodal line crosses the Fermi surface. The arrow indicates the distance in $\mathbf{k}$-space leading to the optical gap.

where the mean-field polarization operator $\mathbf{P}_{\mathrm{MF}}$ contains the charge-carrying particles c_i and $\bar{f}_i$:

$$\mathbf{P}_{\mathrm{MF}} = \sum_{i\sigma} \mathbf{R}_i \left(c^\dagger_{i\sigma} c_{i\sigma} + \bar{f}^\dagger_{i\sigma} \bar{f}_{i\sigma} \right) . \tag{11.25}$$

Details of the calculation are discussed in Appendix D.1. The result becomes

$$\mathbf{j}_{\mathrm{MF}} = \sum_{\mathbf{k}\sigma} \left(\nabla_{\mathbf{k}} \epsilon_{\mathbf{k}} c^\dagger_{\mathbf{k}\sigma} c_{\mathbf{k}\sigma} + r \nabla_{\mathbf{k}} V_{\mathbf{k}} \left(c^\dagger_{\mathbf{k}\sigma} \bar{f}_{\mathbf{k}\sigma} + \bar{f}^\dagger_{\mathbf{k}\sigma} c_{\mathbf{k}\sigma} \right) \right) . \tag{11.26}$$

For a constant hybridization the second term vanishes and the current is exclusively carried by the conduction electrons. In this case it becomes irrelevant if the pseudo-fermions $\bar{f}$ carry charge or not.

A current operator that is first calculated in the framework of the full Hamiltonian and undergoes a mean-field approximation afterwards has a different contribution arising from the $\bar{f}$-electrons. The corresponding current vertex cannot be combined with the mean-field propagators in the bare bubble diagram: Vertex corrections become necessary.

The evaluation of the current-current correlation function contained in Eq. (11.20) for $\mathbf{j}_{\mathrm{MF}}$ leads to an isotropic conductivity with the finite-frequency real part

$$\sigma_1(\omega > 0) = \frac{\pi}{\omega} \sum_{\mathbf{k}} \frac{n_F(z_{2\mathbf{k}})}{2(z_{1\mathbf{k}} - z_{2\mathbf{k}})^2} A_{\mathbf{k}} \delta(\omega - (z_{1\mathbf{k}} - z_{2\mathbf{k}})), \tag{11.27}$$

where

$$\begin{aligned} A_{\mathbf{k}} = {} & (\nabla_{\mathbf{k}} \epsilon_{\mathbf{k}})^2 (z_{2\mathbf{k}} - \widetilde{\epsilon}_f)(z_{1\mathbf{k}} - \widetilde{\epsilon}_f) + r^2 (\nabla_{\mathbf{k}} V_{\mathbf{k}})^2 \left((z_{1\mathbf{k}} - z_{2\mathbf{k}}) + 4r^2 V_{\mathbf{k}}^2 \right) + \\ & + 2r^2 V_{\mathbf{k}} \nabla \epsilon_{\mathbf{k}} \nabla V_{\mathbf{k}} (z_{2\mathbf{k}} + z_{1\mathbf{k}} - 2\widetilde{\epsilon}_f) \end{aligned} \tag{11.28}$$

and $\widetilde{\epsilon}_f = \epsilon_f - \lambda$. Appendix D.2 provides a detailed description of the calculation.

Plots of the finite-frequency part of σ_1 for different hybridization types introduced in Eq. (11.2) are displayed in Fig. 11.7. Every plot has a finite optical gap Δ_{opt}. In the case of s-wave and extended s-wave these gaps are given by $2b$ and $|\lambda_0 - \mu|/\sqrt{b^2 + t^2}$, therefore both are proportional to $\sqrt{T_{\mathrm{coh}} D}$. For $\mathrm{d}_{x^2-y^2}$ symmetry the bands $z_{1\mathbf{k}}$ and $z_{2\mathbf{k}}$ touch at a point on the nodal line, which in general does not lie on the Fermi surface. For an illustration, see Fig. 11.8. The

minimal energy distance of the two band at the Fermi level is given by $|\lambda_0| \sim T_{\mathrm{coh}}$. In the vicinity of the gap $\sigma_1(\omega)$ behaves like $\sqrt{\omega - \Delta_{\mathrm{opt}}}$, derived in Appendix D.3.

Qualitative results are expected to remain valid even beyond mean-field theory. A momentum-dependent hybridization with nodal lines crossing the Fermi surface is expected to shift optical spectral weight from $\sqrt{T_{\mathrm{coh}} D}$ to T_{coh}. In experiments this would correspond to a situation with no visible gap due to a broadened Drude peak, which is in agreement with data for CeMIn$_5$, compare Fig. 8.6(b).

In the next section thermal and electrical conductivity are studied with a focus on the possible anisotropic effects arising from a momentum-dependent hybridization.

11.5 Thermal and electrical transport

For the observation of anisotropies in momentum space the low-energy d.c. transport quantities are good candidates. Measurements of thermal conductivity and magnetothermal resistance were for example able to reveal the **k**-dependent structure of the superconducting gap in unconventional superconductors like the high-temperature superconductors YBCO (Yu et al., 1995; Aubin et al., 1997), the spin-triplet superconductor Sr_2RuO_4 (Izawa et al., 2001a), and also in the 115-compounds $CeCoIn_5$ (Izawa et al., 2001b) and $CeIrIn_5$ (Shakeripour et al., 2007, 2009).

As theoretically shown by Moreno and Coleman (2000), thermal transport in a three-dimensional Kondo insulator becomes anisotropic in the presence of a momentum-dependent hybridization.

In this section we study the behavior of electrical and thermal transport in the presence of elastic scattering processes. The calculation is based on the non-interacting two-band mean-field description in two dimensions with a momentum-dependent hybridization. We investigate possible direction-dependencies and check the validity of the Wiedemann-Franz law.

The electrical conductivity is defined by $\sigma^{(ij)}(\omega = 0)$, which is given by taking the zero-frequency limit of Eq. (11.20). In a non-interacting system like the one we studied up to now the lack of scattering processes renders the electrical conductivity infinite. Therefore, we include elastic impurity scattering, which would only have subleading influence on the previously studied optical conductivity.

The quasiparticles in the $z_{1,2\mathbf{k}}$-band, described by the operators $\gamma_{1,2\mathbf{k}}$, scatter elastically on impurities with a scattering rate $\Gamma(\omega)$. Their Green functions change into

$$\mathcal{G}_{1,2}(\mathbf{k}, z) = \frac{1}{z - z_{1,2\mathbf{k}} - \Sigma_{1,2}(z)}, \tag{11.29}$$

where $\Sigma_{1,2}(z)$ is the self-energy of the quasiparticles due to these scattering processes. In relaxation time approximation the real part of the electrical conductivity becomes

$$\mathrm{Re}(\sigma^{(ij)}(\omega = 0)) = -\sum_{\mathbf{k}\sigma} \frac{n_F'(z_{2\mathbf{k}})}{\Gamma(z_{2\mathbf{k}})} \xi_{22}^{(ij)}(\mathbf{k}). \tag{11.30}$$

The quasiparticle scattering particle rate $\Gamma(\epsilon)$ is equal to $-\mathrm{Im}\Sigma_2(\epsilon)$ and the coefficient $\xi_{22}^{(ij)}(\mathbf{k})$ is defined by

$$\begin{aligned}\xi_{22}^{(ij)}(\mathbf{k}) &= 4u_{\mathbf{k}}^2 v_{\mathbf{k}}^2 r^2 \nabla V_{\mathbf{k}}^{(i)} \nabla V_{\mathbf{k}}^{(j)} + v_{\mathbf{k}}^4 \nabla \epsilon_{\mathbf{k}}^{(i)} \nabla \epsilon_{\mathbf{k}}^{(j)} + 2u_{\mathbf{k}} v_{\mathbf{k}}^3 r \left(\nabla V_{\mathbf{k}}^{(i)} \nabla \epsilon_{\mathbf{k}}^{(j)} + \nabla \epsilon_{\mathbf{k}}^{(i)} \nabla V_{\mathbf{k}}^{(j)} \right) \\ &= \nabla z_{2\mathbf{k}}^{(i)} \nabla z_{2\mathbf{k}}^{(j)} \,.\end{aligned} \tag{11.31}$$

The complete derivation is discussed in Appendix E.

Thermal transport is calculated in full analogy to electrical conductivity. Following the argumentation of Moreno and Coleman (1996, 2000) the thermal current operator can be obtained by using Noether's theorem relating the continuity of energy flow to the covariance of the action under coordinate transformations. In analogy to their calculation the thermal current operator is given by

$$\mathbf{j}_T = \sum_{\mathbf{k}\sigma} \left(z_{1\mathbf{k}} (\nabla_{\mathbf{k}} z_{1\mathbf{k}}) \gamma_{1\mathbf{k}}^\dagger \gamma_{1\mathbf{k}} + z_{2\mathbf{k}} (\nabla_{\mathbf{k}} z_{2\mathbf{k}}) \gamma_{2\mathbf{k}}^\dagger \gamma_{2\mathbf{k}} \right) , \tag{11.32}$$

reflecting the existence of two bands in the system.

The thermal conductivity tensor $\kappa^{(ij)}$ can be expressed by the Kubo formula (Mahan, 1990)

$$\kappa^{(ij)} = \frac{1}{T^2} \lim_{\omega \to 0} Z^{(ij)}(\mathrm{i}\omega_n \to \omega + \mathrm{i}\delta) \,, \tag{11.33}$$

using

$$Z^{(ij)}(\mathrm{i}\omega_n) = \frac{\mathrm{i}}{\mathrm{i}\omega_n} \int_0^\beta \mathrm{d}\tau e^{\mathrm{i}\omega\tau} \langle T_\tau \mathbf{j}_T^{(i)\dagger}(\tau) \mathbf{j}_T^{(j)}(0) \rangle. \tag{11.34}$$

Apart from $\mathbf{k}$-dependent prefactors the correlation function $Z^{(ij)}$ and the current-current correlation function $\Pi^{(ij)}$ are similar in their structure.

In relaxation-time approximation and by neglecting the influence of the upper band $z_{1\mathbf{k}}$ the low-temperature thermal conductivity reads

$$\mathrm{Re}(\kappa^{(ij)}) = -\frac{1}{T^2} \sum_{\mathbf{k}\sigma} z_{2\mathbf{k}}^2 (\nabla_{\mathbf{k}} z_{2\mathbf{k}}^{(i)}) (\nabla_{\mathbf{k}} z_{2\mathbf{k}}^{(j)}) \frac{n_F'(z_{2\mathbf{k}})}{\Gamma(z_{2\mathbf{k}})}. \tag{11.35}$$

In three-dimensional systems the thermal conductivity can acquire a strong angle dependence produced e.g. by line nodes. Moreno and Coleman (2000) discussed this issue for gap-anisotropic Kondo insulators. For 2D-systems a $\mathrm{d}_{x^2-y^2}$-hybridization as well as hybridizations for higher angular momentum ℓ lead to anisotropic hybridization functions $\beta_{\mathbf{k}}$ that change their sign upon rotation. However, the conductivity tensor does not have enough degrees of freedom in order to reflect this kind of anisotropy. Technically speaking only the absolute value of $\beta_{\mathbf{k}}$ enters the calculation. Therefore, higher order correlation functions, like e.g. angle-dependent magnetoresistance, would be needed to detect the anisotropy.

Only a p_x- or p_y-wave ($\ell = 1$) hybridization which explicitly breaks down the C_4 rotational symmetry of the lattice to C_2 has an anisotropic conductivity tensor. A lattice configuration favoring such a p-wave hybridization has to be distorted, which would be detectable in the entire band structure.

The Wiedemann-Franz law expresses the universal relation between electrical and thermal conductivity and is given by

$$\frac{\kappa}{\sigma T} = L, \tag{11.36}$$

where the Lorentz number L is a constant. The derivation of this relation in the context of isotropic Fermi liquid theory is discussed in Appendix F. For an anisotropic Fermi liquid the ratio becomes

$$\frac{\kappa_{ii}}{\sigma_{ii} T} = \frac{\sum_{\mathbf{k}} z_{2\mathbf{k}}^2 \left(\nabla_{\mathbf{k}} z_{2\mathbf{k}}^{(i)}\right)^2 \frac{n_F'(z_{2\mathbf{k}})}{\Gamma(z_{2\mathbf{k}})}}{T^2 \sum_{\mathbf{k}} \left(\nabla_{\mathbf{k}} z_{2\mathbf{k}}^{(i)}\right)^2 \frac{n_F'(z_{2\mathbf{k}})}{\Gamma(z_{2\mathbf{k}})}} \,. \tag{11.37}$$

Like the conductivities themselves this ratio is direction-independent. Due to the $\mathbf{k}$-dependent Fermi velocity the $\mathbf{k}$ summations cannot be transformed into energy integrals. However, the substitution $\widetilde{z}_{2\mathbf{k}} = z_{2\mathbf{k}}/(k_B T)$ shows the temperature-independence of this ratio, analogously to the isotropic case.

Since the considered approach only takes into account elastic scattering processes, it does not capture the anisotropic violation of the Wiedemann-Fanz law observed in $CeCoIn_5$ at its field-induced quantum critical point (Tanatar et al., 2007), which has been shown to arise from inelastic spin scattering processes (Smith and McKenzie, 2008).

In the next chapter we access the temperature-dependent resistivity at temperatures above T_K with a perturbational approach in the Kondo coupling.

12 Temperature-dependent resistivity

Within this chapter we study the effect of an unconventional hybridization on the resistivity at elevated temperatures ($T > T_K$) in the presence of nodal hybridization lines crossing the Fermi surface.

The temperature dependence of the resistivity $\rho(T)$ in heavy-fermion systems exhibits specific features depicted in Fig. 12.1, which shows measurements for $CeAl_3$. The peak position marks the coherence temperature T_{coh}, below which the resistivity drops due to coherent magnetic scattering. In this regime the material obeys Fermi liquid behavior ($\rho(T) = \rho_0 + AT^2$). For temperatures higher than T_{coh} the magnetic scattering decreases and phonon scattering sets in. A minimum evolves (not shown in Fig. 12.1) determining the Kondo temperature T_{K}.

In the following we set up a perturbational approach in the Kondo coupling in order to access the behavior of ρ due to magnetic scattering for $T > T_{\mathrm{K}}$. This calculation is in the spirit of Kondo's original perturbational approach for the single-impurity problem (Kondo, 1964). The influence of phonon scattering will be neglected here.

In d spatial dimensions the electrical conductivity can be written as

$$\sigma_{ij} \sim \int_{\mathrm{FS}} \frac{d^{d-1}k}{(2\pi)^d} v_i(\mathbf{k}) v_j(\mathbf{k}) \tau_{\mathbf{k}} \,, \tag{12.1}$$

where $v_i(\mathbf{k}) = d\epsilon_{\mathbf{k}}/dk_i$ is the quasiparticle velocity and $\tau_{\mathbf{k}}^{-1}$ is the transport scattering rate. We neglect vertex corrections and assume that Umklapp processes lead to a similar structure

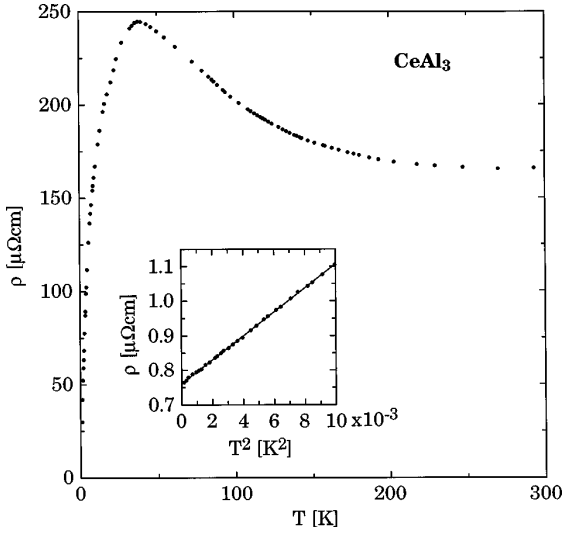

Figure 12.1: Resistivity ρ as a function of temperature T measured in the heavy fermion compound $CeAl_3$. The position of the maximum marks the temperature scale T_{coh} - at lower temperatures the particles scatter coherently. The inset shows the resistivity in the low-temperature regime plotted as a function of T^2 emphasizing the Fermi liquid behavior at low temperatures. (Figure from Degiorgi, 1999).

in the scattering rate as processes for which the momentum is conserved. This can be seen in analogy to an ordinary metal, whose resistivity behavior is correctly reproduced by Fermi liquid theory, because both kind of processes lead to a T^2 behavior. Henceforth, $\tau_{\mathbf{k}}^{-1}$ can be approximated by the single particle scattering rate given by

$$\tau_{\mathbf{k}}^{-1} = -\mathrm{Im}\Sigma_c(\mathbf{k}, \epsilon_{\mathbf{k}})\,, \tag{12.2}$$

where Σ_c is the self-energy of the conduction electrons.

In Sec. 12.1 we calculate the first orders of the perturbation series for the self-energy, which lead to an expression for the scattering rate. A discussion of the results follows in Sec. 12.2.

12.1 Perturbation series for the self-energy

In this section we develop a diagrammatic expansion for the KLM, valid for the temperature regime $T > T_{\mathrm{K}}$, where the Kondo coupling term can be treated as a perturbation. We consider the Kondo lattice Hamiltonian (9.3) and express the spins by Abrikosov pseudo-fermions $\widetilde{f}$ (Abrikosov, 1965):

$$\begin{aligned}\mathcal{H}_{\mathrm{KLM}} = &\sum_{\mathbf{k}\sigma} \epsilon_{\mathbf{k}} c^\dagger_{\mathbf{k}\sigma} c_{\mathbf{k}\sigma} + \\ &+ 2J_0 \sum_{\mathbf{k}\mathbf{k}'\mathbf{p}\mathbf{p}'} \beta_{\mathbf{k}}\beta_{\mathbf{k}'}\delta_{\mathbf{k}-\mathbf{k}'+\mathbf{p}-\mathbf{p}',0} \left(\sum_{\alpha\alpha'} \widetilde{f}^\dagger_{\mathbf{p}\alpha} \frac{\boldsymbol{\sigma}_{\alpha\alpha'}}{2} \widetilde{f}_{\mathbf{p}'\alpha'}\right) \cdot \left(\sum_{\sigma\sigma'} c^\dagger_{\mathbf{k}\sigma} \frac{\boldsymbol{\sigma}_{\sigma\sigma'}}{2} c_{\mathbf{k}'\sigma'}\right).\end{aligned} \tag{12.3}$$

The number of pseudo-fermions per site is subjected to a constraint

$$Q_i = \sum_\sigma \widetilde{f}^\dagger_{i\sigma} \widetilde{f}_{i\sigma} \equiv 1\,. \tag{12.4}$$

In order to set up a perturbation theory it is desirable to fix this constraint in the style of Coleman (1984). He considered a single-impurity Hamiltonian with slave particles that have to fulfill only one constraint, $Q_0 = 1$, and was able to show that a diagrammatic expansion can be developed in the grand-canonical (GC) ensemble, whose result is connected to the result in the physical subspace obeying $Q_0 = 1$. A term λQ_0 is added to the Hamiltonian, where λ acts like a chemical potential. In contrast to the stationary approach discussed in Chapter 10, λ is not fixed to its saddle-point value, but stays finite and undetermined in the diagrammatic calculation, and is sent to infinity afterwards for projecting out unphysical states. A detailed explanation of this formalism is given in Appendix G. For operators O with vanishing expectation value in the $\{Q_0 = 0\}$ subspace, the expectation value in the canonical ensemble with $Q_0 = 1$, i.e., in the physical subspace, can be obtained via

$$\langle O\rangle_C = \lim_{\lambda\to\infty} \frac{\langle O\rangle_{GC}}{\langle Q_0\rangle_{GC}} = \lim_{\lambda\to\infty} e^{\beta\lambda} \langle O\rangle_{GC}\,. \tag{12.5}$$

Unfortunately, such an approach is only exact for the case of a single-impurity problem. If we e.g. try to fix the lattice constraint on average and apply the same kind of formalism as

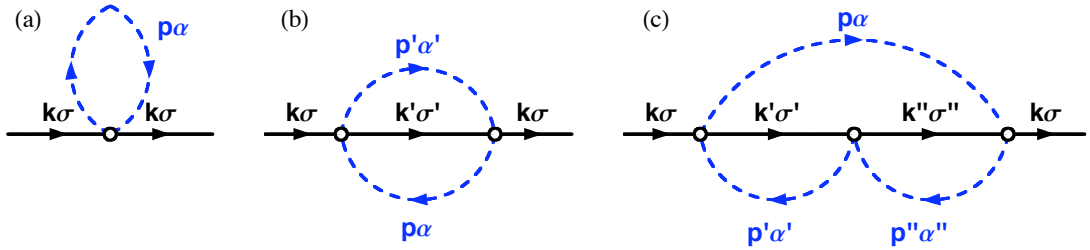

Figure 12.2: Diagrammatic expansion for the self-energy Σ_c in first (a), second (b) and third order (c). Dashed lines denote the pseudo-fermion propagators $\widetilde{f}$, while solid lines represent propagators of the conduction electrons c. Vertices are proportional to the Kondo coupling J_0.

for the impurity case, problems occur, since $\sum_i Q_i/\mathcal{N}$ ($\mathcal{N}$ being the number of lattice sites in the system) is not restricted to integer values.

However, as the following diagrammatic expansion will show, at least up to third order, only single-impurity scattering processes are present. We therefore expect the approach by Coleman to be valid for our lattice model to good approximation. We consider the Hamiltonian $\mathcal{H}_{\mathrm{KLM}} + \lambda \sum_i Q_i$. In analogy to relation (12.5), the physical self-energy $\Sigma_c(\mathbf{k}, z)$ is obtained from the grand-canonical self-energy $\Sigma_c(\mathbf{k}, z, \lambda)$ by

$$\Sigma_c(\mathbf{k}, z) = \lim_{\lambda \to \infty} e^{\beta\lambda} \Sigma_c(\mathbf{k}, z, \lambda). \tag{12.6}$$

The bare Green functions for $\widetilde{f}$ and c electrons are

$$\mathcal{G}^{(0)}_{\widetilde{f}}(\mathrm{i}k_n, \mathbf{k}) = \frac{1}{\mathrm{i}k_n - \lambda} \qquad \text{and} \qquad \mathcal{G}^{(0)}_{c}(\mathrm{i}k_n, \mathbf{k}) = \frac{1}{\mathrm{i}k_n - \epsilon_{\mathbf{k}}}. \tag{12.7}$$

The vertex arising from the Kondo term connects four propagators: an ingoing and outgoing c- and $\widetilde{f}$-electron. The vertex has the value $\frac{J_0}{2}\beta_{\mathbf{k}}\beta_{\mathbf{k}'}\boldsymbol{\sigma}_{\sigma\sigma'}\boldsymbol{\sigma}_{\alpha\alpha'}$. The lowest order diagrams contributing to the self-energy Σ_c are depicted in Fig. 12.2. In first order the diagram consists of the Hartree contribution, which vanishes in the considered paramagnetic phase. The second and third order diagram can be identified as contributions without multiple impurity scattering processes, which serves as a justification for the above claim regarding the applicability of Coleman's approach.

Calculating the values for the second order terms leads to

$$\begin{aligned}
\Sigma^{(2)}_c(\mathbf{k}, \mathrm{i}k_n, \lambda) &= \left(\frac{J_0}{2\beta}\right)^2 \sum_{\mathbf{k}', \mathrm{i}k'_n} \sum_{\mathbf{p}, \mathrm{i}p_n} \beta^2_{\mathbf{k}} \beta^2_{\mathbf{k}'} \left(\sum_{\sigma,\sigma'} \boldsymbol{\sigma}_{\sigma\sigma'} \sum_{\alpha,\alpha'} \boldsymbol{\sigma}_{\alpha\alpha'} \right)^2 \mathcal{G}^{(0)}_c(\mathbf{k}', \mathrm{i}k'_n) \cdot \\
&\qquad \cdot \mathcal{G}^{(0)}_{\widetilde{f}}(\mathbf{p}, \mathrm{i}p_n) \mathcal{G}^{(0)}_{\widetilde{f}}(\mathbf{k} + \mathbf{p} - \mathbf{k}', \mathrm{i}k_n + \mathrm{i}p_n - \mathrm{i}k'_n) \\
&= \frac{3}{2} J_0^2 \sum_{\mathbf{k}'} \beta^2_{\mathbf{k}} \beta^2_{\mathbf{k}'} \left(n_F(\epsilon_{\mathbf{k}'}) - n_F(-\lambda)\right) \frac{1}{\beta} \sum_{\mathrm{i}p_n} \frac{1}{(\mathrm{i}p_n - \lambda)(\mathrm{i}p_n + \mathrm{i}k_n - \epsilon_{\mathbf{k}'} - \lambda)} \\
&= \frac{3}{2} J_0^2 \sum_{\mathbf{k}'} \beta^2_{\mathbf{k}} \beta^2_{\mathbf{k}'} \left(n_F(\epsilon_{\mathbf{k}'}) - n_F(-\lambda)\right) \left(n_F(\lambda) - n_F(\epsilon_{\mathbf{k}'} + \lambda)\right) \frac{1}{\mathrm{i}k_n - \epsilon_{\mathbf{k}'}}.
\end{aligned}$$

(12.8)

The third order contribution is

$$\begin{aligned}\Sigma_c^{(3)}(\mathbf{k},\mathrm{i}k_n,\lambda) &= \frac{3}{2}J_0^3\frac{1}{\beta^3}\sum_{\mathbf{k}',\mathrm{i}k_n'}\sum_{\mathbf{k}'',\mathrm{i}k_n''}\sum_{\mathrm{i}p_n}\beta_{\mathbf{k}}^2\beta_{\mathbf{k}'}^2\beta_{\mathbf{k}''}^2\cdot \\ &\quad\cdot\frac{1}{(\mathrm{i}k_n'-\epsilon_{\mathbf{k}'})(\mathrm{i}k_n''-\epsilon_{\mathbf{k}''})(\mathrm{i}k_n+\mathrm{i}p_n-\mathrm{i}k_n'-\lambda)(\mathrm{i}k_n+\mathrm{i}p_n-\mathrm{i}k_n''-\lambda)(\mathrm{i}p_n-\lambda)} \\ &= \frac{3}{2}J_0^3\sum_{\mathbf{k}',\mathbf{k}''}\beta_{\mathbf{k}}^2\beta_{\mathbf{k}'}^2\beta_{\mathbf{k}''}^2\left(n_F(\epsilon_{\mathbf{k}'})-n_F(-\lambda)\right)\left(n_F(\epsilon_{\mathbf{k}''})-n_F(-\lambda)\right)\cdot \\ &\quad\cdot\left(\frac{n_F(\lambda)}{(\mathrm{i}k_n-\epsilon_{\mathbf{k}'})(\mathrm{i}k_n-\epsilon_{\mathbf{k}''})}-\frac{n_B(\lambda+\epsilon_{\mathbf{k}'})}{(\mathrm{i}k_n-\epsilon_{\mathbf{k}'})(\epsilon_{\mathbf{k}'}-\epsilon_{\mathbf{k}''})}+\frac{n_F(\lambda+\epsilon_{\mathbf{k}''})}{(\mathrm{i}k_n-\epsilon_{\mathbf{k}''})(\epsilon_{\mathbf{k}'}-\epsilon_{\mathbf{k}''})}\right).\end{aligned} \tag{12.9}$$

The occurring Matsubara summations are evaluated using residue theorem.

For obtaining the scattering rate we are interested in the imaginary part of the physical self-energy at an energy $\omega=\epsilon_{\mathbf{k}}$:

$$\mathrm{Im}\Sigma_c(\mathbf{k},\epsilon_{\mathbf{k}}) = \lim_{\lambda\to\infty}e^{\beta\lambda}\left(\mathrm{Im}\Sigma_c(\mathbf{k},\mathrm{i}k_n\to\omega+\mathrm{i}\eta,\lambda)|_{\omega=\epsilon_{\mathbf{k}}}\right). \tag{12.10}$$

The second order contribution

$$\mathrm{Im}\Sigma_c^{(2)}(\mathbf{k},\epsilon_{\mathbf{k}}) = \frac{3}{2}\pi J_0^2\beta_{\mathbf{k}}^2\sum_{\mathbf{k}'}\beta_{\mathbf{k}'}^2\delta(\epsilon_{\mathbf{k}}-\epsilon_{\mathbf{k}'})\sim\beta_{\mathbf{k}}^2, \tag{12.11}$$

is temperature-independent and its $\mathbf{k}$ space structure is proportional to $\beta_{\mathbf{k}}^2$. The third order contribution

$$\mathrm{Im}\Sigma_c^{(3)}(\mathbf{k},\epsilon_{\mathbf{k}}) = 3\pi J_0^3\beta_{\mathbf{k}}^2\sum_{\mathbf{k}'\mathbf{k}''}\beta_{\mathbf{k}'}^2\beta_{\mathbf{k}''}^2\frac{1}{\epsilon_{\mathbf{k}'}-\epsilon_{\mathbf{k}''}}\left(n_F(\epsilon_{\mathbf{k}''})-1\right)\delta(\epsilon_{\mathbf{k}}-\epsilon_{\mathbf{k}'})\propto\beta_{\mathbf{k}}^2 \tag{12.12}$$

has the same $\mathbf{k}$-dependence arising from the two external lines, while other from factors are averaged out by the internal momentum summations. Its temperature dependence is determined by the prefactor

$$\sum_{\mathbf{k}'\mathbf{k}''}\frac{\beta_{\mathbf{k}'}^2\beta_{\mathbf{k}''}^2}{\epsilon_{\mathbf{k}'}-\epsilon_{\mathbf{k}''}}\left(n_F(\epsilon_{\mathbf{k}''})-1\right)\delta(\epsilon_{\mathbf{k}}-\epsilon_{\mathbf{k}'}) = \sum_{\mathbf{k}''}\frac{\beta_{\mathbf{k}''}^2}{\epsilon_{\mathbf{k}}-\epsilon_{\mathbf{k}''}}\left(n_F(\epsilon_{\mathbf{k}''})-1\right)\sum_{\mathbf{k}'}\beta_{\mathbf{k}'}^2\delta(\epsilon_{\mathbf{k}}-\epsilon_{\mathbf{k}'}). \tag{12.13}$$

The momentum summation over $\mathbf{k}''$ can be rewritten as an energy integral:

$$\begin{aligned}\sum_{\mathbf{k}''}\frac{\beta_{\mathbf{k}''}^2}{\epsilon_{\mathbf{k}}-\epsilon_{\mathbf{k}''}}\left(n_F(\epsilon_{\mathbf{k}''})-1\right) &= \int d\Omega\beta^2(\Omega)\int_{-D}^{D}d\epsilon''\rho_0(\epsilon'')\frac{1-n_F(\epsilon'')}{\epsilon''-\epsilon_{\mathbf{k}}} \\ &\approx \int d\Omega\beta^2(\Omega)\left(\underbrace{\int_{-T}^{T}d\epsilon''\rho_0(\epsilon'')\frac{1/2+\epsilon''/(2T)}{\epsilon''-\epsilon_{\mathbf{k}}}}_{\text{non-divergent}}+\underbrace{\int_{T}^{D}d\epsilon''\frac{\rho_0(\epsilon'')}{\epsilon''-\epsilon_{\mathbf{k}}}}_{\sim\ln\frac{D}{T}}\right).\end{aligned}$$

(12.14)

Therefore, the third order diagram has a logarithmic divergence. These results lead to a scattering rate

$$\tau_{\mathbf{k}}^{-1} \sim J_0^2 \beta_{\mathbf{k}}^2 \left(1 + \frac{J_0}{D} \ln \frac{D}{T}\right). \tag{12.15}$$

The implications of such a scattering rate are discussed in the next section.

12.2 Discussion

The above calculation was accomplished in the framework of perturbation theory in the Kondo coupling describing the physics in an elevated temperature regime $T > T_{\mathrm{K}}$ and neglecting phonon scattering. The perturbational approach for calculating the resistivity was, historically, the method followed by Kondo in his first paper introducing the single-impurity Kondo model (Kondo, 1964). Apart from $\mathbf{k}$-dependent prefactors we recover the analog result for the scattering rate $\tau_{\mathbf{k}}^{-1}$ as in the original calculation with a logarithmic divergence in $\tau_{\mathbf{k}}^{-1}$ at $T = 0$.

However, for a hybridization with nodes crossing the Fermi surface these prefactors drastically change the resulting resistivity: In the vicinity of a node at k_n the scattering rate diverges as $\tau_{\mathbf{k}} \sim (k - k_n)^{-2}$ implying a vanishing electrical resistivity $\rho = 1/\sigma$ (where σ is determined by Eq. (12.1))! This means that Kondo scattering itself is not able to produce a finite resistivity. Physically speaking the conduction electrons with momenta where the hybridization vanishes do not scatter off the local spins at all; this process shortcircuits all others.

In a physical system additional scattering mechanisms occur, like electron-electron scattering, interaction between electrons and phonons or scattering between conduction electrons and static impurities. These processes are likely to render the resistivity finite and influence the temperature-dependence $\rho(T)$ in a basic manner.

In conclusion we find that the electrical current for $T > T_{\mathrm{K}}$ is mostly carried by nodal quasiparticles, i.e. weakly hybridized c and f electrons, whereas the low temperature thermodynamics is controlled by the behavior of antinodal, i.e., heavy quasiparticles.

13 Beyond static mean-field theory

The mean-field approximation developed in Chapter 10 provides an appropriate description of the Fermi liquid phase in the regime $T \ll T_{\mathrm{K}}$. Its great advantage lies in its easy applicability to the lattice problems and it allows an analytic treatment of most of the calculations. However, this method has its limitations arising from the lack of fluctuations.

In this chapter we explain how two approaches going beyond the static mean-field level can be adapted to our model. We discuss the method of dynamical mean-field theory (Sec. 13.1) and how a non-local hybridization is treated within this approach. We furthermore take a look on what happens upon including gauge fluctuations on top of the static mean-field approach (Sec. 13.2).

13.1 Static vs. dynamical mean-field theory: DMFT

The dynamical mean-field theory (DMFT) (Metzner and Vollhardt, 1989; Georges et al., 1996) is able to go beyond the level of the static mean-field approach by taking into account local quantum fluctuations. DMFT maps lattice models onto impurity models - the problem reduces to the degrees of freedom of a single site coupled to an external dynamical, self-consistent bath. This bath, which can be viewed as a generalized Weiss field, is expressed by an effective Green function $\mathcal{G}_0$ containing the influence of all other sites. The dynamics is carried by this Green function taking care of local quantum fluctuation. The mapping between lattice and single-site problem is accomplished by a self-consistency condition, equating the local lattice Green function with the impurity Green function. The single-site problem can be solved by different methods. Popular impurity solvers are e.g. a perturbative expansion, the numerical renormalization group (NRG) (Bulla, 1999), or Quantum Monte Carlo (QMC) (Georges et al., 1996) with its recently developed continuous time version (Rubtsov et al., 2005). DMFT becomes exact in the limit of infinite spatial dimensions.

Within DMFT the Anderson lattice model is reduced to an effective single-impurity Anderson problem (Jarrell, 1995; Tahvildar-Zadeh et al., 1997; Pruschke et al., 2000; Grenzebach et al., 2006). DMFT results confirm the heavy-fermion character in the thermodynamic properties arising from the ALM. It exhibits a band structure that is in agreement with the static mean-field result: a heavy coherent band crossing the Fermi level and a well-seperated second band at higher energies. Grenzebach et al. (2006) studied the transport properties in the paramagnetic phase. The gap in the optical conductivity in the presence of a local hybridization is smeared out due to quantum fluctuations, but is still distinguishable.

An ALM with a momentum-dependent hybridization has not yet been considered in a numerical implementation of the DMFT. In the following we will (i) present the DMFT self-consistency equation for a non-local hybridization and (ii) discuss the slave boson method as

an impurity solver for this problem. It will be shown that the results are equivalent to the ones obtained from the slave boson treatment of the lattice model.

Starting with the full ALM, Eq. (9.2), and integrating out the c-electrons, the DMFT reduces the original problem to one for a single f-level coupled to a bath with the effective action

$$\mathcal{S}_{\text{eff}} = -\int_0^\beta d\tau d\tau' \sum_\sigma f_\sigma^\dagger(\tau)\mathcal{G}_0^{-1}(\tau-\tau')f_\sigma(\tau') + U\int_0^\beta d\tau n_{f\uparrow}(\tau)n_{f\downarrow}(\tau)\,. \tag{13.1}$$

The bath is represented by the Green function $\mathcal{G}_0$ containing all interactions that couple to the f-electron. With the ansatz

$$\mathcal{G}_0^{-1}(\mathrm{i}\omega_n) = \mathrm{i}\omega_n - \epsilon_f - \widetilde{\Delta}(\mathrm{i}\omega_n)\,, \tag{13.2}$$

we introduce the effective hybridization function $\widetilde{\Delta}(z)$. The full f-electron Green function

$$\mathcal{G}_f(z) = \left(\mathcal{G}_0^{-1}(z) - \Sigma_f(z)\right)^{-1}\,, \tag{13.3}$$

contains the self energy Σ_f resulting from the Coulomb interaction U.

The self-consistency equation for the ALM with a momentum-dependent hybridization term mapped on a single impurity Anderson model (SIAM) reads

$$\begin{aligned} G_{\text{ALM,loc}}(z) &= \sum_{\mathbf{k}} \frac{1}{z-\epsilon_f-\Sigma_f(z)-\frac{V_{\mathbf{k}}^2}{z-\bar{\epsilon}_{\mathbf{k}}}} \\ &= \frac{1}{z-\epsilon_f-\widetilde{\Delta}(z)-\Sigma_f(z)} = G_{\text{SIAM}}(z). \end{aligned} \tag{13.4}$$

The effective hybridization function $\widetilde{\Delta}(z)$ is determined by the second equality sign in this self-consistency equation.

By construction, the self energy $\Sigma_f(z)$ and the effective hybridization $\widetilde{\Delta}(z)$ are momentum-independent within the DMFT approach. This can be cured by a cluster extension of DMFT (for a review see Maier et al., 2005).

Thermodynamical and one-particle properties are easily extractable from DMFT calculations. Please note that in principle the calculation of transport properties requires a DMFT ansatz with c-electrons not being integrated out. However, as apparent from static mean-field results (Sec. 11.5), the presence of a non-local hybridization leads to transport that explicitly depends on the momentum-space structure of $V_{\mathbf{k}}$, which cannot be captured in the standard DMFT approach.

By using the slave boson method as an impurity solver for the SIAM, the DMFT method becomes equivalent to the slave boson treatment of the ALM. This can be confirmed by an explicit calculation. The Coulomb term in the effective action (13.1) is decoupled by slave bosons (where the physical f-electrons are represented by $\bar{f}$-particles and slave bosons r),

which in combination with the ansatz for the Weiss field $\mathcal{G}_0$, Eq. (13.2), leads to

$$\begin{aligned}\mathcal{S}_{\text{eff}}^{\text{MF}} = &\int d\tau \sum_\sigma \bar{f}_\sigma^\dagger(\tau)(\partial_\tau + \epsilon_f - \lambda)\bar{f}_\sigma(\tau) + \\ &+ \int d\tau d\tau' \sum_\sigma \bar{f}_\sigma^\dagger(\tau) r^2 \widetilde{\Delta}(\tau - \tau')\bar{f}_\sigma(\tau') - \lambda \int d\tau (r^2 - 1)\end{aligned} \tag{13.5}$$

We think of introducing these slave bosons as operators in the corresponding Hamiltonian and not as bosonic fields on the level of the path-integral formalism, implying a differing factor of r^2 in the first term of $\mathcal{S}_{\text{eff}}^{\text{MF}}$, see the discussion in Sec. 10.1.

The saddle point equations are

$$\lambda = \frac{1}{\beta}\sum_{\mathrm{i}\omega_n} \mathcal{G}_{\bar{f}}(\mathrm{i}\omega_n)\widetilde{\Delta}(\mathrm{i}\omega_n), \tag{13.6a}$$

$$r^2 = 1 - \frac{2}{\beta}\sum_{\mathrm{i}\omega_n} \mathcal{G}_{\bar{f}}(\mathrm{i}\omega_n). \tag{13.6b}$$

The effective mean-field action $\mathcal{S}_{\text{eff}}^{\text{MF}}$ allows to extract an expression for the full f-electron Green function $\mathcal{G}_f(z) = r^2 \mathcal{G}_{\bar{f}}(z)$:

$$\mathcal{G}_f(z) = \frac{r^2}{z - (\epsilon_f - \lambda) - r^2\widetilde{\Delta}(z)}. \tag{13.7}$$

The high-frequency behavior of this Green function is not given by $1/z$, which is due to the violation of the sum rule for the spectral weight arising from mapping out the Hubbard satellites in the slave boson approach.

By comparison with Eq. (13.3) we can write down the interaction self energy as

$$\Sigma_f(z) = \left(1 - \frac{1}{r^2}\right)(z - \epsilon_f) - \frac{\lambda}{r^2}\,. \tag{13.8}$$

In combination with the self-consistency condition (13.4), the hybridization function is determined as

$$\widetilde{\Delta}(z) = \frac{1}{r^2}\left(z - (\epsilon_f - \lambda) - \frac{1}{\sum_{\mathbf{k}}\left(z - (\epsilon_f - \lambda) - \frac{r^2 V_{\mathbf{k}}^2}{z - \epsilon_{\mathbf{k}}}\right)^{-1}}\right). \tag{13.9}$$

The saddle point equations

$$\lambda = \frac{1}{\beta}\sum_{\mathrm{i}\omega_n}\sum_{\mathbf{k}} \frac{V_{\mathbf{k}}^2}{(\mathrm{i}\omega_n - (\epsilon_f - \lambda))(\mathrm{i}\omega_n - \epsilon_{\mathbf{k}}) - r^2 V_{\mathbf{k}}^2}, \tag{13.10a}$$

$$r^2 = 1 - \frac{2}{\beta}\sum_{\mathrm{i}\omega_n} \frac{V_{\mathbf{k}}^2}{(\mathrm{i}\omega_n - \epsilon_{\mathbf{k}})(\mathrm{i}\omega_n - \epsilon_{\mathbf{k}}) - r^2 V_{\mathbf{k}}^2}, \tag{13.10b}$$

become equivalent to Eq. (10.5), which proves our initial claim.

13.2 Gauge fluctuations

After the introduction of slave bosons r in the ALM or the auxiliary fields b in the KLM both models obey a local U(1) gauge invariance expressed by simultaneous phase rotations in r (b) and $\bar{f}$ ($\widetilde{f}$):

$$\text{ALM:} \quad r \to r e^{\mathrm{i}\theta}, \quad \bar{f} \to \bar{f} e^{\mathrm{i}\theta} \tag{13.11a}$$

$$\text{KLM:} \quad b \to b e^{\mathrm{i}\theta}, \quad \widetilde{f} \to \widetilde{f} e^{\mathrm{i}\theta} \tag{13.11b}$$

In the stationary approximation r condenses to a static value with $\langle r \rangle = r$ and $\langle r^\dagger \rangle = r$, which breaks the local gauge invariance between $\bar{f}$ and r (for b analogous expressions hold). In analogy to the superconducting phase the evolving Fermi-liquid phase corresponds to a Higgs/confining phase due to this local U(1) gauge symmetry breaking.

The mean-field condensation in the framework of the Kondo model not only breaks a local gauge symmetry but also violates charge conservation: By construction the Abrikosov pseudo-fermion $\widetilde{f}$ is neutral and the auxiliary field b carries one electron charge. After condensation the contribution $bc^\dagger \widetilde{f}$ in the mean-field Hamiltonian (10.11) does not preserve charge conservation.

In order to treat small gauge fluctuation on top of the mean-field level the slave boson operator r and the Lagrange parameter λ can be substituted prior to condensation by (Millis and Lee, 1987; Hewson, 1997)

$$r = a + r_0, \qquad r^\dagger = a^\dagger + r_0, \qquad \lambda = \Lambda + \Lambda_0 \,. \tag{13.12}$$

The parameters r_0 and Λ_0 represent the former mean-field values. A perturbation theory for the bosonic a-operators can be developed. As a result these fluctuations lead to corrections to the mean-field result of the order of $1/N$ where N denotes the spin degeneracy. These corrections are subleading and the Fermi-liquid phase can be considered as stable.

In the context of the Kondo model the consideration of gauge fluctuations restores the charge conservation: the $\widetilde{f}$ electrons minimally couple to the U(1) gauge field Λ and therefore acquire charge.

Since the breaking of the local gauge invariance is an artifact of the mean-field approximation and not related to a physical symmetry breaking, the mean-field transition at T_K between phases with finite and zero parameter b is only artificial. It does not survive upon the inclusion of gauge fluctuations, but corresponds to a crossover in a physical system.

14 Competition between Kondo screening and ordering

The local magnetic moments in heavy fermion compounds feel a more or less strong intersite exchange coupling, which can arise from different mechanisms like direct exchange, superexchange (Anderson, 1950) or the RKKY mechanism (Ruderman and Kittel, 1950; Kasuya, 1956; Yosida, 1957). For the latter one the spin coupling is mediated by spin oscillations of the conduction electrons, while in superexchange the magnetic moments interact via an intermediate ion.

Such an intermoment exchange can produce not only a magnetically ordered state, but also other interesting phases like metallic spin liquid phases or magnetically mediated superconductivity. All the arising phases compete for the localized f-electrons, which order magnetically, form Kondo-singlets with the conduction electrons in the Fermi liquid phase or intermoment-singlets in the metallic spin liquid phase. Already the Doniach phase diagram, Fig. 8.3, is able to illustrate the interplay between antiferromagnetism and the evolution of a heavy Fermi liquid phase depending on the Kondo coupling and the conduction electron density.

In the presence of a strongly **k**-dependent hybridization and unconventional superconductivity, where the pairing function also becomes **k**-dependent, it is conceivable that the phase competition depends on the interplay of symmetries between hybridization and pairing function.

Within this chapter we study the phase competition between Kondo screening, unconventional superconductivity and antiferromagnetic ordering on a mean-field level. In Sec. 14.1 we introduce the Kondo-Heisenberg model, which contains all essential effects that will be discussed here. In Sec. 14.2 we focus on the competition between magnetically mediated superconductivity and Kondo screening for different **k**-dependent hybridization and pairing functions. In Sec. 14.3 we expand this theory by allowing for an additional magnetically ordered phase and include the presence of a magnetic field.

14.1 Kondo-Heisenberg model

The Anderson and Kondo lattice models, Eqs. (9.2) and (9.3), already contain an intermoment-exchange mediated by the conduction electrons. At the mean-field level this information is lost due to the introduction and condensation of slave boson and auxiliary fields r and b. In order to restore this coupling we introduce an additional term

$$\mathcal{H}_{\mathrm{H}} = \sum_{ij} \frac{J_{\mathrm{H}}^{ij}}{2} \mathbf{S}_i \cdot \mathbf{S}_j \,, \tag{14.1}$$

which explicitly describes the exchange interaction between two local moments at different sites i and j. The model $\mathcal{H}_{\mathrm{KLM}} + \mathcal{H}_{\mathrm{H}}$ is known as the Kondo-Heisenberg model.

A mean-field treatment of this model is accomplished by combining the mean-field approximation for $\mathcal{H}_{\mathrm{KLM}}$ developed in Sec. 10.2 with a mean-field decoupling of the Heisenberg term $\mathcal{H}_{\mathrm{H}}$. In general possible decoupling channels are the particle-particle channel (or Cooper channel) producing superconductivity, the particle-hole channel leading to a RVB-like phase consisting of gapless spinons without broken symmetry and the magnetic channel accounting for magnetically ordered phases.

The Kondo-Heisenberg model with local hybridization at the mean-field level was studied by Senthil et al. (2003, 2004). In these references the focus lies on the existence of a RVB-like metallic spin liquid phase FL*, which can be stabilized e.g. by geometric frustrations. FL* consists of conduction electrons forming a small Fermi surface and a spin liquid out of spinons, which have fractionalized excitations due to spin-charge separation and are coupled by a Z_2 or U(1) gauge structure. Beyond mean-field theory a quantum critical point (QCP) between FL* and FL phase develops, which in contrast to the QCP between antiferromagnetic and FL phase is not connected to a symmetry breaking but only associated with the breakdown of the Kondo effect. The mean-field approximation shows the existence of a superconducting phase in the vicinity of this QCP.

Furthermore, Senthil et al. (2003) study the interplay of this FL* phase with superconductivity on a two-dimensional triangular lattice, while the mean-field treatment in (Senthil et al., 2004) accounts for such a FL* phase and a weak antiferromagnetic instability computed for a cubic lattice structure.

In the remainder of this chapter we investigate the effects of a superconducting and a magnetic instability in the presence of an unconventional hybridization. At the mean-field level the Heisenberg term $\mathcal{H}_{\mathrm{H}}$ has to be simultaneously decoupled in the Cooper and the magnetic channel, which is accomplished by a splitting

$$\mathcal{H}_{\mathrm{H,MF}} = (1-x)\mathcal{H}_{\mathrm{H,SC,MF}} + x\mathcal{H}_{\mathrm{H,AFM,MF}} \tag{14.2}$$

with a balancing factor x.

In Sec. 14.2 we develop the formalism for the mean-field description of a magnetically mediated superconductor with unconventional pairing and study its phase competition with unconventional Kondo screening, while suppressing a possible magnetic instability by setting $x = 0$. This approach is supplemented by Sec. 14.3, where an additional antiferromagnetic ordering is considered, implemented by a finite value of x.

14.2 Magnetically mediated superconductivity

Superconductivity mediated by magnetic fluctuations instead of lattice vibrations is a widely accepted scenario for heavy fermion compounds. The mean-field approach is based on a spin representation in the symplectic symmetry group $\mathrm{Sp}(N)$ (Read and Sachdev, 1991; Sachdev and Read, 1991; Sachdev and Wang, 1991).

In this section we introduce the mean-field formalism (Sec. 14.2.1), present phase diagrams as a function of Kondo coupling and temperature illustrating the competition between Kondo

screening and superconductivity related to their symmetry in momentum space (Sec. 14.2.2), and discuss general analytical aspects of pairing in the presence of an unconventional hybridization (Sec. 14.2.3).

14.2.1 Mean-field formalism

For a decoupling in the Cooper channel it is favorable to express the spin operators in the Heisenberg term $\mathcal{H}_{\mathrm{H}}$ by Abrikosov fermions $\widetilde{f}$ and approximately rewrite it as

$$\mathcal{H}_{\mathrm{H}} = -\sum_{ij} \frac{J_{\mathrm{H}}^{ij}}{2} \left(\widetilde{f}_{i\uparrow}\widetilde{f}_{j\downarrow} - \widetilde{f}_{i\downarrow}\widetilde{f}_{j\uparrow} \right) \left(\widetilde{f}_{i\uparrow}^{\dagger}\widetilde{f}_{j\downarrow}^{\dagger} - \widetilde{f}_{i\downarrow}^{\dagger}\widetilde{f}_{j\uparrow}^{\dagger} \right). \tag{14.3}$$

Expressing a product of spins in terms of singlet pairs corresponds to a Sp(N) spin representation (Read and Sachdev, 1991; Sachdev and Read, 1991; Sachdev and Wang, 1991). For a spin 1/2 the corresponding group is SU(2)≅Sp(1); the differing factor of 2 in the argument originates in the fact, that Sp(N) describes a group of $2N \times 2N$ matrices, whereas SU(N) is a group of $N \times N$ matrices.

By introducing the non-local bond field

$$\Delta_{ij} = -\langle \widetilde{f}_{i\uparrow}\widetilde{f}_{j\downarrow} - \widetilde{f}_{i\downarrow}\widetilde{f}_{j\uparrow} \rangle \,, \tag{14.4}$$

the Hamiltonian can be decoupled to

$$\mathcal{H}_{\mathrm{H,SC,MF}} = -\sum_{ij} \frac{J_{\mathrm{H},ij}}{4} \left[\left(2\Delta_{ij}\widetilde{f}_{i\uparrow}^{\dagger}\widetilde{f}_{j\downarrow}^{\dagger} + h.c. \right) - |\Delta_{ij}|^2 \right] . \tag{14.5}$$

Under the assumption of time reversal invariance the bond field can be chosen as real and the relation $\Delta_{ij} = \Delta_{ji}$ holds.

Due to the representation in Sp(N) this mean-field approximation is controlled by the parameter N: In the limit of large N the mean-field solution becomes exact and corresponds to a saddle point of the Sp(N) theory, which explicitly selects the particle-particle channel.

In order to get a consistent large-N limit in the total Hamiltonian $\mathcal{H}_{\mathrm{KLM}} + \mathcal{H}_{\mathrm{H}}$ the particle-particle decoupling in the Heisenberg term should be accompanied by a particle-particle decoupling in the Kondo term of $\mathcal{H}_{\mathrm{KLM}}$ based on Sp(N) instead of SU(N). However, in the presence of time-reversal invariance and with the condition $n_{\widetilde{f}} = 1$ the mean-field approximations arising from particle-particle or particle-hole decoupling in the Kondo term become equivalent. Therefore, $\mathcal{H}_{\mathrm{H,SC,MF}}$ can be combined with the $\mathcal{H}_{\mathrm{KLM,MF}}$ introduced in Sec. 10.2.

Depending on the structure of the bond field Δ_{ij} the translational invariance of the lattice can be broken leading to so-called valence bond solids. A phase with non-zero Δ_{ij} preserving the lattice symmetries is described by a spin liquid. Since we are only interested in the latter scenario, the condition of a translationally invariant Δ_{ij} is imposed by hand.

The spatial structure of Δ_{ij} within the unit cell is intimately connected to the structure of the Heisenberg coupling $J_{\mathrm{H},ij}$ between the f electrons. For a nearest-neighbor interaction the unit cell contains two distinguishable bonds - a horizontal and a vertical one. Under the already mentioned restrictions of conserved translational and time reversal symmetry, only

two configurations are possible solutions to the mean-field problem: $\Delta_{i,i+\hat{x}} = \Delta_{i,i+\hat{y}} = \Delta$, which will be denoted as the extended s-wave configuration, and $\Delta_{i,i+\hat{x}} = -\Delta_{i,i+\hat{y}} = \Delta$, where horizontal and vertical bonds acquire different signs. The latter configuration is called $\mathrm{d}_{x^2-y^2}$-wave. If the Heisenberg interaction is assumed to only be finite for f electrons on next-nearest neighbored sites, a mean-field solution with differing signs for diagonal bonds ($\Delta_{i,i+(\hat{x}+\hat{y})/2} = -\Delta_{i,i+(\hat{x}-\hat{y})/2} = \Delta$) becomes possible leading to a d_{xy} pairing function.

In momentum space the mean-field Hamiltonian can be written as

$$\mathcal{H}_{\mathrm{H,SC,MF}} = \sum_{\mathbf{k}} \widetilde{W}_{\mathbf{k}} \left(\widetilde{f}^{\dagger}_{\mathbf{k}\uparrow} \widetilde{f}^{\dagger}_{-\mathbf{k}\downarrow} + h.c. \right) + J_{\mathrm{H}} \mathcal{N} \Delta^2 \tag{14.6}$$

using the shortcut

$$\widetilde{W}_{\mathbf{k}} = -J_{\mathrm{H}} \Delta \alpha_{\mathbf{k}}, \tag{14.7}$$

where $\alpha_{\mathbf{k}}$ contains the momentum space structure of the mentioned spinon pairings:

$$\alpha_{\mathbf{k}} = \begin{cases} \cos k_x + \cos k_y & \text{extended s-wave} \\ \cos k_x - \cos k_y & \mathrm{d}_{x^2-y^2}\text{-wave} \\ 2 \sin k_x \sin k_y & \mathrm{d}_{xy}\text{-wave} \end{cases} . \tag{14.8}$$

The self-consistency equations for the mean-field parameters, Eqs. (10.11), are extended by

$$\sum_{\mathbf{k}} \alpha_{\mathbf{k}} \langle \widetilde{f}^{\dagger}_{\mathbf{k}\uparrow} \widetilde{f}^{\dagger}_{-\mathbf{k}\downarrow} + h.c. \rangle = 2 \mathcal{N} \Delta \,, \tag{14.9}$$

which is obtained by minimizing the free energy with respect to Δ. The occurring Green functions are listed in Appendix B.2. The quasiparticle energies, the eigenvalues of the mean-field Hamiltonian, read

$$\begin{aligned} \bar{z}_{1,2,3,4\mathbf{k}} = \pm \frac{1}{\sqrt{2}} \Bigg(& \lambda_0^2 + \bar{\epsilon}_{\mathbf{k}}^2 + 2 b^2 \beta_{\mathbf{k}}^2 + \widetilde{W}_{\mathbf{k}}^2 + \\ & \pm \left(-4 \left(\lambda_0 \bar{\epsilon}_{\mathbf{k}} + b^2 \beta_{\mathbf{k}}^2 \right)^2 - 4 \bar{\epsilon}_{\mathbf{k}}^2 \widetilde{W}_{\mathbf{k}}^2 + \left(\lambda_0^2 + \bar{\epsilon}_{\mathbf{k}}^2 + 2 b^2 \beta_{\mathbf{k}}^2 + \widetilde{W}_{\mathbf{k}}^2 \right)^2 \right)^{1/2} \Bigg)^{1/2} . \end{aligned} \tag{14.10}$$

In the limit of vanishing Δ these bands evolve into the quasiparticle bands $z_{1,2\mathbf{k}}$, Eq. (11.4).

The spinon pairing is given by $\langle \widetilde{f}^{\dagger}_{\mathbf{k}\uparrow} \widetilde{f}^{\dagger}_{-\mathbf{k}\downarrow} \rangle \propto \Delta \alpha_{\mathbf{k}}$, which can be extracted from the self-consistency condition, Eq. (14.9). However, the momentum space structure of the conduction electron pairing also takes into account the momentum-dependent hybridization. Determined by the corresponding Green function, Eq. (B.5d), it reads $\langle c^{\dagger}_{\mathbf{k}\uparrow} c^{\dagger}_{-\mathbf{k}\downarrow} \rangle \propto \Delta \beta_{\mathbf{k}}^2 \alpha_{\mathbf{k}} M_{\mathbf{k}}$. The function $M_{\mathbf{k}}$ is smooth and respects the lattice symmetries. The pairing acquires additional zeros in momentum space arising from the factor $\beta_{\mathbf{k}}^2$. This will affect the thermodynamical properties of the system: power-laws, e.g. for the specific heat, are sensitive on additional nodal lines crossing the Fermi surface. For a two-channel Kondo model such a composite pairing also arises (Dzero and Coleman, 2008).

In the next section we present phase diagrams based on a numerical solution of the mean-field equations illustrating the interplay of symmetries between hybridization and pairing function.

14.2.2 Numerical results: Phase diagrams

In order to focus on the phase competition between Kondo screening and superconductivity we keep the balancing factor x to zero and solve the mean-field equations (10.11) and (14.9) in a fully self-consistent manner by numerical iteration.

The resulting phase diagrams as a function of Kondo coupling J_0 and temperature T for various hybridization and pairing symmetries are depicted in Fig. 14.1. The phases are determined by the two parameters b and Δ occurring in the mean-field Hamiltonian $\mathcal{H}_{\mathrm{KLM,MF}} + \mathcal{H}_{\mathrm{H,SC,MF}}$. Only Δ is an order parameter in the strict sense, since beyond the mean-field description b is not associated with symmetry breaking. Four different fully translationally invariant phases evolve. For both Δ and b vanishing, the resulting phase is decoupled and therefore trivial. It develops at sufficiently high temperatures. If J_{H} dominates over J_0, we get $\Delta \neq 0$ and $b = 0$: The conduction electrons and the spinons form decoupled liquids, which corresponds to the already mentioned fractionalized Fermi liquid FL*. Although a phase with non-zero Δ has off-diagonal order in the sense that the anomalous expectation value $\langle f^\dagger f^\dagger \rangle$ is finite, this phase is not superconducting, since the spinons do not carry physical charge. For $b \neq 0$ and $\Delta = 0$ the resulting phase is the conventional Fermi liquid (FL), whose thermodynamical and transport properties are extensively studied in Chapter 11. If both parameters Δ and b are non-zero, the coexistence of Kondo screening and spinon pairing leads to superconductivity that is mediated by the magnetic interaction between the f electrons. As the phase diagrams show, at any non-zero J_{H} and sufficiently low temperature the FL phase is always unstable towards superconductivity.

Adding fluctuations in the mean-field approach (e.g. by coupling the order parameter to a gauge field) turns the finite-temperature mean-field phase transition of FL and FL* into crossovers (Senthil et al., 2003, 2004). Only the boundaries to the superconducting phase remain real phase transitions, as they are connected to a symmetry breaking.

Each pairing symmetry represents a different saddle solution in the large-N mean-field theory. The channel with the lowest free energy is the physically relevant state. For each pairing symmetry we compute the corresponding free energy

$$F = -\frac{1}{\beta} \sum_{\mathbf{k},i} \ln\left(1 + e^{-\beta \tilde{z}_i}\right) + \sum_{\mathbf{k}} (\epsilon_{\mathbf{k}} - \lambda_0) + \mathcal{N}\mu n_c + \mathcal{N}\lambda_0 + \mathcal{N} J_H \Delta^2 + \mathcal{N}\frac{b^2}{J_0}\,, \qquad (14.11)$$

see Fig. 14.2. From these results we can conclude, that the extended s-wave hybridization favors the $\mathrm{d}_{x^2-y^2}$ superconductivity, while $\mathrm{d}_{x^2-y^2}$ hybridization prefers d_{xy} superconductivity.

Regarding the shape of the Fermi surface in the Fermi liquid state, Fig. 11.3, we can explain this behavior in the following way: If both symmetries are of s-wave type, the pairing interaction at the Fermi surface is small, implying a weak superconducting phase. However, a s-wave hybridization combined with a d-wave pairing produces a much more stable superconductivity. For $\mathrm{d}_{x^2-y^2}$ hybridization the Fermi surface is located near the nodal area, where the pairing of d_{xy} type is strong. Please note that the pairing symmetry with the lowest free energy produces the most extended superconducting phase.

We supplement this numerical approach by an analytic estimate of the critical superconducting temperature T_c presented in the next section.

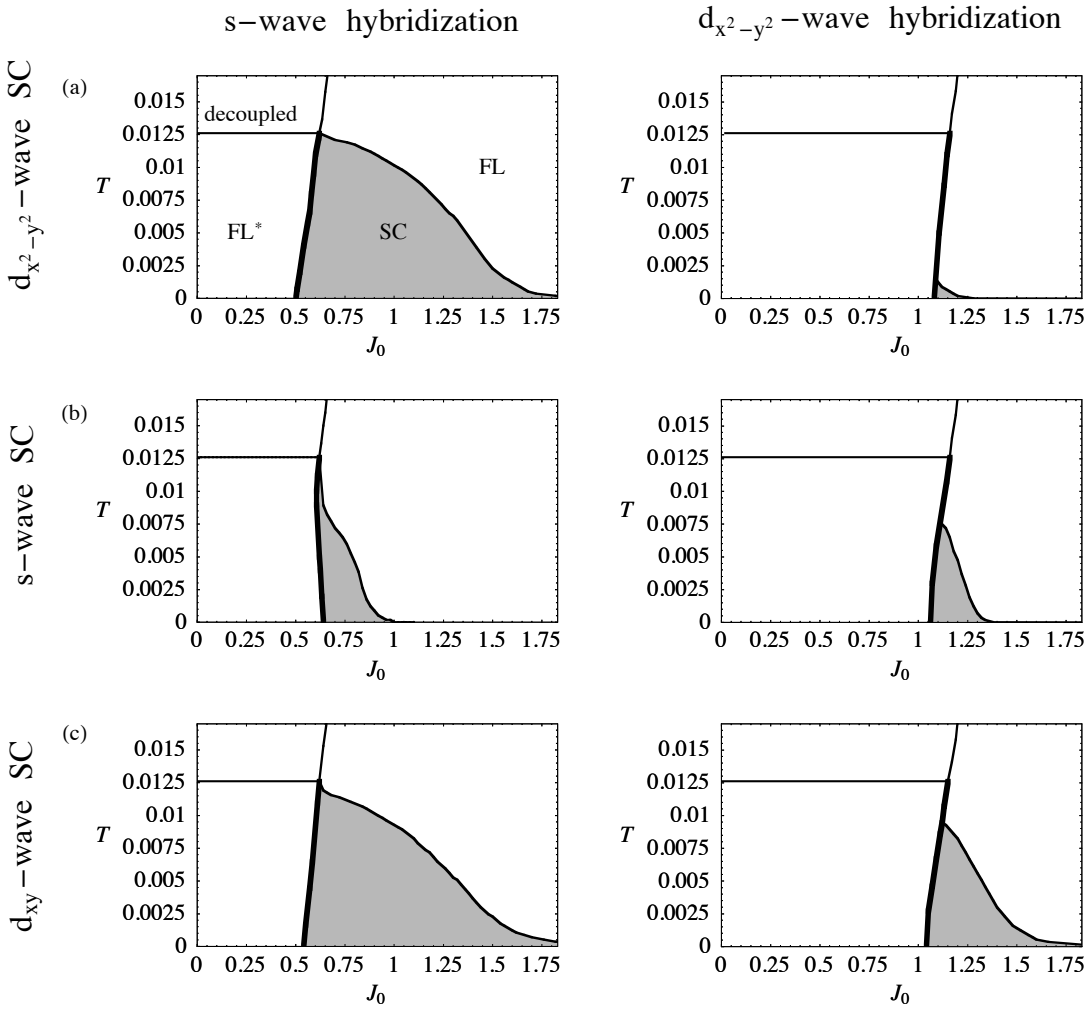

Figure 14.1: Phase diagrams as a function of Kondo coupling J_0 and temperature T at a band filling $n_c = 0.3$ for extended s-wave (left) and $d_{x^2-y^2}$-wave hybridization (right) in combination with different pairing symmetries: (a) $d_{x^2-y^2}$-wave, (b) extended s-wave and (c) d_{xy}-wave. Thick (thin) lines refer to first (second) order phase transitions. The Heisenberg exchange is $J_H = 0.05$ and the hopping parameter is set to $t = 1$.

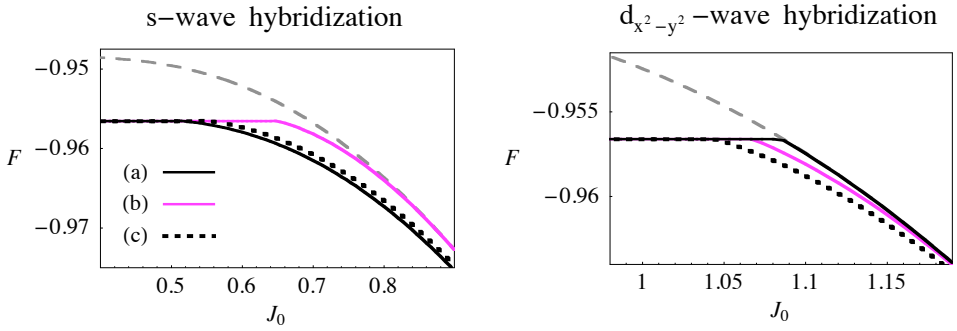

Figure 14.2: Free energy as a function of the Kondo coupling J_0 at $T = 10^{-5}$ and $n_c = 0.3$ for extended s-wave (left) and $d_{x^2-y^2}$-wave hybridization (right) for (a) $d_{x^2-y^2}$-wave, (b) extended s-wave, and (c) d_{xy}-wave pairing symmetries. The plots correspond to the phase diagrams shown in Fig. 14.1 with the same parameters, $J_H = 0.05$ and $t = 1$. The dashed line shows the free energy for the normal state solution with $\Delta = 0$.

14.2.3 Analytic estimate: Pairing in the regimes $T_c \ll T_K$ and $T_c \sim T_K$

In general, we can differentiate between the pairing mechanisms in the two regimes $T_c \ll T_K$ and $T_c \sim T_K$. In the former one the superconducting phase can be thought of as being evolved out of the heavy Fermi liquid, whereas for $T_c \sim T_K$ a strong competition between Kondo screening and BCS pairing exists. In the regime $T_c \gg T_K$ simply a non-superconducting FL*-phase evolves.

Within the mean-field approach the value of T_c is determined by the mean-field equation (14.9) by setting Δ to zero:

$$\frac{2}{J_H} = \frac{1}{\mathcal{N}} \sum_{\mathbf{k}} \alpha_{\mathbf{k}}^2 \left(\frac{z_{1\mathbf{k}}^2 - \bar{\epsilon}_{\mathbf{k}}^2}{z_{1\mathbf{k}}^2 - z_{2\mathbf{k}}^2} \frac{1}{z_{1\mathbf{k}}} \tanh \frac{z_{1\mathbf{k}}}{2T_c} + (1 \leftrightarrow 2). \right) \tag{14.12}$$

For $\Delta = 0$ the band-structure is given by the two bands $z_{1,2\mathbf{k}}$ (Eq. (11.4)) determining the physics in the Fermi liquid regime. The factor $\alpha_{\mathbf{k}}^2$ arises, because gap and pairing function are equal in our approach.

In the limit $T_c \ll T_K$ several approximations can be made. We neglect the influence of the upper band $z_{1\mathbf{k}}$, which is located well above the Fermi level, and only take into account contributions from $z_{2\mathbf{k}}$ close to the Fermi surface. The $\mathbf{k}$ summation is replaced by an integral over isoenergetic lines $\int d\omega \int_{\omega=z_{2\mathbf{k}}} dA_k/|\nabla z_{2\mathbf{k}}|$. In analogy to the BCS approximation we substitute

$$\tanh\left(\frac{\omega}{2T_c}\right) = \begin{cases} 1 & \text{for } \omega \geq 2T_c \\ -1 & \text{for } \omega \leq -2T_c \\ 0 & \text{else} \end{cases} . \tag{14.13}$$

The $\mathbf{k}$-dependence of the occurring factor

$$\kappa \equiv \frac{\bar{\epsilon}_{\mathbf{k}}^2 - z_{2\mathbf{k}}^2}{z_{1\mathbf{k}}^2 - z_{2\mathbf{k}}^2} \approx \text{const} \tag{14.14}$$

is assumed to have minor influence and is therefore omitted. The velocity $|\nabla_{\mathbf{k}} z_{2\mathbf{k}}|$ and $\alpha_{\mathbf{k}}$ are approximated by their value at the Fermi surface, which is determined by $z_{2\mathbf{k}} \equiv 0$, compare Figs. 11.3. The dependence of $|\nabla_{\mathbf{k}} z_{2\mathbf{k}}|$ and $\alpha_{\mathbf{k}}$ on the direction orthogonal to the Fermi surface is neglected. As a result we get

$$\frac{2}{J_H} = \int_{2T_c}^{\Lambda} \frac{d\omega}{\omega} \int_{\mathrm{FS}} \frac{dA_k}{2\pi} \frac{\kappa \alpha_{\mathbf{k}}^2}{|\nabla_{\mathbf{k}} z_{2\mathbf{k}}|}, \tag{14.15}$$

from which we can extract an expression for T_c,

$$T_c = \frac{\Lambda}{2} \exp\left(-\frac{4\pi}{J_H \kappa \int dA_k \alpha_{\mathbf{k}}^2 / |\nabla z_{2\mathbf{k}}|} \right), \tag{14.16}$$

where Λ is of the order of bandwidth. T_c is especially large, if the pairing is strong in antinodal regions, which are characterized by flat bands and small velocity $|\nabla z_{2\mathbf{k}}|$.

In the regime $T_c \sim T_{\mathrm{K}}$ both bands contribute to the integral. In this case the major contribution arises from the flat parts of $z_{1\mathbf{k}}$ and $z_{2\mathbf{k}}$ in the weakly hybridized regions, illustrating the strong competion between Kondo and superconducting pairing. In contrast to the previously discussed regime *nodal* instead of antinodal quasiparticles are more susceptible to pairing.

At temperatures of the order of the Kondo scale T_{K} inelastic processes occur, especially for particles in the antinodal regions, limiting the applicability of the mean-field approximation. Pairing of incoherent particles, which is also discussed in the context of the pseudogap phase in underdoped cuprates (Emery and Kivelson, 1995; Franz and Millis, 1998), cannot be described with this mean-field approach.

In conclusion, the numerical and analytical calculations are complementary approaches showing the favoring and disfavoring of certain hybridization and pairing symmetries. While analytics is able to extract some qualitative arguments, the numerical evaluation is also sensible on microscopic properties like band structure and band filling.

In the next section we allow for an additional antiferromagnetic phase on the mean-field level and study the competition among Kondo screening, superconductivity and magnetic ordering, while tuning the Kondo coupling and an external magnetic field.

14.3 Magnetic ordering

As illustrated by the phase diagram of the heavy fermion compounds CeMIn$_5$ (Fig. 8.5(b)) and predicted by the Doniach argument (see Fig. 8.3), Kondo screening not only competes with superconducting order, but also with antiferromagnetism. The members of the 115-family exhibit different phenomena regarding the coexistence and the suppression of superconductivity (SC) and antiferromagnetism (AFM) upon applying a magnetic field or pressure, which we will briefly review here.

In a finite magnetic field that is oriented orthogonal to the basal plane, CeCoIn$_5$ exhibits a quantum critical point at the breakdown of superconductivity, although any direct evidence

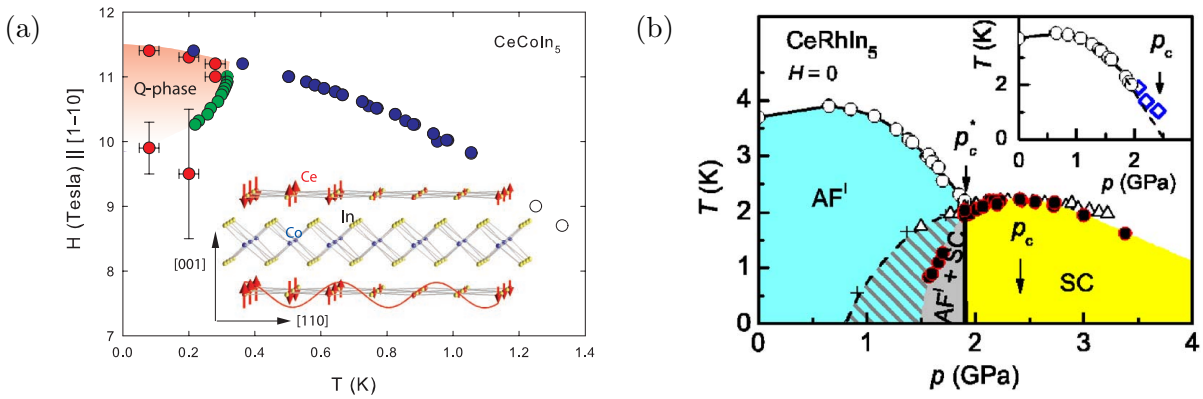

Figure 14.3: Experimental phase diagrams for $CeCoIn_5$ and $CeRhIn_5$ illustrating the interplay between superconductivity and antiferromagnetism upon applying a magnetic field or pressure. (a) Magnetic field-temperature phase diagram for $CeCoIn_5$. Blue dots mark the superconducting critical temperature T_c and the Q-phase denotes the coexistence region between superconductivity and antiferromagnetism. (Figure from Kenzelmann et al., 2008). (b) Temperature-pressure phase diagram for $CeRhIn_5$. Superconductivity (SC) and antiferromagnetism (AFM) coexist in a specific pressure range. (Figure from Knebel et al., 2006).

of magnetic ordering is missing (Tanatar et al., 2007). This quantum critical point was speculated to be produced by an antiferromagnetic instability that is suppressed by the emerging superconducting order over wide ranges in the phase diagram. For a magnetic field aligned parallel to the basal plane a region close to the upper critical field $H_{c2} \approx 11$T develops, showing signatures of a coexistence between superconductivity and magnetic order, see Fig. 14.3(a) (Young et al., 2007; Kenzelmann et al., 2008).

The ambient-pressure antiferromagnet $CeRhIn_5$ is driven to a superconducting state upon applying pressure. A coexistence region of SC and AFM develops, see Fig. 14.3(b) (Knebel et al., 2006; Chen et al., 2006).

In this section we study the interplay of Kondo screening, superconductivity and magnetic ordering at a mean-field level. The hybridization as well as the superconductivity are assumed to be unconventional.

Superconductivity in $CeCoIn_5$ is assumed to be Pauli-limited (Bianchi et al., 2002), i.e., the breakdown of superconductivity in a magnetic field is produced by spin alignment breaking up the spin-singlets, rather than orbital pair breaking effects due to the Lorentz force ripping apart the electrons in a Cooper pair with opposite momentum. Therefore, we include the presence of a magnetic field only by coupling it to the spin degrees of freedom in a Zeeman term. The influence on the orbital sector, which manifests itself in the appearance of vortices and an acquired Peierls phase factor upon hopping, would require a real-space description with an enormous number of lattice sites and is omitted in the following. The mean-field parameters are assumed to be field-independent.

The Hamiltonian, now including the Zeeman term $\mathcal{H}_Z$, reads

$$\mathcal{H} = \mathcal{H}_{\mathrm{KLM}} + \mathcal{H}_{\mathrm{H}} + \mathcal{H}_Z \tag{14.17}$$

with

$$\mathcal{H}_Z = -\mathbf{B}\sum_i (\mathbf{S}_i + \mathbf{s}_i), \tag{14.18}$$

where $\mathbf{s}_i$ denotes the spin density operator of a c-electron at site i: $\mathbf{s}_i = \sum_{\sigma\sigma'} c^\dagger_{i\sigma}\boldsymbol{\sigma}_{\sigma\sigma'}c_{i\sigma'}/2$. The Landé factors for c-electrons and localized spins are assumed to be equivalent and are set to 1 here.

The decoupling of the Heisenberg term $\mathcal{H}_\mathrm{H}$ in the magnetic channel accounting for a possible magnetic instability is presented in Sec. 14.3.1. Section 14.3.2 shows the phase diagrams obtained from a numerical solution of the mean-field equations. A discussion of the results is given in Sec. 14.3.3.

14.3.1 Mean-field approximation

In order to consider superconductivity and magnetic ordering in the mean-field approach, we now assume a finite value of the balancing factor x in the split Hamiltonian (14.2). $\mathcal{H}_\mathrm{H,SC,MF}$ already studied in Sec. 14.2.1 is given by Eq. (14.6). In the magnetic channel the decoupling leads to

$$\mathcal{H}_\mathrm{H,AFM,MF} = J_\mathrm{H}\sum_{\langle ij\rangle}\left[\mathbf{M}_i\cdot\left(\sum_{\sigma\sigma'}\widetilde{f}^\dagger_{j,\sigma}\boldsymbol{\sigma}_{\sigma\sigma'}\widetilde{f}_{j,\sigma'}\right) - \mathbf{M}_i\cdot\mathbf{M}_j\right] \tag{14.19}$$

with the on-site magnetization

$$\mathbf{M}_i = \left\langle \frac{1}{2}\sum_{\sigma\sigma'}\widetilde{f}^\dagger_{i,\sigma}\boldsymbol{\sigma}_{\sigma\sigma'}\widetilde{f}_{i,\sigma'}\right\rangle, \tag{14.20}$$

while the spin-spin interaction in the Heisenberg term is assumed to be restricted to nearest-neighbored sites.

In contrast to the previously discussed decouplings of the Kondo term and the Heisenberg term in the Cooper channel, which were based on a spin representation in SU(N) and Sp(N) respectively, this mean-field approximation is not equivalent to a large-N saddle point solution. It is rather in the spirit of classical mean-field theory introduced by Weiss, which becomes exact in the limit of infinite coordination number.

The magnetic field is aligned in z-direction, $\mathbf{B} = B\hat{z}$, orthogonal to the two-dimensional lattice. The magnetization is modeled by the ansatz

$$\mathbf{M}_i = M_s e^{\mathrm{i}\mathbf{Q}\mathbf{r}_i}\widehat{x} + M_u\widehat{z}, \tag{14.21}$$

with the staggered part M_s and the uniform part M_u. The antiferromagnetic ordering wave vector $\mathbf{Q} = (\pi,\pi)$ leads to alternating signs in a checkerboard pattern and requires a division of the lattice into two sublattices A and B. The arrangement of A- and B-sites is depicted in Fig. 14.4(a). $\mathbf{r}_i$ is the vector connecting a specific corner of the unit cell with the two contained sites A and B. Due to the doubling of the unit cell the real-space operators c_i and

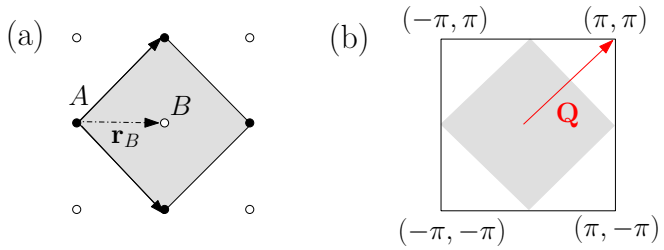

Figure 14.4: (a) The lattice is divided into two sublattice A (black points) and B (white points). The reference point for each unit cell is chosen to be the left corner leading to $\mathbf{r}_A = (0, 0)$ and $\mathbf{r}_B = (1, 0)$. The gray shaded region shows the unit cell. (b) The Brillouin zone corresponding to the enlarged unit cell (colored in gray) is obtained from the original BZ by backfolding with the vector $\mathbf{Q}$.

$\widetilde{f}_i$ are substituted by $c_{\nu,r}$ and $\widetilde{f}_{\nu,r}$, where $\nu = A, B$ is the sublattice index and r refers to position of the unit cell. The Fourier transformed operators

$$c_{\nu,\mathbf{p}} = \sqrt{\frac{\mathcal{N}}{2}} \sum_r e^{-\mathrm{i}\mathbf{p}(\mathbf{R}_r + \mathbf{r}_\nu)} c_{\nu,r} \,, \tag{14.22}$$

are defined for $\mathbf{p}$ lying within the new, reduced BZ, see Fig. 14.4(b).

The total mean-field Hamiltonian can be compactly written as

$$\mathcal{H}_{\mathrm{MF}} = \frac{1}{2} \sum_{\mathbf{p}} \Psi_{\mathbf{p}}^\dagger \hat{A}_{\mathbf{p}} \Psi_{\mathbf{p}} + E_{\mathrm{const}} \,, \tag{14.23}$$

with the constant

$$E_{\mathrm{const}} = \mathcal{N} \left(\mu(n_c - 1) + \frac{b^2}{J_0} + (1 - x) J_{\mathrm{H}} \Delta^2 + 2x J_{\mathrm{H}} (M_s^2 - M_u^2) \right) \,, \tag{14.24}$$

and the 16-component spinor

$$\Psi_{\mathbf{p}}^T = \left(\Phi_{c,\mathbf{p}}^T, \Phi_{\widetilde{f},\mathbf{p}}^T \right) \,, \tag{14.25}$$

where

$$\Phi_{c,\mathbf{p}}^T = \left(c_{A,\mathbf{p},\uparrow}, c_{A,\mathbf{p},\downarrow}, c_{A,-\mathbf{p},\uparrow}^\dagger, c_{A,-\mathbf{p},\downarrow}^\dagger, c_{B,\mathbf{p},\uparrow}, c_{B,\mathbf{p},\downarrow}, c_{B,-\mathbf{p},\uparrow}^\dagger, c_{B,-\mathbf{p},\downarrow}^\dagger \right) \,. \tag{14.26}$$

$\Phi_{\widetilde{f},\mathbf{p}}^T$ is defined in an analogous way. The matrix $\hat{A}_{\mathbf{p}}$ is presented in Appendix H, as well as the steps that are necessary to rewrite the Hamiltonian in terms of the operators $c_{\mathbf{p}\nu}$ and $\widetilde{f}_{\mathbf{p}\nu}$.

The mean-field equations for the set of mean-field variables $\{\lambda_0, \mu, b, \Delta, M_s, M_u\}$ are obtained by varying the free energy with respect to the particular variable:

$$\mathcal{N} = \left\langle \sum_{\mathbf{p},\sigma,\nu} \widetilde{f}_{\nu,\mathbf{p},\sigma}^\dagger \widetilde{f}_{\nu,\mathbf{p},\sigma} \right\rangle \,, \tag{14.27a}$$

$$\mathcal{N}n_c = \left\langle \sum_{\mathbf{p},\sigma,\nu} c^\dagger_{\nu,\mathbf{p},\sigma} c_{\nu,\mathbf{p},\sigma} \right\rangle , \tag{14.27b}$$

$$-\mathcal{N}\frac{2b}{J_0} = \left\langle \sum_{\mathbf{p},\sigma,\nu} \left[\frac{\beta_{\mathbf{p}} + \beta_{\mathbf{p}+\mathbf{Q}}}{2} c^\dagger_{\nu\mathbf{p}\sigma} \widetilde{f}_{\nu\mathbf{p}\sigma} + \frac{\beta_{\mathbf{p}} - \beta_{\mathbf{p}+\mathbf{Q}}}{2} c^\dagger_{\nu\mathbf{p}\sigma} \widetilde{f}_{\bar{\nu}\mathbf{p}\sigma} + \text{h.c.} \right] \right\rangle , \tag{14.27c}$$

$$2\mathcal{N}\Delta = \left\langle \sum_{\mathbf{p},\nu} \left[\frac{\alpha_{\mathbf{p}} + \alpha_{\mathbf{p}+\mathbf{Q}}}{2} \widetilde{f}^\dagger_{\nu,\mathbf{p},\uparrow} \widetilde{f}^\dagger_{\nu,-\mathbf{p},\downarrow} + \frac{\alpha_{\mathbf{p}} - \alpha_{\mathbf{p}+\mathbf{Q}}}{2} \widetilde{f}^\dagger_{\nu,\mathbf{p},\uparrow} \widetilde{f}^\dagger_{\bar{\nu},-\mathbf{p},\downarrow} + \text{h.c.} \right] \right\rangle , \tag{14.27d}$$

$$M_s = \frac{1}{2\mathcal{N}} \left\langle \sum_{\mathbf{p},\sigma,} \left(\widetilde{f}^\dagger_{A,\mathbf{p},\sigma} \widetilde{f}_{A,\mathbf{p},\bar{\sigma}} - \widetilde{f}^\dagger_{B,\mathbf{p},\sigma} \widetilde{f}_{B,\mathbf{p},\bar{\sigma}} \right) \right\rangle , \tag{14.27e}$$

$$M_u = \frac{1}{2\mathcal{N}} \left\langle \sum_{\mathbf{p},\sigma,\nu} \sigma \widetilde{f}^\dagger_{\nu,\mathbf{p},\sigma} \widetilde{f}_{\nu,\mathbf{p},\sigma} \right\rangle . \tag{14.27f}$$

The eigenvalues of the 16×16 matrix $\hat{A}_{\mathbf{p}}$ are not accessible analytically. In the next section results from a self-consistent numerical solution of the mean-field equations are presented based on a numerical diagonalization of the Hamiltonian.

14.3.2 Phase diagrams

The phase diagrams are extracted from the fully self-consistent numerical solution of the mean-field equations (14.27). The required eigenvalues of $\hat{A}_{\mathbf{p}}$ are determined via exact diagonalization for a grid of vectors $\mathbf{p}$ in the magnetic Brillouin zone implemented by a LAPACK routine.

We focus on a specific choice for the hybridization symmetry, namely a $\mathrm{d}_{x^2-y^2}$-wave hybridization, and combine it with a d_{xy} superconducting pairing, which favors the emergence of a large superconducting phase, see Sec. 14.2.2. Since the Heisenberg interaction does not have a $\mathbf{k}$-space structure, the competition between the antiferromagnetic phase with the superconducting and Kondo phase is not expected to crucially depend on their $\mathbf{k}$ space symmetry. The parameter x, the balancing factor introduced in the decoupling of the Heisenberg term, influences the effective Heisenberg interaction in the magnetic channel tuning the ground state of the system. We therefore consider it as an input parameter to our theory. Numerical results are shown for $x = 0.3$, slightly favoring the superconducting instability, and are supplemented by a discussion on how the results are affected by different values of x.

Within this mean-field approach the phases are distinguished by the values of the parameters b, Δ and M_s. For zero staggered magnetization, $M_s = 0$, the phases are classified as in Sec. 14.2.1: a heavy Fermi liquid phase FL, a spin Fermi liquid FL*, a superconducting phase SC and a decoupled phase arise depending on the values of b and Δ. Theoretically, a nonzero M_s can coexist with all these phases. However, numerically we simply find a phase with $M_s \neq 0$ and $b = \Delta = 0$, which is denoted by AFM. An overview of the configuration of parameters in each phase is given by Table 14.1.

Numerical phase diagrams are depicted in Fig. 14.5: The ground state phase diagram (Fig. 14.5(a)) as a function of the applied magnetic field B and the Kondo coupling J_0 and

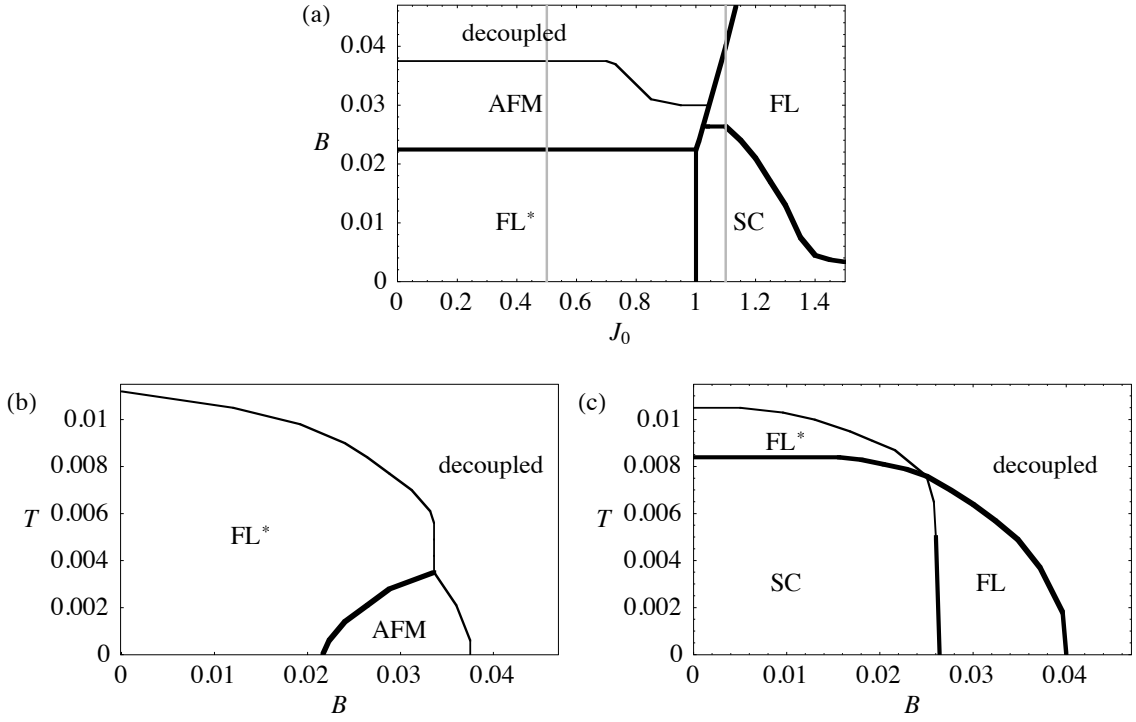

Figure 14.5: Mean-field phase diagram for a $d_{x^2-y^2}$-hybridization and a d_{xy} superconducting pairing in the presence of a Heisenberg term with the parameters $J_H = 0.05$, $x = 0.3$, $n_c = 0.3$ and $t = 1$. (a) Ground state phase diagram in dependence of magnetic field B and Kondo coupling J_0. (b,c) Temperature-field phase diagrams for $J_0 = 0.5$ and $J_0 = 1.1$, respectively, which are marked by a gray line in (a). Thick (thin) lines refer to first (second) order phase transitions.

two examples for temperature-field phase diagrams (Fig. 14.5(b) and (c)) for different Kondo couplings leading to FL* and a SC ground state. Please note that the uniform magnetization M_u is finite for non-zero field. The system becomes fully polarized ($M_u = 1/2$) in the decoupled phase at $B > 0$ and $T = 0$.

Upon tuning the balancing factor x the phase diagrams change. Let us focus on the ground state phase diagram as a function of magnetic field B and Kondo coupling J_0. Increasing the value of x enlarges the AFM phase suppressing the FL* phase. The SC phase shrinks in favor of the FL phase. The phase diagram for $x = 0.5$ depicted in Fig. 14.6 already shows a complete suppression of the FL* phase and a first-order phase transition between AFM and SC down to $B = 0$.

14.3.3 Discussion

Depending on the relation of the couplings J_0/J_H and the balancing factor x between superconductivity and magnetic ordering the ground state of the mean-field system can be tuned modeling an ambient-pressure superconductor like $CeCoIn_5$ and $CeIrIn_5$ or antiferromagnet like $CeRhIn_5$.

	b	Δ	M_s
decoupled	0	0	0
FL	×	0	0
FL*	0	×	0
SC	×	×	0
AFM	0	0	×

Table 14.1: Parameter assignments for the phases occurring in the phase diagrams, Fig. 14.5. A cross denotes a finite value of the specific parameter.

If we consider e.g. the configuration with $J_{\mathrm{H}} = 0.05$ and $x = 0.5$ (Fig. 14.6), superconductivity and antiferromagnetism do not coexist, but are separated by a first order phase transition in mean-field theory, which is in contrast to the experimental situation in $CeRhIn_5$, where a coexistence region develops.

Within mean-field theory SC and FL phase are neither separated by an AFM phase, nor a suppression of the AFM in favor of the SC phase is observable. As expected for a Pauli-limited superconductor in a magnetic field, whose pair breaking is determined by spin and not orbital pair breaking effects, the phase transition between SC and FL phase is of first order in the low-temperature range (Maki, 1966), see Fig. 14.5(c). Therefore, this mean-field approach is not sufficient to explain the emergence of a quantum critical point at the breakdown of superconductivity in $CeCoIn_5$ and support the picture of a suppressed magnetic phase producing the quantum criticality.

In general, mean-field theory is a good approach to obtain analytical and numerical results in a non-pertubative regime. This work was able to illustrate the competition between Kondo screening and superconductivity based on the momentum space structure of the hybridization and the pairing function. A possible additional instability towards antiferromagnetism can be captured at the level of mean-field theory. However, concerning the phase competition between antiferromagnetism and superconductivity, it was shown that the presented mean-field approximation is too simplistic for describing the physics in the considered 115-materials.

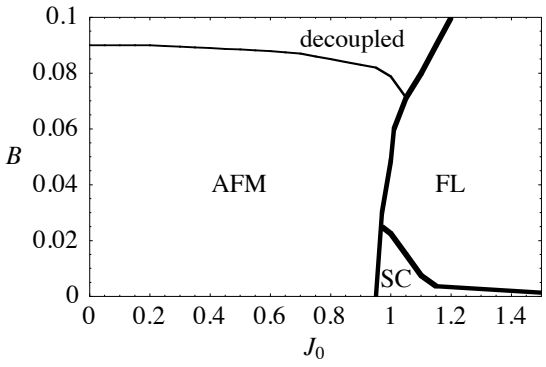

Figure 14.6: Ground state phase diagram as a function of magnetic field B and Kondo coupling J_0 acquired from mean-field theory for $d_{x^2-y^2}$-hybridization and d_{xy}-superconductivity with $x = 0.5$, $J_{\mathrm{H}} = 0.05$, $n_c = 0.3$ and $t = 1$. Thick (thin) lines refer to first (second) order phase transitions.

15 Conclusion

This part was concerned with the aspects arising from a non-local hybridization in a heavy fermion metal, studied in the framework of a large-N like mean-field approach. The focus was on two-dimensional systems, however the generalization to three-dimensional systems is straightforward

The low-temperature properties in the metallic Fermi liquid phase are determined by the strongly anisotropic band structure. Along the Fermi surface we can distinguish between regions with vanishing and strong hybridization, which directly influence the character of the quasiparticles: While quasiparticles in nodal direction are light and of c-character, the ones in antinodal direction are heavy and more f-like. In general, thermodynamic properties are dominated by the antinodal quasiparticles, transport is made by light nodal quasiparticles.

For a two-dimensional system, transport properties like thermal and electrical conductivity do not reflect the anisotropy of the system. The Wiedemann-Franz law is conserved. The optical conductivity in the Fermi liquid regime is sensitive on nodal lines crossing the Fermi surface: Spectral weight is shifted to lower frequencies and essentially fills the optical gap.

The momentum-dependence of the hybridization function has strong influence on the phase competition with unconventional superconductivity. For energies or temperatures well below the Kondo temperature T_{K}, pairing is dominated by antinodal quasiparticles favoring those pairing symmetries with large contributions in the antinodal regions. At $T \sim T_{\mathrm{K}}$ nodal quasiparticles are more susceptible to pairing. However, strong interaction effects and inelastic processes limit the applicability of mean-field theory.

Depending on the coupling strengths an instability towards an additional antiferromagnetic phase competes with Kondo screening and superconductivity. Experimentally observed coexistence regions of antiferromagnetic ordering and superconductivity cannot be recovered at the level of mean-field theory.

The suggested scenario is likely to be realized in the CeMIn$_5$ compound series or other heavy fermion compounds based on Ce or Yb with a similar gapless signature in the optical conductivity (Burch et al., 2007). For CeIrIn$_5$ microscopic considerations using a local density approximation in combination with DMFT (LDA+DMFT) support the existence of a momentum-dependent hybridization (Shim et al., 2007).

Ways to detect an anisotropic hybridization might e.g. be given by angle-resolved photoemission spectroscopy or X-ray absorption (Hansmann et al., 2008). Transport properties in two-dimensional systems stay isotropic even for an anisotropic hybridization. However, probing higher-order correlation functions, e.g. by measuring angle-dependent magnetoresistance, might reveal the system's anisotropy.

B Green functions

In this appendix, we list the expressions of Green functions required for the implementation of the mean-field theory.

B.1 Green functions for the Kondo lattice model

The Kondo-lattice mean-field Hamiltonian (10.10) can be rewritten in a matrix form:

$$\mathcal{H}_{\mathrm{KLM,MF}} = \sum_{\mathbf{k}\sigma} \Psi^{\dagger}_{\mathbf{k}} \underbrace{\begin{pmatrix} \bar{\epsilon}_{\mathbf{k}} & b\beta_{\mathbf{k}} \\ b\beta_{\mathbf{k}} & -\lambda_0 \end{pmatrix}}_{\hat{H}_{\mathbf{k}}} \Psi_{\mathbf{k}} + \mathrm{const.} \tag{B.1}$$

with $\Psi_{\mathbf{k}} = \left(c_{\mathbf{k}\sigma}, \widetilde{f}_{\mathbf{k}\sigma}\right)^T$. In the following, we shall denote retarded Green functions

$$\hat{G}_{AB}(z) = \int_0^{\infty} \mathrm{d}t e^{\mathrm{i}zt} \left(-\mathrm{i}\theta(t)\langle[\hat{A}(t), \hat{B}(0)]_+\rangle\right) \tag{B.2}$$

as $\langle\langle \hat{A}; \hat{B}\rangle\rangle_z$. Defining the matrix propagator

$$\hat{G}(\mathbf{k}, z) = \langle\langle \hat{\Psi}^{\dagger}_{\mathbf{k}}; \hat{\Psi}_{\mathbf{k}}\rangle\rangle = \left(z - \hat{H}_{\mathbf{k}}\right)^{-1}, \tag{B.3}$$

we obtain by explicit inversion

$$\begin{aligned} \hat{G}(\mathbf{k}, z) &= \begin{pmatrix} \langle\langle c^{\dagger}_{\mathbf{k}\sigma}; c_{\mathbf{k}\sigma}\rangle\rangle_z & \langle\langle c^{\dagger}_{\mathbf{k}\sigma}; \widetilde{f}_{\mathbf{k}\sigma}\rangle\rangle_z \\ \langle\langle \widetilde{f}^{\dagger}_{\mathbf{k}\sigma}; c_{\mathbf{k}\sigma}\rangle\rangle_z & \langle\langle \widetilde{f}^{\dagger}_{\mathbf{k}\sigma}; \widetilde{f}_{\mathbf{k}\sigma}\rangle\rangle_z \end{pmatrix} \\ &= \frac{1}{(z - z_{1\mathbf{k}})(z - z_{2\mathbf{k}})} \begin{pmatrix} z + \lambda_0 & b\beta_{\mathbf{k}} \\ b\beta_{\mathbf{k}} & z - \bar{\epsilon}_{\mathbf{k}} \end{pmatrix}. \end{aligned} \tag{B.4}$$

The thermal expectation values required for the mean-field equation are obtained by summing over Matsubara frequencies; this can be done analytically, since the excitation energies, Eq. (11.4), are known.

B.2 Green functions in the presence of a Heisenberg term

The Hamiltonian containing the additional Heisenberg term, Eq. (14.1), has to be rewritten in a matrix form in analogy to Appendix B.1. The inversion of $(z - \hat{H}_{\mathbf{k}})$ provides the needed

Green functions. We use the shorthand $h(\mathbf{k}, z) = \prod_i (z - \bar{z}_{\mathbf{k},i})$ with $\bar{z}_{\mathbf{k},i}$ given by Eq. (14.10).

$$\langle\langle \widetilde{f}^{\dagger}_{\mathbf{k}\uparrow}; \widetilde{f}_{\mathbf{k}\uparrow}\rangle\rangle_z = \frac{(z-\bar{\epsilon}_{\mathbf{k}})((z-\lambda_0)(z+\bar{\epsilon}_{\mathbf{k}}) - b^2\gamma_k^2)}{h(\mathbf{k}, z)}\,, \tag{B.5a}$$

$$\langle\langle \widetilde{f}_{-\mathbf{k}\downarrow}; \widetilde{f}^{\dagger}_{-\mathbf{k}\downarrow}\rangle\rangle_z = \frac{(z+\bar{\epsilon}_{\mathbf{k}})((z+\lambda_0)(z-\bar{\epsilon}_{\mathbf{k}}) - b^2\gamma_k^2)}{h(\mathbf{k}, z)}\,, \tag{B.5b}$$

$$\langle\langle \widetilde{f}^{\dagger}_{\mathbf{k}\uparrow}; \widetilde{f}^{\dagger}_{-\mathbf{k}\downarrow}\rangle\rangle_z = \langle\langle \widetilde{f}_{-\mathbf{k}\downarrow}; \widetilde{f}_{\mathbf{k}\uparrow}\rangle\rangle_z = \frac{\widetilde{W}_{\mathbf{k}}(z^2 - \bar{\epsilon}_{\mathbf{k}}^2)}{h(\mathbf{k}, z)}\,, \tag{B.5c}$$

$$\langle\langle c^{\dagger}_{\mathbf{k}\uparrow}; c^{\dagger}_{-\mathbf{k}\downarrow}\rangle\rangle_z = \langle\langle c_{-\mathbf{k}\downarrow}; c_{\mathbf{k}\uparrow}\rangle\rangle_z = -\frac{\widetilde{W}_{\mathbf{k}} b^2 \beta_{\mathbf{k}}^2}{h(\mathbf{k}, z)}\,, \tag{B.5d}$$

$$\langle\langle c^{\dagger}_{\mathbf{k}\uparrow}; \widetilde{f}_{\mathbf{k}\uparrow}\rangle\rangle_z = \langle\langle \widetilde{f}^{\dagger}_{\mathbf{k}\uparrow}; c_{\mathbf{k}\uparrow}\rangle\rangle_z = \frac{b\beta_{\mathbf{k}}((z-\lambda_0)(z+\bar{\epsilon}_{\mathbf{k}}) - b^2\beta_{\mathbf{k}}^2)}{h(\mathbf{k}, z)}\,, \tag{B.5e}$$

$$\langle\langle \widetilde{f}_{-\mathbf{k}\downarrow}; c^{\dagger}_{-\mathbf{k}\downarrow}\rangle\rangle_z = \langle\langle c_{-\mathbf{k}\downarrow}; \widetilde{f}^{\dagger}_{-\mathbf{k}\downarrow}\rangle\rangle_z = \frac{-b\beta_{\mathbf{k}}((z+\lambda_0)(z-\bar{\epsilon}_{\mathbf{k}}) - b^2\beta_{\mathbf{k}}^2)}{h(\mathbf{k}, z)}\,, \tag{B.5f}$$

$$\langle\langle c^{\dagger}_{\mathbf{k}\uparrow}; c_{\mathbf{k}\uparrow}\rangle\rangle_z = \frac{-b^2\beta_{\mathbf{k}}^2(z+\lambda_0) + (z+\bar{\epsilon}_{\mathbf{k}})(z^2 - \widetilde{W}_{\mathbf{k}}^2 - \lambda_0^2)}{h(\mathbf{k}, z)}\,, \tag{B.5g}$$

$$\langle\langle c_{-\mathbf{k}\downarrow}; c^{\dagger}_{-\mathbf{k}\downarrow}\rangle\rangle_z = \frac{-b^2\beta_{\mathbf{k}}^2(z-\lambda_0) + (z-\bar{\epsilon}_{\mathbf{k}})(z^2 - \widetilde{W}_{\mathbf{k}}^2 - \lambda_0^2)}{h(\mathbf{k}, z)}\,. \tag{B.5h}$$

C Specific heat at low T

The specific heat in the framework of the mean-field theory is defined by

$$C_V = -T\frac{d^2\mathcal{F}[T,b,\mu,\lambda_0]}{dT^2}\,, \tag{C.1}$$

where the free energy $\mathcal{F}$ is given by Eq. (11.5). In this appendix we show that the occurring temperature derivatives can approximately be substituted by partial derivatives in the low-temperature limit.

The first derivative by T is equivalent to a partial derivative,

$$C_V = -T\frac{d}{dT}\left(\frac{d\mathcal{F}[T,b,\mu,\lambda_0]}{dT}\right) = -T\frac{d}{dT}\left(\frac{\partial\mathcal{F}[T,b,\mu,\lambda_0]}{\partial T}\right)\,, \tag{C.2}$$

because the partial derivatives by the mean-field parameters vanish at the saddle point, e.g. $\partial\mathcal{F}/\partial b \equiv 0$. The specific heat can be explicitly written as

$$C_V = -T\left[\frac{\partial^2\mathcal{F}}{\partial T^2} + \frac{\partial b}{\partial T}\left(\frac{\partial}{\partial b}\left(\frac{\partial\mathcal{F}}{\partial T}\right)\right) + \frac{\partial\mu}{\partial T}\left(\frac{\partial}{\partial\mu}\left(\frac{\partial\mathcal{F}}{\partial T}\right)\right) + \frac{\partial\lambda_0}{\partial T}\left(\frac{\partial}{\partial\lambda_0}\left(\frac{\partial\mathcal{F}}{\partial T}\right)\right)\right]\,. \tag{C.3}$$

In the following we focus on the second term,

$$\Delta C_V^{(b)} = -T\frac{\partial b}{\partial T}\left(\frac{\partial}{\partial b}\left(\frac{\partial\mathcal{F}}{\partial T}\right)\right)\,, \tag{C.4}$$

which contains corrections in the specific heat arising from the temperature dependence of b. The third and the fourth term behave in an analogous fashion.

While the temperature derivative of the mean-field parameter is linear in T,

$$\frac{\partial b}{\partial T} = -\frac{2b_0}{T_{\mathrm{coh}}^2}T\,, \tag{C.5}$$

the expression

$$\frac{\partial}{\partial b}\left(\frac{\partial\mathcal{F}}{\partial T}\right) = -\sum_{\alpha=1,2}\sum_{\mathbf{k}} n_F'(z_{\alpha\mathbf{k}})\frac{\partial z_{\alpha\mathbf{k}}}{\partial b}\,, \tag{C.6}$$

with the Fermi function $n_F(x) = (1+\exp(x/T))^{-1}$ is of the order $\mathcal{O}(1)$ for $T\to 0$. Therefore, the correction

$$\Delta C_V^{(b)} \sim T^2\,, \tag{C.7}$$

can be neglected in the low-temperature limit and we can approximate

$$C_V \approx -T\frac{\partial^2\mathcal{F}[T,b,\mu,\lambda_0]}{\partial T^2}\,. \tag{C.8}$$

D Optical conductivity

D.1 Current operator

The polarization operator within the ALM mean-field description, given by Eq. (11.25) is rewritten by using the Fourier transforms of the contained operators according to $a_i = 1/\sqrt{\mathcal{N}} \sum_{\mathbf{k}} e^{-\mathrm{i}\mathbf{k}\mathbf{R}_i} a_{\mathbf{k}}$:

$$\mathbf{P}_{\mathrm{MF}} = \frac{1}{\mathcal{N}} \sum_{i,\sigma',\mathbf{k}',\mathbf{k}''} \mathbf{R}_i e^{\mathrm{i}(\mathbf{k}'-\mathbf{k}'')\mathbf{R}_i} \left(c^\dagger_{\mathbf{k}'\sigma'} c_{\mathbf{k}''\sigma'} + \bar{f}^\dagger_{\mathbf{k}'\sigma'} \bar{f}_{\mathbf{k}''\sigma'} \right) . \tag{D.1}$$

Simplified with the commutation relations

$$\left[c^\dagger_{\mathbf{k}\sigma} c_{\mathbf{k}\sigma}, c^\dagger_{\mathbf{k}'\sigma'} c_{\mathbf{k}''\sigma'} \right] = c^\dagger_{\mathbf{k}\sigma} c_{\mathbf{k}''\sigma} \delta_{\mathbf{k},\mathbf{k}'} \delta\sigma\sigma' - c^\dagger_{\mathbf{k}'\sigma} c_{\mathbf{k}\sigma} \delta_{\mathbf{k},\mathbf{k}''} \delta\sigma\sigma' , \tag{D.2}$$

$$\left[c^\dagger_{\mathbf{k}\sigma} \bar{f}_{\mathbf{k}\sigma}, \bar{f}^\dagger_{\mathbf{k}'\sigma'} \bar{f}_{\mathbf{k}''\sigma'} \right] = c^\dagger_{\mathbf{k}\sigma} \bar{f}_{\mathbf{k}''\sigma} \delta_{\mathbf{k},\mathbf{k}'} \delta\sigma\sigma' , \tag{D.3}$$

$$\left[\bar{f}^\dagger_{\mathbf{k}\sigma} c_{\mathbf{k}\sigma}, \bar{f}^\dagger_{\mathbf{k}'\sigma'} \bar{f}_{\mathbf{k}''\sigma'} \right] = -\bar{f}^\dagger_{\mathbf{k}'\sigma} c_{\mathbf{k}\sigma} \delta_{\mathbf{k},\mathbf{k}''} \delta\sigma\sigma' , \tag{D.4}$$

the mean-field current operator becomes

$$\begin{aligned} \mathbf{j}_{\mathrm{MF}} = \mathrm{i}\frac{1}{\mathcal{N}} \sum_{i,\sigma,\mathbf{k}',\mathbf{k}''} \mathbf{R}_i e^{\mathrm{i}(\mathbf{k}'-\mathbf{k}'')\mathbf{R}_i} \Big(\Big(\epsilon_{\mathbf{k}'} - \epsilon_{\mathbf{k}''} \Big) c^\dagger_{\mathbf{k}'\sigma} c_{\mathbf{k}''\sigma} + \\ + r \left(-V_{\mathbf{k}''} \left(\bar{f}^\dagger_{\mathbf{k}'\sigma} c_{\mathbf{k}''\sigma} + c^\dagger_{\mathbf{k}'\sigma} \bar{f}_{\mathbf{k}''\sigma} \right) + V_{\mathbf{k}'} \left(\bar{f}^\dagger_{\mathbf{k}'\sigma} c_{\mathbf{k}''\sigma} + c^\dagger_{\mathbf{k}'\sigma} \bar{f}_{\mathbf{k}''\sigma} \right) \right) \Big) . \end{aligned} \tag{D.5}$$

We substitute the momentum $\mathbf{k}''$ by $\mathbf{p} = \mathbf{k}' - \mathbf{k}''$ and exploit the relation $\sum_i \mathbf{R}_i e^{\mathrm{i}\mathbf{k}\mathbf{R}_i} = \mathcal{N}\mathrm{i}\delta'(\mathbf{k})$:

$$\begin{aligned} \mathbf{j}_{\mathrm{MF}} = \sum_{\mathbf{k}',\mathbf{p},\sigma} \delta'(\mathbf{p}) \Big(\Big(\epsilon_{\mathbf{k}'} - \epsilon_{\mathbf{k}'-\mathbf{p}} \Big) c^\dagger_{\mathbf{k}'\sigma} c_{\mathbf{k}'-\mathbf{p}\sigma} + \\ + r \left(-V_{\mathbf{k}'-\mathbf{p}} \left(\bar{f}^\dagger_{\mathbf{k}'\sigma} c_{\mathbf{k}'-\mathbf{p}\sigma} + c^\dagger_{\mathbf{k}'\sigma} \bar{f}_{\mathbf{k}'-\mathbf{p}\sigma} \right) + V_{\mathbf{k}'} \left(\bar{f}^\dagger_{\mathbf{k}'\sigma} c_{\mathbf{k}'-\mathbf{p}\sigma} + c^\dagger_{\mathbf{k}'\sigma} \bar{f}_{\mathbf{k}'-\mathbf{p}\sigma} \right) \right) \Big) . \end{aligned} \tag{D.6}$$

The δ-function derivative is replaced by using a discretized version of the relation $\int_{x-a}^{x+a} dt \delta'(t-x) F(t) = -F'(x)$:

$$\sum_{\mathbf{p}} \delta'(\mathbf{p}) F(\mathbf{p}) = -\sum_{\mathbf{p}} \delta_{\mathbf{p},0} \nabla_{\mathbf{p}} F(\mathbf{p}). \tag{D.7}$$

The mean-field current operator becomes

$$\begin{aligned} \mathbf{j}_{\mathrm{MF}} &= \sum_{\mathbf{k}',\mathbf{p},\sigma} \delta_{\mathbf{p},0} \left(\left(-\nabla_{\mathbf{p}} \epsilon_{\mathbf{k}'-\mathbf{p}} \right) c^\dagger_{\mathbf{k}'\sigma} c_{\mathbf{k}'-\mathbf{p}\sigma} + r \left(-\nabla_{\mathbf{p}} V_{\mathbf{k}'-\mathbf{p}} \right) \left(\bar{f}^\dagger_{\mathbf{k}'\sigma} c_{\mathbf{k}'-\mathbf{p}\sigma} + c^\dagger_{\mathbf{k}'\sigma} \bar{f}_{\mathbf{k}'-\mathbf{p}\sigma} \right) \right) \\ &= \sum_{\mathbf{k}\sigma} \left(\nabla_{\mathbf{k}} \epsilon_{\mathbf{k}} c^\dagger_{\mathbf{k}\sigma} c_{\mathbf{k}\sigma} + r \nabla_{\mathbf{k}} V_{\mathbf{k}} (c^\dagger_{\mathbf{k}\sigma} \bar{f}_{\mathbf{k}\sigma} + \bar{f}^\dagger_{\mathbf{k}\sigma} c_{\mathbf{k}\sigma}) \right) . \end{aligned} \tag{D.8}$$

D.2 Current-current correlation function

Within the mean-field approximation the system consists of non-interacting particles. Therefore, the current-current correlation function, defined by Eq. (11.21), reduces to the bare bubble diagram containing mean-field propagators and a current vertex given by $\mathbf{j}_{\mathrm{MF}}$, Eq. (11.26).

Four-operator expectation values occurring in $\Pi(\mathrm{i}\omega)$ are simplified with the Wick theorem, e.g.

$$\left\langle T_\tau \left(\bar{f}^\dagger_{\mathbf{k}\sigma} c_{\mathbf{k}\sigma} \right)(\tau) \left(\bar{f}^\dagger_{\mathbf{k}'\sigma'} c_{\mathbf{k}'\sigma'} \right)(0) \right\rangle = \delta_{\mathbf{k}\mathbf{k}'} \delta_{\sigma\sigma'} \mathcal{G}_{\bar{f}c}(\mathbf{k}, -\tau) \mathcal{G}_{c\bar{f}}(\mathbf{k}, \tau) \,. \tag{D.9}$$

$\Pi(\mathrm{i}\omega_n)$ can be split into

$$\Pi^{(ij)}(\mathrm{i}\omega_n) = \Pi_0^{(ij)}(\mathrm{i}\omega_n) + \Pi_{\mathrm{mixed}}^{(ij)}(\mathrm{i}\omega_n) + \Pi_{\mathrm{hybr}}^{(ij)}(\mathrm{i}\omega_n) \tag{D.10}$$

with

$$\Pi_0^{(ij)}(\mathrm{i}\omega_n) = -\frac{1}{\beta} \sum_{\mathbf{k}, \mathrm{i}k_n} \nabla\epsilon_{\mathbf{k}}^{(i)} \nabla\epsilon_{\mathbf{k}}^{(j)} \mathcal{G}_c(\mathbf{k}, \mathrm{i}k_n + \mathrm{i}\omega_n) \mathcal{G}_c(\mathbf{k}, \mathrm{i}k_n) \,, \tag{D.11a}$$

$$\begin{aligned} \Pi_{\mathrm{mixed}}^{(ij)}(\mathrm{i}\omega_n) = -\frac{1}{\beta} \sum_{\mathbf{k}, \mathrm{i}k_n} r \left(\nabla\epsilon_{\mathbf{k}}^{(i)} \nabla V_{\mathbf{k}}^{(j)} + \nabla\epsilon_{\mathbf{k}}^{(j)} \nabla V_{\mathbf{k}}^{(i)} \right) \cdot \\ \cdot \left[\mathcal{G}_{c\bar{f}}(\mathbf{k}, \mathrm{i}k_n + \mathrm{i}\omega_n) \mathcal{G}_c(\mathbf{k}, \mathrm{i}k_n) + \mathcal{G}_c(\mathbf{k}, \mathrm{i}k_n + \mathrm{i}\omega_n) \mathcal{G}_{c\bar{f}}(\mathbf{k}, \mathrm{i}k_n) \right] \,, \end{aligned} \tag{D.11b}$$

$$\begin{aligned} \Pi_{\mathrm{hybr}}^{(ij)}(\mathrm{i}\omega_n) = -\frac{1}{\beta} \sum_{\mathbf{k}, \mathrm{i}k_n} r^2 \nabla V_{\mathbf{k}}^{(i)} \nabla V_{\mathbf{k}}^{(j)} \left[2\mathcal{G}_{c\bar{f}}(\mathbf{k}, \mathrm{i}k_n + \mathrm{i}\omega_n) \mathcal{G}_{c\bar{f}}(\mathbf{k}, \mathrm{i}k_n) + \right. \\ \left. + \mathcal{G}_c(\mathbf{k}, \mathrm{i}k_n + \mathrm{i}\omega_n) \mathcal{G}_{\bar{f}}(\mathbf{k}, \mathrm{i}k_n) + \mathcal{G}_{\bar{f}}(\mathbf{k}, \mathrm{i}k_n + \mathrm{i}\omega_n) \mathcal{G}_c(\mathbf{k}, \mathrm{i}k_n) \right] \,. \end{aligned} \tag{D.11c}$$

The superscript (i) denotes the ith vector component. The Green functions are given in Appendix B.1 The Matsubara summation over $\mathrm{i}k_n$ is replaced by a Contour integral, which can easily be performed with the residue theorem. As we work in the low-temperature regime we neglect the thermal occupation of the upper band $z_{1\mathbf{k}}$. This is accomplished by setting $n_F(z_{1\mathbf{k}})$ to zero. Averaging over x- and y-direction by $\Pi(\mathrm{i}\omega_n) = 1/2 \sum_{i=x,y} \Pi^{(ii)}(\mathrm{i}\omega_n)$ leads to

$$\Pi_0(\mathrm{i}\omega_n) = \sum_{\mathbf{k}} (\nabla\epsilon_{\mathbf{k}})^2 \, n_F(z_{2\mathbf{k}}) \frac{(z_{2\mathbf{k}} - \widetilde{\epsilon}_f)(z_{1\mathbf{k}} - \widetilde{\epsilon}_f)}{2(z_{1\mathbf{k}} - z_{2\mathbf{k}})^2} \mathcal{F}(\mathbf{k}, \mathrm{i}\omega_n) \,, \tag{D.12a}$$

$$\Pi_{\mathrm{mixed}}(\mathrm{i}\omega_n) = 2r^2 \sum_{\mathbf{k}} V_{\mathbf{k}} \nabla\epsilon_{\mathbf{k}} \nabla V_{\mathbf{k}} n_F(z_{2\mathbf{k}}) \frac{z_{2\mathbf{k}} + z_{1\mathbf{k}} - 2\widetilde{\epsilon}_f}{2(z_{1\mathbf{k}} - z_{2\mathbf{k}})^2} \mathcal{F}(\mathbf{k}, \mathrm{i}\omega_n) \,, \tag{D.12b}$$

$$\Pi_{\mathrm{hybr}}(\mathrm{i}\omega_n) = r^2 \sum_{\mathbf{k}} (\nabla V_{\mathbf{k}})^2 \, n_F(z_{2\mathbf{k}}) \frac{(z_{1\mathbf{k}} - z_{2\mathbf{k}})^2 + 4r^2 V_{\mathbf{k}}^2}{2(z_{1\mathbf{k}} - z_{2\mathbf{k}})^2} \mathcal{F}(\mathbf{k}, \mathrm{i}\omega_n) \,, \tag{D.12c}$$

where the abbreviations $\widetilde{\epsilon}_f = \epsilon_f - \lambda$ and $\mathcal{F}(\mathbf{k}, \mathrm{i}\omega_n) = \left(\frac{1}{\mathrm{i}\omega_n - (z_{1\mathbf{k}} - z_{2\mathbf{k}})} - \frac{1}{\mathrm{i}\omega_n + (z_{1\mathbf{k}} - z_{2\mathbf{k}})} \right)$ are used. The real part of the optical conductivity is

$$\sigma_1(\omega) = \frac{\pi}{\omega} \sum_{\mathbf{k}} \frac{n_F(z_{2\mathbf{k}})}{2(z_{1\mathbf{k}} - z_{2\mathbf{k}})^2} A_{\mathbf{k}} \delta(\omega - (z_{1\mathbf{k}} - z_{2\mathbf{k}})) \tag{D.13}$$

with

$$A_{\mathbf{k}} = (\nabla_{\mathbf{k}}\epsilon_{\mathbf{k}})^2 (z_{2\mathbf{k}} - \widetilde{\epsilon}_f)(z_{1\mathbf{k}} - \widetilde{\epsilon}_f) + r^2 (\nabla_{\mathbf{k}} V_{\mathbf{k}})^2 \left((z_{1\mathbf{k}} - z_{2\mathbf{k}}) + 4r^2 V_{\mathbf{k}}^2\right) + \\ + 2r^2 V_{\mathbf{k}} \nabla\epsilon_{\mathbf{k}} \nabla V_{\mathbf{k}} (z_{2\mathbf{k}} + z_{1\mathbf{k}} - 2\widetilde{\epsilon}_f)\,. \tag{D.14}$$

D.3 Behavior of σ_1 in the vicinity of the gap

This section is concerned with an estimate for the behavior of the real part of the optical conductivity σ_1 near the optical gap at $\omega = -\lambda_0$ for a $\mathrm{d}_{x^2-y^2}$-wave hybridization. It is dominated by the δ-function in Eq. (D.13),

$$\delta\left(\omega - \underbrace{\sqrt{(\lambda_0 + \bar{\epsilon}_{\mathbf{k}})^2 + 4b^2\beta_{\mathbf{k}}^2}}_{\Delta E(k_x, k_y)}\right), \tag{D.15}$$

while the non-singular matrix elements only have influence on the prefactor without changing the general behavior.

A change of variables to

$$\widetilde{k}_x = \frac{1}{\sqrt{2}}(k_x + k_y - 2k_0) \tag{D.16a}$$

$$\widetilde{k}_y = \frac{1}{\sqrt{2}}(-k_x + k_y) \tag{D.16b}$$

with k_0 determined by $\bar{\epsilon}(k_0, k_0) = 0$ is favorable here. For small values of $\omega + \lambda_0$ the function $\Delta E(\widetilde{k}_x, \widetilde{k}_y)$ can be approximated in a second-order Taylor expansion in $\widetilde{k}_x$ and $\widetilde{k}_y$ around 0,

$$\Delta E(\widetilde{k}_x, \widetilde{k}_y) \approx -\lambda_0 - \sqrt{8t^2 - \frac{\mu^2}{2}}\widetilde{k}_x + \frac{\mu}{4}\widetilde{k}_x^2 + \frac{\lambda_0\mu t^2 + b^2(\mu^2 - 16t^2)}{4\lambda_0 t}\widetilde{k}_y^2, \tag{D.17}$$

which allows to rewrite the δ function as

$$\delta(\omega - \Delta E(\widetilde{k}_x, \widetilde{k}_y)) = \frac{1}{|\partial_{\widetilde{k}_x}\Delta E(\widetilde{k}_x, \widetilde{k}_y|}\delta\left(\widetilde{k}_x - g(\widetilde{k}_y, \omega)\right) \tag{D.18}$$

where $g(\widetilde{k}_y, \omega)$ is implicitly determined by $\omega - \Delta E(g(\widetilde{k}_y, \omega), \widetilde{k}_y) = 0$.

We approximate

$$\sigma_1(\omega) \propto \frac{1}{\omega}\sum_{\mathbf{k}} n_F(z_{2\mathbf{k}})\delta(\omega - (z_{1\mathbf{k}} - z_{2\mathbf{k}}))\,. \tag{D.19}$$

The factor $n_F(z_{2\mathbf{k}})$ in σ_1 restricts the $\mathbf{k}$-summation to the Fermi sea. The integration boundaries given by the Fermi surface can as well be approximated by expanding around $\widetilde{k}_x$, $\widetilde{k}_y = 0$. The evaluation of this integral shows that the first non-vanishing contribution to the optical conductivity for a $\mathrm{d}_{x^2-y^2}$-wave hybridization is $\sim \sqrt{\omega + \lambda_0}$.

E Electrical conductivity

The electrical conductivity is given as the zero-frequency part of $\sigma^{(ij)}(\omega)$, which is defined by Eq. (11.20). In order to account for elastic scattering processes among the quasiparticles, the Green functions (11.29) are used for the calculation of the zero-frequency current-current correlation function. Due to the additional self-energy $\Sigma_{1,2}$ the Wick theorem is not applicable in this situation. We start this calculation with the expression for the current-current correlation function $\Pi^{(ij)}(\mathrm{i}\omega_n)$ in terms of the Green functions $\mathcal{G}_c$, $\mathcal{G}_{\bar{f}}$ and $\mathcal{G}_{\bar{f}c}$, given by Eqs. (D.10) and (D.11). These Green functions are related to the quasiparticle Green functions $\mathcal{G}_{1,2}$ via

$$\mathcal{G}_c = u_{\mathbf{k}}^2\mathcal{G}_1 + v_{\mathbf{k}}^2\mathcal{G}_2\,, \tag{E.1}$$
$$\mathcal{G}_f = v_{\mathbf{k}}^2\mathcal{G}_1 + u_{\mathbf{k}}^2\mathcal{G}_2\,, \tag{E.2}$$
$$\mathcal{G}_{\bar{f}c} = u_{\mathbf{k}}v_{\mathbf{k}}(\mathcal{G}_1 - \mathcal{G}_2)\,, \tag{E.3}$$
$$\mathcal{G}_{c\bar{f}} = v_{\mathbf{k}}u_{\mathbf{k}}(\mathcal{G}_1 - \mathcal{G}_2)\,. \tag{E.4}$$

The prefactors $u_{\mathbf{k}}$ and $v_{\mathbf{k}}$ originate in the Bogoliubov transformation

$$c_{\mathbf{k}} = u_{\mathbf{k}}\gamma_{1\mathbf{k}} + v_{\mathbf{k}}\gamma_{2\mathbf{k}}\,, \tag{E.5}$$
$$\bar{f}_{\mathbf{k}} = v_{\mathbf{k}}\gamma_{1\mathbf{k}} - u_{\mathbf{k}}\gamma_{2\mathbf{k}}\,, \tag{E.6}$$

and are defined by

$$u_{\mathbf{k}}^2 = \frac{(z_{2\mathbf{k}} - \widetilde{\epsilon}_f)^2}{V_{\mathbf{k}}^2 + (z_{2\mathbf{k}} - \widetilde{\epsilon}_f)^2}, \tag{E.7}$$
$$v_{\mathbf{k}}^2 = \frac{V_{\mathbf{k}}^2}{V_{\mathbf{k}}^2 + (z_{2\mathbf{k}} - \epsilon_{\mathbf{k}})^2}, \tag{E.8}$$
$$u_{\mathbf{k}} = -\frac{V_{\mathbf{k}}}{z_{1\mathbf{k}} - \epsilon_{\mathbf{k}}}v_{\mathbf{k}}. \tag{E.9}$$

The current-current correlation function can be written as

$$\Pi^{(ij)}(\mathrm{i}\omega_n) = -\frac{1}{\beta}\sum_{\mathbf{k},\mathrm{i}k_n}\sum_{\mu,\nu=1,2}\mathcal{G}_\mu(\mathbf{k},\mathrm{i}k_n + \mathrm{i}\omega_n)\mathcal{G}_\nu(\mathbf{k},\mathrm{i}k_n)\xi_{\mu\nu}^{(ij)}(\mathbf{k}) \tag{E.10}$$

with

$$\xi_{11}^{(ij)}(\mathbf{k}) = 4u_{\mathbf{k}}^2v_{\mathbf{k}}^2r^2\nabla V_{\mathbf{k}}^{(i)}\nabla V_{\mathbf{k}}^{(j)} + u_{\mathbf{k}}^4\nabla\epsilon_{\mathbf{k}}^{(i)}\nabla\epsilon_{\mathbf{k}}^{(j)} + 2u_{\mathbf{k}}^3v_{\mathbf{k}}r\left(\nabla V_{\mathbf{k}}^{(i)}\nabla\epsilon_{\mathbf{k}}^{(j)} + \nabla\epsilon_{\mathbf{k}}^{(i)}\nabla V_{\mathbf{k}}^{(j)}\right) \tag{E.11}$$

$$\xi_{12}^{(ij)}(\mathbf{k}) = \left(v_{\mathbf{k}}^2 - u_{\mathbf{k}}^2\right)^2r^2\nabla V_{\mathbf{k}}^{(i)}\nabla V_{\mathbf{k}}^{(j)} + u_{\mathbf{k}}^2v_{\mathbf{k}}^2\nabla\epsilon_{\mathbf{k}}^{(i)}\nabla\epsilon_{\mathbf{k}}^{(j)} + \tag{E.12}$$
$$+ u_{\mathbf{k}}v_{\mathbf{k}}(v_{\mathbf{k}}^2 - u_{\mathbf{k}}^2)r\left(\nabla V_{\mathbf{k}}^{(i)}\nabla\epsilon_{\mathbf{k}}^{(j)} + \nabla\epsilon_{\mathbf{k}}^{(i)}\nabla V_{\mathbf{k}}^{(j)}\right)$$

$$\xi_{22}^{(ij)}(\mathbf{k}) = 4u_{\mathbf{k}}^2v_{\mathbf{k}}^2r^2\nabla V_{\mathbf{k}}^{(i)}\nabla V_{\mathbf{k}}^{(j)} + v_{\mathbf{k}}^4\nabla\epsilon_{\mathbf{k}}^{(i)}\nabla\epsilon_{\mathbf{k}}^{(j)} - 2u_{\mathbf{k}}v_{\mathbf{k}}^3r\left(\nabla V_{\mathbf{k}}^{(i)}\nabla\epsilon_{\mathbf{k}}^{(j)} + \nabla\epsilon_{\mathbf{k}}^{(i)}\nabla V_{\mathbf{k}}^{(j)}\right) \tag{E.13}$$

and $\xi_{21}^{(ij)}(\mathbf{k}) = \xi_{12}^{(ij)}(\mathbf{k})$.

We introduce the abbreviation

$$A_{\mu\nu}(\mathbf{k}, \mathrm{i}\omega_n) = \frac{1}{\beta} \sum_{\mathrm{i}k_n} \mathcal{G}_\mu(\mathbf{k}, \mathrm{i}k_n) \mathcal{G}_\nu(\mathbf{k}, \mathrm{i}k_n + \mathrm{i}\omega_n) \tag{E.14}$$

and evaluate the contained Matsubara summation by integrating along the branch cut in the Contour integral. The self-energies $\Sigma_{1,2}$ prevent an evaluation with the residue theorem.

$$\begin{aligned} A_{\mu\nu}(\mathbf{k}, \mathrm{i}\omega_n) = -\int_{-\infty}^{\infty} \frac{d\epsilon}{2\pi\mathrm{i}} n_F(\epsilon) \{ &[\mathcal{G}_\mu(\epsilon + \mathrm{i}\eta) - \mathcal{G}_\mu(\epsilon - \mathrm{i}\eta)] \mathcal{G}_\nu(\epsilon + \mathrm{i}\omega_n) + \\ &+ \mathcal{G}_\mu(\epsilon - \mathrm{i}\omega_n) [\mathcal{G}_\nu(\epsilon + \mathrm{i}\eta) - \mathcal{G}_\nu(\epsilon - \mathrm{i}\eta)] \} \, . \end{aligned} \tag{E.15}$$

Substituting $\mathrm{i}\omega_n \to \omega + \mathrm{i}\eta$ and using the relation

$$\mathcal{G}(\epsilon + \mathrm{i}\eta) - \mathcal{G}(\epsilon - \mathrm{i}\eta) = 2\mathrm{i}\mathrm{Im}G^{\mathrm{ret}}(\epsilon) \tag{E.16}$$

leads to

$$\begin{aligned} A_{\mu\nu}(\mathbf{k}, \omega + \mathrm{i}\eta) = -\int_{-\infty}^{\infty} \frac{d\epsilon}{\pi} \big\{ &n_F(\epsilon) \mathrm{Im}G_\mu^{\mathrm{ret}}(\mathbf{k}, \epsilon) G_\nu^{\mathrm{ret}}(\mathbf{k}, \epsilon + \omega) + \\ &+ n_F(\epsilon + \omega) G_\mu^{\mathrm{av}}(\mathbf{k}, \epsilon) \mathrm{Im}G_\nu^{\mathrm{ret}}(\mathbf{k}, \epsilon + \omega) \big\} \, . \end{aligned} \tag{E.17}$$

The real part of the electrical conductivity is given by

$$\mathrm{Re}(\sigma^{(ij)}(\omega = 0)) = -\sum_{\mathbf{k}} \gamma_{\mu\nu}^{(ij)}(\mathbf{k}) \lim_{\omega \to 0} \frac{1}{\omega} \mathrm{Im}A_{\mu\nu}(\mathbf{k}, \omega + \mathrm{i}\eta) \, , \tag{E.18}$$

where in the zero-frequency limit we can write

$$\lim_{\omega \to 0} \frac{1}{\omega} \mathrm{Im}A_{\mu\nu}(\mathbf{k}, \omega + \mathrm{i}\eta) = \frac{1}{\beta} \int_{-\infty}^{\infty} \frac{d\epsilon}{2\pi} n_F'(\epsilon) \mathrm{Im}G_\mu^{\mathrm{ret}}(\mathbf{k}, \epsilon) \mathrm{Im}G_\nu^{\mathrm{ret}}(\mathbf{k}, \epsilon), \tag{E.19}$$

while exploiting the relation $\mathrm{Im}G^{\mathrm{av}}(\epsilon) = -\mathrm{Im}G^{\mathrm{ret}}(\epsilon)$ and

$$\lim_{\omega \to 0} (n_F(\epsilon + \omega) - n_F(\epsilon))/\omega = n_F'(\epsilon). \tag{E.20}$$

In relaxation-time approximation

$$\left(\mathrm{Im}G_\mu^{\mathrm{ret}}(\mathbf{k}, \epsilon)\right)^2 \to \frac{2\pi\delta(\epsilon - z_{\mu\mathbf{k}})}{\Gamma_\mu(\epsilon)}, \tag{E.21}$$

where the quasiparticle scattering rate fulfills the relation $\Gamma_\mu(\epsilon) = -\mathrm{Im}\Sigma_\mu(\epsilon)$.

The influence of the upper band $z_{1\mathbf{k}}$ will now be neglected and therefore the electrical conductivity tensor becomes

$$\mathrm{Re}(\sigma^{(ij)}(\omega = 0)) = -\sum_{\mathbf{k}\sigma} \frac{n_F'(z_{2\mathbf{k}})}{\Gamma(z_{2\mathbf{k}})} \xi_{22}^{(ij)}(\mathbf{k}) \, , \tag{E.22}$$

where we set $\Gamma = \Gamma_2$.

F Wiedemann-Franz law in isotropic Fermi liquid theory

Within this appendix we give a derivation of the Wiedemann-Franz law in the context of isotropic Fermi liquid theory. For a one-band system with elastic scattering the ratio between thermal and electrical conductivity becomes

$$\frac{\kappa_{ii}}{\sigma_{ii}T} = \frac{\sum_{\mathbf{k}} \left(\epsilon_{\mathbf{k}}^{QP}\right)^2 \left(\left(\nabla_{\mathbf{k}} \epsilon_{\mathbf{k}}^{QP}\right)^{(i)}\right)^2 n_F'(\epsilon_{\mathbf{k}}^{QP})/\Gamma(\epsilon_{\mathbf{k}}^{QP})}{T^2 \sum_{\mathbf{k}} \left(\left(\nabla_{\mathbf{k}} \epsilon_{\mathbf{k}}^{QP}\right)^{(i)}\right)^2 n_F'(\epsilon_{\mathbf{k}}^{QP})/\Gamma(\epsilon_{\mathbf{k}}^{QP})}\,. \tag{F.1}$$

The isotropic quasi-particle energy $\epsilon_{\mathbf{k}}^{QP}$ is approximated as

$$\epsilon_{\mathbf{k}}^{QP} = v_F(|\mathbf{k}| - k_F)\,. \tag{F.2}$$

The Fermi velocity $v_F = \left|\nabla_{\mathbf{k}} \epsilon_{\mathbf{k}}^{QP}\right|$ is a constant and the $\mathbf{k}$-summations occurring in Eq. (F.1) can be transformed into energy integrals. The density of states for the dispersion $\epsilon_{\mathbf{k}}^{QP}$ is constant in two dimensions and we can write

$$\frac{\kappa_{ii}}{\sigma_{ii}T} = \frac{\int \mathrm{d}\epsilon \epsilon^2 n_F'(\epsilon)/\Gamma(\epsilon)}{T^2 \int \mathrm{d}\epsilon n_F'(\epsilon)/\Gamma(\epsilon)}. \tag{F.3}$$

In order to show the temperature-independence of this ratio the T-dependence contained in the Fermi function $n_F(\epsilon) = (1 + \exp(\epsilon/(k_B T)))^{-1}$ is pulled out of the integral by substituting $\mathcal{E} = \epsilon/(k_B T)$. Under the assumption that the scattering rate Γ can be expressed by its leading polynomial contribution, the ratio reduces to a constant L

$$\frac{\kappa_{ii}}{\sigma_{ii}T} = \frac{k_B^2 \int \mathrm{d}\mathcal{E} \mathcal{E}^2 n_F'(\mathcal{E})/\Gamma(\mathcal{E})}{\int \mathrm{d}\epsilon n_F'(\mathcal{E})/\Gamma(\mathcal{E})} = L. \tag{F.4}$$

In the limit of constant scattering rate, L can be evaluated as

$$L_0 = \frac{\pi^2}{3}\left(\frac{k_B}{e}\right)^2. \tag{F.5}$$

Please note, that the electron charge e was set to 1 in previous calculations and is now reintroduced for consistency reasons.

G Calculation of observables with constrained slave particles

Given a Hamiltonian H containing a single impurity, whose degrees of freedom are parametrized by slave particles that have to fulfill the constraint $Q = 1$, where Q is the slave particle number, a diagrammatic expansion can be developed in the grand-canonical (GC) ensemble and the grand-canonical result can be connected to the result in the physical subspace obeying $Q = 1$ (Coleman, 1984).

The constraint is fixed by a Lagrange parameter λ acting like a chemical potential. The Hamiltonian can be written as $H' = H + \lambda Q$. Under the condition that the Hamiltonian H preserves the number of slave particles, the GC partition function can be written as a sum of canonical partition functions for each subspace:

$$Z_{GC} = \mathrm{Tr}\left[e^{-\beta(H+\lambda Q)}\right] = \sum_{Q=0}^{\infty} Z_C(Q) e^{-\beta\lambda Q}. \tag{G.1}$$

The canonical partition function in the physical subspace with $\{Q = 1\}$ can be expressed as

$$Z_C(Q = 1) = \lim_{\lambda\to\infty} \frac{\partial}{\partial\xi} Z_{GC}\,, \tag{G.2}$$

where $\xi = \exp(-\beta\lambda)$ is the fugacity.

In the GC ensemble the expectation values of the operator Q and the product OQ, where O is an arbitrary operator, read

$$\langle OQ\rangle_{GC} = \frac{\mathrm{Tr}\left[OQe^{-\beta(H+\lambda Q)}\right]}{\mathrm{Tr}\left[e^{-\beta(H+\lambda Q)}\right]}\,, \qquad \langle Q\rangle_{GC} = \frac{\mathrm{Tr}\left[Qe^{-\beta(H+\lambda Q)}\right]}{\mathrm{Tr}\left[e^{-\beta(H+\lambda Q)}\right]}, \tag{G.3}$$

which can be combined to

$$\frac{\langle OQ\rangle_{GC}}{\langle Q\rangle_{GC}} = \frac{\mathrm{Tr}\left[OQe^{-\beta(H+\lambda Q)}\right]}{\mathrm{Tr}\left[Qe^{-\beta(H+\lambda Q)}\right]}. \tag{G.4}$$

Taking the limit $\lambda \to \infty$ in the last expression, the numerator and denominator have to be considered separately. The contribution from the subspace with $Q = 0$ is zero, while terms of the order $\mathcal{O}(e^{-2\beta\lambda})$ vanish for $\lambda \to \infty$. Only the terms in $\{Q = 1\}$-subspace remain and we can identify the expectation value of O in the physical subspace as

$$\langle O\rangle_{\mathrm{phys}} = \frac{\mathrm{Tr}\left[Oe^{-\beta H}\right]_{Q=1}}{Z_C(Q = 1)} \tag{G.5}$$

with the described limit

$$\langle O \rangle_{\text{phys}} = \lim_{\lambda \to \infty} \frac{\langle OQ \rangle_{GC}}{\langle Q \rangle_{GC}}. \tag{G.6}$$

If $\langle O \rangle_{GC}$ vanishes in the subspace with $Q = 0$, this relation can be further simplified to

$$\langle O \rangle_{\text{phys}} = \left(\lim_{\lambda \to \infty} \right) \frac{\langle O \rangle_{GC}}{\langle Q \rangle_{GC}}. \tag{G.7}$$

The expression in the denominator can be calculated as

$$\langle Q \rangle_{GC} = \frac{\sum_{Q=0}^{\infty} Q e^{-\beta \lambda Q}}{\sum_{Q=0}^{\infty} e^{-\beta \lambda Q}} = \left(e^{-\beta \lambda} + \mathcal{O}(e^{-2\beta \lambda}) \right), \tag{G.8}$$

leading to

$$\langle O \rangle_{\text{phys}} = \lim_{\lambda \to \infty} e^{\beta \lambda} \langle O \rangle_{GC}. \tag{G.9}$$

H Mean-field Hamiltonian with magnetic ordering

In order to allow for antiferromagnetic ordering with the wave vector $\mathbf{Q} = (\pi, \pi)$, the considered unit cell consists of two lattice sites. This doubling of the unit cell is accounted for by introducing a new set of operators $c_{\mathbf{p}\nu}$ and $\widetilde{f}_{\mathbf{p}\nu}$, where $\nu = A, B$ is the sublattice index. In this appendix we present the rewriting of all terms of the mean-field Hamiltonian $\mathcal{H}_{\mathrm{KLM,MF}} + x\mathcal{H}_{\mathrm{H,AFM,MF}} + (1-x)\mathcal{H}_{\mathrm{H,SC,MF}} + \mathcal{H}_Z$ with respect to the new operators. The resulting Hamiltonian is compactly written in matrix form.

H.1 Rewriting

$\mathcal{H}_{\mathrm{H,AFM,MF}}$ (Eq. (14.19)) and $\mathcal{H}_Z$ (Eq. (14.18)) can be expressed in terms of the new operators in a straightforward way:

$$\begin{aligned}\mathcal{H}_{\mathrm{H,AFM,MF}} &= 2J_H \sum_{r,\sigma} \left[M_s \left(\widetilde{f}^\dagger_{A,r,\sigma} \widetilde{f}_{A,r,\bar{\sigma}} - \widetilde{f}^\dagger_{B,r,\sigma} \widetilde{f}_{B,r,\bar{\sigma}} \right) + M_u \sum_\nu \sigma \widetilde{f}^\dagger_{\nu,r,\sigma} \widetilde{f}_{\nu,r,\sigma} \right] + \\ &\qquad + 2J_H \mathcal{N}(M_s^2 - M_u^2) \qquad \text{(H.1)} \\ &= 2J_H \sum_{\mathbf{p},\sigma} \left[M_s \left(\widetilde{f}^\dagger_{A,\mathbf{p},\sigma} \widetilde{f}_{A,\mathbf{p},\bar{\sigma}} - \widetilde{f}^\dagger_{B,\mathbf{p},\sigma} \widetilde{f}_{B,\mathbf{p},\bar{\sigma}} \right) + M_u \sum_\nu \sigma \widetilde{f}^\dagger_{\nu,\mathbf{p},\sigma} \widetilde{f}_{\nu,\mathbf{p},\sigma} \right] + \\ &\qquad + 2J_H \mathcal{N}(M_s^2 - M_u^2) \qquad \text{(H.2)}\end{aligned}$$

and

$$\begin{aligned}\mathcal{H}_Z &= -\frac{B}{2} \sum_{r,\sigma,\nu} \sigma \left(c^\dagger_{\nu,r,\sigma} c_{\nu,r,\sigma} + \widetilde{f}^\dagger_{\nu,r,\sigma} \widetilde{f}_{\nu,r,\sigma} \right) \qquad \text{(H.3)} \\ &= -\frac{B}{2} \sum_{\mathbf{p},\sigma,\nu} \sigma \left(c^\dagger_{\nu,\mathbf{p},\sigma} c_{\nu,\mathbf{p},\sigma} + \widetilde{f}^\dagger_{\nu,\mathbf{p},\sigma} \widetilde{f}_{\nu,\mathbf{p},\sigma} \right) . \qquad \text{(H.4)}\end{aligned}$$

The index ν refers to the sublattice and r to the unit cell; $\mathbf{p}$ lies in the reduced Brillouin zone. For rewriting the other parts of the Hamiltonian, $\mathcal{H}_{\mathrm{KLM,MF}}$ (Eq. (10.10)) and $\mathcal{H}_{\mathrm{H,SC,MF}}$ (Eq. (14.6)), which are given as sums over operators in $\mathbf{k}$ space, the operators $c_{\mathbf{k}}$ and $\widetilde{f}_{\mathbf{k}}$ have to be rewritten in terms of $c_{\nu,\mathbf{p}}$ and $\widetilde{f}_{\nu,\mathbf{p}}$. First, a different set of operators is defined,

$$\bar{c}_{1,\mathbf{p}} = c_{\mathbf{p}} \qquad \text{and} \qquad \bar{c}_{2,\mathbf{p}} = c_{\mathbf{p}+\mathbf{Q}}, \qquad \text{(H.5)}$$

which evolve from $c_{\mathbf{k}}$ by backfolding the original to the reduced BZ with the vector $\mathbf{Q}$. Then they can be expressed as:

$$\begin{aligned}\bar{c}_{1,\mathbf{p}} \equiv c_{\mathbf{p}} &= \frac{1}{\sqrt{\mathcal{N}}}\sum_i e^{-\mathrm{i}\mathbf{p}\mathbf{R}_i} c_i = \frac{1}{\sqrt{\mathcal{N}}}\sum_r \left(e^{-i\mathbf{p}(\mathbf{R}_r+\mathbf{r}_A)} c_{A,r} + e^{-\mathrm{i}\mathbf{p}(\mathbf{R}_r+\mathbf{r}_B)} c_{B,r}\right) \\ &= \frac{1}{\sqrt{2}}\left(c_{A,\mathbf{p}} + c_{B,\mathbf{p}}\right), \end{aligned} \tag{H.6a}$$

$$\begin{aligned}\bar{c}_{2,\mathbf{p}} \equiv c_{\mathbf{p}+\mathbf{Q}} &= \frac{1}{\sqrt{\mathcal{N}}}\sum_i e^{-\mathrm{i}(\mathbf{p}+\mathbf{Q})\mathbf{R}_i} c_i = \frac{1}{\sqrt{\mathcal{N}}}\sum_r \left(e^{-\mathrm{i}(\mathbf{p}+\mathbf{Q})(\mathbf{R}_r+\mathbf{r}_A)} c_{A,r} + e^{-\mathrm{i}(\mathbf{p}+\mathbf{Q})(\mathbf{R}_r+\mathbf{r}_B)} c_{B,r}\right) \\ &= \frac{1}{\sqrt{2}}\left(c_{A,\mathbf{p}} - c_{B,\mathbf{p}}\right). \end{aligned} \tag{H.6b}$$

For $\widetilde{f}$ analogous expressions hold.

Using the relations (H.5) and (H.6), we can write

$$\begin{aligned}\mathcal{H}_{\mathrm{H,SC,MF}} = \sum_{\mathbf{p},\nu}\Bigg[&\frac{\widetilde{W}_{\mathbf{p}} + \widetilde{W}_{\mathbf{p}+\mathbf{Q}}}{2}\widetilde{f}^{\dagger}_{\nu,\mathbf{p},\uparrow}\widetilde{f}^{\dagger}_{\nu,-\mathbf{p},\downarrow} + \frac{\widetilde{W}_{\mathbf{p}} - \widetilde{W}_{\mathbf{p}+\mathbf{Q}}}{2}\widetilde{f}^{\dagger}_{\nu,\mathbf{p},\uparrow}\widetilde{f}^{\dagger}_{\bar{\nu},-\mathbf{p},\downarrow} + \mathrm{h.c.}\Bigg] + \\ &+ J_H\mathcal{N}\Delta^2, \end{aligned} \tag{H.7}$$

where $\widetilde{W}_{\mathbf{p}} = -J_{\mathrm{H}}\Delta\alpha_{\mathbf{p}}$ contains the symmetry of the superconducting pairing, and

$$\begin{aligned}\mathcal{H}_{\mathrm{KLM,MF}} = \sum_{\mathbf{p},\sigma,\nu}\Bigg\{&\left[\frac{\bar{\epsilon}_{\mathbf{p}} + \bar{\epsilon}_{\mathbf{p}+\mathbf{Q}}}{2} c^{\dagger}_{\nu,\mathbf{p},\sigma} c_{\nu,\mathbf{p},\sigma} + \frac{\bar{\epsilon}_{\mathbf{p}} - \bar{\epsilon}_{\mathbf{p}+\mathbf{Q}}}{2} c^{\dagger}_{\nu,\mathbf{p},\sigma} c_{\bar{\nu},\mathbf{p},\sigma}\right] - \lambda_0 \widetilde{f}^{\dagger}_{\nu,\mathbf{p},\sigma}\widetilde{f}_{\nu,\mathbf{p},\sigma} + \\ &+ \left[\frac{b(\beta_{\mathbf{p}} + \beta_{\mathbf{p}+\mathbf{Q}})}{2} c^{\dagger}_{\nu,\mathbf{p},\sigma}\widetilde{f}_{\nu,\mathbf{p},\sigma} + \frac{b(\beta_{\mathbf{p}} - \beta_{\mathbf{p}+\mathbf{Q}})}{2} c^{\dagger}_{\nu,\mathbf{p},\sigma}\widetilde{f}_{\bar{\nu},\mathbf{p},\sigma} + \mathrm{h.c.}\right]\Bigg\} + \\ &+ \mu\mathcal{N}n_c + \lambda_0\mathcal{N} + \mathcal{N}\frac{b^2}{J_0}. \end{aligned} \tag{H.8}$$

H.2 Matrix form

The complete Hamiltonian containing the parts Eqs. (H.2), (H.4), (H.7) and (H.8) is summarized to

$$\mathcal{H}_{\mathrm{MF}} = \frac{1}{2}\sum_{\mathbf{p}} \Psi^{\dagger}_{\mathbf{p}} \hat{A}_{\mathbf{p}} \Psi_{\mathbf{p}} + \mathrm{const.} \tag{H.9}$$

with

$$\hat{A}_{\mathbf{p}} = \begin{pmatrix} \hat{h}_{11\mathbf{p}} & \hat{h}_{12\mathbf{p}} \\ \hat{h}_{21\mathbf{p}} & \hat{h}_{22\mathbf{p}} \end{pmatrix}. \tag{H.10}$$

The off-diagonal elements are equal ($\hat{h}_{12\mathbf{p}} = \hat{h}_{21\mathbf{p}}$). The matrices read:

$$\hat{h}_{11\mathbf{p}} = \begin{pmatrix} -\mu - \frac{B}{2} & 0 & 0 & 0 & \bar{\epsilon}_{\mathbf{p}} & 0 & 0 & 0 \\ 0 & -\mu - \frac{B}{2} & 0 & 0 & 0 & \bar{\epsilon}_{\mathbf{p}} & 0 & 0 \\ 0 & 0 & \mu + \frac{B}{2} & 0 & 0 & 0 & -\bar{\epsilon}_{\mathbf{p}} & 0 \\ 0 & 0 & 0 & \mu + \frac{B}{2} & 0 & 0 & 0 & -\bar{\epsilon}_{\mathbf{p}} \\ \bar{\epsilon}_{\mathbf{p}} & 0 & 0 & 0 & -\mu - \frac{B}{2} & 0 & 0 & 0 \\ 0 & \bar{\epsilon}_{\mathbf{p}} & 0 & 0 & 0 & -\mu - \frac{B}{2} & 0 & 0 \\ 0 & 0 & -\bar{\epsilon}_{\mathbf{p}} & 0 & 0 & 0 & \mu + \frac{B}{2} & 0 \\ 0 & 0 & 0 & -\bar{\epsilon}_{\mathbf{p}} & 0 & 0 & 0 & \mu + \frac{B}{2} \end{pmatrix}, \tag{H.11}$$

$$\hat{h}_{12\mathbf{p}} = \begin{pmatrix} v^+_{\mathbf{p}} & 0 & 0 & 0 & v^-_{\mathbf{p}} & 0 & 0 & 0 \\ 0 & v^+_{\mathbf{p}} & 0 & 0 & 0 & v^-_{\mathbf{p}} & 0 & 0 \\ 0 & 0 & -v^+_{\mathbf{p}} & 0 & 0 & 0 & -v^-_{\mathbf{p}} & 0 \\ 0 & 0 & 0 & -v^+_{\mathbf{p}} & 0 & 0 & 0 & -v^-_{\mathbf{p}} \\ v^-_{\mathbf{p}} & 0 & 0 & 0 & v^+_{\mathbf{p}} & 0 & 0 & 0 \\ 0 & v^-_{\mathbf{p}} & 0 & 0 & 0 & v^+_{\mathbf{p}} & 0 & 0 \\ 0 & 0 & -v^-_{\mathbf{p}} & 0 & 0 & 0 & -v^+_{\mathbf{p}} & 0 \\ 0 & 0 & 0 & -v^-_{\mathbf{p}} & 0 & 0 & 0 & -v^+_{\mathbf{p}} \end{pmatrix}, \tag{H.12}$$

with the shorthand $v^{\pm}_{\mathbf{p}} = b(\beta_{\mathbf{p}} \pm \beta_{\mathbf{p}+\mathbf{Q}})/2$, and

$$\hat{h}_{22\mathbf{p}} = \begin{pmatrix} -\lambda_0 - m_u & -m_s & 0 & w^+_{\mathbf{p}} & 0 & 0 & 0 & w^-_{\mathbf{p}} \\ -m_s & -\lambda_0 + m_u & -w^+_{\mathbf{p}} & 0 & 0 & 0 & -w^-_{\mathbf{p}} & 0 \\ 0 & -w^+_{\mathbf{p}} & \lambda_0 + m_u & m_s & 0 & -w^-_{\mathbf{p}} & 0 & 0 \\ w^+_{\mathbf{p}} & 0 & m_s & \lambda_0 - m_u & w^-_{\mathbf{p}} & 0 & 0 & 0 \\ 0 & 0 & 0 & w^-_{\mathbf{p}} & -\lambda_0 - m_u & m_s & 0 & w^+_{\mathbf{p}} \\ 0 & 0 & -w^-_{\mathbf{p}} & 0 & m_s & -\lambda_0 + m_u & -w^+_{\mathbf{p}} & 0 \\ 0 & -w^-_{\mathbf{p}} & 0 & 0 & 0 & -w^+_{\mathbf{p}} & \lambda_0 + m_u & -m_s \\ w^-_{\mathbf{p}} & 0 & 0 & 0 & w^+_{\mathbf{p}} & 0 & -m_s & \lambda_0 - m_u \end{pmatrix}, \tag{H.13}$$

with $w^{\pm}_{\mathbf{p}} = (1-x)(\widetilde{W}_{\mathbf{p}} \pm \widetilde{W}_{\mathbf{p}+\mathbf{Q}})/2$, $m_s = 2xJ_{\mathrm{H}}M_s$ and $m_u = \frac{B}{2} - 2xJ_{\mathrm{H}}M_u$.

Bibliography: Heavy fermion compounds

Abrikosov, A. A. *Electron scattering on magnetic impurities in metals and anomalous resistivity effects.* Physics **2**, 5 (1965).

Anderson, P. W. *Antiferromagnetism. Theory of superexchange interaction.* Phys. Rev. **79**, 350–6 (1950).

Anderson, P. W. *Localized magnetic states in metals.* Phys. Rev. **124**, 41 (1961).

Anderson, P. W. *A poor man's derivation of scaling laws for the Kondo problem.* J. Phys. C: Solid St. Phys. **3**, 2436 (1970).

Andres, K., J. E. Graebner, and H. R. Ott. *4f-virtual-bound-state formation in $CeAl_3$ at low temperatures.* Phys. Rev. Lett. **35**, 1779 (1975).

Aubin, H., K. Behnia, M. Ribault, R. Gagnon, and L. Taillefer. *Angular position of nodes in the superconducting gap of YBCO.* Phys, Rev. Lett. **78**, 2624 (1997).

Beach, K. S. D. *Ground state properties of a Zeeman-split heavy metal.* arXiv:cond-mat/0509778 (2005).

Bianchi, A., R. Movshovich, C. Capan, P. G. Pagliuso, and J. L. Sarrao. *Possible Fulde-Ferrell-Larkin-Ovchinnikov superconducting state in $CeCoIn_5$.* Phys. Rev. Lett. **91**, 187 004 (2003).

Bianchi, A., R. Movshovich, N. Oeschler, P. Gegenwart, F. Steglich, J. D. Thompson, P. G. Pagliuso, and J. L. Sarrao. *First-order superconducting phase transition in $CeCoIn_5$.* Phys. Rev. Lett. **89**, 137 002 (2002).

Bulla, R. *Zero temperature metal-insulator transition in the infinite-dimensional Hubbard model.* Phys. Rev. Lett. **83**, 136 (1999).

Burch, K. S., S. V. Dordevic, F. P. Mena, D. van der Marel, J. L. Sarrao, J. R. Jeffries, E. D. Bauer, M. B. Maple, and D. N. Basov. *Optical signatures of momentum-dependent hybridization of the local moments and conduction electrons in Kondo lattices.* Phys. Rev. B **75**, 054 523 (2007).

Burdin, S. *Le réseau Kondo à basse température: du liquide de Fermi au liquide de spin.* Ph.D. thesis, Université Joseph Fourier-Grenoble (2001).

Burdin, S. *Low energy scales of Kondo lattices: mean-field perspective.* In *Proceedings of the NATO Advanced Research Workshop of Hvar, Croatia* (2008).

Burdin, S., A. Georges, and D. R. Grempel. *Coherence scale of the Kondo lattice.* Phys. Rev. Lett **85**, 1048 (2000).

Chen, G. F., K. Matsubayashi, S. Ban, K. Deguchi, and N. K. Sato. *Competitive coexistence of superconductivity with antiferromagnetism in $CeRhIn_5$.* Phys. Rev. Lett. **97**, 017 005 (2006).

Coleman, P. *New approach to the mixed-valence problem.* Phys. Rev. B **29**, 3035 (1984).

Coleman, P. *Handbook of magnetism and advanced magnetic materials*, volume 1, page 95. Wiley, New York (2007).

Coleman, P. and A. M. Tsvelik. *Local moments in an interacting environment.* Phys. Rev. B **57**, 12 757 (1998).

Coqblin, B. and J. R. Schrieffer. *Exchange interaction in alloys with Cerium impurities.* Phys. Rev. **185**, 847 (1969).

Cox, D. L. and A. Zawadowski. *Exotic Kondo effects in metals: Magnetic ions in a crystalline electric field and tunneling centers.* Taylor and Francis Inc. (1999).

Degiorgi, L. *The electrodynamic response of heavy-electron compounds.* Rev. Mod. Phys. **71**, 687 (1999).

Degiorgi, L., F. Anders, and G. Grüner. *Charge excitations in heavy electron metals.* Eur. Phys. J. B **19**, 167 (2001).

Doniach, S. *The Kondo lattice and weak antiferromagnetism.* Physica B **91**, 231 (1977).

Doniach, S. *Magnetic instability of a highly degenerate Kondo lattice.* Phys. Rev. B **35**, 1814 (1987).

Dordevic, S. V., D. N. Basov, N. R. Dilley, E. D. Bauer, and M. B. Maple. *Hybridization gap in heavy fermion compounds.* Phys. Rev. Lett. **86**, 684 (2001).

Dzero, M. and P. Coleman. *Superconductivity due to co-operative Kondo effect in Pu 115's.* Physica B **403**, 955 (2008).

Emery, V. J. and S. A. Kivelson. *Importance of phase fluctuations in superconductors with small superfluid density.* Nature **374**, 434 (1995).

Flouquet, J. *Progress in Low Temperature Physics, Edited by W. Halperin*, volume 15, chapter 2. Elsevier, Amsterdam (2005).

Franz, M. and A. J. Millis. *Phase fluctuations and spectral properties of underdoped cuprates.* Phys. Rev. B **58**, 14 572 (1998).

Fulde, P. and R. Ferrell. *Superconductivity in a strong spin-exchange field.* Phys. Rev. **135**, A550 (1964).

Georges, A., G. Kotliar, W. Krauth, and M. J. Rozenberg. *Dynamical mean-field theory of strongly correlated fermion systems and the limit of infinite dimensions.* Rev. Mod. Phys. **68**, 13 (1996).

Ghaemi, P. and T. Senthil. *Higher angular momentum Kondo liquids.* Phys. Rev. B **75**, 144 412 (2007).

Ghaemi, P., T. Senthil, and P. Coleman. *Angle dependent quasiparticle weights in correlated metals.* Phys. Rev. B **77**, 245 108 (2008).

Grenzebach, C., F. B. Anders, G. Czycholl, and T. Pruschke. *Transport properties of heavy-fermion systems.* Phys. Rev. B **74**, 195 119 (2006).

Grewe, N. and F. Steglich. *Handbook on the physics and chemistry of rare earths*, volume 14, page 343. Elsevier, Amsterdam (1991).

de Haas, W. J., J. H. de Boer, and G. J. van den Berg. *The electrical resistance of gold, copper and lead at low temperatures.* Physica **1**, 1115 (1934).

Hall, D., E. C. Palm, T. P. Murphy, S. W. Tozer, Z. Fisk, U. Alver, R. G. Goodrich, J. L. Sarrao, P. G. Pagliuso, and T. Ebihara. *Fermi surface of the heavy-fermion superconductor $CeCoIn_5$: The de Haas - van Alphen effect in the normal state.* Phys. Rev. B **64**, 212 508 (2001).

Hancock, J. N., T. McKnew, Z. Schlesinger, J. L. Sarrao, and Z. Fisk. *Kondo scaling in the optical response of $YbIn_{1-x}Ag_xCu_4$.* Phys. Rev. Lett. **92**, 186 405 (2004).

Hansmann, P., A. Severing, Z. Hu, M. W. Haverkort, C. F. Chang, S. Klein, A. Tanaka, H. H. Hsieh, H.-J. Lin, C. T. Chen, B. Fåk, P. Lejay, and L. H. Tjeng. *Determining the crystal-field ground state in rare earth heavy fermion materials using soft-X-ray absorption spectroscopy.* Phys. Rev. Lett. **100**, 066 405 (2008).

Hegger, H., C. Petrovic, E. G. Moshopoulou, M. F. Hundley, J. L. Sarrao, Z. Fisk, and J. D. Thompson. *Pressure-induced superconductivity in quasi-2D $CeRhIn_5$.* Phys. Rev. Lett. **84**, 4986 (2000).

Hewson, A. C. *The Kondo problem to heavy fermions.* Cambridge University Press, Cambridge (1997).

Ikeda, H. and K. Miyake. *A theory of anisotropic semiconductor of heavy fermions.* J. Phys. Soc. Jpn. **65**, 1769 (1996).

Izawa, K., H. Takahashi, H. Yamaguchi, Y. Matsuda, M. Suzuki, T. Sasaki, T. Fukase, Y. Yoshida, R. Settai, and Y. Onuki. *Superconducting gap structure of spin-triplet superconductor Sr_2RuO_4 studied by thermal conductivity.* Phys. Rev. Lett. **86**, 2653 (2001a).

Izawa, K., H. Yamaguchi, Y. Matsuda, H. Shishido, R. Settai, and Y. Onuki. *Angular position of nodes in the superconducting gap of quasi-2D heavy-fermion superconductor $CeCoIn_5$.* Phys. Rev. Lett. **87**, 057 002 (2001b).

Jarrell, M. *Symmetric periodic Anderson model in infinite dimensions.* Phys. Rev. B **51**, 7429 (1995).

Kasuya, T. *A theory of metallic ferro- and antiferromagnetism on Zener's model.* Prog. Theor. Phys. **16**, 45 (1956).

Kenzelmann, M., T. Strässle, C. Niedermayer, M. Sigrist, B. Padmanabhan, M. Zolliker, A. D. Bianchi, R. Movshovich, E. D. Bauer, J. L. Sarrao, and J. D. Thompson. *Coupled superconducting and magnetic order in $CeCoIn_5$.* Science **321**, 1652 (2008).

Knebel, G., D. Aoki, D. Braithwaite, B. Salce, and J. Flouquet. *Coexistence of antiferromagnetism and superconductivity in $CeRhIn_5$ under high pressure and magnetic eld.* Phys. Rev. B **74**, 020 501(R) (2006).

Kondo, J. *Resistance minimum in dilute magnetic alloys.* Prog. Theor. Phys. **32**, 37 (1964).

Kondo, J. *Resistance minimum and heavy fermions.* Proc. Jpn. Acad., Ser. B **82**, 328 (2006).

Lacroix, C. and M. Cyrot. *Phase diagram of the Kondo lattice.* Phys. Rev. B **20**, 1969 (1979).

Larkin, A. I. and Y. N. Ovchinnikov. *Inhomogeneous state of superconductors.* Sov. Phys. JETP **20**, 762 (1965).

von Löhneysen, H., A. Rosch, M. Vojta, and P. Wölfle. *Fermi-liquid instabilities at magnetic quantum phase transitions.* Rev. Mod. Phys. **79**, 1015 (2007).

Maehira, T., T. Hotta, K. Ueda, and A. Hasegawa. *Relativistic band-structure calculations for $CeTIn_5$ (T = Ir and Co) and analysis of the energy bands by using tight-binding method.* J. Phys. Soc. Jpn. **72**, 854 (2003).

Mahan, G. D. *Many-particle physics.* Plenum Press, New York (1990).

Maier, T., M. Jarrell, T. Pruschke, and M. H. Hettler. *Quantum cluster theories.* Rev. Mod. Phys. **77**, 1027 (2005).

Maki, K. *Effect of Pauli paramagnetism on magnetic properties of high-field superconductors.* Phys. Rev. **148**, 362 (1966).

Mena, F. P., D. van der Marel, and J. L. Sarrao. *Optical conductivity of $CeMIn_5$ (M = Co, Rh, Ir).* Phys. Rev. B **72**, 045 119 (2005).

Metzner, W. and D. Vollhardt. *Correlated lattice fermions in $d = \infty$ dimensions.* Phys. Rev. Lett. **62**, 324 (1989).

Millis, A. J. and P. A. Lee. *Large-orbital-degeneracy expansion for the lattice Anderson model.* Phys. Rev. B **35**, 3394 (1987).

Moreno, J. and P. Coleman. *Thermal currents in highly correlated systems.* arxiv:cond-mat/9603079 (1996).

Moreno, J. and P. Coleman. *Gap-anisotropic model for the narrow-gap Kondo insulators.* Phys. Rev. Lett. **84**, 342 (2000).

Nagaoka, Y. *Self-consistent treatment of Kondo's effect in dilute alloys.* Phys. Rev. **138**, A1112 (1965).

Nozières, P. *A "Fermi-liquid" description of the Kondo problem at low temperatures.* J. Low Temp. Phys. **17**, 31 (1974).

Nozières, P. *Impuretés magnétiques et effet Kondo.* Ann. de Phys. **10**, 19 (1985).

Nozières, P. *Kondo lattices and the Mott metal-insulator transition.* J. Phys. Soc. Jpn. **74**, 4 (2005).

Nozières, P. and A. Blandin. *Kondo effect in real metals.* J. Phys. France **41**, 193 (1980).

Okamura, H., T. Watanabe, M. Matsunami, T. Nishihara, N. Tsujii, T. Ebihara, H. Sugawara, H. Sato, Y. Onuki, Y. Isikawa, T. Takabatake, and T. Nanba. *Universal scaling in the dynamical conductivity of heavy fermion Ce and Yb compounds.* J. Phys. Soc. Jpn. **76**, 023 703 (2007).

Pagliuso, P., R. Movshovich, A. Bianchi, M. Nicklas, N. Moreno, J. Thompson, M. Hundley, J. Sarrao, and Z. Fisk. *Multiple phase transitions in Ce(Rh,Ir,Co)In_5.* Physica B **312-313**, 129 (2002).

Petrovic, C., R. Movshovich, M. Jaime, P. G. Pagliuso, M. F. Hundley, J. L. Sarrao, Z. Fisk, and J. D. Thompson. *A new heavy-fermion superconductor $CeIrIn_5$: A relative of the cuprates?* Europhys. Lett. **53**, 354 (2001a).

Petrovic, C., P. G. Pagliuso, M. F. Hundley, R. Movshovich, J. L. Sarrao, J. D. Thompson, Z. Fisk, and P. Monthoux. *Heavy-fermion superconductivity in $CeCoIn_5$ at 2.3 K.* J. Phys. Cond. Mat. **13**, L337 (2001b).

Pruschke, T., R. Bulla, and M. Jarrell. *Low-energy scale of the periodic Anderson model.* Phys. Rev. B **61**, 12 799 (2000).

Read, N. *Role of infrared divergences in the $1/N$ expansion of the $U = \infty$ Anderson model.* J. Phys. C **18**, 2651 (1985).

Read, N. and D. M. Newns. *A new functional integral formalism for the degenerate Anderson model.* J. Phys. C **16**, L1055 (1983a).

Read, N. and D. M. Newns. *On the solution of the Coqblin-Schrieffer Hamiltonian by the large-N expansion technique.* J. Phys. C **16**, 3273 (1983b).

Read, N., D. M. Newns, and S. Doniach. *Stability of the Kondo lattice in the large-N limit.* Phys. Rev. B **30**, 3841 (1984).

Read, N. and S. Sachdev. *Large-N expansion for frustrated quantum antiferromagnets.* Phys. Rev. Lett. **66**, 1773 (1991).

Rubtsov, A. N., V. V. Savkin, and A. I. Lichtenstein. *Continuous-time quantum Monte Carlo method for fermions.* Phys. Rev. B **72**, 035 122 (2005).

Ruderman, M. A. and C. Kittel. *Indirect exchange coupling of nuclear magnetic moments by conduction electrons.* Phys. Rev. **96**, 99 (1950).

Sachdev, S. and N. Read. *Large N expansion for frustrated and doped quantum antiferromagnets.* Int. J. Mod. Phys. B **5**, 219 (1991).

Sachdev, S. and Z. Wang. *Pairing in two dimensions: A systematic approach.* Phys. Rev. B **43**, 10 229 (1991).

Schrieffer, J. R. and P. A. Wolff. *Relation between the Anderson and Kondo Hamiltonians.* Phys. Rev. **149**, 491 (1966).

Senthil, T., S. Sachdev, and M. Vojta. *Fractionalized Fermi liquids.* Phys. Rev. Lett. **90**, 216 403 (2003).

Senthil, T., M. Vojta, and S. Sachdev. *Weak magnetism and non-Fermi liquids near heavy-fermion critical points.* Phys. Rev. B **69**, 035 111 (2004).

Settai, R., H. Shishido, S. Ikeda, Y. Murakawa, M. Nakashima, D. Aoki, Y. Haga, H. Harima, and Y. Onuki. *Quasi-two-dimensional Fermi surfaces and the de Haas-van Alphen oscillation in both the normal and superconducting mixed states of $CeCoIn_5$.* J. Phys.: Condens. Matter **13**, L627 (2001).

Shakeripour, H., M. A. Tanatar, S. Y. Li, C. Petrovic, and L. Taillefer. *Hybrid gap structure of the heavy-fermion superconductor $CeIrIn_5$.* Phys, Rev. Lett. **99**, 187 004 (2007).

Shakeripour, H., M. A. Tanatar, C. Petrovic, and L. Taillefer. *Universal heat transport in a heavy-fermion superconductor.* arXiv:0902.1190v1 (2009).

Shim, J. H., K. Haule, and G. Kotliar. *Modeling the localized-to-itinerant electronic transition in the heavy fermion system $CeIrIn_5$.* Science **318**, 1615 (2007).

Shishido, H., R. Settai, D. Aoki, S. Ikeda, H. Nakawaki, N. Nakamura, T. Iizuka, Y. Inada, K. Sugiyama, T. Takeuchi, K. Kindo, T. C. Kobayashi, Y. Haga, H. Harima, Y. Aoki, T. Namiki, H. Sato, and Y. Onuki. *Fermi surface, magnetic and superconducting properties of $LaRhIn_5$ and $CeTIn_5$ (T: Co, Rh and Ir).* J. Phys. Soc. Jpn. **71**, 162 (2002).

Sigrist, M. and K. Ueda. *Phenomenological theory of unconventional superconductivity.* Rev. Mod. Phys. **63**, 239 (1991).

Singley, E. J., D. N. Basov, E. D. Bauer, and M. B. Maple. *Optical conductivity of the heavy fermion superconductor $CeCoIn_5$.* Phys. Rev. B **65**, 161 101 (2002).

Smith, M. F. and R. H. McKenzie. *Apparent violation of the Wiedemann-Franz law near a magnetic field tuned metal-antiferromagnetic quantum critical point.* Phys. Rev. Lett. **101**, 266 403 (2008).

Steglich, F., J. Aarts, C. D. Bredl, W. Lieke, D. Meschede, W. Franz, and H. Schäfer. *Superconductivity in the presence of strong Pauli paramagnetism: $CeCu_2Si_2$.* Phys. Rev. Lett. **43**, 1892 (1979).

Stewart, G. *Non-Fermi-liquid behavior in d- and f-electron metals.* Rev. Mod. Phys. **73**, 797 (2001).

Stewart, G. *Addendum: Non-Fermi-liquid behavior in d- and f-electron metals.* Rev. Mod. Phys. **78**, 743 (2006).

Suhl, H. *Dispersion theory of the Kondo effect.* Phys. Rev. **138**, A515 (1965).

Tahvildar-Zadeh, A. N., M. Jarrell, and J. K. Freericks. *Protracted screening in the periodic Anderson model.* Phys. Rev. B **55**, R3332 (1997).

Tanatar, M. A., J. Paglione, C. Petrovic, and L. Taillefer. *Anisotropic violation of the Wiedemann-Franz law at a quantum critical point.* Science **316**, 1320 (2007).

Thalmeier, P. and G. Zwicknagl. *Handbook on the physics and chemistry of rare earths*, volume 34, page 135. Elsevier, Amsterdam (2005).

Weber, H. and M. Vojta. *Heavy-fermion metals with hybridization nodes: Unconventional Fermi liquids and competing phases.* Phys. Rev. B **77**, 125 118 (2008).

Wilson, K. G. *The renormalization group: Critical phenomena and the Kondo problem.* Rev. Mod. Phys. **47**, 773 (1975).

Yosida, K. *Magnetic properties of Cu-Mn alloys.* Phys. Rev. **106**, 893 (1957).

Young, B.-L., R. R. Urbano, N. J. Curro, J. D. Thompson, J. L. Sarrao, A. B. Vorontsov, and M. J. Graf. *Microscopic evidence for field-induced magnetism in $CeCoIn_5$.* Phys. Rev. Lett. **98**, 036 402 (2007).

Yu, F., M. B. Salamon, A. J. Leggett, W. C. Lee, and D. M. Ginsberg. *Tensor magnetothermal resistance in $YBa_2Cu_3O_{7-x}$ via Andreev scattering of quasiparticles.* Phys. Rev. Lett. **74**, 5136 (1995).

Part III

Cuprate superconductors: Quantum oscillations from Fermi arcs

16 Introduction

The existence of a Fermi surface in cuprate superconductors is a long-standing issue and important for the understanding of the underlying pairing mechanism. The recent discovery of de Haas-van Alphen and Shubnikov-de Haas oscillations in underdoped YBCO (Doiron-Leyraud et al., 2007) was considered as the long awaited proof that a Fermi surface indeed exists. However, the observed quantum oscillations seem to be in disagreement with measurements of angle-resolved photoemission spectroscopy (ARPES), which suggests the existence of Fermi arcs, truncated segments of the Fermi surface.

In this work we make an attempt to establish a coherent picture for the underdoped phase in cuprates: In contrast to the semiclassical approach suitable for metals we show that quantum oscillations do not necessarily require closed Fermi surfaces but can be reconciled with Fermi arcs, when they are terminated by a pairing gap.

This introductory chapter covers three aspects. It gives a short overview over cuprate superconductors, which were extensively studied in the last twenty years. It discusses the semiclassical theory explaining quantum oscillations in metals, and reviews the experimental situation of quantum oscillation in cuprates.

16.1 Cuprate superconductors

In the year 1986, Bednorz and Müller (1986) discovered superconductivity in the material $La_{2-x}Ba_xCuO_4$ with a transition temperature of 30 K, which corresponds to an increase of around 7 K in comparison with the conventional superconductors known at that time. The properties found in this material are highly non-trivial and the way was paved for a new era in condensed matter physics.

Besides LaBaCuO, several cuprate materials display high-temperature superconductivity; the first one with a transition temperature T_c above the boiling point of liquid nitrogen (77 K) was $YBa_2Cu_3O_{7-x}$ (YBCO) (Wu et al., 1987) with $T_c = 93$ K, discovered in 1987, only one year after the breakthrough of Bednorz and Müller. The current record with $T_c = 133$ K is held by $HgBa_2Ca_2Cu_3O_{8+x}$ (Schilling et al., 1993).

Compared to conventional superconductors evolving from a metal, the features of cuprate superconductors are highly unusual and the mechanism producing the superconductivity is to date not fully understood. They all have in common a layered structure with CuO_2 layers orthogonal to the c-direction, which are believed to contain the carriers involved in the superconductivity. These carriers are sharply localized within these planes leading to a strongly anisotropic behavior. In comparison to ordinary metals the carrier density is small, which is accompanied by a large Coulomb repulsion between the carriers. As an effect, the penetration depth λ is significantly enhanced compared to a conventional superconductor. In

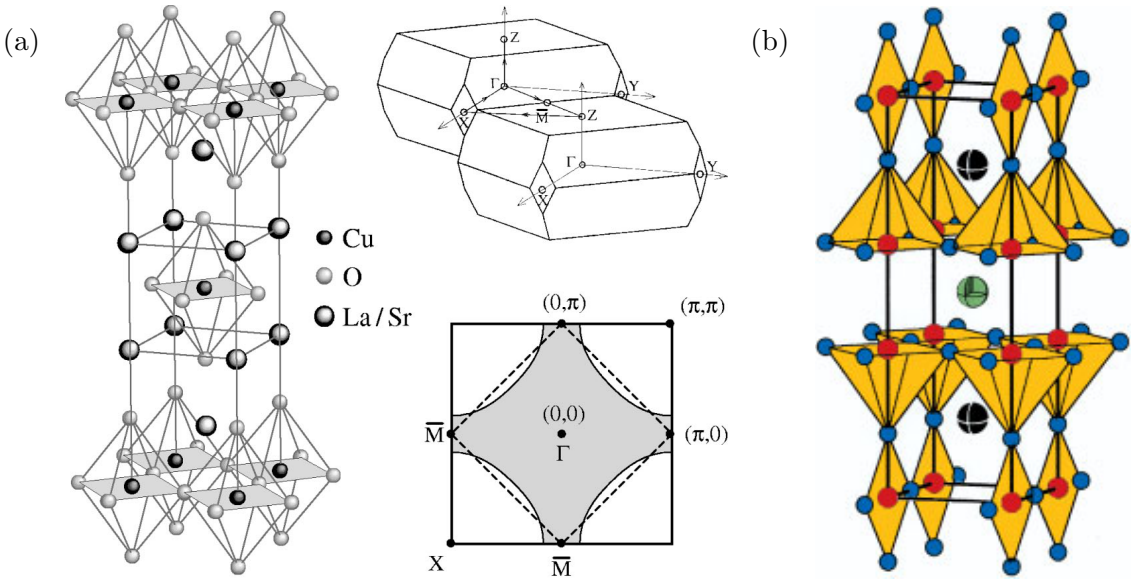

Figure 16.1: Structure of cuprate parent compounds. (a) Crystal structure, Brillouin zone and Fermi surface in 3D and 2D for M_2CuO_4, M=La (which are substituted by Sr atoms upon doping), in the tetragonal phase. For an explanation of the Fermi surface see text. (Figure from Damascelli et al., 2003) (b) Crystal structure for $YBa_2Cu_3O_7$ with tetragonal symmetry, Cu (red), O (blue), Ba (black) and Y (green). (Figure from Schwaigerer et al., 2002)

addition, the superconducting coherence length ξ is low, turning the cuprates into extreme type-II superconductors.

In the following we will shortly discuss the microscopic structure of cuprates and give an overview on the overall phase diagram with an explanation of the contained phases and the attempts to model this behavior.

Microscopic structure

Depending on temperature and doping level the cuprates are classified as tetragonal or orthorhombic and close to tetragonal. The crystal structure is basically a distorted perovskite, but due to the large variety of copper oxide compounds a more detailed discussion is needed. We will first focus on the structure of the (non-superconducting) parent compound and comment on the different doping mechanisms afterwards.

The unifying aspect among the cuprates is the existence of CuO_2 layers. One or more CuO_2 layers are directly stacked upon each other (mono-, bi-, trilayer compounds) and separated by at least a layer of MO where M is e.g. Ba or La. Figure 16.1(a) shows the high-temperature tetragonal crystal structure for the monolayer compound M_2CuO_4, which contains the planes $(CuO_2)(MO)(MO)$. The anion O and the cation M in the interleaved planes are in contact due to large ionic radii, whereas the Cu cation is smaller and surrounded by six O anions. Upon cooling a structural phase transition towards an orthorhombic structure occurs (see e.g. Kastner et al., 1998). A different example is shown in Fig. 16.1(b): $YBa_2Cu_3O_7$ has a

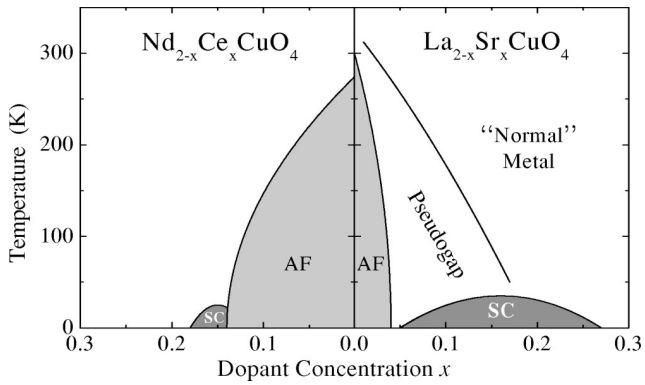

Figure 16.2: General temperature-doping phase diagram for cuprates. For a detailed explanation see text. (Figure from Damascelli et al., 2003)

tetragonal structure and contains CuO_2 planes, BaO planes, Y planes and CuO chains.

Doping the parent compound inserts charge carriers into the system, which is an essential requirement for the formation of superconductivity. Generally speaking, the Cu atoms are the source for charge carriers. The dopants are mostly inserted into the interleaved layers. One can (i) substitute the cations by ions with different valency, e.g. Sr^{2+} for La^{3+}, (ii) remove or (iii) add oxygen ions. Also a mixture of these procedures is possible. Upon doping, the interleaved layers stay ionic and serve as a charge reservoir by changing the effective Cu valency. In YBCO, Fig. 16.1(b), where copper ions not only occur in the CuO_2 layers but also in layers in between in the form of CuO chains, the situation is different. It is doped by changing the oxygen content in the interleaved layer CuO_x, now consisting of CuO chains with O vacancies. These chains themselves contain free carriers contributing to the supercurrent.

The superconducting transition temperature is not only sensitive to the doping level, but also to the number of CuO_2 layers within one block: T_c increases from monolayer over bilayer to trilayer compounds within each family (Tarascon et al., 1988; Di Stasio et al., 1990).

In reciprocal space the tetragonal lattice of La_2CuO_4 translates into a body centered tetragonal structure with a 3D Brillouin zone (BZ) depicted in the upper right panel of Fig. 16.1(a). The layers are only weakly coupled and the dispersion along the z-axis can be neglected in almost all situations. The projection of the BZ in two dimensions is depicted in the lower right panel of Fig. 16.1(a). The dashed diamond denotes the Fermi surface at half filling (without doping) derived in a tight-binding approximation assuming a nearest neighbor hopping. The solid line enclosing the gray shaded area represents the Fermi surface upon inclusion of an additional next-nearest neighbor hopping.

Phase diagram

For all cuprate superconductors the occurring phases can be summarized in a doping-temperature phase diagram, Fig. 16.2. A dopant concentration $x = 0$ represents the parent compound. On the left-hand side of $x = 0$, the compounds are electron doped, while the right-hand side

describes hole doping.

Local density approximation (LDA) band structure calculations for the parent compound (Mattheiss, 1987; Horsch et al., 1989) suggest a partially filled band, implying metallic behavior, which is not consistent with the experimentally observed insulating behavior. Therefore, the LDA, which is based on an independent-particle picture, is not able to capture the essential physics. This indicates the importance of electronic correlations and suggests the existence of a Mott-Hubbard insulator (Mott, 1949, 1956; Hubbard, 1964a,b), produced by an on-site Coulomb repulsion U, which is much larger than the bandwidth W. A simple model for the microscopic properties is the (one-band) Hubbard model (Hubbard, 1963)

$$\mathcal{H} = -t \sum_{\langle ij \rangle, \sigma} (c^\dagger_{i\sigma} c_{j\sigma} + \text{h.c.}) + U \sum_i n_{i\uparrow} n_{i\downarrow} \,, \tag{16.1}$$

where $c^\dagger_{i\sigma}$ creates a charge carrier at site i with spin σ and $n_{i\sigma} = c^\dagger_{i\sigma} c_{i\sigma}$ is the corresponding number operator. $\langle ij \rangle$ refers to nearest-neighbored site pairs. t is the hopping amplitude and U the on-site Coulomb repulsion between two charge carriers. This one-band Hubbard model can be thought of as an effective model for a three-band Hubbard model, which explicitly considers the Cu($3d_{x^2-y^2}$) and the O($2p_x$) and O($2p_y$) orbitals (see e.g. Emery, 1987). Band structure calculations show the emergence of three dominant bands, a review is given e.g. by Dagotto (1994).

In the limit of $U \gg t$, the charge carriers $c_{i\sigma}$ become localized and the relevant degrees of freedom are captured in the t-J model, originally derived from the Hubbard model by Spałek and Oleś (1977) and discussed in the context of high-T_c by Anderson (1987):

$$\mathcal{H} = -t \sum_{\langle ij \rangle, \sigma} (\bar{c}^\dagger_{i\sigma} \bar{c}_{j\sigma} + \text{h.c.}) + J \sum_{\langle ij \rangle} \left(\mathbf{S}_i \cdot \mathbf{S}_j - \frac{n_i n_j}{4} \right) . \tag{16.2}$$

The coupling constant can be expressed as $J = 4t^2/U$ and the $\bar{c}_{i\sigma} = c_{i\sigma}(1 - n_{i,-\sigma})$ are projected operators, whose construction excludes double occupancy. How to project out the irrelevant degrees of freedom is e.g. shown by Auerbach (1994).

Besides the Néel ordered state appearing in the low doping regime a variety of other phases occurs. The compound with a dopant concentration leading to maximal T_c is called optimally doped. Higher and lower concentrations are respectively denoted as over- and underdoped. The superconducting phase is rather unconventional: In contrast to the conventional phonon-mediated superconductors with an s-wave pairing, the superconducting order parameter in cuprates exhibits a strong anisotropy observable by angle resolved photoemission spectroscopy (ARPES) (Wells et al., 1992; Shen et al., 1993). Its symmetry is d-wave; a review about unconventional superconductivity and the symmetry classifications is given by Sigrist and Ueda (1991). As previously mentioned, the cuprate superconductors are strongly type II; SQUID (superconducting quantum interference device) measurements (Gough et al., 1987) show that the penetrating flux is quantized in half-flux quanta $\phi_0/2 = h/2e$, indicating the existence of pairs in the superconducting phase.

In the hole doped regime of the phase diagram a highly unusual phase appears - the pseudogap phase (Marshall et al., 1996; Loeser et al., 1996; Ding et al., 1996). It is characterized by a normal-state energy gap, which opens up at specific regions along the underlying Fermi

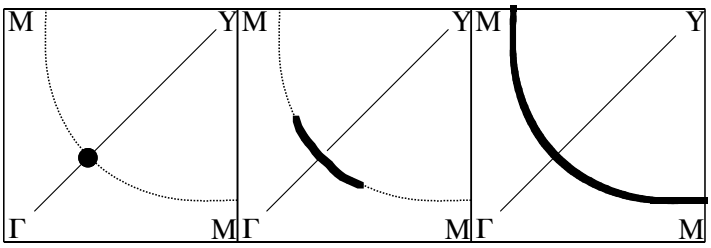

Figure 16.3: Schematic illustration of the Fermi surface evolution for increasing temperature in the underdoped regime of hole doped cuprates. Left: Point-like Fermi surface below T_c in the d-wave superconductor. Center: Arc-like Fermi surface in the pseudogap phase. Right: Cylindrical Fermi surface above the pseudogap temperature T^*. (Figure after Norman et al., 1998)

surface. The properties of this gap can be summarized as follows (Shen et al., 1997): (i) It mainly occurs in the underdoped regime, compare the phase diagram in Fig. 16.2. (ii) The maximum gap value for pseudo- and superconducting gap at the same doping level are equal. It does not follow the value estimated from BCS-theory, which scales linearly with T_c. Moreover the pseudogap value increases for decreasing transition temperature T_c, i.e., for decreasing hole doping. (iii) The pseudogap momentum space structure is also strongly anisotropic: It vanishes along the diagonal $(0,0) \rightarrow (\pi,\pi)$ and is maximal for $(\pi,0) \rightarrow (\pi,\pi)$.

The pseudogap temperature T^* can be determined by comparing the ARPES spectrum at the $(\pi,0) - (\pi,\pi)$ Fermi surface crossing to a reference spectrum, e.g. the spectrum of Pt: As soon as T^* is reached, no shifts in the leading edge between sample and reference spectrum are visible (Ding et al., 1996).

As indicated by ARPES experiments, the region with zero gap in the pseudogap phase is extended around the diagonal leading to a Fermi surface shaped like arcs (Norman et al., 1998), illustrated in Fig. 16.3. The arc length scales as T/T^*, extrapolating to zero in the $T \rightarrow 0$ limit (Kanigel et al., 2006). Above T^* the Fermi surface is cylindrical and below T_c is it given by a nodal point. However, even below T_c ARPES spectra show Fermi arc-like signatures (Shen et al., 2005; Hossain et al., 2008). The pseudogap phase has been interpreted as a precursor of superconductivity; for $T \gtrsim T_c$ preformed pairs are believed to exist, which eventually become phase coherent below T_c.

The "normal" metal regime in the phase diagram is normal only to some extend. Fermi-liquid theory works best for extreme overdoping. For a decreasing doping level antiferromagnetic fluctuations appear and the Fermi-liquid picture becomes less and less applicable. For a review of the normal state transport properties, see Waldram (1996).

Theories

Until now the rich physics of the cuprates could not be consistently explained with a unique microscopic theory. Moreover, the Fermi liquid and the BCS theory, two well-established theories for metals, are applicable only to a certain extent and do not provide an explanation for the observed phenomenology. For example, electron-phonon interactions, which stabilize

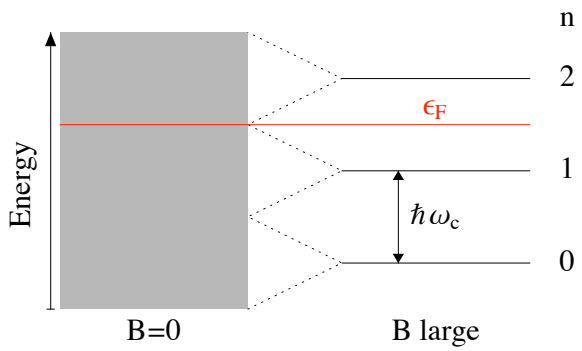

Figure 16.4: Schematic illustration of Landau levels $\epsilon_n = \hbar\omega_c(n + 1/2)$, which evolve for sufficiently large magnetic field B.

the superconductivity in the conventional case, is for itself not able to produce transition temperatures of the order of 100 K.

New theoretical approaches tackling this problem are e.g. a resonance valence bond state (Anderson, 1987), stripe phases (Tranquada et al., 1995; Salkola et al., 1996), the physics of quantum phase transitions (Sachdev, 2000) and fractionalized electrons (Senthil and Fisher, 2001), just to mention some of them. A recent review on the physics arising from a doped Mott insulator is given by Lee et al. (2006).

Before discussing quantum oscillations in cuprates, we recall the properties and the underlying theory for quantum oscillations in metals in the next section.

16.2 Quantum oscillations in metals

Discovered in the year 1930 in bismuth by de Haas and van Alphen (1930), oscillations in the magnetic susceptibility as a function of inverse magnetic field are nowadays a popular tool for investigating Fermi surfaces. They result from oscillations in the density of states at the Fermi level, which also lead to other quantum oscillation phenomena like Shubnikov - de Haas oscillations in the conductivity, oscillations in the magnetostriction or nearly all other observable quantities.

In the limit of free electrons the equally distributed states in reciprocal space condense on Landau levels under the influence of a magnetic field. The evolving energy levels are given by

$$\epsilon_n = \hbar\omega_c \left(n + \frac{1}{2}\right), \quad \text{with} \quad \omega_c = \frac{eB}{m}, \tag{16.3}$$

the so-called cyclotron frequency. Notice the spacing between ϵ_n depends on the magnetic field strength B. For a given electron density ρ, the Fermi level ϵ_F lies at ϵ_n or between ϵ_n and ϵ_{n+1}, see Fig. 16.4. By changing B with ρ fixed, Landau levels pass by the Fermi level, implying an oscillatory behavior in the density of states at the Fermi level as a function of inverse magnetic field.

In a metal, where electrons are not free, but their motions are determined by the band structure with a dispersion given by $\epsilon_{\mathbf{k}}$, this fully quantum-mechanical picture has to be substituted by a semiclassical one, developed by Onsager (1952) and Lifshitz and Kosevich (1955). The semiclassical equations of motion are combined with an artificially imposed Bohr-Sommerfeld quantization condition.

In a magnetic field the Lagrangian for a particle with mass m and charge e reads

$$\mathcal{L} = \frac{1}{2}m\mathbf{v}^2 - e\mathbf{v}\mathbf{A}\,, \tag{16.4}$$

with the vector potential $\mathbf{A}$, the canonical momentum

$$\mathbf{p} = \frac{\partial \mathcal{L}}{\partial \mathbf{v}} = m\mathbf{v} - e\mathbf{A} \tag{16.5}$$

and the kinetic momentum

$$m\mathbf{v} \equiv \hbar\mathbf{k}. \tag{16.6}$$

The semiclassical equations of motion

$$\hbar\dot{\mathbf{k}} = -\frac{e}{\hbar}\nabla_{\mathbf{k}}\epsilon_{\mathbf{k}} \times \mathbf{B}\,, \tag{16.7a}$$

$$\dot{\mathbf{r}} = \frac{1}{\hbar}\nabla_{\mathbf{k}}\epsilon_{\mathbf{k}} \tag{16.7b}$$

lead to closed orbits in real and momentum space described by

$$\mathbf{r}(t) - \mathbf{r}_0 = \left(\frac{\hbar}{eB}\right)(\mathbf{k}(t) - \mathbf{k}_0) \times \widehat{z} \tag{16.8}$$

where $(\mathbf{r}_0, \mathbf{k}_0)$ are initial coordinate and momentum and the magnetic field is aligned along the z-axis ($\mathbf{B} = B\widehat{z}$). These orbits encircle an area $\mathcal{A}^{\text{real}}$ and $\mathcal{A}^{\text{mom}}$, respectively, and are connected via

$$\mathcal{A}^{\text{real}} = \left(\frac{\hbar}{eB}\right)^2 \mathcal{A}^{\text{mom}}\,. \tag{16.9}$$

The Bohr-Sommerfeld quantization condition is imposed by hand:

$$\oint \mathbf{p} \cdot d\mathbf{r} = (n+\gamma)2\pi\hbar\,. \tag{16.10}$$

In a straightforward calculation its left-hand side can be rewritten by the semiclassical equations of motion (16.7) and can be expressed by the area $\mathcal{A}^{\text{real}}$ as

$$\frac{eB}{c}\mathcal{A}^{\text{real}} = (n+\gamma)2\pi\hbar, \tag{16.11}$$

leading to

$$\mathcal{A}^{\text{mom}} = (n+\gamma)\Delta\mathcal{A} \quad \text{with} \quad \Delta\mathcal{A} = \frac{2\pi e}{\hbar}B\,. \tag{16.12}$$

The areas $\mathcal{A}^{\text{real}}$ and $\mathcal{A}^{\text{mom}}$ only take discretized values. An index n is omitted in the following.

In the non-interacting case the density of states (DOS) at the Fermi level is given by

$$\mathcal{D}(\epsilon_F) = \sum_n \delta(\epsilon_F - \epsilon_n) = \sum_n \delta\left(\epsilon_F - \hbar\omega_c\left(n + \frac{1}{2}\right)\right) . \tag{16.13}$$

Whenever the condition $n + \frac{1}{2} \equiv \epsilon_F/(\hbar\omega_c)$ is fulfilled, the DOS has a peak; it is zero elsewhere. Therefore, it oscillates as a function of $\epsilon_F/\hbar\omega_c = \frac{\epsilon_F m}{\hbar e}\frac{1}{B}$, implying $1/B$ oscillations. For an arbitrary dispersion $\epsilon_{\mathbf{k}}$ the behavior of the DOS is analogous. From Eq. (16.12) the oscillatory argument is extracted as

$$\frac{\mathcal{A}^{\text{mom}}(\epsilon_F)}{\Delta\mathcal{A}} = \frac{F}{B} \quad \text{with} \quad F = \frac{\hbar\mathcal{A}^{\text{mom}}(\epsilon_F)}{2\pi e} , \tag{16.14}$$

where $\mathcal{A}^{\text{mom}}(\epsilon_F)$ decribes the momentum space area encircled by an electron at the Fermi energy.

In the free electron picture the dispersion becomes $\epsilon_{\mathbf{k}} = \hbar^2/(2m)\mathbf{k}^2$ and $\mathcal{A}^{\text{mom}}$ can be identified as the area covered by a Landau ring, where the area between two adjacent rings is given by

$$\Delta\mathcal{A} = \frac{2\pi eB}{\hbar}, \tag{16.15}$$

which is in agreement to Eq. (16.12). In the limit of free electrons the quantum mechanical result is recovered from the semiclassical one.

This semiclassical analysis has shown the well-established relation between a closed Fermi surface and the emergence of quantum oscillations in physical observables based on the Fermi-liquid behavior of the sample.

In the next section we discuss the recently observed quantum oscillations in cuprate superconductors and point out which puzzles arise for the underdoped regime.

16.3 Quantum oscillations in cuprate superconductors - an experimental survey

Not until 2007 quantum oscillations were observed in cuprate superconductors (Doiron-Leyraud et al., 2007; Yelland et al., 2008; Bangura et al., 2008; Jaudet et al., 2008; Sebastian et al., 2008; Vignolle et al., 2008). The bottleneck to this discovery was given by the fabrication of high quality single crystals and the difficulty of producing high magnetic fields of the order of 50 T. Although initially claimed as the proof for a closed Fermi surface, the interpretation of these data is not as simple as in the case of metals. In the following we discuss the results for the over- and underdoped regime, while pointing out which results do not match the semiclassical Onsager approach.

In the regime of elevated temperature and zero magnetic field ARPES measurements suggest Fermi surfaces that are depicted in Fig. 16.5: In the overdoped sample with an effective hole doping of $p = 0.28$, a closed hole Fermi surface centered around (π, π) exists, whereas in the

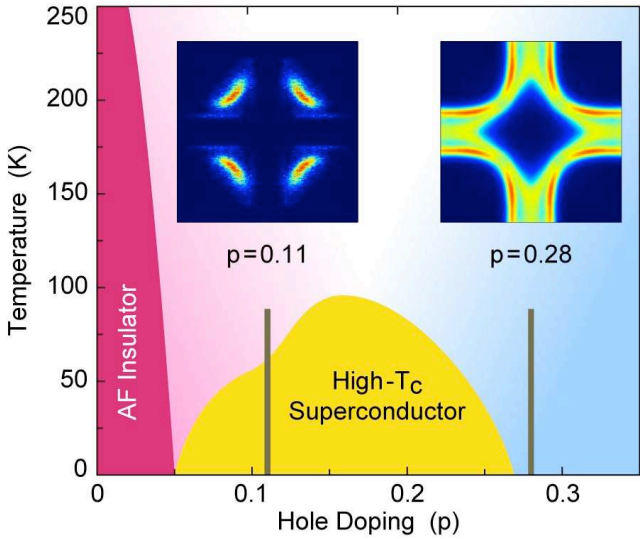

Figure 16.5: Schematic phase diagram for $YBa_2Cu_3O_{7-\delta}$ as a function of temperature and hole doping p with marks at the doping levels $p = 0.11$ and $p = 0.28$, which are in the underdoped and the overdoped regime, respectively. The insets show the corresponding ARPES spectral intensities over one Brillouin zone measured at 20 K. (Figure from Hossain et al., 2008)

underdoped case with $p = 0.11$, the Fermi surface develops into disconnected arcs located in the vicinity of the diagonals, reflecting the properties of the pseudogap phase. Please note that the study of the surface of YBCO is hampered by its polarity, which induces self-doping. Therefore, the surface doping significantly deviates from the bulk doping, and was suggested to be controlled by the deposition of potassium atoms on the cleavage plane (Hossain et al., 2008). The ARPES spectra shown in Fig. 16.5 are taken from $YBa_2Cu_3O_{6.5}$ without K-deposition, which has an effective surface hole doping of $p = 0.28$, and the same material with a heavy deposition of potassium atoms leading to an effective hole doping of $p = 0.11$.

De Haas - van Alphen oscillation data (Vignolle et al., 2008) for the overdoped material $Tl_2Ba_2CuO_{6+\delta}$ (Tl2201) reveal an excellent agreement between the oscillation frequency and the size of the Fermi surface predicted by ARPES. This result does not come as a surprise regarding the fact that Fermi liquid properties dominate in the overdoped regime and the oscillations were seen in the field-induced normal state.

The underdoped case is more subtle and cannot be reconciled with the ARPES results in a simple way. Two different underdoped YBCO compounds were studied - $YBa_2Cu_3O_{6.51}$ with a hole doping of $p = 0.1$ and $YBa_2Cu_4O_8$ with $p = 0.14$. Upon careful investigation, Sebastian et al. (2008) extracted two different frequencies for $YBa_2Cu_3O_{6.51}$ with $p = 0.1$, see Fig. 16.6: a dominant one at $F_\alpha = 500 \pm 20$T, which is in agreement with the observations of Doiron-Leyraud et al. (2007) and Jaudet et al. (2008), and $F_\beta = 1650 \pm 40$T with significantly smaller amplitude.

The dominant frequencies in the over- and underdoped case approximately differ by a factor of 30; while in the overdoped case the size of the ARPES Fermi surface fits the result for the

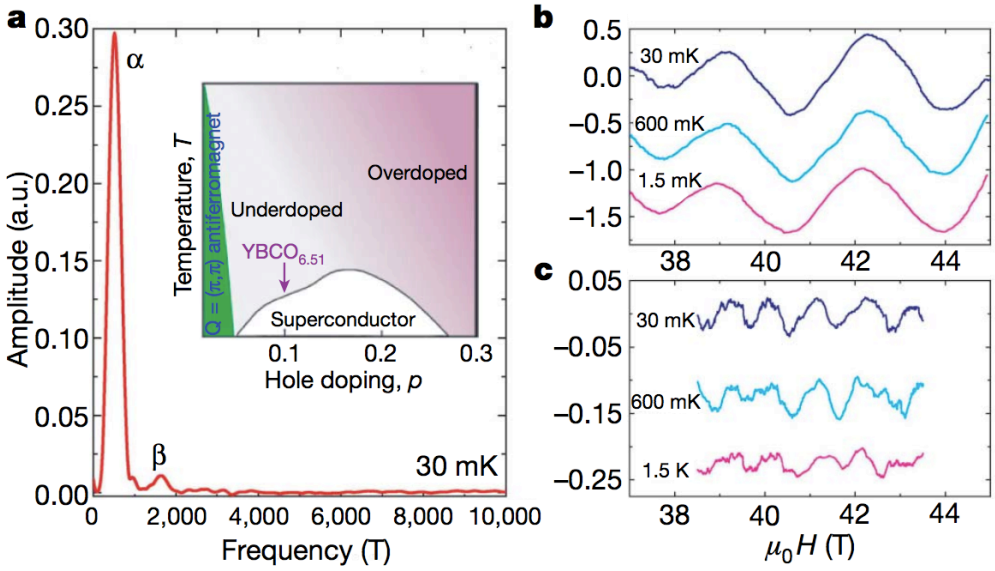

Figure 16.6: de Haas - van Alphen oscillations in $YBa_2Cu_3O_{6.51}$. (a) Fourier transform of the oscillation signal revealing peaks at two different frequencies $F_\alpha = 500 \pm 20$T and $F_\beta = 1650 \pm 40$T. The inset shows the temperature-doping phase diagram of YBCO. (b) Data for de Haas - van Alphen oscillations at various temperatures with subtracted background. (c) de Haas - van Alphen oscillations after subtraction of the F_α contribution. For details of the fitting and subtracting procedure see Sebastian et al. (2008). (Figure from Sebastian et al., 2008)

observed frequency via the Onsager-Lifshitz formula, the situation for underdoping is less clear, because ARPES does not show a closed Fermi surface, but indicates disconnected Fermi arcs! The attempt was made explaining the oscillatory behavior in the underdoped regime by the existence of broken translational symmetry (Millis and Norman, 2007; Chakravarty and Kee, 2008; Chen et al., 2008) leading to a complicated band structure and multiple Fermi pockets. It was argued that Fermi pockets cannot be seen by ARPES e.g. because of coherence factors suppressing the photoemission intensity at the pocket's back side. A different line of argument is based on the fact that ARPES measurements are conducted in zero magnetic field and high temperature, while the oscillations are seen at low temperature in a high magnetic: Possibly, these two regimes exhibit two different Fermi surfaces.

A generalization of the Lifshitz-Kosevich formalism to the mixed state of type-II superconductors based on a perturbative treatment of the scattering at the vortex centers, developed by Maki (1991) and Stephen (1992), connects the oscillation frequency to the Fermi surface in the temperature induced normal state. While this theory is applicable to e.g. the organic superconductor κ-(BEDT-TTF)$_2$Cu(NCS)$_2$ (Wosnitza et al., 2000; Sasaki et al., 2003), the underlying constraints are not fulfilled in cuprate superconductors: For cuprates the condition $\Delta^2 < \sqrt{\mu\omega_c}$, where Δ is the gap size, μ the Fermi energy and ω_c the cyclotron frequency, does not hold, since the gap size is more than one order of magnitude larger than ω_c and this pertubative analysis cannot be applied.

16.4 Outline

In this study a completely different approach is taken for resolving the question of how to combine the Fermi arc picture suggested by ARPES measurements with the recently observed quantum oscillations in cuprate superconductors at high magnetic field.

We start off with the basic assumption that Fermi arcs exist in the regime where quantum oscillations are observed. We consider a real-space version of a BCS-like Hamiltonian with a pairing gap leading to truncated Fermi surface segments. The influence of an applied magnetic field manifests itself in the hopping amplitude carrying the usual Peierls factor and in the superconducting order parameter, which takes into account the existence of an Abrikosov vortex lattice. By a fully quantum mechanical treatment of the model, we show that the density of states at the Fermi level exhibits an oscillatory behavior. The results presented in the framework of this thesis are contained in (Pereg-Barnea et al.). In this reference an additional semiclassical analysis is presented, whose results we will compare to the ones obtained from our numerical treatment of the quantum-mechanical approach.

The remainder of this part is organized as follows: In Chapter 17 we introduce an ansatz for a modified gap function leading to Fermi arcs, discuss its consequences for the density of states in zero magnetic field, and compare it to the behavior of an ordinary d-wave gap function. The considered quantum mechanical lattice model in magnetic field is presented in Chapter 18. By applying a Franz-Tešanović transformation (Franz and Tešanović, 2000), a bipartite singular gauge transformation, the Hamiltonian becomes explicitly translationally invariant. Therefore, a description of the problem in terms of Bloch equations can be established. Finally, in Chapter 19 we provide numerical results for the spectrum and the density of states, a detailed frequency analysis, and a discussion. Chapter 20 concludes this part with a summary of the results.

17 Fermi arcs produced by a pairing gap

In this chapter we introduce a phenomenological approach that is able to produce truncated segments of the Fermi surface terminated by a pairing gap. Therefore, a BCS-like model is considered with a modified d-wave gap function that is adiabatically connected to the standard d-wave gap observed in cuprates at $T = 0$. We study the Fermi arcs evolving from this ansatz, discuss justifications for this approach and its connection to a BCS theory with a standard d-wave gap function, and compare the density of states for both modified and standard d-wave gap functions.

In general, a BCS-Hamiltonian is given by

$$H = \sum_{\mathbf{k},\sigma} (\epsilon_{\mathbf{k}} - \epsilon_F) c^\dagger_{\mathbf{k}\sigma} c_{\mathbf{k}\sigma} + \sum_{\mathbf{k}} \left(\Delta_{\mathbf{k}} c^\dagger_{\mathbf{k}\uparrow} c^\dagger_{-\mathbf{k}\downarrow} + \text{h.c.} \right) . \tag{17.1}$$

$c_{\mathbf{k}\sigma}$ is a fermionic operator that creates an electron with momentum $\mathbf{k}$ and energy $\epsilon_{\mathbf{k}}$. The electron dispersion is set in reference to the Fermi level ϵ_F. In a tight-binding approximation, where only the nearest-neighbor hopping amplitude t is included, the dispersion becomes $\epsilon_{\mathbf{k}} = -2t(\cos k_x + \cos k_y)$. For simplicity, a next-nearest neighbor hopping is omitted in the following. The gap function $\Delta_{\mathbf{k}}$ is introduced in BCS theory as $\langle c_{\mathbf{k}\uparrow} c_{-\mathbf{k}\downarrow} \rangle$. The well-established gap function for the ground state of a cuprate superconductor, $\Delta_{\mathbf{k}} = \Delta_0 \chi_{\mathbf{k}}$ with $\chi_{\mathbf{k}} = \frac{1}{2}(\cos k_x - \cos k_y)$, is of $\mathrm{d}_{x^2-y^2}$ symmetry. It exhibits nodal lines along the diagonals $k_x = \pm k_y$.

The Hamiltonian (17.1) can be diagonalized via a canonical (Bogoliubov) transformation, yielding the quasiparticle excitation energies

$$E_{\mathbf{k}} = \sqrt{(\epsilon_{\mathbf{k}} - \epsilon_F)^2 + \Delta^2_{\mathbf{k}}} \, . \tag{17.2}$$

ARPES measurements in the underdoped regime of YBCO and other high-temperature copper-based superconductors suggest the existence of Fermi arcs. Not only the pseudogap phase, but also the superconducting phase at elevated temperatures shows such arc signatures (Shen et al., 2005; Hossain et al., 2008); these two phases seem to be intimately connected. It has been argued that Fermi arcs evolve from thermal destruction of the phase coherence in the superconducting state (Franz and Millis, 1998; Berg and Altman, 2007). Several properties of the pseudogap phase look like remnants of the superconducting order: Under the influence of a magnetic field it exhibits vortices (Corson et al., 1999; Xu et al., 2000; Wang et al., 2005) and ARPES measurements reveal a Bogoliubov type dispersion above T_c (Kanigel et al., 2008).

In order to establish a description of the Fermi arcs on a mean-field level we introduce the modified d-wave gap function

$$\widetilde{\Delta}_{\mathbf{k}} = \Delta_0 \frac{\chi_{\mathbf{k}}}{e^{(\nu^2 - \chi^2_{\mathbf{k}})/\tau^2} + 1} \, , \tag{17.3}$$

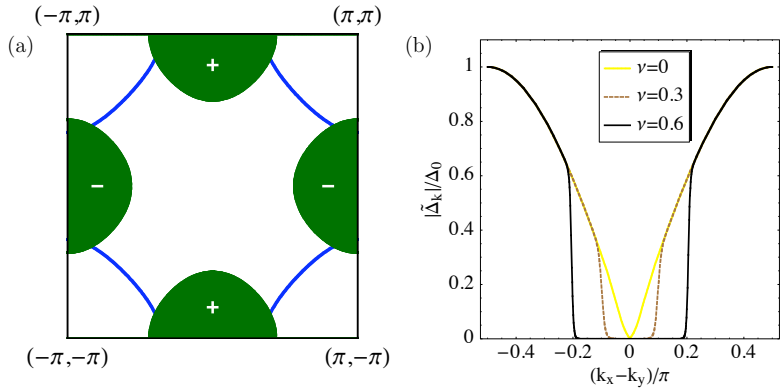

Figure 17.1: Structure of the modified d-wave gap. (a) In the green regions of the BZ the gap is non-zero, while it is exponentially suppressed elsewhere. The sign changes corresponds to those of an ordinary d-wave gap function. The blue lines represent the truncated segments of the Fermi surface with an underlying nearest neighbor hopping and $\epsilon_F = -1.1t$. The length of these so-called Fermi arcs is determined by $\nu = 0.6$. (b) Amplitude of the modified d-wave gap $\widetilde{\Delta}_{\mathbf{k}}$ in units of Δ_0 along the line connecting the points $(0, \pi)$ and $(\pi, 0)$ in the BZ for $\tau = 0.1$ and different values of ν.

which is adiabatically connected to and constructed from the ordinary $\mathrm{d}_{x^2-y^2}$-wave gap function with an additional factor in the style of the Fermi distribution function leading to an exponential suppression of the pairing gap in specific regions in the vicinity of the nodal lines of $\chi_{\mathbf{k}}$. The behavior of $\widetilde{\Delta}_{\mathbf{k}}$ is illustrated in Fig. 17.1(a) showing regions in the Brillouin zone (BZ) with a normal d-wave gap (green) and with exponential suppression (white). The two introduced parameters τ and ν control the sharpness of the step and the extension of the region with exponentially suppressed gap, respectively. The parameter ν is connected to the length of the considered Fermi arc: In the limit of $\nu \to 0$ and $\tau \to 0$, the arc shrinks to a point and the modified d-wave gap transforms smoothly into the ordinary d-wave gap $\Delta_{\mathbf{k}}$. For $\nu \to 1$ and $\tau \to 0$ the gap vanishes and the result is a a normal metal with a closed Fermi surface. In Fig. 17.1(b), the absolute value of $\widetilde{\Delta}_{\mathbf{k}}$ is plotted along the line $k_y = \pi - k_x$ for different values of ν. If $\nu \in (0, 1)$ and $\tau \to 0$, the range of the real space correlations is infinite due to the existence of a sharp step in $\mathbf{k}$ space.

The BCS-Hamiltonian with the modified gap function still describes a superconducting system - however, the superfluid density is significantly lower than in the ordinary d-wave case due to large ungapped regions along the Fermi surface. A microscopic Hamiltonian with an interaction favoring this kind of pairing is not known, but a suitable type of electron-electron interaction might certainly lead to the gap function (17.3). On the level of mean-field models, the existence of a pairing gap truncating the Fermi surface is the only way to produce genuine Fermi arcs; all kinds of particle-hole instabilities, e.g. those accompanied by a symmetry breaking, simply lead to closed Fermi surfaces, terminated by the boundaries of the BZ.

For a finite value of τ, the modified gap function is exponentially suppressed, but finite. The gap only becomes exactly zero along the diagonals. Strictly speaking, the corresponding Fermi surface consists of four nodal points and not of arcs. In ARPES such a distinction is

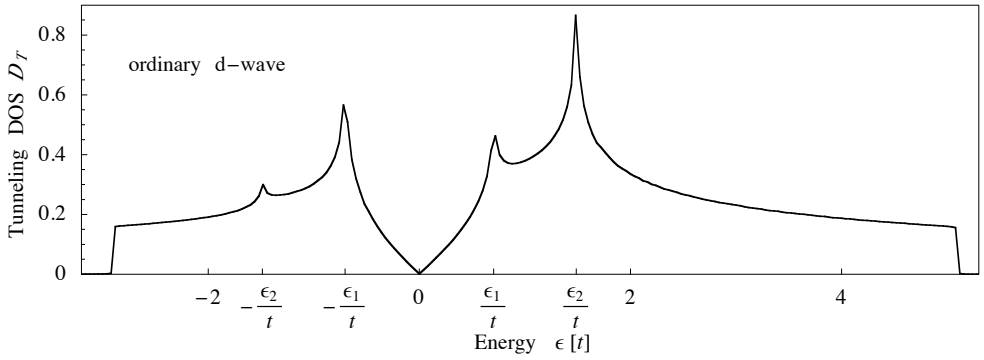

Figure 17.2: Tunneling density of states for ordinary d-wave pairing with coherence peaks at $\pm\epsilon_1$. Parameters are set to $\Delta_0/t = 1$ and $\epsilon_F/t = -1.1$, and the energy is given in units of t.

not visible, however for the validity of the Luttinger theorem it is of great importance.

Density of states: Ordinary vs. modified d-wave gap

The superconducting tunneling density of states (DOS) is defined by

$$D_T(\epsilon) = \frac{1}{\mathcal{N}} \sum_{\mathbf{k}} \left(|u_{\mathbf{k}}|^2 \delta(\epsilon - E_{\mathbf{k}}) + |v_{\mathbf{k}}|^2 \delta(\epsilon + E_{\mathbf{k}}) \right) \tag{17.4}$$

where $\delta(x)$ is the delta function and the prefactors arise from the Bogoliubov transformation

$$|u_{\mathbf{k}}|^2 = \frac{1}{2}\left(1 + \frac{\epsilon_{\mathbf{k}} - \epsilon_F}{E_{\mathbf{k}}}\right) \qquad \text{and} \qquad |v_{\mathbf{k}}|^2 = \frac{1}{2}\left(1 - \frac{\epsilon_{\mathbf{k}} - \epsilon_F}{E_{\mathbf{k}}}\right). \tag{17.5}$$

Please note that the tunneling DOS defined here does not refer to what would be measured in a scanning tunneling spectroscopy (STM) experiment, but rather denotes an energy-dependent, spatially averaged DOS. It is related to the normal DOS via:

$$D(\epsilon) = \frac{1}{\mathcal{N}} \sum_{\mathbf{k}} \delta(\epsilon - E_{\mathbf{k}}) = D_T(\epsilon) + D_T(-\epsilon). \tag{17.6}$$

In the following we will review the structure of the tunneling DOS for the ordinary d-wave case (Zhou and Schulz, 1992) and compare it to the results for the modified d-wave gap function. The data for the plots shown within this section are obtained numerically by replacing $\delta(x)$ in the definition of D_T, Eq. (17.4), by a Lorentzian with small width.

Away from half filling ($\epsilon_F \neq 0$) the ordinary d-wave tunneling DOS, see Fig. 17.2, shows features, which can be ascribed to the behavior of $E_{\mathbf{k}}$ in $\mathbf{k}$ space: (i) The nodal lines of $\Delta_{\mathbf{k}}$ lead to isolated zeros in the excitation energy $E_{\mathbf{k}}$ at $(\pm k_0, \pm k_0)$ with $\cos k_0 = -\epsilon_F/4t$, which manifest themselves in a linear behavior of $D_T(\epsilon)$ at low energy. (ii) The two saddle points of $E_{\mathbf{k}}$ give rise to logarithmic van Hove singularities at the energies $\pm\epsilon_1$ and $\pm\epsilon_2$. For $4t|\epsilon_F| \geq \Delta_0^2$ the saddle points sit at $\mathbf{k}_1 = (0, k_-)$ and $\mathbf{k}_2 = (\pi, \pi - k_+)$ with $\cos k_\pm = \frac{\Delta_0^2 \pm t\epsilon_F - 16t^2}{\Delta_0^2 + 16t^2}$ implying

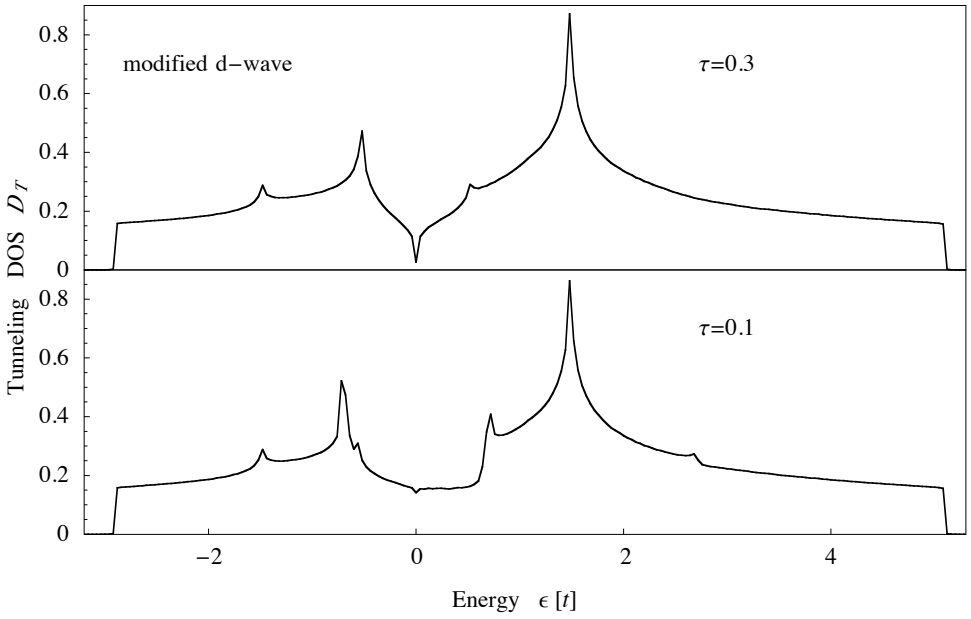

Figure 17.3: Tunneling density of states as a function of energy in units of t with $\Delta_0/t = 1$, $\nu = 0.6$ and $\epsilon_F/t = -1.1$.

$\epsilon_1 = \frac{\Delta_0(4t+\epsilon_F)}{\sqrt{16t^2+\Delta_0^2}}$ and $\epsilon_2 = \frac{\Delta_0(4t-\epsilon_F)}{\sqrt{16t^2+\Delta_0^2}}$. In the case of $4t|\epsilon_F| < \Delta_0^2$ the second saddle point changes to $\mathbf{k}_2 = (0, \pi)$, leading to an energy $\epsilon_2 = \sqrt{\epsilon_F^2 + \Delta_0^2}$. The van Hove singularities at $\pm\epsilon_1$ are intrinsically due to the superconducting order and are therefore called coherence peaks. The ones at $\pm\epsilon_2$ have their origin in the two-dimensional tight-binding band structure. Adding a third dimension renders all singularities finite.

In the case of a modified d-wave gap a numerical evaluation of Eq. (17.4) substituting the δ-function by a Lorentzian ($\delta(x) \to s/(\pi(s^2 + x^2)$ with $s \ll \tau$) shows that the van Hove singularity features survive and the coherence peaks are located at approximately the same position as for an ordinary d-wave function (compare Fig. 17.3). The low-energy behavior changes significantly depending on the value of the parameter τ. For every $\tau > 0$ a little dip evolves with $D_T(\epsilon \to 0) = 0$, which cannot fully be reflected by the numerics underlying Fig. 17.3 due to the finite width of the Lorentzian. As the value of τ grows, the dip becomes larger and the low-energy feature transforms into the one for ordinary d-wave originating from the fact that a large τ smears out the step between large- and zero gap region. For subsequent numerical evaluations τ is fixed to 0.1.

In this chapter we discussed a way to produce truncated segments of the Fermi surface terminated by a superconducting pairing gap in a two-parameter phenomenological ansatz for a modified d-wave gap function. In order to investigate the properties of a BCS-like model exhibiting such a gap function in a magnetic field, the next chapter presents a method for treating a strongly type-II superconductor in the vortex state with an arbitrary pairing function.

18 Lattice model in a magnetic field

This chapter deals with the fully quantum mechanical treatment of a strongly type-II superconductor in the mixed state with an arbitrary pairing function. The special focus lies on the previously introduced pairing gap leading to Fermi arcs. Section 18.1 introduces the BCS-like real-space model on a lattice, which undergoes a Franz-Tešanović (FT) gauge transformation in Sec. 18.2. The presence of a periodic vortex arrangement in the system allows us to rewrite the gauge-transformed Hamilton operator: Section 18.3 presents explicit calculations of expressions contained in the Hamiltonian. Finally, the discrete translational invariance of the considered system, which is explicitly restored by the FT gauge transformation, is exploited by formulating Bloch equations in Sec. 18.4.

18.1 Model

For a fully quantum mechanical treatment, we consider the real-space model

$$H = -\sum_{\langle mn\rangle} t e^{\mathrm{i}\theta_{mn}} c^\dagger_{m\sigma} c_{n\sigma} + \sum_{mn} \Big(\Delta(\mathbf{r}_m, \mathbf{r}_n) c^\dagger_{m\uparrow} c^\dagger_{n\downarrow} + \text{h.c.} \Big), \tag{18.1}$$

where the electrons $c_{m\sigma}$ sit on a two-dimensional square lattice and hop between nearest-neighbored sites. In the strong type-II superconductor limit the penetration depth λ is much larger than the intervortex distance. The electrons feel the influence of the external field upon hopping, which manifests itself in the Peierls factor $e^{\mathrm{i}\theta_{mn}}$ with

$$\theta_{mn} = \frac{2\pi}{\phi_0} \int_{\mathbf{r}_m}^{\mathbf{r}_n} \mathbf{A}(\mathbf{r}) \cdot d\mathbf{l}\,. \tag{18.2}$$

Here, $\mathbf{A}$ is the vector potential associated with the external magnetic field and $\phi_0 = h/e$ is the flux quantum. The superconducting pairing function depends on the positions of both involved electrons and can be split into

$$\Delta(\mathbf{r}_m, \mathbf{r}_n) = e^{\mathrm{i}\varphi(\mathbf{r}_m, \mathbf{r}_n)} \Delta_{\mathrm{rel}}(\mathbf{r}_m - \mathbf{r}_n), \tag{18.3}$$

where the phase $\varphi(\mathbf{r}_m, \mathbf{r}_n)$ contains the information about the vortex configuration and the "amplitude" $\Delta_{\mathrm{rel}}(\mathbf{r}_m - \mathbf{r}_n)$ reflects the real-space pairing type, which only depends on the relative coordinate $\mathfrak{r} = \mathbf{r}_m - \mathbf{r}_n$.

The well-known cases of s-, d- and p-wave pairing constructed from on-site and nearest-neighbor interaction, respectively, can be expressed by real-space functions $\Delta^s_{\mathrm{rel}}(\mathfrak{r}) = \delta(\mathfrak{r})/4$

and $\Delta_{\mathrm{rel}}^{d,p}(\mathfrak{r}) = \sum_{\boldsymbol{\delta}} f_{d,p}(\boldsymbol{\delta})\delta(\mathfrak{r}-\boldsymbol{\delta})$, where $\boldsymbol{\delta}$ denotes the vector to nearest neighbored sites and the functions $f_{d,p}$ are given by

$$f_d(\boldsymbol{\delta}) = \begin{cases} 1 & \text{for } \boldsymbol{\delta} = \pm\widehat{x} \\ -1 & \text{for } \boldsymbol{\delta} = \pm\widehat{y} \end{cases} \qquad \text{and} \qquad f_p(\boldsymbol{\delta}) = \begin{cases} \mp\mathrm{i} & \text{for } \boldsymbol{\delta} = \pm\widehat{x} \\ \pm 1 & \text{for } \boldsymbol{\delta} = \pm\widehat{y} \end{cases} . \tag{18.4}$$

The modified d-wave pairing is not related to a simple real-space structure, but is defined by its $\mathbf{k}$ space behavior. In real space we can write $\Delta_{\mathrm{rel}}^{mod-d}(\mathfrak{r}) = \sum_{\mathbf{k}} e^{\mathrm{i}\mathbf{k}\mathfrak{r}}\widetilde{\Delta}(\mathbf{k})$, where $\widetilde{\Delta}_{\mathbf{k}}$ is given by Eq. (17.3).

The phase $\varphi(\mathbf{r}_m, \mathbf{r}_n)$ can approximately expressed by the on-site phase $\phi(\mathbf{r})$ as

$$\varphi(\mathbf{r}_m, \mathbf{r}_n) = \frac{1}{2}\left(\phi(\mathbf{r}_m) + \phi(\mathbf{r}_n)\right) , \tag{18.5}$$

see Appendix I. The phase $\phi(\mathbf{r})$ contains the information about the positions $\{\mathbf{r}_i\}$ of the vortices via

$$\nabla \times \nabla\phi(\mathbf{r}) = 2\pi\widehat{z}\sum_i \delta(\mathbf{r}-\mathbf{r}_i) , \tag{18.6}$$

which translates into a 2π phase winding around the vortex cores. The singularities appearing on the right-hand side act as magnetic half-fluxes at the center of the vortex core. Their polarity is opposite to the applied magnetic field $\mathbf{B}$, which is described by the conventional London equation for intermediate field values $H_{c1} < B \ll H_{c2}$, for which the vortex spacings are large:

$$\mathbf{B} - \lambda^2\nabla^2\mathbf{B} = \frac{1}{2}\phi_0\widehat{z}\sum_i \delta(\mathbf{r}-\mathbf{r}_i), \tag{18.7}$$

with the London penetration depth λ. This equation connects $\mathbf{B}$ to the number of vortices in the system.

The magnetic field seen by the electrons is the external magnetic field $\mathbf{B}$. It is constant in space and therefore does not vanish in average ($\langle\mathbf{B}\rangle \neq 0$, where the brackets denote the spatial average). As a consequence, the corresponding vector potential $\mathbf{A}$ by construction cannot be periodic in space.

Given a periodic arrangement of vortices the physical system itself is translationally invariant with the magnetic unit cell determined by the shape of the vortex lattice.

The magnetic response related to the appearance of the Abrikosov vortices compensates the effect of the applied magnetic field in average due the flux quantization in a high-temperature superconductor. A specific type of gauge transformation, which is discussed in the next section, is able to restore this explicit translational symmetry of the Hamiltonian. Exploiting the translational invariance leads to great advantages in the numerical implementation of the problem.

18.2 Gauge transformation

In this section we introduce a special bipartite gauge transformation that removes the non-trivial off-diagonal phase in the Hamiltonian arising from the phase windings around the vortex cores, while restoring the discrete translational invariance in the Hamiltonian.

In terms of a Bogoliubov-de Gennes Hamiltonian, Eq. (18.1) becomes

$$\mathcal{H} = \begin{pmatrix} \widehat{h} & \widehat{\Delta} \\ \widehat{\Delta}^* & -\widehat{h}^* \end{pmatrix} \tag{18.8}$$

with

$$\widehat{h} = -t \sum_{\boldsymbol{\delta}} e^{\mathrm{i}\theta(\mathbf{r},\mathbf{r}+\boldsymbol{\delta})} \widehat{s}_{\boldsymbol{\delta}} - \epsilon_F \qquad \text{and} \qquad \widehat{\Delta} = \sum_{\mathbf{r}_0} \Delta_{\mathrm{rel}}(\mathbf{r}_0) e^{\mathrm{i}\phi(\mathbf{r})/2} \widehat{s}_{\mathbf{r}_0} e^{\mathrm{i}\phi(\mathbf{r})/2}, \tag{18.9}$$

where $\widehat{s}_{\mathbf{r}_0}$ is the shifting operator ($\widehat{s}_{\mathbf{r}_0} u(\mathbf{r}) = u(\mathbf{r}+\mathbf{r}_0)$). The wave function is a two-component spinor in Nambu space, $\Psi^T(\mathbf{r}) = (u(\mathbf{r}), v(\mathbf{r}))$, satisfying the Bogoliubov-de Gennes equation

$$\mathcal{H}\psi = \epsilon\psi. \tag{18.10}$$

When solving for eigenstates of $\mathcal{H}$ in the vortex phase, two main difficulties arise: the non-trivial order parameter phase winding around the vortex cores and the missing explicit translational invariance of the Hamiltonian. As we will see, both problems can be cured at once by applying a specific gauge transformation.

In general, an off-diagonal phase is removed by a gauge transformation U with

$$\mathcal{H} \to U^{-1}\mathcal{H}U, \qquad U = \begin{pmatrix} e^{\mathrm{i}\phi(\mathbf{r})/2} & 0 \\ 0 & e^{-\mathrm{i}\phi(\mathbf{r})/2} \end{pmatrix}, \tag{18.11}$$

leading to a phase $\int_{\mathbf{r}}^{\mathbf{r}+\boldsymbol{\delta}} \left(\nabla\phi - \frac{e}{\hbar c}\mathbf{A}\right) \cdot d\mathbf{l}$ in the diagonal part. Then, quasi-particles and quasi-holes see an effective magnetic field, which consists both of the applied field and the opposing half-flux spikes:

$$\mathbf{B}_{\mathrm{eff}} = \mathbf{B} - \frac{\phi_0}{2}\widehat{z} \sum_i \delta(\mathbf{r} - \mathbf{r}_i)\,. \tag{18.12}$$

It can be expressed via the superfluid velocity

$$\mathbf{v}_s(\mathbf{r}) = \frac{\hbar}{2m}\nabla\phi(\mathbf{r}) - \frac{e}{m}\mathbf{A}, \tag{18.13}$$

as $\mathbf{B}_{\mathrm{eff}} = -m/e\nabla \times \mathbf{v}_s$. By rewriting $\mathbf{v}_s$ as

$$\mathbf{v}_s(\mathbf{r}) = \frac{\pi\hbar}{m} \int \frac{d^2k}{(2\pi)^2} \frac{\mathrm{i}\mathbf{k} \times \widehat{z}}{\lambda^{-2} + k^2} \sum_i e^{\mathrm{i}\mathbf{k}(\mathbf{r}-\mathbf{r}_i)}, \tag{18.14}$$

compare Appendix J.1.1, we can easily see that the spatial average of the effective field $\langle \mathbf{B}_{\mathrm{eff}} \rangle \sim \langle \nabla \times \mathbf{v}_s \rangle$ vanishes, since $\langle e^{\mathrm{i}\mathbf{k}\mathbf{r}} \rangle = 0$.

Basically, this would be the desired result: The off-diagonal phase is removed and the spatial average of the effective magnetic field vanishes, paving the road for a translationally invariant formulation. However, the order parameter phase is *not* a pure gauge field, which can be seen by the non-vanishing right-hand side of Eq. (18.6). It winds around the vortex core by 2π

and therefore takes values in the interval $\phi(\mathbf{r}) \in [0, 2\pi]$. Thus, the factor $1/2$ in the exponent of the diagonal elements of U causes complications - the gauge transformation is not single-valued! In principle this could be compensated by introducing branch cuts in the quasiparticle wave function. A more elegant solution to this problem is given by the Franz-Tešanović gauge transformation (Franz and Tešanović, 2000), a bipartite singular gauge transformation:

$$\mathcal{H} \to U^{-1}\mathcal{H}U, \qquad U = \begin{pmatrix} e^{\mathrm{i}\phi_A(\mathbf{r})} & 0 \\ 0 & e^{-\mathrm{i}\phi_B(\mathbf{r})} \end{pmatrix} \tag{18.15}$$

with

$$\phi_A(\mathbf{r}) + \phi_B(\mathbf{r}) = \phi(\mathbf{r})\,. \tag{18.16}$$

Since no factor of $1/2$ occurs in the off-diagonal phase of U, the tranformation is rendered single-valued. The set of vortices contained in $\phi(\mathbf{r})$ is divided into two subsets A and B with vortices at $\{\mathbf{r}_i^A\}$ and $\{\mathbf{r}_i^B\}$ obeying the relation

$$\nabla \times \nabla\phi_\mu(\mathbf{r}) = 2\pi\widehat{z}\sum_i \delta(\mathbf{r} - \mathbf{r}_i^\mu), \qquad \mu = A, B. \tag{18.17}$$

Therefore, quasi-electrons and quasi-holes in the transformed system see different vortices, namely those contained in $\phi_A(\mathbf{r})$ and $\phi_B(\mathbf{r})$, respectively. The gauge-transformed Hamiltonian becomes

$$\mathcal{H}_N = \begin{pmatrix} -t\sum_{\boldsymbol{\delta}} e^{\mathrm{i}\nu_{\boldsymbol{\delta}}^A(\mathbf{r})}\widehat{s}_{\boldsymbol{\delta}} - \epsilon_F & \sum_{\mathbf{r}_0}\Delta_{\mathrm{rel}}(\mathbf{r}_0)e^{-\mathrm{i}\delta\phi(\mathbf{r})/2}\widehat{s}_{\mathbf{r}_0}e^{\mathrm{i}\delta\phi(\mathbf{r})/2} \\ \sum_{\mathbf{r}_0}\Delta_{\mathrm{rel}}^*(\mathbf{r}_0)e^{-\mathrm{i}\delta\phi(\mathbf{r})/2}\widehat{s}_{\mathbf{r}_0}e^{\mathrm{i}\delta\phi(\mathbf{r})/2} & t\sum_{\boldsymbol{\delta}} e^{-\mathrm{i}\nu_{\boldsymbol{\delta}}^B(\mathbf{r})}\widehat{s}_{\boldsymbol{\delta}} + \epsilon_F \end{pmatrix} \tag{18.18}$$

using $\delta\phi(\mathbf{r}) = \phi_A(\mathbf{r}) - \phi_B(\mathbf{r})$ and

$$\nu_{\boldsymbol{\delta}}^\mu = \int_{\mathbf{r}}^{\mathbf{r}+\boldsymbol{\delta}} \left(\nabla\phi_\mu - \frac{e}{\hbar}\mathbf{A}\right)\cdot d\mathbf{l} \equiv \frac{m}{\hbar}\int_{\mathbf{r}}^{\mathbf{r}+\boldsymbol{\delta}} \mathbf{v}_s^\mu \cdot d\mathbf{l} \tag{18.19}$$

for $\mu = A, B$. The second equality defines $\mathbf{v}_s^\mu$, the counterpart of the superfluid velocity $\mathbf{v}_s$, which acts as an effective vector potential. Therefore, quasi-electrons and -holes move in different effective magnetic fields

$$\mathbf{B}_{\mathrm{eff}}^\mu = -\frac{m}{e}\left(\nabla \times \mathbf{v}_s^\mu\right) = \mathbf{B} - \phi_0\widehat{z}\sum_i \delta(\mathbf{r} - \mathbf{r}_i^\mu)\,. \tag{18.20}$$

Analogous to $\mathbf{v}_s$ an expression involving the vortex positions can be derived for $\mathbf{v}_s^\mu$:

$$\mathbf{v}_s^\mu = \frac{2\pi\hbar}{m}\int \frac{d^2k}{(2\pi)^2}\frac{\mathrm{i}\mathbf{k}\times\widehat{z}}{\lambda^{-2} + k^2}\sum_i e^{\mathrm{i}\mathbf{k}(\mathbf{r} - \mathbf{r}_i^\mu)} \tag{18.21}$$

Details of this calculation are discussed in Appendix J.1.2. As for $\mathbf{B}_{\mathrm{eff}}$, the spatial average $\langle\mathbf{B}_{\mathrm{eff}}^\mu\rangle \sim \langle\nabla\times\mathbf{v}_s^\mu\rangle$ vanishes due to $\langle e^{\mathrm{i}\mathbf{k}\mathbf{r}}\rangle = 0$. Therefore, the number of A and B vortices in

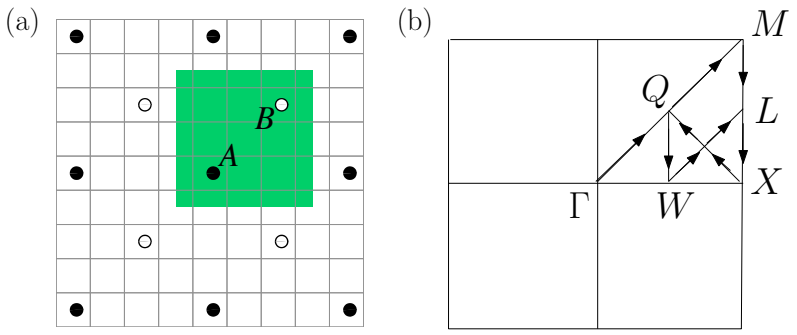

Figure 18.1: (a) Arrangement of A and B vortices on top of the lattice, on which the electrons live (gray grid). The green colored region denotes the magnetic unit cell. In this example the magnetic unit cell contains $(N_{sx} = 4) \times (N_{sy} = 4)$ lattice sites, implying a magnetic field strength of $B = \phi_0/(16\delta^2)$. (b) First magnetic BZ for the square vortex lattice in (a). (Figure based on Vafek et al., 2001)

the system is equal and for a periodic arrangement of vortices their distribution can be chosen in a way that the magnetic unit cell contains one of each vortex type.

The off-diagonal phase in the gauge-transformed Hamiltonian $\mathcal{H}_N$ can be summarized as

$$A_{\mathbf{r}_0}(\mathbf{r}) = \frac{1}{2}\left(\delta\phi(\mathbf{r}+\mathbf{r}_0) - \delta\phi(\mathbf{r})\right) = \frac{1}{2}\int_{\mathbf{r}}^{\mathbf{r}+\mathbf{r}_0} (\nabla\phi_A - \nabla\phi_B)\cdot d\mathbf{l}\,. \tag{18.22}$$

In the following we consider the setup depicted in Fig. 18.1(a). In the absence of pinning effects the vortices are arranged in a periodic fashion. For simplicity we assume a square vortex lattice instead of the triangular lattice indicated by experimental and theoretical results. However, this should not affect the validity of the results. The electrons hop on an underlying square lattice with bond length δ. For the FT gauge transformation all vortices $\{\mathbf{r}_i\}$ are divided into two subgroups $\{\mathbf{r}_i^A\}$ and $\{\mathbf{r}_i^B\}$ containing the same number of vortices. We consider A and B vortices to be distributed in a checkerboard pattern. Vortex and electron lattice are commensurate in the way that the magnetic unit cell contains one vortex of each type. The magnetic unit cell comprises $N_s = N_{sx}N_{sy}$ lattice sites, where N_{si} denotes the number of sites in ith direction. Via the London equation (18.7) the size of the magnetic unit cell and the strength of the external magnetic field B are connected as $B = \phi_0/(N_{sx}N_{xy}\delta^2)$.

This periodic arrangement of vortices significantly simplifies the expressions for the off-diagonal and the hopping phase, which will be discussed in the next section.

18.3 Off-diagonal and hopping phase

In the gauge transformed Hamiltonian $\mathcal{H}_N$, Eq. (18.18), two different phases occur: the off-diagonal phase $A_{\mathbf{r}_0}(\mathbf{r})$, defined by Eq. (18.22), and the hopping phase in the diagonal block $\nu^{\mu}_{\boldsymbol{\delta}}$, Eq. (18.19). For both phases explicit expressions in terms of summations over the reciprocal

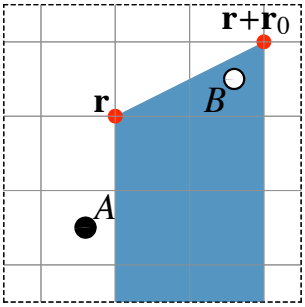

Figure 18.2: Magnetic 4×4 unit cell containing one vortex of each type. The derived expression for the off-diagonal phase $A_{\mathbf{r}_0}(\mathbf{r})$ between the points $\mathbf{r}$ and $\mathbf{r}+\mathbf{r}_0$ depends on the number of vortices n_V in the trapezoid spanned by the points $\mathbf{r}$ and $\mathbf{r}+\mathbf{r}_0$ and their projection to the x-axis (blue colored region) The point of origin is given by the lower left corner of the magnetic unit cell. In this example $n_V = 1$.

lattice vectors of the vortex lattice, $\mathbf{G}$, can be derived exploiting the London equation for intermediate field values, Eq. (18.7), and the periodic structure. While the description of the reciprocal space is presented in Appendix J.2 and the detailed derivation of the phase expressions are explained in Appendix J.3 and J.4, we will now give a summary of the results.

The hopping phase is given by

$$\nu^{\mu}_{\boldsymbol{\delta}}(\mathbf{r}) = \frac{2\pi}{N_s \delta^2} \sum_{\mathbf{G}} \frac{1}{\lambda^{-2} + G^2} e^{-\mathrm{i}\mathbf{G}\bar{\mathbf{r}}^{\mu}} e^{\mathrm{i}\mathbf{G}\mathbf{r}} \left[-\frac{G_y}{G_x} \left(1 - e^{\mathrm{i}G_x\delta_x}\right) + \frac{G_x}{G_y} \left(1 - e^{\mathrm{i}G_y\delta_y}\right) \right] , \quad (18.23)$$

where λ is the London penetration depth and $\bar{\mathbf{r}}_{\mu}$ is the offset of the position of vortex μ to the lower left corner of the magnetic unit cell. As a cross-check for the derived expression of the hopping phase, the magnetic flux through each plaquette is calculated in Appendix J.5.

The off-diagonal phase $A_{\mathbf{r}_0}(\mathbf{r})$, Eq. (18.22), requires some preliminary considerations. The closed line integral over $\nabla\phi_A - \nabla\phi_B$ is not zero, but depends on the number of encircled vortices due to the non-vanishing curl of $\nabla\phi^{\mu}$, Eq. (18.17). The occurring line integral is therefore path-dependent. Although not known in detail, the underlying microscopic interaction stabilizing the considered arbitrary pairing is assumed to be distance-dependent, which represents the simplest case. Under this assumption, the integral in Eq. (18.22) has to be evaluated along the path that directly connects the points $\mathbf{r}$ and $\mathbf{r}+\mathbf{r}_0$. If we consider vortices slightly shifted from the center of a plaquette by an irrational fraction of the lattice spacing δ, this prevents vortex cores sitting on the straight connection line between two lattice sites, rendering all occurring line integrals well-defined. The off-diagonal phase becomes

$$\begin{aligned} A_{\mathbf{r}_0}(\mathbf{r}) = \frac{\pi}{N_s \delta^2} \sum_{\mathbf{G}} \frac{e^{-\mathrm{i}\mathbf{G}\bar{\mathbf{r}}^B} - e^{-\mathrm{i}\mathbf{G}\bar{\mathbf{r}}^A}}{G^2} \Bigg[\frac{G_y}{G_x} \left(1 - e^{\mathrm{i}G_x x_0}\right) e^{\mathrm{i}G_x x} + \\ - \frac{G_x}{G_y} \left(e^{\mathrm{i}\mathbf{G}\mathbf{r}} - e^{\mathrm{i}\mathbf{G}(\mathbf{r}+\mathbf{r}_0)} + e^{\mathrm{i}G_x x_0} + e^{\mathrm{i}G_x(x+x_0)} \right) \Bigg] + n_V \pi \,, \end{aligned} \quad (18.24)$$

where n_V denotes the number of vortices in the trapezoid spanned by the points $\mathbf{r}$, $\mathbf{r}+\mathbf{r}_0$ and their projection to the x-axis, $(x,0)^T$ and $(x+x_0,0)^T$. An illustration is given in Fig. 18.2.

The gauge-transformed Hamiltonian $\mathcal{H}_N$ reflects the discrete translational invariance of the system. This can be exploited by formulating Bloch equations, which will be discussed in the next section.

18.4 Bloch equations

The advantage of the FT gauge transformation is two-fold: It restores explicitly the discrete translational invariance with the vortex lattice in the gauge-transformed Hamiltonian $\mathcal{H}_N$ while conserving single-valuedness.

The translational symmetry $\mathcal{H}_N(\mathbf{r}) = \mathcal{H}_N(\mathbf{r}+\mathbf{R})$, where $\{\mathbf{R}\}$ denote the vectors pointing to the magnetic unit cells, simply requires the phases $\nu^{\mu}_{\boldsymbol{\delta}}(\mathbf{r})$ and $A_{\mathbf{r}_0}(\mathbf{r})$ to be invariant under $\mathbf{r} \to \mathbf{r}+\mathbf{R}$. For both $\nu^{\mu}_{\boldsymbol{\delta}}(\mathbf{r})$ and $A_{\mathbf{r}_0}(\mathbf{r})$, this can be seen from the derived expressions (18.23) and (18.24), because for reciprocal lattice vectors $\mathbf{G}$ the relation $e^{\mathrm{i}\mathbf{G}\mathbf{r}} = e^{\mathrm{i}\mathbf{G}(\mathbf{r}+\mathbf{R})}$ holds.

For the FT-gauge transformed real-space Hamiltonian $\mathcal{H}_N$ the Bogoliubov-de Gennes equation reads

$$\mathcal{H}_N \Psi_n(\mathbf{r}) = \epsilon_n \Psi_n(\mathbf{r}), \tag{18.25}$$

where $\Psi_n(\mathbf{r})$ is a two-component spinor. Due to the discrete translational invariance the eigenfunctions can be modeled as Bloch waves

$$\Psi_{n,\mathbf{k}} = e^{\mathrm{i}\mathbf{k}\mathbf{r}}\Phi_{n,\mathbf{k}}(\mathbf{r}), \qquad \Phi_{n,\mathbf{k}} = \left(U_{n,\mathbf{k}}(\mathbf{r}), V_{n,\mathbf{k}}(\mathbf{r})\right)^T, \tag{18.26}$$

where $\Phi_{n,\mathbf{k}}(\mathbf{r})$ is periodic with the magnetic unit cell. With this ansatz, the eigenvalue problem becomes a Schrödinger-like equation in $\mathbf{k}$-space, also denoted as Bloch equations

$$\mathcal{H}_{\mathbf{k}} \Phi_{n,\mathbf{k}}(\mathbf{r}) = \epsilon_{n\mathbf{k}} \Phi_{n,\mathbf{k}}(\mathbf{r}), \tag{18.27}$$

with $\mathcal{H}_{\mathbf{k}} = e^{-\mathrm{i}\mathbf{k}\mathbf{r}}\mathcal{H}_N e^{\mathrm{i}\mathbf{k}\mathbf{r}}$. Notice that the transformation between $\mathcal{H}_N$ and $\mathcal{H}_{\mathbf{k}}$ is *not* unitary due to the periodic boundary conditions at the edge of the magnetic unit cell. The gauge transformed Hamiltonian in $\mathbf{k}$ space is given by

$$\mathcal{H}_{\mathbf{k}}(\mathbf{r}) = \begin{pmatrix} -t\sum_{\boldsymbol{\delta}} e^{\mathrm{i}\nu^A_{\boldsymbol{\delta}}(\mathbf{r})} e^{\mathrm{i}\mathbf{k}\boldsymbol{\delta}} \widehat{s}_{\boldsymbol{\delta}} - \epsilon_F & \sum_{\mathbf{r}_0} \Delta(\mathbf{r}_0) e^{\mathrm{i}A_{\mathbf{r}_0}(\mathbf{r})} e^{\mathrm{i}\mathbf{k}\mathbf{r}_0} \widehat{s}_{\mathbf{r}_0} \\ \sum_{\mathbf{r}_0} \Delta^*(\mathbf{r}_0) e^{\mathrm{i}A_{\mathbf{r}_0}(\mathbf{r})} e^{\mathrm{i}\mathbf{k}\mathbf{r}_0} \widehat{s}_{\mathbf{r}_0} & t\sum_{\boldsymbol{\delta}} e^{-\mathrm{i}\nu^B_{\boldsymbol{\delta}}(\mathbf{r})} e^{\mathrm{i}\mathbf{k}\boldsymbol{\delta}} \widehat{s}_{\boldsymbol{\delta}} + \epsilon_F \end{pmatrix} \tag{18.28}$$

Under the assumption that every magnetic unit cell contains two vortices, the strength of the applied magnetic field and the size of the magnetic unit cell are connected to each other via the London equation. The size of the magnetic BZ follows from the shape of the magnetic unit cell. Equation (18.28) describes an eigenvalue problem for every $\mathbf{k}$ vector in the magnetic BZ; $\mathcal{H}_{\mathbf{k}}$ becomes a $(2N_s \times 2N_s)$-matrix, with N_s being the number of sites in the magnetic unit cell.

In the following the off-diagonal matrix entry between site i and j with $\mathbf{r}_{ij} = \mathbf{r}_j - \mathbf{r}_i$ is denoted by $h^{\text{off-diag}}_{ij,\mathbf{k}}$. For a system with only one unit cell, $h^{\text{off-diag}}_{ij,\mathbf{k}}$ simply consists of $\Delta(\mathbf{r}_{ij}) e^{\mathrm{i}A_{\mathbf{r}_{ij}}(\mathbf{r}_i)} e^{\mathrm{i}\mathbf{k}\mathbf{r}_{ij}}$. With more than one unit cell and a pairing term $\Delta(\mathbf{r}_{ij})$ that is not restricted to short-ranged interactions, a summation over all unit cells has to be introduced:

$$h^{\text{off-diag}}_{ij,\mathbf{k}} = \sum_{\mathbf{R}} \Delta(\mathbf{r}_{ij}+\mathbf{R}) e^{\mathrm{i}A_{\mathbf{r}_{ij}+\mathbf{R}}(\mathbf{r}_i)} e^{\mathrm{i}\mathbf{k}\mathbf{r}_{ij}+\mathbf{R}}\,. \tag{18.29}$$

As derived in Appendix J.6, $A_{\mathbf{r}_0+\mathbf{R}}(\mathbf{r})$ can be split into

$$A_{\mathbf{r}_0+\mathbf{R}}(\mathbf{r}) = A_{\mathbf{r}_0}(\mathbf{r}) + \mathbf{q}_{\mathbf{r}+\mathbf{r}_0} \cdot \mathbf{R} + (\bar{n}_V - n_V)\pi\,. \tag{18.30}$$

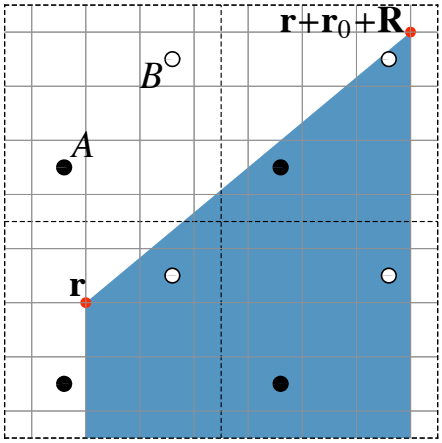

Figure 18.3: Four magnetic 4×4 unit cells, each containing one vortex of each type. The trapezoid spanned by the points $\mathbf{r}$, $\mathbf{r} + \mathbf{r}_0 + \mathbf{R}$ and their projection to the x-axis $(x, 0)$ and $(x + x_0 + R_x, 0)$ is shaded in gray and covers $\bar{n}_V = 5$ vortices.

using

$$\mathbf{q}_{\mathbf{r}+\mathbf{r}_0} = \frac{\pi}{2} \begin{pmatrix} 1/N_{sx} \\ -\text{sign}(x + x_0 - x_A)\text{sign}(x + x_0 - x_B)/N_{sy} \end{pmatrix}, \tag{18.31}$$

where x_μ is the x-component of $\bar{\mathbf{r}}^\mu$. $\bar{n}_V$ denotes the number of vortices in the trapezoid spanned by the points $\mathbf{r}$, $\mathbf{r} + \mathbf{r}_0 + \mathbf{R}$ and their projection to the x-axis $(x, 0)$ and $(x + x_0 + R_x, 0)$. This is illustrated in Fig. 18.3. Equation (18.29) simplifies to

$$h_{ij,\mathbf{k}}^{\text{off-diag}} = e^{\mathrm{i}A_{\mathbf{r}_{ij}}(\mathbf{r}_i)}(-1)^{\bar{n}_V - n_V} \sum_{\mathbf{R}} \Delta(\mathbf{r}_{ij} + \mathbf{R}) e^{\mathrm{i}\mathbf{q}_{\mathbf{r}_j}\cdot\mathbf{R}} e^{i\mathbf{k}\mathbf{r}_{ij} + \mathbf{R}} \tag{18.32}$$

$$= e^{\mathrm{i}A_{\mathbf{r}_{ij}}(\mathbf{r}_i)}(-1)^{\bar{n}_V - n_V} \sum_{\mathbf{R}} \frac{1}{N_u N_s \delta^2} \sum_{\mathbf{k}'} \Delta(\mathbf{k}') e^{\mathrm{i}(\mathbf{k}+\mathbf{k}')(\mathbf{r}_{ij}+\mathbf{R})} e^{\mathrm{i}\mathbf{q}_{\mathbf{r}_j}\mathbf{R}} \tag{18.33}$$

$$= e^{\mathrm{i}A_{\mathbf{r}_{ij}}(\mathbf{r}_i)}(-1)^{\bar{n}_V - n_V} \frac{1}{N_s \delta^2} \sum_{\mathbf{G}} \sum_{\mathbf{k}'} \Delta(\mathbf{k}') e^{\mathrm{i}(\mathbf{k}+\mathbf{k}')\mathbf{r}_{ij}} \delta_{\mathbf{k}+\mathbf{k}'+\mathbf{q}_{\mathbf{r}_j}, \mathbf{G}} \tag{18.34}$$

$$= e^{\mathrm{i}A_{\mathbf{r}_{ij}}(\mathbf{r}_i)}(-1)^{\bar{n}_V - n_V} \frac{1}{N_s \delta^2} \sum_{\mathbf{G}} \Delta(\mathbf{G} - \mathbf{k} - \mathbf{q}_{\mathbf{r}_j}) e^{\mathrm{i}(\mathbf{G} - \mathbf{q}_{\mathbf{r}_j})\mathbf{r}_{ij}}, \tag{18.35}$$

where N_u denotes the number of magnetic unit cells in the system.

In this chapter a quantum-mechanical description was developed, modeling a strongly type-II superconductor in the mixed state in the presence of an arbitrary superconducting pairing. Applying a Franz-Tešanović gauge transformation, a bipartite singular gauge transformation, leads to a Hamiltonian reflecting the discrete translational invariance of the system in the presence of an Abrikosov vortex lattice. Within this framework eigenstates are Bloch states, which significantly simplify the problem.

In the next chapter, we discuss the numerical implementation of this model with a pairing gap leading to Fermi arcs and present numerical results for the spectrum and the density of states.

19 Numerical results

This chapter presents numerical results for the spectrum and the density of states for the model introduced in the previous section, a strongly type-II superconductor in the mixed state, in combination with a pairing function that produces Fermi arcs. The Schrödinger equation in $\mathbf{k}$ space, Eq. (18.27), that takes advantage of the periodicity of the vortex lattice, is solved numerically by diagonalizing the Hamiltonian for a grid of $\mathbf{k}$ vectors in the magnetic BZ.

The numerical diagonalization was accomplished by LAPACK and ARPACK routines. LAPACK (Linear Algebra PACKage) (Anderson et al., 1999) comprises various routines for linear algebra including eigenvalue problems, for which the full spectrum and the complete set of eigenvectors is provided. In contrast, ARPACK (ARnoldi PACKage) (Lehoucq et al., 1998) is exclusively designed to solve large-scale eigenvalue problems. It uses the implicitly restarted Arnoldi method and provides a set of low-lying eigenvalues. This allows to deal with larger matrices and takes up significantly less run time. The performance was further improved by Fast Fourier Transformation (FFT) implemented by the FFTPACK routine: The calculation of (i) the hopping and off-diagonal phases $\nu_{\boldsymbol{\delta}}^{\mu}$ and $A_{\mathbf{r}_0}(\mathbf{r})$, which can be written as sums over reciprocal lattice vectors, and (ii) the Fourier transform occurring in the off-diagonal matrix elements, Eq. (18.35), were realized with a FFT.

In the following we first consider both ordinary and modified d-wave pairing functions and compare their results for the spectrum and the density of states. It will become clear that the behavior of the DOS in the proximity of the Fermi surface is crucially different - the modified d-wave pairing leads to an oscillatory behavior of the DOS in the vicinity of the Fermi level! We provide a detailed frequency analysis in terms of the given parameters and compare the results to experimental data. Furthermore, we show the local density of states (LDOS) at the Fermi level, data, which corresponds to what would be seen in a Scanning Tunneling Microscopy (STM) measurement. A short summary concludes this chapter.

19.1 Spectrum and DOS

The magnetic unit cell has the size $(N_{sx}\delta)\times(N_{sy}\delta)$ and contains one A and one B vortex. The vortices are arranged in a square lattice as shown in Fig. 18.1(a). The size of the magnetic unit cell determines the strength of the magnetic field via the London equation (18.7) as $B = \phi_0/(N_{sx}N_{sy}\delta^2)$, where $\phi_0 = h/e = 4.137\times10^5\mathrm{T\AA}^2$ denotes the magnetic flux quantum. For a lattice spacing $\delta = 4\text{Å}$, which is the appropriate value for $YBa_2Cu_3O_7$, a 16×16 unit cell corresponds to a field strength of about 101 T. The experimentally relevant regime between 40 and 65 T is modeled by unit cell sizes between $24\delta\times24\delta$ and $20\delta\times20\delta$. The London penetration depth λ is chosen to be 5000δ in numerics, which is much larger than the width of the unit cell.

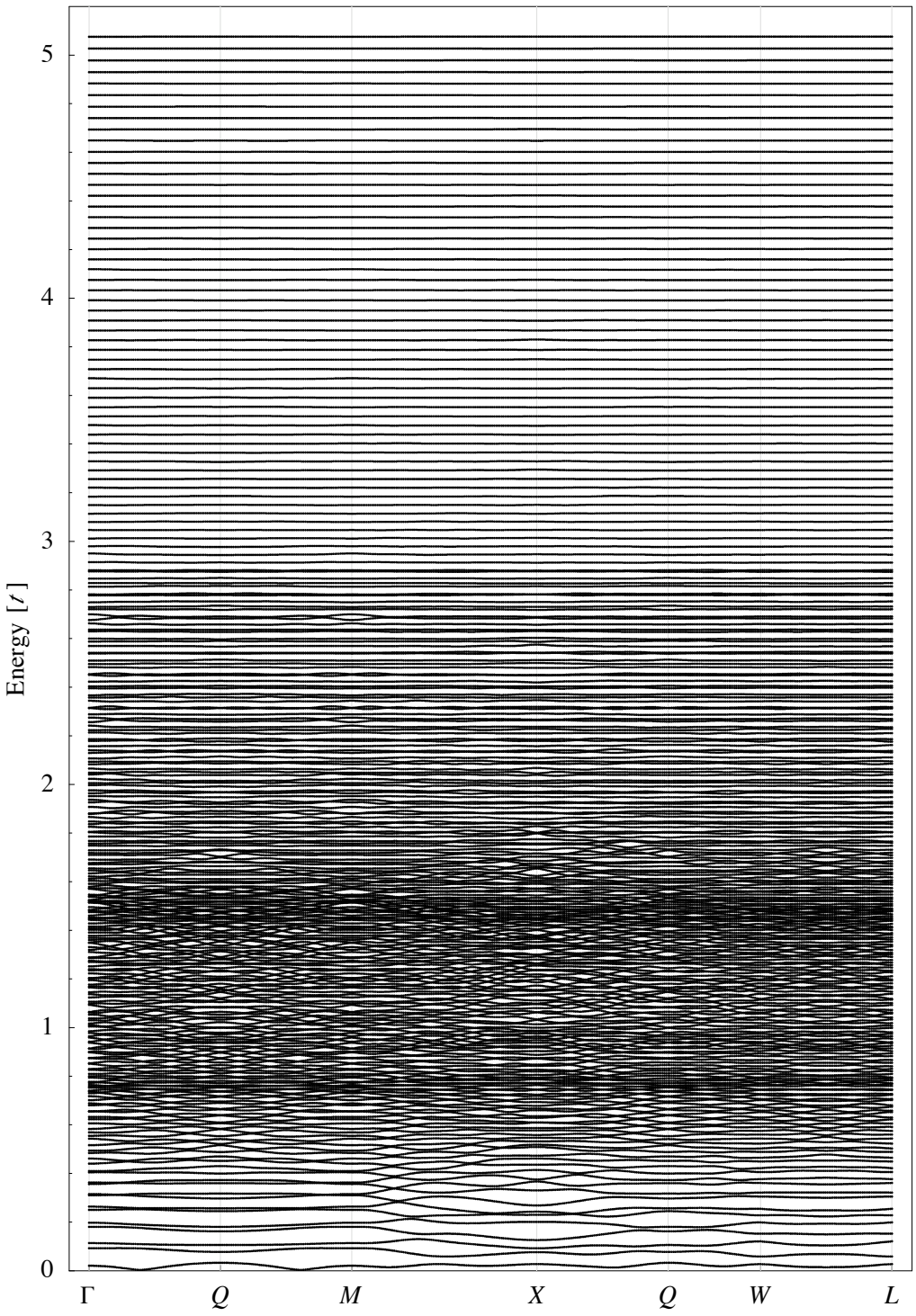

Figure 19.1: Spectrum along a specific walk in the magnetic BZ, illustrated in Fig. 18.1(b), for an ordinary d-wave pairing with $\Delta_0 = t$ and $\epsilon_F = -1.1t$ in the presence of an external magnetic field. The magnetic unit cell size is $16\delta \times 16\delta$, which corresponds to approximately 101 T.

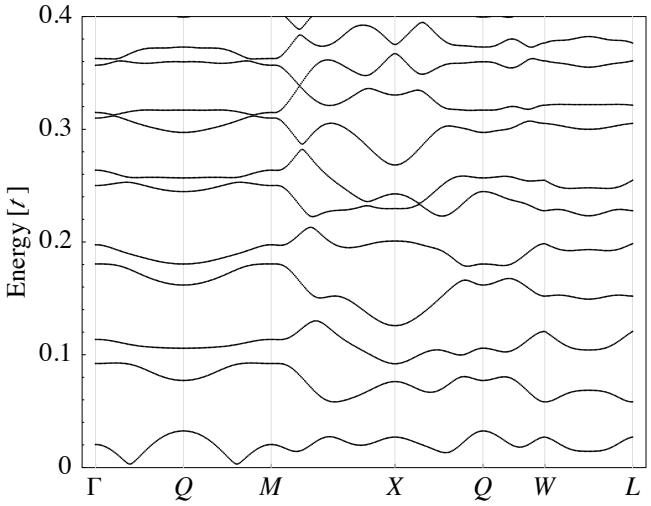

Figure 19.2: Low-energy spectrum for ordinary d-wave pairing: Zoom into the low-energy part of Fig. 19.1.

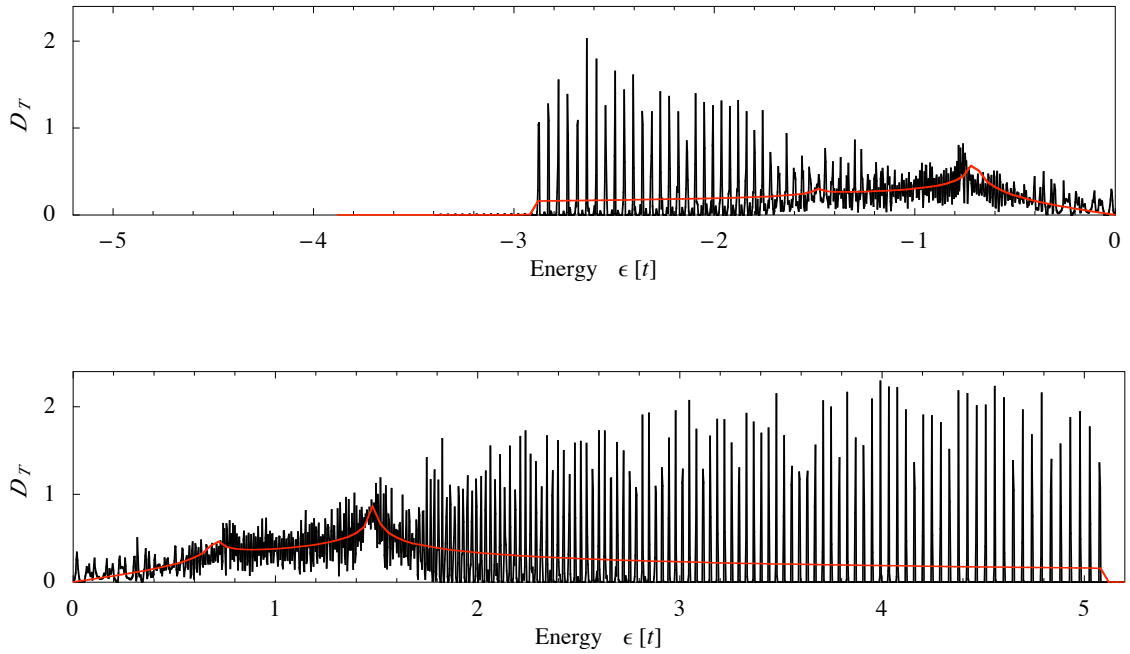

Figure 19.3: Tunneling density of states for ordinary d-wave pairing in the presence of a magnetic field of roughly 101 T (black), which corresponds to a $16\delta \times 16\delta$ magnetic unit cell, and without magnetic field (red). Parameters correspond to the ones in Fig. 19.1.

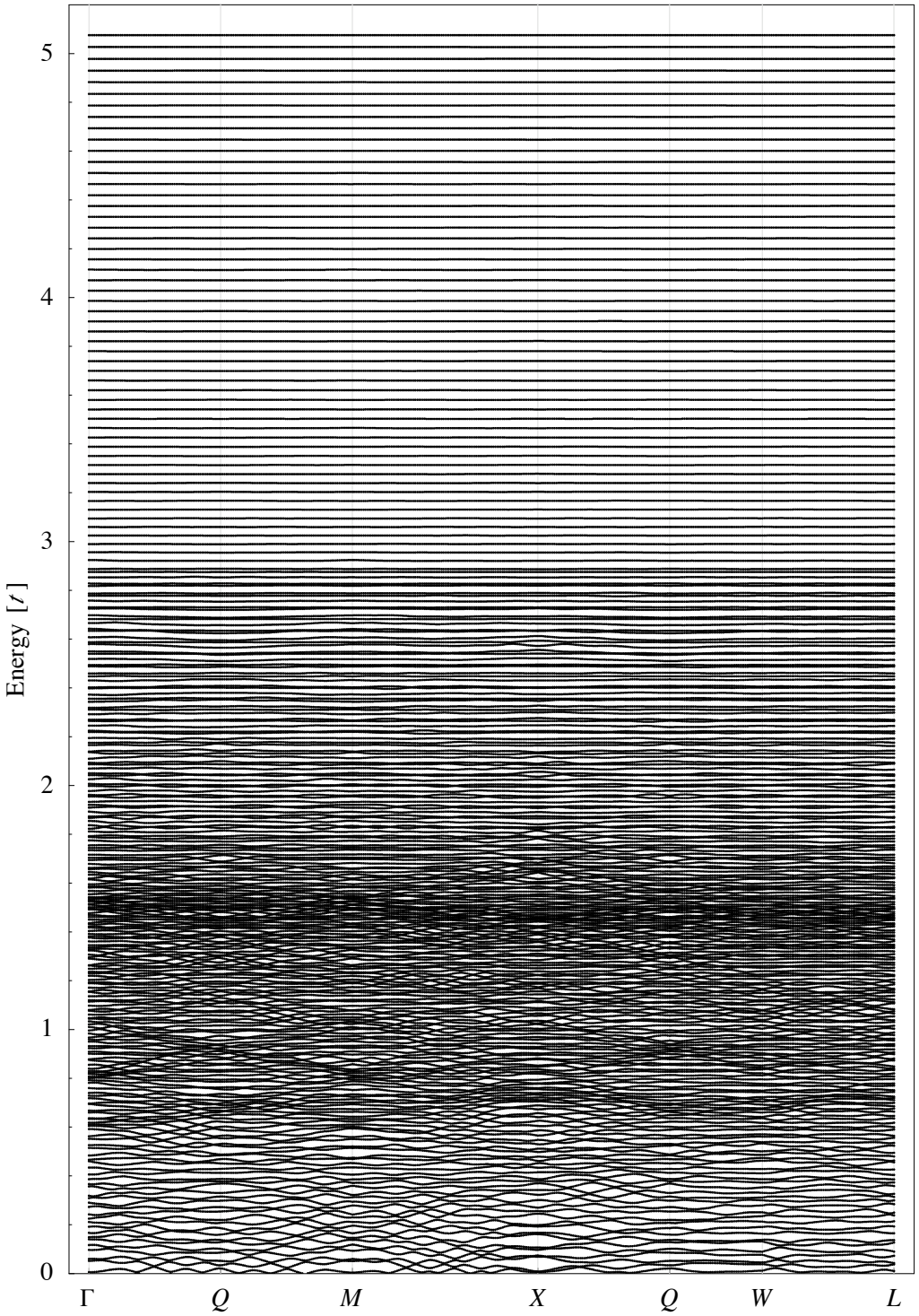

Figure 19.4: Spectrum along a walk in the magnetic BZ, shown in Fig. 18.1(b) for a modified d-wave pairing with the parameters $\tau = 0.1$, $\nu = 0.6$, $\Delta_0 = t$ and $\epsilon_F = -1.1t$. The magnetic unit cell has a size of $16\delta \times 16\delta$.

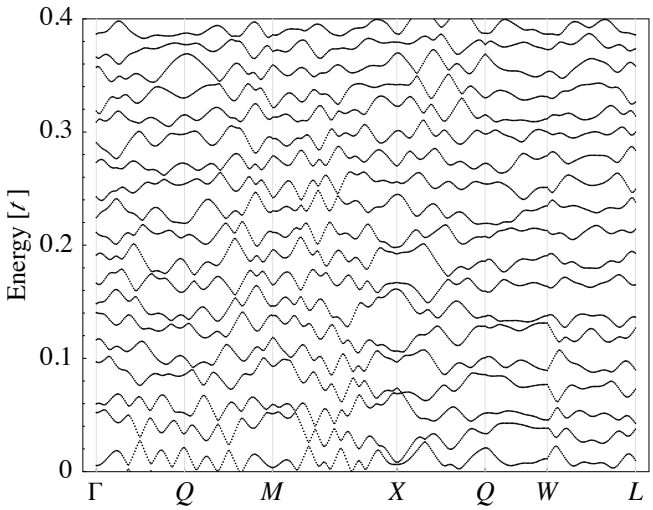

Figure 19.5: Zoom into the low energy spectrum for modified d-wave pairing, parameters are the same as in Fig. 19.4.

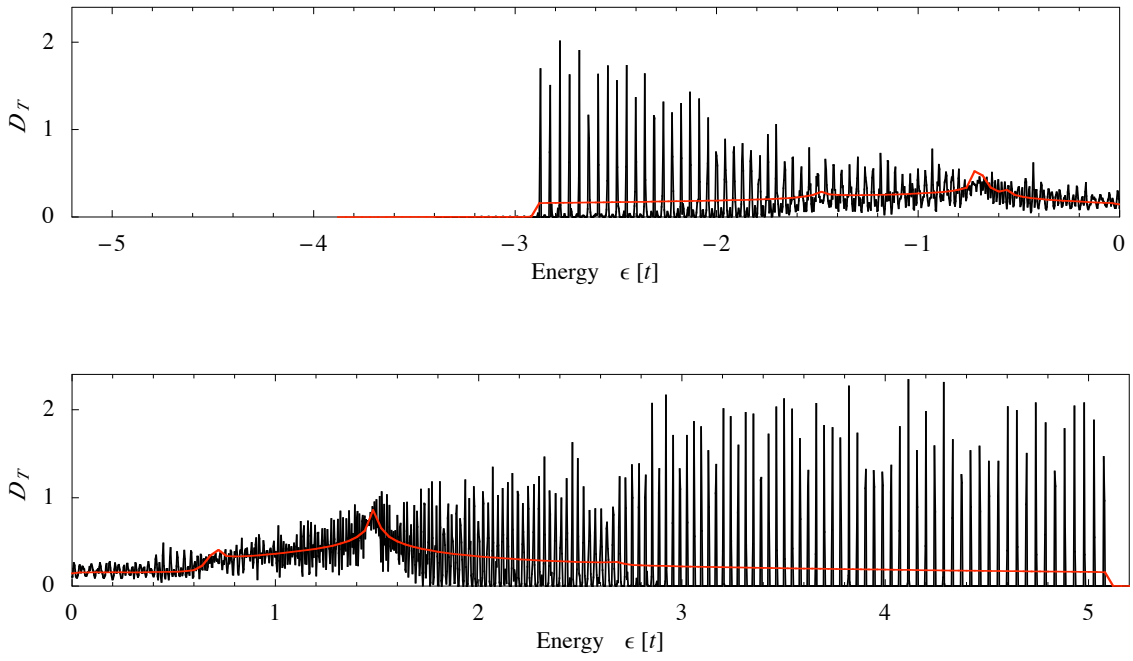

Figure 19.6: Tunneling DOS for a modified d-wave pairing in the presence of a magnetic field (black) and without magnetic field (red). Parameters are the same as in Fig. 19.4.

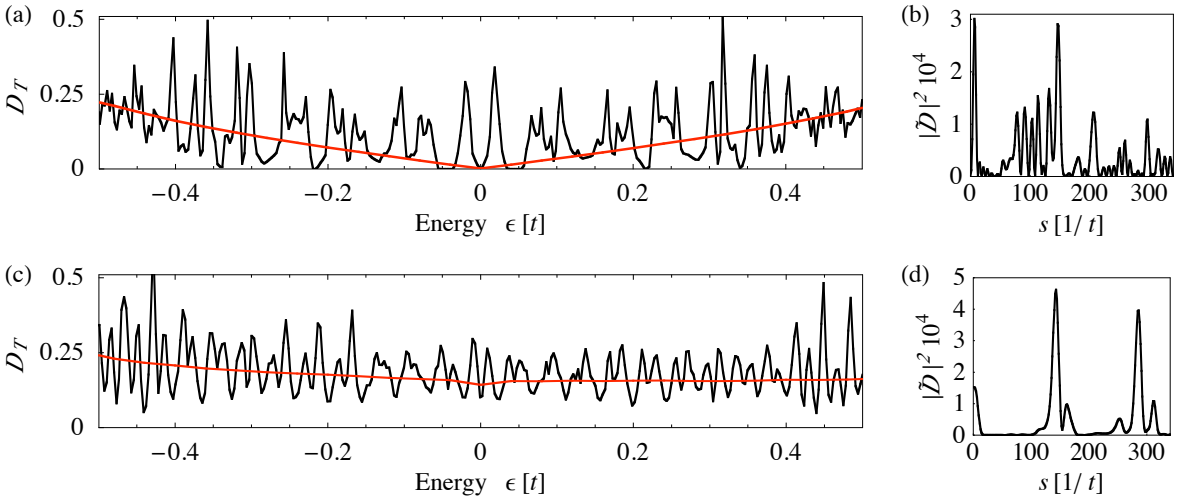

Figure 19.7: Zoom into the low energy part of the density of states for (a) ordinary (compare Fig. 19.3) and (c) modified d-wave pairing (compare Fig. 19.6) with (black) and without (red) magnetic field. The two panels on the right-hand side show the corresponding power spectrum $|\widetilde{D}(s)|^2$ for ordinary (b) and modified (d) pairing.

Unless otherwise noted numerical data are shown for a 16×16 unit cell. For magnetic fields in the experimental regime results are qualitatively the same. We consider a system of finite size with $(N_{ux} = 80) \times (N_{uy} = 80)$ unit cells, which determines the number of states in the magnetic unit cell and therefore the resolution of the DOS.

Ordinary d-wave superconductivity in the mixed state was already discussed by Vafek et al. (2001). In this reference, only the low-energy part of the spectrum is shown. We, however, compute the full spectrum, Figs. 19.1 and 19.2, and the complete tunneling DOS, Fig. 19.3. The spectrum is symmetric with respect to $\epsilon = 0$, and it is sufficient to show only the positive energy range. The asymmetry in the tunneling DOS D_T, produced by the broken particle-hole symmetry ($\epsilon_F = -1.1t$), arises from the Bogoliubov prefactors $|u_{\mathbf{k}}|^2$ and $|v_{\mathbf{k}}|^2$, which are related to the eigenvectors of the Hamiltonian (18.28). The spectrum of a modified d-wave pairing with the pairing function defined by Eq. (17.3) is plotted in Figs. 19.4 and 19.5, the corresponding tunneling DOS is shown in Fig. 19.6. In all cases the spectrum is plotted for a specific walk in the magnetic BZ, shown in Fig. 18.1(b).

At energies much larger than Δ_0, the off-diagonal matrix elements become irrelevant and a regular level structure evolves, similar to Landau levels. In the limit $\Delta_0 \ll t$, the Landau level frequency observed at higher energies ϵ is expected to correspond to the frequency that would be obtained from the semiclassical analysis discussed in Sec. 16.2.

Zooming into the low-energy part of the DOS around the Fermi level reveals the crucial difference between ordinary and modified d-wave pairing: As we can see in the two left panels in Fig. 19.7, the former one shows an irregular structure, whereas for the latter one an oscillatory behavior is observed. This behavior will be quantitatively studied in the next section.

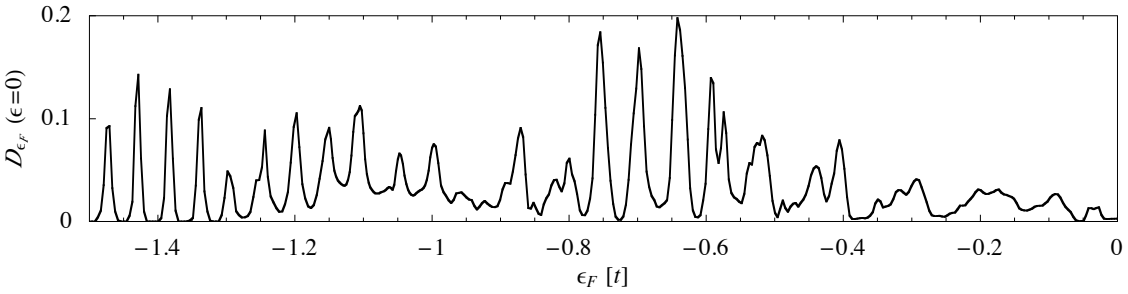

Figure 19.8: DOS as a function of ϵ_F at the Fermi level for $\nu = 0.6$, $\tau = 0.1$ and a $16\delta \times 16\delta$ unit cell.

19.2 Frequency analysis

The observed oscillatory behavior around the Fermi level for the modified d-wave pairing, Fig. 19.7(c), implies oscillations in most of the physical observables. Before analyzing the frequency behavior quantitatively, we first note, that in the absence of superconductivity the following relation holds:

$$D_{\epsilon_F}(\epsilon) = \frac{1}{\mathcal{N}} \sum_{\mathbf{k}} \delta(\epsilon - (\epsilon_{\mathbf{k}} - \epsilon_F)) = D_0(\epsilon + \epsilon_F)\,, \tag{19.1}$$

where $D_{\epsilon_F}(\epsilon)$ denotes the density of states at energy ϵ and Fermi level ϵ_F. It implies the fact that oscillations (i) in the DOS $D(\epsilon)$ for a fixed value of ϵ_F and (ii) in the DOS as a function of ϵ_F, $D_{\epsilon_F}(\epsilon = 0)$, at the Fermi level are equivalent. In the presence of superconductivity this relation is no longer valid and we have to differentiate between these two functions. A plot of $D_{\epsilon_F}(\epsilon = 0)$ is depicted in Fig. 19.8, showing clear deviations from $D_{\epsilon_F=-1.1t}(\epsilon)$, Fig. 19.7(c), while the set of parameters stays the same.

The qualitative observation of oscillatory behavior in the DOS for modified d-wave pairing can now be furnished by considering the power spectrum. Details for its calculation are discussed in Appendix K. The power spectrum (Fig. 19.7(d)) for the DOS depicted in Fig. 19.7(c) reveals peaks at the dominating frequency and its higher harmonics. By contrast, the power spectrum for ordinary d-wave pairing, Fig. 19.7(b), does not show a distinct peak, but rather has contributions from many different frequencies.

In the following we systematically study how the dominating frequency depends on the arc length ν, the magnetic field B and the gap parameter Δ_0, while comparing to the results of the semiclassical analysis presented in (Pereg-Barnea et al.), whose basic ideas are sketched in Appendix L. In the semiclassical approach, a frequency

$$F_\epsilon = \frac{\theta_a}{\pi \hbar \omega_c} \tag{19.2}$$

is found for energy oscillations in the DOS and a frequency

$$F = \Delta_0 \frac{(\pi/2 - \theta_a) m_c}{\pi \hbar e} \tag{19.3}$$

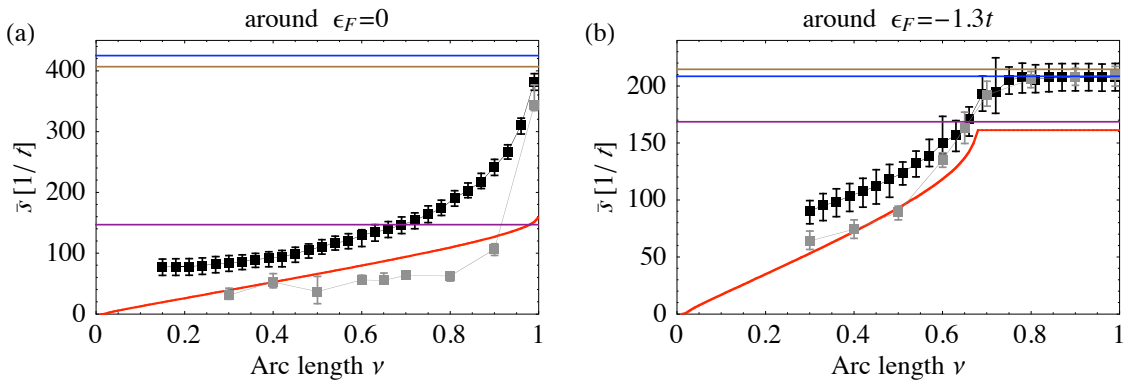

Figure 19.9: Dominating frequency $\bar{s}$ as a function of ν for oscillations in $D_{\epsilon_F=\text{const}}(\epsilon)$ (black squares) and in $D_{\epsilon_F}(\epsilon = 0)$ (gray squares) around $\epsilon_F = 0$ (panel a) and $\epsilon_F = -1.3t$ (panel b). The error bars denote the full width at half maximum of the corresponding peak in the power spectrum. The used parameters are $\Delta_0/t = 1$ and $\tau = 0.1$. The size of the magnetic unit cell is $16 * 16$, implying a magnetic field of $B = 101$T. The red plot represents the semiclassical result, Eq. (19.2), with $m_c = 3m_e$, where m_e is the bare electron mass. The blue, brown and purple colored horizontal lines represent frequencies extracted in specific limits; for a detailed explanation see text.

for oscillations in the DOS as a function of inverse magnetic field, where m_c is the cyclotron mass, $\omega_c = eB/m_c$ the cyclotron frequency and e the electron charge. The parameter θ_a describes the angular size of the arc and is directly associated to the arc length ν by a function $\theta_a(\nu)$, which is approximately linear for small to intermediate values of ν.

An overview, how the first harmonic, denoted in the following by $\bar{s}$, depends on the arc length ν is given in Fig. 19.9: Oscillations both as a function of ϵ_F and ϵ are studied. In addition to these results further frequencies are shown for comparison:

brown: By considering the underlying Fermi surface in the absence of pairing and at zero magnetic field, a semiclassical frequency can be extracted following the Onsager relation, Eq. (16.14). A Taylor expansion of the Fermi surface volume $\mathcal{A}^{\text{mom}}(\epsilon_F)$ in ϵ_F up to first order leads to $\mathcal{A}^{\text{mom}}(\epsilon_F) \approx \mathcal{A}_0 + \mathcal{A}_1(\epsilon_F - \epsilon_{F0})$, where $\epsilon_{F0} = 0$ and $-1.3t$, respectively. The semiclassical frequency is given by $\hbar\mathcal{A}_1/e$.

purple: This frequency is extracted from the DOS $D(\epsilon)$ in the limit $\epsilon \gg \Delta_0$. In this regime the DOS shows the signatures of Landau level quantization, compare e.g. Fig. 19.6.

blue: While using the developed framework of the FT gauge transformation and setting Δ_0 to zero, this frequency can be extracted from the oscillations in $D(\epsilon)$ around the Fermi level.

A few remarks are in order:
(i) While approaching the limit of ordinary d-wave for $\nu \to 0$ the oscillatory behavior breaks down and no frequency can be extracted from the data. The oscillations in $D(\epsilon)$ saturate to a constant in this limit.
(ii) All frequencies shown in Fig. 19.9 vary with ϵ_F, which is related to the doping level.

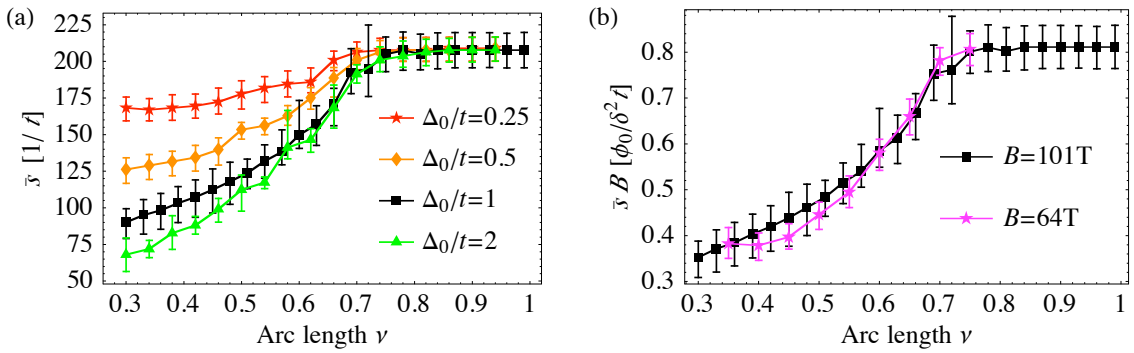

Figure 19.10: (a) Dominating frequency as a function of the arc length ν for different values of the gap parameter Δ_0 for oscillations in $D_{\epsilon_F=-1.3t}(\epsilon)$ around the Fermi level $\epsilon = 0$. ($B = 101$T, $\tau = 0.1$) (b) Dominating frequency scaled the inverse magnetic field, $\bar{s}B$, as a function of ν for oscillations in $D_{\epsilon_F=-1.3t}(\epsilon)$ ($\Delta_0/t = 1$, $\tau = 0.1$).
Please note that the black squares in both plots represent the same data as the ones shown in Fig. 19.9(b).

Experimentally, this is the case as well: $YBa_2Cu_3O_{6.51}$ ($p = 0.1$) exhibits lower frequencies than $YBa_2Cu_4O_8$ ($p = 0.14$).
(iii) The semiclassical frequency (brown line) extracted from the Onsager formula (16.14) matches the frequency obtained from the quantum-mechanical formalism in the limit $\Delta_0 \to 0$ (blue line).
(iv) The two limits $\nu \to 1$ and $\Delta_0 \to 0$ are equivalent. Thus the black squares converge to the blue line for $\nu \to 1$.
(v) For $\epsilon_F = -1.3t$ the frequency behavior in $D_{\epsilon_F}(0)$ (gray squares) resembles the one in $D_{\epsilon_F=\text{const.}}(\epsilon)$ (black squares). At half filling the $\bar{s}(\nu)$ functions have a different structure.

The semiclassical frequency F_ϵ, Eq. (19.2), translates into

$$\bar{s}(\nu) = 2\pi F_\epsilon = \frac{2m_c\theta_a(\nu)}{eB\hbar} \tag{19.4}$$

and is represented by a red line in Fig. 19.9. It shows good agreement with the oscillations as a function of ν for both considered values of ϵ_F. Its saturation to a constant value for high ν in Fig. 19.9(b) results from the structure of the function $\theta_a(\nu)$: For $\epsilon_F = -1.3t$ and $\nu \gtrsim 0.65$, a gapped region is still present in the system, however it does not have contact with the underlying Fermi surface, leading to $\theta_a = \pi/2$.

In contrast to the semiclassical result F_ϵ, the frequencies extracted from the lattice model exhibit a gap dependence, depicted in Fig. 19.10(a), which saturates in the limit of large Δ_0. This is consistent with the fact that the semiclassical analysis requires the condition $\epsilon \ll \Delta_0$ and therefore only holds in the limit of large Δ_0. Furthermore, we observe a linear scaling of the frequencies with inverse magnetic field, compare Fig. 19.10(b), which is in agreement with the B-dependence of F_ϵ.

In experiments the oscillations are observed as a function of inverse magnetic field, which leads

to complications within our theoretical setup: Varying the magnetic field is accomplished by changing the size of the magnetic unit cell. It appears that the DOS value at the Fermi level, $D(0)$, is sensitive to the vortex position. Due to this commensurability effect it is only reasonable to compare configurations, where the vortices sit at the same position within a plaquette, which is only the case for magnetic unit cells, where $N_{s,i}$ is an integer multiple of 4. In the range between 40 and 100 T only three data points can be studied, which clearly does not allow a direct observation of $1/B$ oscillations. This commensurability effect is not of experimental relevance, since disorder effects lead to vortex pinning, which destroys the vortex lattice and a vortex liquid evolves.

For a normal metal as well as for an ordinary d-wave superconductor it is valid to draw conclusions from energy-oscillations to magnetic field-oscillations. A scaling analysis for a metal tells us that for fixed filling three energy scales exist in this problem: the Fermi level ϵ_F, the temperature T and the magnetic field B. Therefore the DOS is a function of the dimensionless ratios between these energy scales $\mathcal{D}(\epsilon_F/B, B/T)$, which reduces to $\mathcal{D}(\epsilon_F/B)$ for fixed temperature. Oscillations in ϵ_F can directly be mapped onto oscillations in $1/B$.

In a d-wave superconductor the situation is different, but another type of scaling can be found, developed by Simon and Lee (1997) and discussed in the context of quantum oscillations by Melikyan and Vafek (2008). This Simon-Lee scaling is based on the existence of Dirac cones, which are present in the spectrum of a d-wave superconductor at the nodal points.

None of these two cases can directly be applied to the considered case of a Fermi arc metal. However, the semiclassical approach, which is furnished by our numerical results for the lattice model, is able to predict the oscillation frequency as a function of inverse magnetic field. In order to give an estimate for this frequency, we plug in experimentally achieved values for Δ_0 and m_c: For $\Delta_0 = 80\text{meV}$ (Hossain et al., 2008), $m_c = 3m_e$ (Bangura et al., 2008), where m_e is the bare electron mass, and $\theta_a = \pi/4$, the resulting frequency $F = 518\text{T}$ lies int the range of the experimentally observed frequency $500 \pm 20\text{T}$ (Sebastian et al., 2008). Please note that the value used for the cyclotron frequency is a result from a fit to the Onsager-Lifshitz picture and, since the Fermi surface cannot be measured in the relevant regime, the value for θ_a is also dressed with uncertainty. Nevertheless, this first estimate shows that the semiclassical result is able to produce frequencies in the experimental range.

19.3 Spatially resolved DOS

Experiments for scanning tunneling microscopy (STM) were conducted for several high-temperature superconductors in the presence and absence of a magnetic field (a review is given by Fischer et al. (2007)) and are able to produce a map of the local density of states (LDOS) at the Fermi level, which reveals the positions of impurities and vortices. The differential tunneling conductance dI/dV as a function of the applied voltage V between the STM tip and the sample at a specific point $\mathbf{r}$ of the sample, where $I(V)$ is the tunneling current, corresponds to the LDOS at $\mathbf{r}$.

The local tunneling DOS is defined by

$$D_T(\mathbf{r}, \epsilon) = \frac{1}{\mathcal{N}} \sum_{\mathbf{k}} \left(|u_{\mathbf{k}}(\mathbf{r})|^2 \delta(\epsilon - E_{\mathbf{k}}) + |v_{\mathbf{k}}(\mathbf{r})|^2 \delta(\epsilon + E_{\mathbf{k}}) \right) , \tag{19.5}$$

(a)

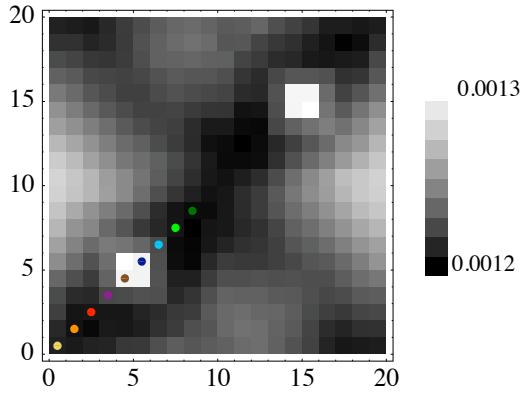

(b)

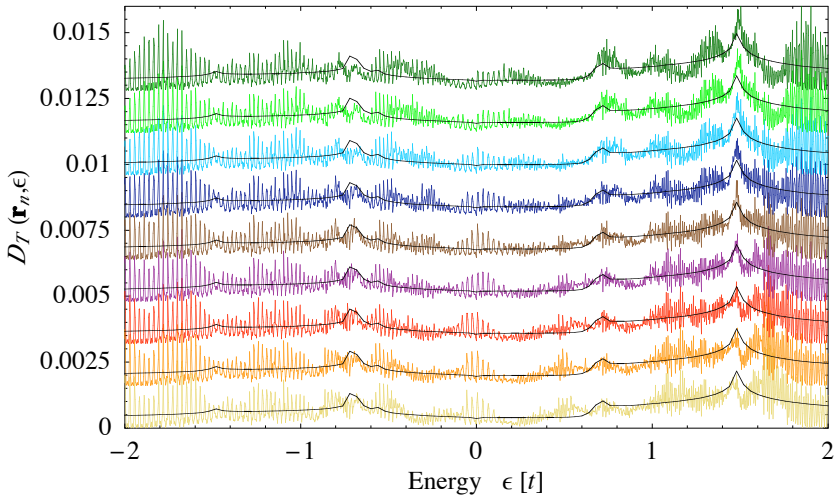

Figure 19.11: (a) Density plot of the local tunneling density of states at the Fermi level $D_T(\mathbf{r}, \epsilon = 0)$ for a 20×20 unit cell with $\epsilon_F = -1.1t$, $\nu = 0.6$, $\tau = 0.1$ and $\Delta_0 = t$. Lattice sites are located in the center of the squares. The vortices are sitting close to the center of a plaquette, slightly shifted by an irrational fraction of the lattice spacing and are accompanied by an enhanced DOS (bright regions). (b) Local DOS tunneling spectra as a function of energy. The various spectra are taken along a line across a vortex, compare to the corresponding sites shown in (a), and have an offset of 0.0016 for clarity. The averaged local tunneling DOS at zero magnetic field (black curve) is shown for comparison.

where $|u_{\mathbf{k}}(\mathbf{r})|^2$ and $|v_{\mathbf{k}}(\mathbf{r})|^2$ can be extracted from the eigenvectors of the Bogoliubov-de Gennes Hamiltonian (18.28). Our numerical results enable us to plot a LDOS map, compare Fig. 19.11(a). The resolution is restricted to the number of lattice sites per magnetic unit cell. Furthermore, we show the corresponding local tunneling DOS spectra, Fig. 19.11(b), along a line across a vortex core. In experiment this would correspond to differential tunneling conductance spectra. The positions of the two vortices in the magnetic unit cell are clearly distinguishable - the LDOS near the vortex core is enhanced (lighter color). The slight asymmetry is due to a small constant shift of the vortices along the x-direction by an irrational fraction of the lattice spacing, see discussion above.

Maggio-Aprile et al. (1995) were the first to observe vortices with STM in a high-temperature superconductor. In the vortex core region they recognized a vanishing of the coherence peaks, which shows the suppression of the superconducting order parameter in the vicinity of a vortex. Since the amplitude Δ_0 of the superconducting order parameter is not acquired from a self-consistent calculation, but set to a fixed value for all sites, its suppression in the vicinity of a vortex core is not describes by the theoretical setup. Furthermore, the magnetic field strength of 64 T, determined by the 20×20 magnetic unit cell, is more than a factor of 10 higher than in the experiment conducted by Maggio-Aprile et al. The peak features in Fig. 19.11(b) are washed out by the wiggles resulting from the magnetic field.

19.4 Summary

The numerical results for the spectrum and the density of states were obtained from diagonalizing the gauge transformed Bogoliubov-de Gennes Hamiltonian in $\mathbf{k}$ space, Eq. (18.28). For the modified d-wave pairing the density of states exhibits oscillatory behavior in the vicinity of the Fermi level, while such a property is not seen for ordinary d-wave pairing. The extracted frequencies depend on the arc length ν and the gap parameter Δ_0, and scale with inverse magnetic field. Commensurability effects prevent a direct observation of oscillations as a function of the inverse magnetic field. The agreement with the semiclassical analysis by (Pereg-Barnea et al.) is shown, which is able to recover the experimental results.

20 Conclusion

This part of the thesis was concerned with quantum oscillations in the underdoped regime of cuprate superconductors. While semiclassical arguments for normal metals lead to the well-established paradigm that quantum oscillations are connected to the existence of a closed Fermi surface, this study shows that also truncated segments of a Fermi surface can imply oscillatory behavior.

The considered theoretical setup describes a type-II superconductor in a magnetic field leading to an Abrikosov vortex lattice and a pairing gap that produces Fermi arcs. The shape of the pairing gap is based on a phenomenological ansatz reflecting the properties observed in ARPES measurements. Numerical diagonalization of the gauge-transformed Hamiltonian in $\mathbf{k}$ space reveals oscillations in the density of states with a frequency that depends on the length of the arc and the size of the maximum gap. The frequencies scale linearly with the inverse magnetic field. The oscillatory behavior breaks down when the Fermi arcs shrink to nodal points, which correspond to an ordinary d-wave pairing.

The used method only allows for the observation of oscillations as a function of energy, while for the comparison with experimental date their relation to oscillations as a function of inverse magnetic field becomes necessary. The acquired results are in good agreement with the semiclassical analysis by (Pereg-Barnea et al.), which significantly deviates from the conventional Onsager-Lifshitz picture: The occurring frequency is not associated with an area in momentum space, but with the periodic appearance of Andreev bound states. Semiclassics is able to extract a frequency for magnetic field oscillations that recovers the experimental result for the dominating frequency F_α. At this stage there is no prediction for a second, higher frequency with lower amplitude. In order to confirm the semiclassical approach in a fully quantum-mechanical treatment, further investigation is needed, e.g. by considering a vortex liquid, for which the density of states can be found by a transfer matrix method (Lee and Fisher, 1981).

Altogether, the suggested model provides a possible scenario synthesizing the Fermi arc picture arising from ARPES measurements with the observation of quantum oscillations in the underdoped regime of cuprates. The direct observation of Fermi arcs at low temperature and high magnetic field would be able to confirm this picture.

I Bond phase

In this appendix we discuss how the bond phase $\varphi(\mathbf{r}_m, \mathbf{r}_n)$ is expressed in terms of on-site phases in the case of longer-ranged Cooper pairs. This simplifies the formulation of a Bogoliubov-de Gennes Hamiltoninan.

In BCS theory the order parameter $\Delta_{mn} = D_{mn} e^{\mathrm{i}\varphi_{m,n}}$ (with $\varphi_{m,n} \equiv \varphi(\mathbf{r}_m, \mathbf{r}_n)$ for simplicity) is determined as the self-consistent solution of the gap equation. For a nearest-neighbor interaction producing the superconducting instability, the phase $\varphi_{m,n}$ is naturally defined on a bond of nearest neighbored sites (m, n). If the Cooper pair is located far away from a vortex core, $\varphi_{m,n}$ can be expressed by the phases ϕ_m and ϕ_n, which are associated to the sites m and n. For the choice of averaging over all neighboring sites

$$e^{\mathrm{i}\phi_m} = \frac{1}{4} \sum_{\sigma} e^{\mathrm{i}\varphi_{m,m+\sigma}} \tag{I.1}$$

the replacement

$$e^{\mathrm{i}\varphi_{m,n}} \to e^{\mathrm{i}(\phi_m + \phi_n)/2} \tag{I.2}$$

is correct in first order lattice derivatives of ϕ (Vafek et al., 2001).

Considering an arbitrary pairing that is not restricted to nearest neighbored sites, the corresponding underlying interaction is longer-ranged. In the simplest case this interaction is distance-dependent and the phase $\varphi_{m,n}$ lives on the straight line connecting the points m and n. It can be expressed as the sum of phases over neighboring bonds, i.e.,

$$\varphi_{m,n} = \varphi_{m,\ell_1} + \varphi_{\ell_1,\ell_2} + \ldots + \varphi_{\ell_N,n} \,, \tag{I.3}$$

where the sites ℓ_α and $\ell_{\alpha+1}$ ($\alpha = 0, \ldots, N+1$ with $\ell_0 = m$ and $\ell_{N+1} = n$) are nearest neighbors. The Cooper pairs might not be localized in comparison to the vortex core, but rather be extended in space. Nevertheless we assume that Eq. (I.2) can be generalized to arbitrary links m, n as

$$\varphi_{m,n} = \frac{1}{2}(\phi_m + \phi_n) \,. \tag{I.4}$$

J Superfluid velocity and phase factors

J.1 Superfluid velocity

The superfluid velocity serves as a vector potential for the effective magnetic field seen by quasi-particles and quasi-holes after a gauge transformation was applied. The specific shape depends on the considered form of the gauge transformation.

J.1.1 Standard gauge transformation

This section provides a detailed derivation of an expression for the superfluid velcocity $\mathbf{v}_s$ in terms of the vortex positions $\{\mathbf{r}_i\}$ by using the definition of $\mathbf{v}_s$, Eq. (18.13), and the London equation (18.7), compare (Tinkham, 1975).

The London equation has an explicit solution in Fourier space for the magnetic field

$$\mathbf{B}_\mathbf{k} = \frac{1}{2}\phi_0 \widehat{z} \frac{\sum_i e^{-\mathrm{i}\mathbf{k}\mathbf{r}_i}}{1+\lambda^2 k^2} \tag{J.1}$$

with $\mathbf{B}(\mathbf{r}) = (2\pi)^{-2} \iint_{-\infty}^{\infty} d^2k e^{\mathrm{i}\mathbf{k}\mathbf{r}} \mathbf{B}_\mathbf{k}$. By using Eq. (18.6) and the relation $\mathbf{B}(\mathbf{r}) = \nabla \times \mathbf{A}$ the curl of $\mathbf{v}_s$ reads

$$\nabla \times \mathbf{v}_s(\mathbf{r}) = \frac{\pi\hbar}{m} \sum_i \delta(\mathbf{r}-\mathbf{r}_i) - \frac{e}{m}\mathbf{B}\,, \tag{J.2}$$

which becomes

$$\mathrm{i}\mathbf{k} \times \mathbf{v}_{s\mathbf{k}} = \frac{\pi\hbar}{m} \widehat{z} \sum_i e^{-\mathrm{i}\mathbf{k}\mathbf{r}_i} - \frac{e}{m}\mathbf{B}_\mathbf{k} \tag{J.3}$$

upon Fourier transforming. Since the relation $\mathrm{i}\mathbf{k} \times (\mathrm{i}\mathbf{k} \times \mathbf{v}_{s\mathbf{k}}) = k^2 \mathbf{v}_{s\mathbf{k}}$ holds, taking the vector product with $\mathrm{i}\mathbf{k}$ on both sides of the equation projects out the result for $\mathbf{v}_{s\mathbf{k}}$. Plugging in Eq. (J.1) and Fourier transforming into real space provides the desired result

$$\mathbf{v}_s(\mathbf{r}) = \frac{\pi\hbar}{m} \int \frac{d^2k}{(2\pi)^2} \frac{\mathrm{i}\mathbf{k} \times \widehat{z}}{\lambda^{-2}+k^2} \sum_i e^{\mathrm{i}\mathbf{k}(\mathbf{r}-\mathbf{r}_i)}\,. \tag{J.4}$$

J.1.2 Franz-Tešanović gauge transformation

Similar to the case of a standard gauge transformation discussed in the previous subsection, the superfluid velocity for a FT-tranformed system

$$\mathbf{v}_s^\mu = \frac{\hbar}{m}\nabla\phi_\mu - \frac{e}{m}\mathbf{A} \tag{J.5}$$

can be rewritten as a **k**-space integral. In the intermediate regime of the vortex state the Fourier transformed solution of the London equation (J.1) is known, and therefore the Fourier transform of

$$\nabla \times \mathbf{v}_s^\mu(\mathbf{r}) = \frac{2\pi\hbar}{m}\left(\widehat{z}\sum_i \delta(\mathbf{r}-\mathbf{r}_i^\mu) - \frac{\mathbf{B}}{\phi_0}\right), \tag{J.6}$$

is given by

$$\mathrm{i}\mathbf{k} \times \mathbf{v}_{s\mathbf{k}}^\mu = \frac{2\pi\hbar}{m}\left(\widehat{z}\sum_i e^{-\mathrm{i}\mathbf{k}\mathbf{r}_i^\mu} - \frac{\mathbf{B}_\mathbf{k}}{\phi_0}\right). \tag{J.7}$$

As above, we build the vector product with i**k** on both sides of the equation and use Eq. (J.1), which leads to

$$\mathbf{v}_s^A = \frac{2\pi\hbar}{m}\iint_{-\infty}^{\infty}\frac{d^2k}{(2\pi)^2}\frac{\mathrm{i}\mathbf{k}\times\widehat{z}}{k^2}\left(\mathfrak{A}_\mathbf{k} - \frac{1}{2}\frac{\mathfrak{A}_\mathbf{k}+\mathfrak{B}_\mathbf{k}}{1+\lambda^2k^2}\right)e^{\mathrm{i}\mathbf{k}\mathbf{r}}, \tag{J.8}$$

where we introduced the shortcuts $\mathfrak{A}_\mathbf{k} = \sum_i e^{-\mathrm{i}\mathbf{k}\mathbf{r}_i^A}$ and $\mathfrak{B}_\mathbf{k} = \sum_i e^{-\mathrm{i}\mathbf{k}\mathbf{r}_i^B}$. In the limit of $\lambda^2k^2 \sim \lambda^2/d^2 \gg 1$ (d being the intervortex distance), which is satisfied in the considered regime, the brackets can be approximated by $A_\mathbf{k}(\lambda^{-2}+k^2)^{-1}$. Since a similar relation holds for $\mathbf{v}_s^B$, these results can be combined to

$$\mathbf{v}_s^\mu = \frac{2\pi\hbar}{m}\int\frac{d^2k}{(2\pi)^2}\frac{\mathrm{i}\mathbf{k}\times\widehat{z}}{\lambda^{-2}+k^2}\sum_i e^{\mathrm{i}\mathbf{k}(\mathbf{r}-\mathbf{r}_i^\mu)}. \tag{J.9}$$

J.2 Vortex lattice and the Fourier space

This section is concerned with the description of the Fourier space and the simplifications for the Fourier transform in the presence of a periodic vortex arrangement depicted in Fig. 18.1(a).

In the absence of vortices the unit cell contains one site of the underlying lattice and covers the area δ^2, where δ is the lattice spacing. In **k** space the corresponding first Brillouin zone (BZ) covers the area $(0, 2\pi/\delta)\times(0, 2\pi/\delta)$. In the presence of vortices the new, magnetic unit cell comprises $N_s = N_{sx}N_{sy}$ lattice sites, where N_{si} denotes the number of sites in ith direction. We introduce a set of vectors $\{\mathbf{R}\}$ pointing to each magnetic unit cell in the system. The total system is composed of $N_u = N_{ux}N_{uy}$ magnetic unit cells.

The first magnetic BZ is $(0, 2\pi/(N_{sx}\delta))\times(0, 2\pi/(N_{sy}\delta))$. The **k** states therein are given by

$$k_i = 2\pi\frac{m_i}{N_{ui}N_{si}}, \tag{J.10}$$

with $m_i \in [0\ ,\ N_{ui})$, $m_i \in \mathbb{Z}$. The reciprocal vectors of the vortex lattice, **G**, fulfilling $e^{\mathrm{i}\mathbf{G}\mathbf{R}} = 1$ are

$$G_i = 2\pi\frac{n_i}{N_{si}}. \tag{J.11}$$

For $n_i \in [0, N_{si})$, $n_i \in \mathbb{Z}$ the vectors $\mathbf{G}$ lie within the original first BZ.

A Fourier transform for a non-periodic system is accomplished by

$$f(\mathbf{r}) = \iint_{-\infty}^{\infty} \frac{d^2k}{(2\pi)^2} e^{\mathrm{i}\mathbf{k}\mathbf{r}} f(\mathbf{k}). \tag{J.12}$$

If the function $f(\mathbf{r})$ only has non-zero values at the lattice sites $\mathbf{r}_i$, this expression can be reduced to

$$f(\mathbf{r}) = \frac{1}{N_u N_s \delta^2} \sum_{\mathbf{k}} e^{\mathrm{i}\mathbf{k}\mathbf{r}} f(\mathbf{k}), \tag{J.13}$$

where $\mathbf{k}$ runs over all states in the original first BZ. By further assuming that $f(\mathbf{r})$ is periodic with the magnetic unit cell, i.e., $f(\mathbf{r}_i + \mathbf{R}) = f(\mathbf{r}_i)$, we can write

$$f(\mathbf{r}) = \frac{1}{N_s \delta^2} \sum_{\mathbf{G}} e^{\mathrm{i}\mathbf{G}\mathbf{r}} f(\mathbf{G}), \tag{J.14}$$

with the reciprocal lattice vectors $\mathbf{G}$ restricted to the original first BZ.

The following relation will be very useful:

$$\iint_{-\infty}^{\infty} \frac{d^2k}{(2\pi)^2} \sum_i e^{-\mathrm{i}\mathbf{k}\mathbf{r}_i^\mu} f(\mathbf{k}) = \frac{1}{N_s \delta^2} \sum_{\mathbf{G}} e^{-\mathrm{i}\mathbf{G}\bar{\mathbf{r}}^\mu} f(\mathbf{G}), \tag{J.15}$$

where $\bar{\mathbf{r}}^\mu$ is the offset of the vortex position to a specific corner of the unit cell. Since $f(\mathbf{k})$ is an arbitrary function, the number of $\mathbf{G}$ vectors contributing to this sum is infinite, but for practical purposes the summation goes up to a cutoff with $|G_x| < G_{\max}$ and $|G_y| < G_{\max}$.

J.3 The hopping phase

The FT-transformed Hamiltonian $\mathcal{H}_N$ exhibits a hopping phase $\nu_{\boldsymbol{\delta}}^\mu$ in the diagonal block. It is equivalent to a line integral over the superfluid velocity $\mathbf{v}_s^\mu$, Eq. (18.21), for which an explicit expression was found via the London equation for intermediate field values, Eq. (18.7). Thus, we can write

$$\nu_{\boldsymbol{\delta}}^\mu(\mathbf{r}) = 2\pi \iint_{-\infty}^{\infty} \frac{d^2k}{(2\pi)^2} \frac{1}{\lambda^{-2} + k^2} \sum_i e^{-\mathrm{i}\mathbf{k}\mathbf{r}_i^\mu} \underbrace{\int_{\mathbf{r}}^{\mathbf{r}+\boldsymbol{\delta}} e^{\mathrm{i}\mathbf{k}\mathbf{r}} \begin{pmatrix} \mathrm{i}k_y \\ -\mathrm{i}k_x \end{pmatrix} \cdot d\mathbf{l}}_{\equiv \Gamma_{\boldsymbol{\delta}}(\mathbf{k},\mathbf{r})}, \tag{J.16}$$

where the line integral $\Gamma_{\boldsymbol{\delta}}$ can be easily evaluated as

$$\Gamma_{\boldsymbol{\delta}}(\mathbf{k}, \mathbf{r}) = e^{\mathrm{i}\mathbf{k}\mathbf{r}} \left[-\frac{k_y}{k_x} \left(1 - e^{\mathrm{i}k_x\delta_x} \right) + \frac{k_x}{k_y} \left(1 - e^{\mathrm{i}k_y\delta_y} \right) \right]. \tag{J.17}$$

The singularity in the integrand, occuring in the limit $k_x \to 0$ while $k_y \neq 0$ and vice versa, is removable due to $\lim_{k_x \to 0} \frac{1-e^{\mathrm{i}k_x\delta}}{k_x} = -\mathrm{i}\delta$. A periodic vortex arrangement implies the relation (J.15), which simplifies the result for $\nu^{\mu}_{\boldsymbol{\delta}}(\mathbf{r})$ to

$$\nu^{\mu}_{\boldsymbol{\delta}}(\mathbf{r}) = \frac{2\pi}{N_s\delta^2} \sum_{\mathbf{G}} \frac{1}{\lambda^{-2}+G^2} e^{-\mathrm{i}\mathbf{G}\bar{\mathbf{r}}^{\mu}} \Gamma_{\boldsymbol{\delta}}(\mathbf{G},\mathbf{r}). \tag{J.18}$$

J.4 The off-diagonal phase

The off-diagonal phase in the FT-gauge transformed Hamiltonian $\mathcal{H}_N$ is given by

$$A_{\mathbf{r}_0}(\mathbf{r}) = \frac{1}{2} \int_{\mathbf{r}}^{\mathbf{r}+\mathbf{r}_0} (\nabla\phi_A - \nabla\phi_B)\, d\mathbf{l}\,. \tag{J.19}$$

Following the considerations discussed in Sec. 18.3, we evaluate the line integral along the path straightly connecting the points $\mathbf{r}$ and $\mathbf{r}+\mathbf{r}_0$.

An explicit expression for $\nabla\phi_{\mu}$ can be derived, in analogy to the calculation for $\mathbf{v}^{\mu}_s$ presented in Appendix J.1.2. Fourier transforming Eq. (18.17), taking the vector product with $\mathrm{i}\mathbf{k}$ and Fourier transforming the result backwards leads to

$$\nabla\phi_{\mu}(\mathbf{r}) = 2\pi \iint_{-\infty}^{\infty} \frac{\mathrm{i}\mathbf{k}\times\widehat{z}}{k^2} \sum_i e^{\mathrm{i}\mathbf{k}(\mathbf{r}-\mathbf{r}_i^{\mu})} = \frac{2\pi}{N_s\delta^2} \sum_{\mathbf{G}} \frac{\mathrm{i}\mathbf{G}\times\widehat{z}}{G^2} e^{\mathrm{i}\mathbf{G}(\mathbf{r}-\bar{\mathbf{r}}^{\mu})}\,, \tag{J.20}$$

while exploiting the vortex periodicity in the second equality sign. With this result $A_{\mathbf{r}_0}(\mathbf{r})$ becomes

$$A_{\mathbf{r}_0}(\mathbf{r}) = \frac{\pi}{N_s\delta^2} \sum_{\mathbf{G}} \frac{e^{-\mathrm{i}\mathbf{G}\bar{\mathbf{r}}^A} - e^{-\mathrm{i}\mathbf{G}\bar{\mathbf{r}}^B}}{G^2} \int_{\mathbf{r}}^{\mathbf{r}+\mathbf{r}_0} e^{\mathrm{i}\mathbf{G}\mathbf{r}}\, (\mathrm{i}\mathbf{G}\times\widehat{z})\cdot d\mathbf{l}\,. \tag{J.21}$$

For pairing between nearest neighbored sites like for the p- and d-wave cases studied in Ref. (Vafek et al., 2001), this becomes

$$A_{\boldsymbol{\delta}}(\mathbf{r}) = \frac{\pi}{N_s\delta^2} \sum_{\mathbf{G}} \frac{e^{-\mathrm{i}\mathbf{G}\bar{\mathbf{r}}^A} - e^{-\mathrm{i}\mathbf{G}\bar{\mathbf{r}}^B}}{G^2} \Gamma_{\boldsymbol{\delta}}(\mathbf{G},\mathbf{r}). \tag{J.22}$$

In the case of arbitrary pairing the line integral will be evaluated as follows. In order to optimize the numerical effort we decide on an approach that is based on the fact, that the value of a closed integral over $(\nabla\phi_A - \nabla\phi_B)/2$ is an integer multiple of π depending on the number of encircled vortices. We define a function

$$\Xi(\mathbf{r}_0) = \widetilde{A}_{\mathbf{r}_0}(\mathbf{0})\,, \tag{J.23}$$

where $\widetilde{A}_{\mathbf{r}_0}(\mathbf{r})$ is given by Eq. (J.21) with a line integral along a path connecting the three points $\mathbf{r} = (x, y)^T$, $(x + x_0, y)^T$ and $\mathbf{r} + \mathbf{r}_0 = (x + x_0, y + y_0)^T$. Its evaluation yields

$$\widetilde{A}_{\mathbf{r}_0}(\mathbf{r}) = \frac{\pi}{N_s \delta^2} \sum_{\mathbf{G}} \underbrace{\frac{e^{-\mathrm{i}\mathbf{G}\bar{\mathbf{r}}^B} - e^{-\mathrm{i}\mathbf{G}\bar{\mathbf{r}}^A}}{G^2} e^{\mathrm{i}\mathbf{G}\mathbf{r}} \left[\frac{G_y}{G_x} \left(1 - e^{\mathrm{i}G_x x_0}\right) - \frac{G_x}{G_y} \left(1 - e^{\mathrm{i}G_y y_0}\right) e^{\mathrm{i}G_x x_0} \right]}_{\equiv I(\mathbf{G},\mathbf{r})} . \quad \text{(J.24)}$$

In the limit of G_x and G_y to zero the integrand $I(\mathbf{G}, \mathbf{r})$ becomes

$$\lim_{G_x \to 0} I(\mathbf{G}, \mathbf{r}) = -\mathrm{i} x_0 e^{\mathrm{i}G_y y} \frac{e^{-\mathrm{i}G_y y_B} - e^{-\mathrm{i}G_y y_A}}{G_y}, \quad \text{(J.25a)}$$

$$\lim_{G_y \to 0} I(\mathbf{G}, \mathbf{r}) = \mathrm{i} y_0 e^{\mathrm{i}G_x (x + x_0)} \frac{e^{-\mathrm{i}G_x x_B} - e^{-\mathrm{i}G_x x_A}}{G_x}. \quad \text{(J.25b)}$$

The correct off-diagonal phase is given by

$$A_{\mathbf{r}_0}(\mathbf{r}) = \Xi(\mathbf{r} + \mathbf{r}_0) - \Xi(\mathbf{r}) + n_V \pi \,, \quad \text{(J.26)}$$

where n_V is the number of vortices in the trapezoid spanned by the points $\mathbf{r}$, $\mathbf{r} + \mathbf{r}_0$ and their projection to the x-axis $(x, 0)^T$ and $(x + x_0, 0)^T$, illustrated in Fig. 18.2.

J.5 The magnetic flux through each plaquette

The finite value of the hopping phase $\nu^\mu_{\boldsymbol{\delta}}$ is due to the magnetic flux Φ^μ seen by quasi-particles and quasi-holes, respectively, composed of a uniform part associated with the applied magnetic field and the vortex flux. The total flux per plaquette is given by

$$\Phi^\mu = \frac{m}{\hbar} \oint_C \mathbf{v}^\mu_s \cdot d\mathbf{l} \,, \quad \text{(J.27)}$$

which can be evaluated by using the definition of the superfluid velocity $\mathbf{v}^\mu_s = (\hbar/m)\nabla\phi^\mu - (e/m)\mathbf{A}$, implicitly defined by Eq. (18.19):

$$\Phi^\mu = 2\pi \iint \left(\widehat{z} \sum_i \delta(\mathbf{r} - \mathbf{r}^\mu_i) - \mathbf{B}/\phi_0 \right) d\mathbf{F} = 2\pi (n_\mu - \delta^2 B/\phi_0) \,. \quad \text{(J.28)}$$

Here, Stokes' theorem was used and the integral runs over the area enclosed by the path C. n_μ denotes the number of vortices of type μ sitting inside the plaquette and δ is the lattice spacing.

In order to confirm the validity of the derived expression for the hopping phases $\nu^\mu_{\boldsymbol{\delta}}$, Eq. (18.23), the flux through each plaquette can be calculated by summing over the values of $\nu^\mu_{\boldsymbol{\delta}}$ at the bonds of the plaquette. We consider a specific plaquette, whose lower left corner is given by

$\mathbf{r}_0$:

$$\Phi^\mu = \frac{m}{\hbar}\oint_C \mathbf{v}_s^\mu = \nu^\mu_{\delta\widehat{x}}(\mathbf{r}_0) + \nu^\mu_{\delta\widehat{y}}(\mathbf{r}_0+\delta\widehat{x}) + \nu^\mu_{-\delta\widehat{x}}(\mathbf{r}_0+\delta\widehat{x}+\delta\widehat{y}) + \nu^\mu_{-\delta\widehat{y}}(\mathbf{r}_0+\delta\widehat{y}) \tag{J.29}$$

$$= -\frac{2\pi}{N_s\delta^2}\sum_{\mathbf{G}}\frac{1}{\lambda^{-2}+G^2}\frac{G^2}{G_xG_y}e^{\mathrm{i}\mathbf{G}(\mathbf{r}_0-\bar{\mathbf{r}}^\mu)}\left(1-e^{\mathrm{i}\delta G_x}-e^{\mathrm{i}\delta G_y}+e^{\mathrm{i}\delta G_x+\mathrm{i}\delta G_y}\right). \tag{J.30}$$

In the intermediate regime the penetration depth λ is finite and large. The integrand becomes 0 for $\mathbf{G}\to 0$ and is nearly not influenced by λ for all other $\mathbf{G}$. Therefore, we assume that λ^{-2} can be set to zero for all finite values of $\mathbf{G}$. We rewrite Φ^μ as the sum $\Phi^\mu_{\mathrm{V}}+\Phi^\mu_{\mathrm{BG}}$, where

$$\Phi^\mu_{\mathrm{V}} = -\frac{2\pi}{N_s\delta^2}\sum_{\mathbf{G}}\frac{1}{G_xG_y}e^{\mathrm{i}\mathbf{G}(\mathbf{r}_0-\bar{\mathbf{r}}^\mu)}\left(1-e^{\mathrm{i}\delta G_x}-e^{\mathrm{i}\delta G_y}+e^{\mathrm{i}\delta G_x+\mathrm{i}\delta G_y}\right) \tag{J.31}$$

$$= \pi\left(\mathrm{sign}(x_0-x_\mu)-\mathrm{sign}(x_0-x_\mu+\delta)\right)\left(\mathrm{sign}(y_0-y_\mu)-\mathrm{sign}(y_0-y_\mu+\delta)\right) \tag{J.32}$$

and

$$\Phi^\mu_{\mathrm{BG}} = -\frac{2\pi}{N_s} = -2\pi\frac{B\delta^2}{\phi_0}\,. \tag{J.33}$$

In the last equation we used $B=\phi_0/(N_s\delta^2)$. The magnetic background field carries one magnetic flux quantum per magnetic unit cell with the area $N_s\delta^2$, manifesting itself in the fact that the spatial average of B^μ_{eff} vanishes. Φ^μ_{BG} represents the ($\mathbf{G}=0$)-value of the integrand in Φ^μ_{V} and therefore corresponds to the non-localized background flux, whereas Φ^μ_{V} describes the vortex flux.

We have seen that the magnetic flux per plaquette calculated by using the derived expression for the hopping phase $\nu^\mu_{\boldsymbol{\delta}}$ is consistent with the expected result, providing a cross-check for the calculation in Appendix J.3.

J.6 The inter-unit cell off-diagonal phase $A_{\mathbf{r}_0+\mathbf{R}}(\mathbf{r})$

The phase $A_{\mathbf{r}_0+\mathbf{R}}(\mathbf{r})$ occurring in Eq. (18.29) can be expressed via the function Ξ, introduced in Eq. (J.23) as

$$A_{\mathbf{r}_0+\mathbf{R}}(\mathbf{r}) = \Xi(\mathbf{r}+\mathbf{r}_0+\mathbf{R})-\Xi(\mathbf{r})+\bar{n}_V\pi\,, \tag{J.34}$$

where $\bar{n}_V$ denotes the number of vortices in the polygon bounded by the connection line between the points $\mathbf{r}$ and $\mathbf{r}+\mathbf{r}_0$, the x-axis and the connection lines between the points $\mathbf{r}$ and $\mathbf{r}+\mathbf{r}_0$ and their projection onto the x-axis. This is illustrated in Fig. 18.3. We can further rewrite this phase as

$$A_{\mathbf{r}_0+\mathbf{R}}(\mathbf{r}) = \Xi(\mathbf{r}+\mathbf{r}_0)-\Xi(\mathbf{r})+\Delta\Xi(\mathbf{r}+\mathbf{r}_0+\mathbf{R},\mathbf{r}+\mathbf{r}_0)+\bar{n}_V\pi\,, \tag{J.35}$$

while

$$\Delta\Xi(\mathbf{r}+\mathbf{r}_0+\mathbf{R},\mathbf{r}+\mathbf{r}_0) = \Xi(\mathbf{r}+\mathbf{r}_0+\mathbf{R})-\Xi(\mathbf{r}+\mathbf{r}_0). \tag{J.36}$$

The function $\Delta\Xi$ is determined by using the result for $\widetilde{A}_{\mathbf{r}_0}(\mathbf{r})$, Eq. (J.24). Due to the relations $e^{\mathrm{i}\mathbf{G}\mathbf{R}} = 1$ and $\lim_{G_i\to 0}\left(\left(1-e^{\mathrm{i}G_iR_i}\right)/G_i\right) = -\mathrm{i}R_i$, $\Delta\Xi$ reduces to

$$\Delta\Xi(\mathbf{r}+\mathbf{r}_0+\mathbf{R},\mathbf{r}+\mathbf{r}_0) = \frac{\pi}{N_s\delta^2}\left[\sum_{G_x\neq 0}\frac{e^{-\mathrm{i}G_x\bar{x}_B}-e^{-\mathrm{i}G_x\bar{x}_A}}{G_x}e^{\mathrm{i}G_x(x+x_0)}\mathrm{i}R_y + \right. \\ \left. + \sum_{G_y\neq 0}\frac{e^{-\mathrm{i}G_y\bar{y}_B}-e^{-\mathrm{i}G_y\bar{y}_A}}{G_y}(-\mathrm{i}R_x)\right]. \tag{J.37}$$

The Fourier summation can be carried out analytically in the continuum limit, which leads to the relation

$$\frac{1}{N_{sx}}\sum_{G_x}\frac{e^{\mathrm{i}G_xx}}{G_x} = \frac{\mathrm{i}}{2}\mathrm{sign}(x)\,. \tag{J.38}$$

The expression for $\Delta\Xi$ depends on $\mathbf{r}$, $\mathbf{r}_0$ and the vortex core positions $\bar{\mathbf{r}}_A$ and $\bar{\mathbf{r}}_B$. Without loss of generality we assume

$$\bar{x}_A < \bar{x}_B \qquad \text{and} \qquad \bar{y}_A < \bar{y}_B. \tag{J.39}$$

Therefore, we get

$$\Delta\Xi(\mathbf{r}+\mathbf{r}_0+\mathbf{R},\mathbf{r}+\mathbf{r}_0) = -\frac{\pi}{2}\frac{R_y}{N_{sy}}\mathrm{sign}(x+x_0-\bar{x}_A)\mathrm{sign}(x+x_0-\bar{x}_B) + \frac{\pi}{2}\frac{R_x}{N_{sx}}\,. \tag{J.40}$$

This result can be written in a compact way as

$$\Delta\Xi(\mathbf{r}+\mathbf{r}_0+\mathbf{R},\mathbf{r}+\mathbf{r}_0) \equiv \mathbf{q}_{\mathbf{r}+\mathbf{r}_0}\cdot\mathbf{R}\,, \tag{J.41}$$

and

$$\mathbf{q}_{\mathbf{r}+\mathbf{r}_0} = \frac{\pi}{2}\begin{pmatrix} 1/N_{sx} \\ -\mathrm{sign}(x+x_0-\bar{x}_A)\mathrm{sign}(x+x_0-\bar{x}_B)/N_{sy}\end{pmatrix}. \tag{J.42}$$

The total phase can be summarized as

$$A_{\mathbf{r}_0+\mathbf{R}}(\mathbf{r}) = A_{\mathbf{r}_0}(\mathbf{r}) + \mathbf{q}_{\mathbf{r}+\mathbf{r}_0}\cdot\mathbf{R} + (\bar{n}_V - n_V)\pi\,. \tag{J.43}$$

K Power spectrum

For studying the oscillatory behavior and extracting the dominating frequency from the density of states the power spectrum, the absolute squared of the Fourier transform, is studied. In this appendix we introduce the definition for the Fourier transform given a discrete set of data.

Since the numerical results of the DOS are available for a discrete set of energies ϵ_i for $i = 1, ...N$ with $\epsilon_1 = \epsilon_{\min}$ and $\epsilon_N = \epsilon_{\max}$, we consider the discrete Fourier transform

$$\widetilde{D}(s) = \frac{1}{N} \sum_{i=1}^{N} D(\epsilon_i) e^{-\mathrm{i}s\epsilon_i} \Delta\epsilon, \tag{K.1}$$

where the ϵ_i are equally spaced with distance $\Delta\epsilon$. The power spectrum is given by $|\widetilde{D}(s)|^2$.

Fourier transforming data with a hard cutoff leads to oscillations, which is avoided by an additional Gauss factor smoothening the boundaries:

$$f(\epsilon_i) = \frac{1}{\sqrt{2\pi}\sigma} e^{-\frac{(\epsilon_i - \bar{\epsilon})^2}{2\sigma^2}}. \tag{K.2}$$

It is centered around $\bar{\epsilon}$ and the width is related to the variance σ^2. If σ is much smaller than the width of the data $(\epsilon_{\max} - \epsilon_{\min})$, the Gauss factor serves as a window function located e.g. in the high or low energy range.

The discrete Fourier transform for $D_{\epsilon_F}(\epsilon = 0)$, the DOS at the Fermi level as a function of ϵ_F, is

$$\bar{D}(s) = \frac{1}{N_F} \sum_{i=1}^{N_F} D_{\epsilon_{F,i}}(0) e^{-\mathrm{i}s\epsilon_{F,i}} \Delta\epsilon_F \,, \tag{K.3}$$

where the ϵ_F-values form a discrete set in the range $[\epsilon_{F,1}, \epsilon_{F,N_F}]$, spaced at intervals of $\Delta\epsilon_F$.

Please note that s denotes an angular frequency carrying an additional factor of 2π in contrast to the frequencies F_ϵ and F in Eqs. (19.2) and (19.3).

L Semiclassical analysis

In this appendix we shortly sketch the idea behind the semiclassical analysis of the quantum oscillations in a Fermi arc metal presented in (Pereg-Barnea et al.) and summarize the results for the frequency behavior.

The presence of a superconducting gap in a Fermi arc metal requires a re-consideration of the equations of motion, Eq. (16.7). While for a normal metal, electron wave packets move according to these equations, charge is not a good quantum number in the gapped region and it is therefore necessary to construct a semiclassical wave packet with Bogoliubov-de Gennes (BdG) quasiparticles, so-called bogolons. Their wave function $\Psi_{\mathbf{k}} = (u_{\mathbf{k}}, v_{\mathbf{k}})^T$ is an eigenfunction of the BdG Hamiltonian

$$H_{\mathbf{k}} = \begin{pmatrix} \epsilon_{\mathbf{k}} & \widetilde{\Delta}_{\mathbf{k}} \\ \widetilde{\Delta}_{\mathbf{k}} & -\epsilon_{\mathbf{k}} \end{pmatrix} . \tag{L.1}$$

While Eq. (16.7a) still holds, because the charge e and the velocity $\nabla\epsilon_{\mathbf{k}}$ have opposite sign for particles and holes that cancel each other, the second equation has to be substituted by

$$\dot{\mathbf{r}} = \left(|u_{\mathbf{k}}|^2 - |v_{\mathbf{k}}|^2\right) \frac{1}{\hbar} \nabla_{\mathbf{k}} \epsilon_{\mathbf{k}} \, . \tag{L.2}$$

Particles and holes move in opposite directions, and this equation describes the net center of mass motion of the bogolon wave packet.

In the semiclassical approach the influence of a magnetic field is translated into a periodic time dependence, $H(t+T) = H(t)$ with the period $T = 2\pi/\omega_c$. In the gapless case, $H(t) =$ const. However, a finite gap leads to a time-dependence in the gap parameter, $\Delta(t) = \Delta_{\mathbf{k}(t)}$, where $\mathbf{k}(t)$ satisfies Eq. (16.7a), and therefore the new periodicity condition becomes

$$H(t+T) = H(t) \equiv H_{\mathbf{k}(t)} \, . \tag{L.3}$$

The energy $\epsilon = \epsilon_{\mathbf{k}}$ is still a constant of motion.

The time-dependent Schrödinger equation,

$$\mathrm{i}\hbar\dot{\Psi} = H(t)\Psi \, , \tag{L.4}$$

is solved by using the Floquet theorem (Stöckmann, 1999) for Hamiltonians that are periodic in time, which is analogous to the Bloch theorem for space-periodic Hamiltonians. According to this theorem the eigenfunctions are given by $\Psi(t) = e^{-\mathrm{i}Et/\hbar} f_E(t)$ with $f_E(t+T) = f_E(t)$, where $f_E(t)$ is the eigenstate of the Floquet operator

$$\mathcal{F} = \mathcal{T} \exp\left[-\frac{\mathrm{i}}{\hbar} \int_0^T H(t) dt \right] , \tag{L.5}$$

with the time-ordering operator $\mathcal{T}$.

We skip the details for the calculation of the eigenfunctions Ψ, the eigenvalues E and the associated density of states and refer the interested reader to (Pereg-Barnea et al.). The calculation is performed under the assumption of $\tau = 0$, refering to a sharp step in the gap function, and a field-independent gap structure. $\epsilon \ll \Delta_0$ reveals an oscillatory behavior in the density of states as a function of energy with the frequency

$$F_\epsilon = \frac{\theta_a}{\pi\hbar\omega_c}\,, \tag{L.6}$$

and as a function of inverse magnetic field with the frequency

$$F = \Delta_0 \frac{\theta_g m_c}{\pi\hbar e}\,. \tag{L.7}$$

θ_a and θ_g are the angular sizes of the arc and the gapped region with $\theta_g = \pi/2 - \theta_a$. m_c is the cyclotron mass and e the electron charge.

For an illustration of the underlying physics, we now have a closer look at oscillations in the DOS as a function of inverse magnetic field. While tuning $1/B$, maxima and minima periodically appear in the DOS when the condition $\Delta_0\theta_g/\hbar\omega_c = (p + 1/2)\pi$ (for maximum) and $\Delta_0\theta_g/\hbar\omega_c = p\pi$ (for minimum) holds with $p \in \mathbb{Z}$. The states that are present at such a minimum or maximum are rather different. Their real-space trajectories as well as the shape of the wave function (u, v) significantly deviate, which is shown in Fig. L.1. Panel (a) and (b) illustrate the states contributing to a peak in the DOS: On the arc, $|u|^2 - |v|^2$ vanishes implying that the state $(u, v) \sim (1, \pm\mathrm{i})$ is a perfect mixture of particles and holes and resembles an Andreev bound state (Andreev, 1964; Adagideli et al., 1999). The velocity on the arc is zero, compare Eq. (L.2), leading to a small enclosed real-space area. In the gapped region, the pseudospin, that describes the particle-hole mixing, precesses. In contrast, for values of the magnetic field where the DOS is in a minimum (see panel (c) and (d)) the states consist of either particles or holes on the arc ($|u|^2 - |v|^2 = \pm 1$). The large velocity leads to a large enclosed real space area.

In summary, the oscillatory behavior in the density of states as a function of inverse magnetic field is determined by the match between the time needed to traverse the gapped region ($= \theta_g/\omega_c$) and for a pseudospin precession: When the pseudospin precesses for exactly an integer and a half cycle during the motion over the gapped region, compare Fig. L.1(b), the state on the arc is of Andreev-type.

In the limit of $\Delta_0 \to 0$ or $\theta_g \to 0$, which both describe the metallic limit, the recovery of the standard Onsager result is subtle and requires the consideration of the action quantization. In the presented semiclassical approach no quantization condition was imposed by hand. Nevertheless, a calculation of the action,

$$\mathcal{S} \sim \frac{1}{B}\mathcal{A}^{\mathrm{mom}} \left|\cos\left(\frac{\Delta_0\theta_g}{\hbar\omega_c}\right)\right|\,, \tag{L.8}$$

where $\mathcal{A}^{\mathrm{mom}}$ denotes the encircled momentum-space area, shows that it becomes zero for a peak in the DOS (where $\Delta_0\theta_g/\hbar\omega_c = (p+1/2)\pi$ with $p \in \mathbb{Z}$), prooving the existence of a quantized

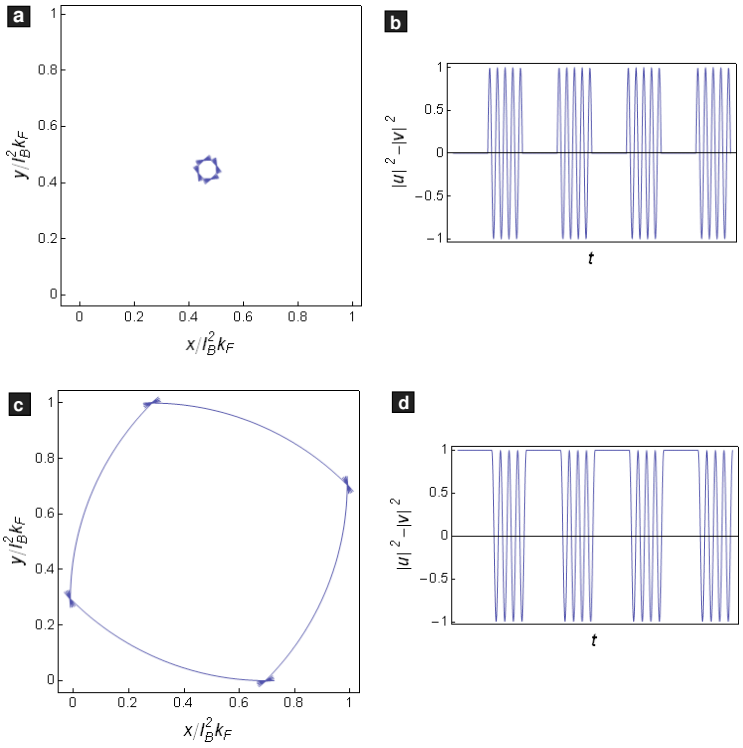

Figure L.1: Real-space trajectories (left column) and $|u|^2 - |v|^2$ as a function of time t for one period (right column). (a) and (b): For a state that is present when the DOS has a peak ($\hbar\omega_c = \Delta_0\theta_g/(4 + 1/2)\pi$). (c) and (d): For a state that is present when the DOS is low ($\hbar\omega_c = \Delta_0\theta_g/4\pi$).
Please note that due to the particle-hole symmetry of the model a state with $u \leftrightarrow v$ also represents an eigenfunction.
l_B denotes the magnetic length and k_F is the Fermi wave vector. (Figure from Pereg-Barnea et al.)

action for the periodically appearing Andreev-type states. For $\Delta_0 \to 0$ or $\theta_g \to 0$, i.e., for a normal metal, the action becomes $\mathcal{S} \sim \mathcal{A}^{\mathrm{mom}}/B$, like in the Onsager approach, compare Eq. (16.10). In this limit, the frequency F goes to zero, and the physics is dominated by an additional frequency arising from the quantization of $\mathcal{S}$, which corresponds to the Onsager frequency and dominates as soon as the gap closes.

In the limit of an ordinary d-wave superconductor, i.e., $\theta_a \to 0$, the oscillation amplitude, which is controlled by a prefactor $\theta_a/\hbar\omega_c$, is suppressed and oscillations break down.

Scaling arguments, like the one that holds for a normal metal or the Simon-Lee scaling for a d-wave superconductor, cannot be established in the considered system. Therefore, no simple way is known to relate the frequencies F and F_ϵ, and e.g. explain their different dependence on the gap parameter Δ_0 and the angular sizes θ_a and θ_g. Unlike in the case of a normal metal described in Sec. 16.2, the oscillation frequency is not associated with an area in momentum space, but rather results from the periodic appearance of Andreev-type states.

Bibliography: Cuprate superconductors

Adagideli, I., P. Goldbart, A. Shnirman, and A. Yazdani. *Low-energy quasiparticle states near extended scatterers in d-wave superconductors and their connection with SUSY quantum mechanics.* Phys. Rev. Lett. **83**, 5571 (1999).

Anderson, E., Z. Bai, C. Bischof, S. Blackford, J. Demmel, J. Dongarra, J. D. Croz, A. Greenbaum, S. Hammarling, A. McKenney, and D. C. Sorensen. *LAPACK users' guide, third edition.* SIAM, Philadelphia (1999).

Anderson, P. W. *The resonating valence bond state in La_2CuO_4 and superconductivity.* Science **235**, 1196 (1987).

Andreev, A. F. Zh. Eksp. Teor. Fiz. **46**, 1823 (1964).

Auerbach, A. *Interacting electrons and quantum magnetism.* Springer-Verlag, New York (1994).

Bangura, A. F., J. D. Fletcher, A. Carrington, J. Levallois, M. Nardone, B. Vignolle, P. J. Heard, N. Doiron-Leyraud, D. LeBoeuf, L. Taillefer, S. Adachi, C. Proust, and N. E. Hussey. *Small Fermi surface pockets in underdoped high temperature superconductors: Observation of Shubnikov - de Haas oscillations in $YBa_2Cu_4O_8$.* Phys. Rev. Lett. **100**, 047 004 (2008).

Bednorz, J. G. and K. A. Müller. *Possible high T_c superconductivity in the Ba-La-Cu-0 system.* Z. Phys. B: Condens. Matt. **64**, 189 (1986).

Berg, E. and E. Altman. *Evolution of the Fermi surface of d-wave superconductors in the presence of thermal phase fluctuations.* Phys. Rev. Lett. **99**, 247 001 (2007).

Chakravarty, S. and H.-Y. Kee. *Fermi pockets and quantum oscillations of the Hall coefficient in high temperature superconductors.* Proc. Natl. Acad. Sci. USA **105**, 8835 (2008).

Chen, W.-Q., K.-Y. Yang, T. M. Rice, and F. C. Zhang. *Quantum oscillations in magnetic field induced antiferromagnetic phase of underdoped cuprates : Application to ortho-II $YBa_2Cu_3O_{6.5}$.* Europhys. Lett. **82**, 17 004 (2008).

Corson, J., R. Mallozzi, J. Orenstein, J. N. Eckstein, and I. Bozovic. *Vanishing of phase coherence in underdoped $Bi_2Sr_2CaCu_2O_{8+\delta}$.* Nature **398**, 221 (1999).

Dagotto, E. *Correlated electrons in high-temperature superconductors.* Rev. Mod. Phys. **66**, 763 (1994).

Damascelli, A., Z. Hussain, and Z.-X. Shen. *Angle-resolved photoemission studies of the cuprate superconductors.* Rev. Mod. Phys. **75**, 473 (2003).

Di Stasio, M., K. A. Müller, and L. Pietronero. *Nonhomogeneous charge distribution in layered high-T_c superconductors.* Phys. Rev. Lett. **64**, 2827 (1990).

Ding, H., T. Yokoya, J. C. Campuzano, T. Takahashi, M. Randeria, M. R. Norman, T. Mochiku, K. Kadowaki, and J. Giapintzakis. *Spectroscopic evidence for a pseudogap in the normal state of underdoped high-T_c superconductors.* Nature **382**, 51 (1996).

Doiron-Leyraud, N., C. Proust, D. LeBoeuf, J. Levallois, J.-B. Bonnemaison, R. Liang, D. A. Bonn, W. N. Hardy, and L. Taillefer. *Quantum oscillations and the Fermi surface in an underdoped high-Tc superconductor.* Nature **447**, 565 (2007).

Emery, V. J. *Theory of high-T_c superconductivity in oxides.* Phys. Rev. Lett. **58**, 2794 (1987).

Fischer, O., M. Kugler, I. Maggio-Aprile, and C. Berthod. *Scanning tunneling spectroscopy of high-temperature superconductors.* Rev. Mod. Phys. **79**, 353 (2007).

Franz, M. and A. J. Millis. *Phase fluctuations and spectral properties of underdoped cuprates.* Phys. Rev. B **58**, 14 572 (1998).

Franz, M. and Z. Tešanović. *Quasiparticles in the vortex lattice of unconventional superconductors.* Phys. Rev. Lett. **84**, 554 (2000).

Gough, C. E., M. S. Colclough, E. M. Forgan, R. G. Jordan, M. Keene, C. M. Muirhead, A. I. M. Rae, N. Thomas, J. S. Abell, and S. Sutton. *Flux quantization in a high-T_c superconductor.* Nature **326**, 855 (1987).

de Haas, W. J. and P. M. van Alphen. *Oscillatory field dependence of susceptibility in bismuth.* Proc. Netherlands Roy. Acad. Sci **33**, 1106 (1930).

Horsch, P., W. H. Stephan, K. v. Szczepanski, M. Ziegler, and W. von der Linden. *Quasiparticles and photoemission spectra in correlated fermion systems.* Physica C **162-164**, 783–784 (1989).

Hossain, M., J. Mottershead, D. Fournier, A. Bostwick, J. L. McChesney, E. Rotenberg, R. Liang, W. N. Hardy, G. A. Sawatzky, I. S. Elfimov, D. A. Bonn, and A. Damascelli. *In situ doping control of the surface of high-temperature superconductors.* Nature Physics **4**, 527 (2008).

Hubbard, J. *Electron correlations in narrow energy bands.* Proc. Roy. Soc. A **276**, 238 (1963).

Hubbard, J. *Electron correlations in narrow energy bands II. The degenerate band case.* Proc. R. Soc. London, Ser. A **277**, 237 (1964a).

Hubbard, J. *Electron correlations in narrow energy bands III. An improved solution.* Proc. R. Soc. London, Ser. A **281**, 401 (1964b).

Jaudet, C., D. Vignolles, A. Audouard, J. Levallois, D. LeBoeuf, N. Doiron-Leyraud, B. Vignolle, M. Nardone, A. Zitouni, R. Liang, D. A. Bonn, W. N. Hardy, L. Taillefer, and C. Proust. *de Haas - van Alphen oscillations in the underdoped high-temperature superconductor $YBa_2Cu_3O_{6.5}$.* Phys. Rev. Lett. **100**, 187 005 (2008).

Kanigel, A., U. Chatterjee, M. Randeria, M. R. Norman, G. Koren, K. Kadowaki, and J. C. Campuzano. *Evidence for pairing above the transition temperature of cuprate superconductors from the electronic dispersion in the pseudogap phase.* Phys. Rev. Lett. **101**, 137 002 (2008).

Kanigel, A., M. R. Norman, M. Randeria, U. Chatterjee, S. Souma, A. Kaminski, H. M. Fretwell, S. Rosenkranz, M. Shi, T. Sato, T. Takahashi, Z. Z. Li, H. Raffy, K. Kadowaki, D. Hinks, L. Ozyuzer, and J. C. Campuzano. *Evolution of the pseudogap from Fermi arcs to the nodal liquid.* Nature Physics **2**, 447 (2006).

Kastner, M. A., R. J. Birgeneau, G. Shirane, and Y. Endoh. *Magnetic, transport, and optical properties of monolayer copper oxides.* Rev. Mod. Phys. **70**, 897 (1998).

Lee, P. A. and D. S. Fisher. *Anderson localization in two dimensions.* Phys. Rev. Lett. **47**, 882 (1981).

Lee, P. A., N. Nagaosa, and X.-G. Wen. *Doping a Mott insulator: Physics of high-temperature superconductivity.* Rev. Mod. Phys. **78**, 17 (2006).

Lehoucq, R. B., D. C. Sorensen, and C. Yang. *ARPACK users' guide: Solution of large-scale eigenvalue problems with implicitly restarted Arnoldi methods.* SIAM, Philadelphia (1998).

Lifshitz, I. and A. Kosevich. Zh. Eksp. Teor. Fiz. **29**, 730 (1955).

Loeser, A. G., Z.-X. Shen, D. S. Dessau, D. S. Marshall, C. H. Park, P. Fournier, and A. Kapitulnik. *Excitation gap in the normal state of underdoped* $Bi_2\ Sr_2CaCu_2O_{8+\delta}$. Science **273**, 325 (1996).

Maggio-Aprile, I., C. Renner, A. Erb, E. Walker, and O. Fischer. *Direct vortex lattice imaging and tunneling spectroscopy of flux lines on* $YBa_2Cu_3O_{7-\delta}$. Phys. Rev. Lett. **75**, 2754 (1995).

Maki, K. *Quantum oscillations in vortex state of type-II superconductors.* Phys. Rev. B **44**, 2861 (1991).

Marshall, D. S., D. S. Dessau, A. G. Loeser, C.-H. Park, A. Y. Matsuura, J. N. Eckstein, I. Bozovic, P. Fournier, A. Kapitulnik, W. E. Spicer, and Z.-X. Shen. *Unconventional electronic structure evolution with hole doping in* $Bi_2Sr_2CaCu_2O_{8+\delta}$ *: Angle-resolved photoemission results.* Phys. Rev. Lett. **76**, 4841 (1996).

Mattheiss, L. F. *Electronic band properties and superconductivity in* $La_{2-y}X_yCuO_4$. Phys. Rev. Lett. **58**, 1028 (1987).

Melikyan, A. and O. Vafek. *Quantum oscillations in the mixed state of d-wave superconductors.* Phys. Rev. B **78**, 020 502 (2008).

Millis, A. J. and M. R. Norman. *Antiphase stripe order as the origin of electron pockets observed in 1/8-hole-doped cuprates.* Phys. Rev. B **76**, 220 503(R) (2007).

Mott, N. F. *The basis of the electron theory of metals, with special reference to the transition metals.* Proc. Phys. Soc. London, Sect. A **62**, 416 (1949).

Mott, N. F. *On the transition to metallic conduction in semiconductors.* Can. J. Phys. **34**, 1356 (1956).

Norman, M. R., H. Ding, M. Randeria, J. C. Campuzano, T. Yokoya, T. Takeuchik, T. Takahashi, T. Mochiku, K. Kadowaki, P. Guptasarma, and D. G. Hinks. *Destruction of the Fermi surface in underdoped high-T_c superconductors.* Nature **392**, 157 (1998).

Onsager, L. *Interpretation of the de Haas - van Alphen effect.* Phil. Mag. **43**, 1006 (1952).

Pereg-Barnea, T., H. Weber, G. Refael, and M. Franz. *Quantum oscillations from Fermi arcs.* submitted to Nature Physics ().

Sachdev, S. *Quantum criticality: Competing ground states in low dimensions.* Science **288**, 475 (2000).

Salkola, M. I., V. J. Emery, and S. A. Kivelson. *Implications of charge ordering for single-particle properties of high-T_c superconductors.* Phys. Rev. Lett. **77**, 155 (1996).

Sasaki, T., T. Fukuda, N. Yoneyama, and N. Kobayashi. *Shubnikov-de Haas effect in the quantum vortex liquid state of the organic superconductor κ-(BEDT-TTF)$_2$Cu(NCS)$_2$.* Phys. Rev. B **67**, 144 521 (2003).

Schilling, A., M. Cantoni, J. D. Guo, and H. R. Ott. *Superconductivity above 130 K in the Hg-Ba-Ca-Cu-0 system.* Nature **363**, 56 (1993).

Schwaigerer, F., B. Sailer, J. Glaser, and H.-J. Meyer. *Strom eiskalt serviert.* Chemie in unserer Zeit **2**, 108 (2002).

Sebastian, S. E., N. Harrison, E. Palm, T. P. Murphy, C. H. Mielke, R. Liang, D. A. Bonn, W. N. Hardy, and G. G. Lonzarich. *A multi-component Fermi surface in the vortex state of an underdoped high-T_c superconductor.* Nature **454**, 200 (2008).

Senthil, T. and M. P. A. Fisher. *More is different: Fifty years of condensed matter physics*, chapter Quantum confinement transition and cuprate criticality. Princeton University Press (2001).

Shen, K. M., F. Ronning, D. H. Lu, F. Baumberger, N. J. C. Ingle, W. S. Lee, W. Meevasana, Y. Kohsaka, M. Azuma, M. Takano, H. Takagi, and Z.-X. Shen. *Nodal quasiparticles and antinodal charge ordering in $Ca_{2-x}Na_xCuO_2Cl_2$.* Science **307**, 901 (2005).

Shen, Z. X., D. S. Dessau, B. O. Wells, D. M. King, W. E. Spicer, A. J. Arko, D. Marshall, L. W. Lombardo, A. Kapitulnik, P. Dickinson, S. Doniach, J. DiCarlo, A. G. Loeser, and C. H. Park. *Anomalously large gap anisotropy in the a-b plane of $Bi_2Sr_2CaCu_2O_{8+\delta}$.* Phys. Rev. Lett. **70**, 1553 (1993).

Shen, Z.-X., J. Harris, and A. Loeser. *Excitation gap in the normal and superconducting state of underdoped $Bi_2Sr_2Ca_{1-x}Dy_xCu_2O_{8+\delta}$ thin film and single crystals.* Hyperfine Interactions **105**, 13 (1997).

Sigrist, M. and K. Ueda. *Phenomenological theory of unconventional superconductivity.* Rev. Mod. Phys. **63**, 239 (1991).

Simon, S. H. and P. A. Lee. *Scaling of the quasiparticle spectrum for d -wave superconductors.* Phys. Rev. Lett. **78**, 1548 (1997).

Spałek, J. and A. M. Oleś. *Ferromagnetism in narrow s-band with inclusion of intersite correlations.* Physica B **86-88**, 375 (1977).

Stephen, M. J. *Superconductors in strong magnetic field: de Haas - van Alphen effect.* Phys. Rev. B **45**, 5481 (1992).

Stöckmann, H. J. *Quantum chaos: An introduction.* Cambridge University Press (1999).

Tarascon, J. M., W. R. McKinnon, P. Barboux, D. M. Hwang, B. G. Bagley, L. H. Greene, G. W. Hull, Y. LePage, N. Stoffel, and M. Giroud. *Preparation, structure, and properties of the superconducting compound series $Bi_2Sr_2Ca_{n-1}Cu_nO_y$ with n=1, 2, and 3.* Phys. Rev. B **38**, 8885 (1988).

Tinkham, M. *Introduction to superconductivity.* Krieger, Malabar (1975).

Tranquada, J. M., B. J. Sternlieb, J. D. Axe, Y. Nakamura, and S. Uchida. *Evidence for stripe correlations of spins and holes in copper oxide superconductors.* Nature **375**, 561 (1995).

Vafek, O., A. Melikyan, M. Franz, and Z. Tešanović. *Quasiparticles and vortices in unconventional superconductors.* Phys. Rev. B **63**, 134 509 (2001).

Vignolle, B., A. Carrington, R. A. Cooper, M. M. J. French, A. P. Mackenzie, C. Jaudet, D. Vignolles, C. Proust, and N. E. Hussey. *Quantum oscillations in an overdoped high-T_c superconductor.* Nature **455**, 952 (2008).

Waldram, J. R. *Superconductivity of metals and cuprates.* Institute of Physics Publishing, Bristol and Philadelphia (1996).

Wang, Y., L. Li, M. J. Naughton, G. D. Gu, S. Uchida, and N. P. Ong. *Field-enhanced diamagnetism in the pseudogap state of the cuprate $Bi_2Sr_2CaCu_2O_8$ superconductor in an intense magnetic field.* Phys. Rev. Lett. **95**, 247 002 (2005).

Wells, B. O., Z. X. Shen, D. S. Dessau, W. E. Spicer, D. B. Mitzi, L. Lombardo, A. Kapitulnik, and A. J. Arko. *Evidence for k-dependent, in-plane anisotropy of the superconducting gap in $Bi_2Sr_2CaCu_2O_{8+\delta}$.* Phys. Rev. B **46**, 11 830 (1992).

Wosnitza, J., S. Wanka, J. Hagel, R. Häussler, H. v. Löhneysen, J. A. Schlueter, U. Geiser, P. G. Nixon, R. W. Winter, and G. L. Gard. *Shubnikov - de Haas effect in the superconducting state of an organic superconductor.* Phys. Rev. B **62**, 1654 (2000).

Wu, M. K., J. R. Ashburn, C. J. Torng, P. H. Hor, R. L. Meng, L. Gao, Z. J. Huang, Y. Q. Wang, and C. W. Chu. *Superconductivity at 93 K in a new mixed-phase Y-Ba-Cu-O compound system at ambient pressure.* Phys. Rev. Lett. **58**, 908 (1987).

Xu, Z. A., N. P. Ong, Y. Wang, T. Kakeshita, and S. Uchida. *Vortex-like excitations and the onset of superconducting phase fluctuation in underdoped* $La_{2-x}Sr_xCuO_4$. Nature **406**, 486 (2000).

Yelland, E. A., J. Singleton, C. H. Mielke, N. Harrison, F. F. Balakirev, B. Dabrowski, and J. R. Cooper. *Quantum oscillations in the underdoped cuprate* $YBa_2Cu_4O_8$. Phys. Rev. Lett. **100**, 047 003 (2008).

Zhou, C. and H. J. Schulz. *Density of states and tunneling spectra in two-dimensional d-wave superconductors.* Phys. Rev. B **45**, 7397 (1992).

Acknowledgments

I would like to express my gratitude to those people who supported me during the time as a PhD student. There are:

- Matthias Vojta, whom I would like to thank for the supervision, scientific input and interesting discussions.
- Marcel Franz for being my host at the University of British Columbia, for the suggestion of interesting projects and for valuable discussions.
- Johann Kroha and Markus Grüninger for being members of my PhD committee.
- Babak Seradjeh for a fruitful collaboration.
- Sébastien Burdin and Ricardo Doretto for interesting discussions and proof-reading.
- The members of the following institutes for a friendly and open atmosphere: the Institute for Theoretical Physics at the University of Cologne, the Department of Physics and Astronomy at the University of British Columbia, and the Institute for Condensed Matter Theory at the University of Karlsruhe.
  Among those a special thanks goes to Fabrizio Anfuso, Benedikt Binz, Jan Brinckmann, Ralf Bulla, Karin Everschor, Serge Florens, Lars Fritz, Markus Garst, Benjamin Gutierrez, Poya Haghnegahdar, Andreas Hackl, Rolf Helmes, Lucas Hollender, Verena Koerting, Justin Malecki, Stephan Mandt, Dominic Marchand, Mohammad Mashayekhi, Tobias Meng, Stephan Rachel, David Rasch, Tanja Rindler-Daller, Oliver Rösch, Gili Rosenberg, Hassan Saadaoui, Holger Schmidt, Peter Schmitteckert, Dirk Schuricht, Matthias Sitte, Tobias Ulbricht, Michiel van der Vegte, Conan Weeks, Alexander Wollny, and Mario Zacharias.
- My parents Elisabeth and Hermann and my sister Sonja for their constant support and their unrestricted believe in my abilities.
- All the friends I found due to moving from one place to another and all the old friends I could stay in contact with.

Erklärung

Ich versichere, dass ich die von mir vorgelegte Dissertation selbständig angefertigt, die benutzten Quellen und Hilfsmittel vollständig angegeben und die Stellen der Arbeit – einschließlich Tabellen, Karten und Abbildungen –, die anderen Werken im Wortlaut oder dem Sinn nach entnommen sind, in jedem Einzelfall als Entlehnung kenntlich gemacht habe; dass diese Dissertation noch keiner anderen Fakultät oder Universität zur Prüfung vorgelegen hat; dass sie – abgesehen von unten angegebenen Teilpublikationen – noch nicht veröffentlicht worden ist sowie, dass ich eine solche Veröffentlichung vor Abschluss des Promotionsverfahrens nicht vornehmen werde. Die Bestimmungen der Promotionsordnung sind mir bekannt. Die von mir vorgelegte Dissertation ist von Prof. Dr. Matthias Vojta betreut worden.

Teilpublikationen

- T. Pereg-Barnea, H. Weber, G. Refael und M. Franz
  Quantum oscillations from Fermi arcs
  eingereicht bei Nature Physics

- B. Seradjeh, H. Weber und M. Franz
  Vortices, zero modes and fractionalization in the bilayer-graphene exciton condensate
  Physical Review Letters 101, 246404 (2008)

- H. Weber und M. Vojta
  Heavy-fermion metals with hybridization nodes: Unconventional Fermi liquids and competing phases
  Physical Review B 77, 125118 (2008)